

Asia Pacific Research Initiative for Sustainable Energy Systems 2012 (APRISES12)

Office of Naval Research
Grant Award Number N00014-13-1-0463

Computational Fluid Dynamics (CFD) Applications at the School of Architecture, University of Hawaii: External CFD Simulation & Field Validation

Task 7

Prepared For
Hawaii Natural Energy Institute

Prepared By
Sustainable Design & Consulting LLC, UH Environmental Research and
Design Laboratory, UH Sea Grant College Program & HNEI

October 2014



HNEI
Hawai'i Natural Energy Institute
University of Hawai'i at Mānoa



Project Phase 1- 7.A

**REPORT ON EXTERNAL CFD
SIMULATION & VALIDATION
FOR SELECTED BUILDING**

4.2

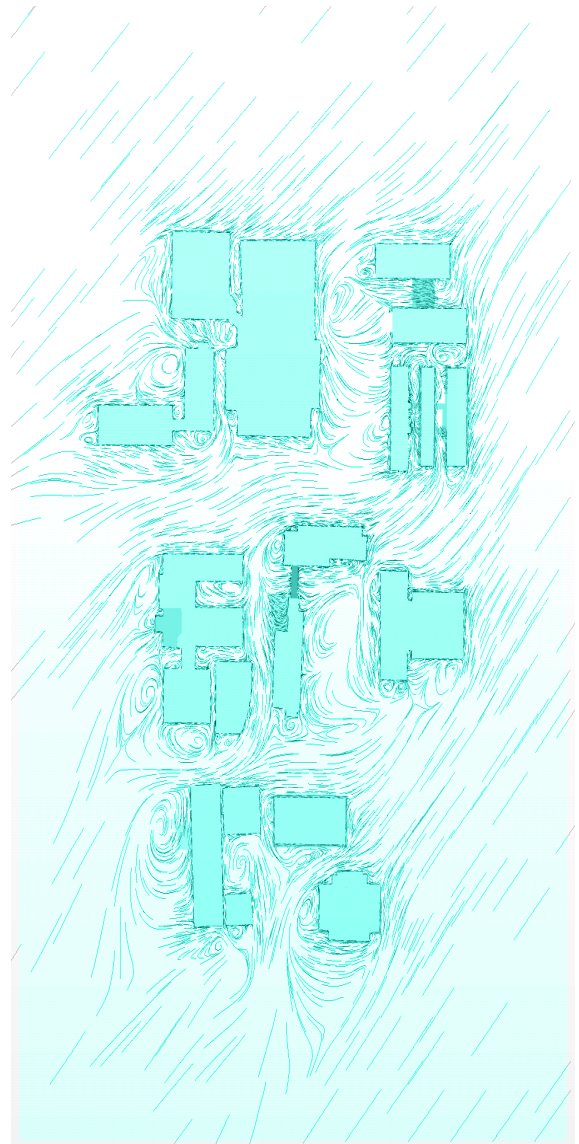
FINAL REPORT

Oct 18, 2014

Prepared by:
Manfred J. Zapka, PhD, PE (Editor)
Tuan Tran, D.Arch
Eileen Peppard, M. Sc.
A. James Maskrey, MEP, MBA, Project Manager
Stephen Meder, D.Arch, Director



Contract # N000-14-13-1-0463



Computational Fluid Dynamics (CFD) Applications at the School of Architecture,
University of Hawaii

Project Phase 1 – 7.A

Develop Skill Set for External CFD Analysis and Verification at the Building

**Project Deliverable No. 4.2: Report on External CFD Simulation & Field
Validation for Selected Building**

FINAL

Prepared for Hawaii Natural Energy Institute

in support of

Contract #N000-14-13-1-0463

October 18, 2014

Prepared by:

Manfred J. Zapka, PhD, PE (Editor) (*)

Tuan Tran, D.Arch (**)

Eileen Peppard, M. Sc. (**)

A. James Maskrey, MEP, MBA, Project Manager (***)

Stephen Meder, D.Arch, Director (**)

(*) Sustainable Design & Consulting LLC

(**) Environmental Research and Design Laboratory (ERDL), School of Architecture, University of Hawaii at
Manoa

(***) Hawaii Natural Energy Institute (HNEI), University of Hawaii at Manoa

ACKNOWLEDGEMENTS

The authors would like to thank the staff of the Environmental Design & Research Laboratory (ERDL) for their assistance in carrying out parts of this research study.

The authors especially acknowledge the dedicated work and valuable input by research assistants Christian Damo and Reed Shinsato, and as well as Post-doctoral fellow Aarthi Padmanabhan.

TABLE OF CONTENTS

EXECUTIVE SUMMARY	I
1. OBJECTIVES	3
2. Approach	4
2.1 Selection of the Site	4
2.2 Initial CFD Simulations.....	7
2.3 Field Measurements.....	8
2.4 Final CFD.....	8
2.5 Comparison of CFD and Field Measurements.....	9
3. METHODOLOGY	10
3.1 Initial CFD Simulations.....	10
3.1.1 3D-Model of Keller Hall (decoupled computational domains)	10
3.1.2 Initial CFD Settings.	13
3.1.3 Evaluation of Initial CFD for Field Verification	15
3.2 Field measurements.....	17
3.2.1 Weather Station on Keller Hall Roof.....	18
3.2.2 Wind Speed Measurement around Keller Hall Building	22
3.2.3 External Pressure Measurements at Keller Hall Building.....	29
3.2.4 Data Acquisition	33
3.3 Final CFD Simulations	34
3.3.1 Refinement of Computational Domain	34
3.3.2 Settings According to Measured Wind Conditions	38
3.3.3 Post Processing	41

4. RESULTS AND DISCUSSION 46

4.1 Results of Field Measurements of Wind Speed and Directions..... 46

4.2 Results of Field Measurements of for Wind Induced Pressure..... 52

4.3 Results of CFD Simulations..... 54

4.4 Discussion of Results 62

5. CONCLUSION AND RECOMMENDATIONS 73

REFERENCES..... 78

ACRONYMS

APPENDIX A: RESULTS OF CFD SIMULATIONS

APPENDIX B: INSTRUMENTATION USED IN THE FIELD TESTS

EXECUTIVE SUMMARY:

The research work presented in this report is part of the ongoing HNEI sponsored research program about the use of Computational Fluid Dynamics (CFD) in building analysis and design, with an emphasis on naturally ventilated buildings. The research program has three parts: Part 1-- use of external CFD simulations to model wind movements around buildings and how they affect natural ventilation; Part 2 - use of internal CFD simulations to study air movement through a building and identify measures to improve naturally ventilation performance; and Part 3 -- use of CFD simulations to study the effectiveness of measures that increase comfort in naturally ventilated spaces. This report presents the last external CFD investigation of Part 1 of the HNEI sponsored research program.

This report describes the results of an applied CFD research study of wind induced wind pattern and pressure distributions around a building on the Manoa campus of the University of Hawaii. The CFD theoretical predictions were validated through full scale measurement of wind velocities and pressures around a selected building.

The work was performed by a research collaboration between Hawaii Natural Energy Institute, Sustainable Design and Consulting, LLC, and the Environmental Design and Research Laboratory (ERDL) of the School of Architecture. The work on this study lasted from March through September 2014. The UH Manoa Keller Hall building was the selected building for the external CFD simulation work. Keller Hall is a partially ventilated building and after the completion of the external CFD investigation the building will also be used for the following internal CFD investigations.

A weather station was installed on the roof of Keller Hall to record wind and other environmental data over the four months period. The data recordings were used to determine the primary wind approach directions. Several differential pressure transducers with connected pressure tubing were installed for four months on the North and South facades of the building to record time series of differential pressures across the building. Differential pressures between upwind and downwind sides are the driving force for natural ventilation in buildings. The pressure recordings were compared with the theoretical CFD predictions of differential pressure around the building.

For selected days, wind speed and direction were measured with six hot-wire anemometers and one temporary weather station at selected locations around the building. Initial CFD simulations identified preferred locations around the building where validation of the theoretical CFD would be obtained.

Final CFD simulation runs with a refined 3D-geometry of the building and a higher resolution mesh of the computational grid were carried out using the measured climatic conditions as boundary conditions. A large number of CFD simulation runs were conducted to benchmark against varying mesh resolution, wind directions and variation of wind directions and obtain consistent CFD results.

The results of the CFD investigation suggest the immediate practical usefulness of numerical CFD analysis to predict wind induced air movement (both speed and direction) as well as pressure distribution around Keller Hall and surrounding buildings. Comparison between theoretical CFD predictions and actual field measurements gave reasonable to good correlation. The magnitude of divergence between values obtained CFD and actual field data obtained in the present study are within a range reported in the literature.

Certain limitations of the available instrumentation, unsteady wind movement pattern around the building and interactions of surrounding buildings were identified as most likely causes for discrepancies against values obtained in CFD simulations and field measurements. By comparing numerically derived and actually observed wind movement phenomena it has to be kept in mind that the type of steady-state CFD simulations used in the study are “snap-shots” in time for a specific set of boundary conditions. Actually measured data in the field, on the other side, represent extensive data series wind velocities and pressures over a long time periods with significant fluctuations dependent on the prevailing wind direction and speed. Therefore, dealing with deviations of data obtained by CFD predictions and actual field measurement presents challenges of correlating non-steady state (field data) with steady-state CFD simulation conditions. The literature reports that CFD predictions and actual field measurements for wind and pressure occurrences around buildings typically differ, sometimes even significantly. The selected approach of this study endeavored to resolve the non-steady and steady state phenomena by establishing a set of values that would emulate some form of range in the CFD simulations, rather than one fixed wind approach. The preferred methodology used up the three main wind approach directions and added two alternative wind direction to each main wind approach direction. The two alternative wind directions were offset 10 degrees to either side of the main wind approach directions. CFD results were obtained for the main wind approach direction plus two alternative wind directions for each main wind approach.

The study provided important theoretical and practical application experience for CFD simulation in building applications as well as data acquisition for full-scale validation of CFD derived predictions. The results of the study provides therefore a significant contribution in better understanding wind movement around buildings, which is an important design consideration for naturally ventilated buildings and other aspects of high performance building design. The experiences gained will support the research team in the continuing applied research efforts on CFD application for the design of high performance and sustainable buildings in Hawaii.

1. OBJECTIVES

The objectives of this part of the research studies are as follows:

- Select a building for which wind induced wind patterns and pressure differentials are studied through CFD analysis and measurements in the field. The selected building is a naturally ventilated building that will allow modeling and measurements of internal air movements in addition to determination of external wind occurrences. The investigation of internal air flow through the building will be carried out in Part 2 of the research program.
- Using the CFD workflow procedures and instrumentation deployment experience developed and gained in the initial stages of Part 1 the research program project, in order to determine the practicality of conventional CFD applications for the assessment of natural ventilation building performance.
- Determine how well steady-state CFD predictions of wind movement around buildings compare with observations carried out in the field. Non-steady state CFD simulations were outside the scope of the present study.
- Identify if there are preferred wind conditions, such as wind speed and approach direction, under which CFD predictions have the most significant prediction value.
- Measure possible non-steady state air movement processes around buildings which cannot be determined with steady-state CFD but which might be an important design consideration for buildings that rely on natural ventilation.

2. APPROACH

This section of the report describes the approach of the external CFD study. The section is divided into five parts which reflect the successive steps of the research work.

2.1 Selection of the Site

The site of this investigation was Keller Hall on the University of Hawaii Manoa campus. The 60,000 sqft building was completed in 1959 and was home of the Engineering School unit 1972, when the engineering school moved to the current location of Holmes Hall. Figure 2.1.1 shows the vicinity map of Keller Hall. The Figure shows that Keller Hall is surrounded by numerous buildings. The prevailing winds for the campus in Manoa Valley are trade winds that approach Keller Hall from the North-East. Figure 2.1.2 shows a vicinity map of Keller Hall with the Main Mall running immediately to the North of Keller Hall.

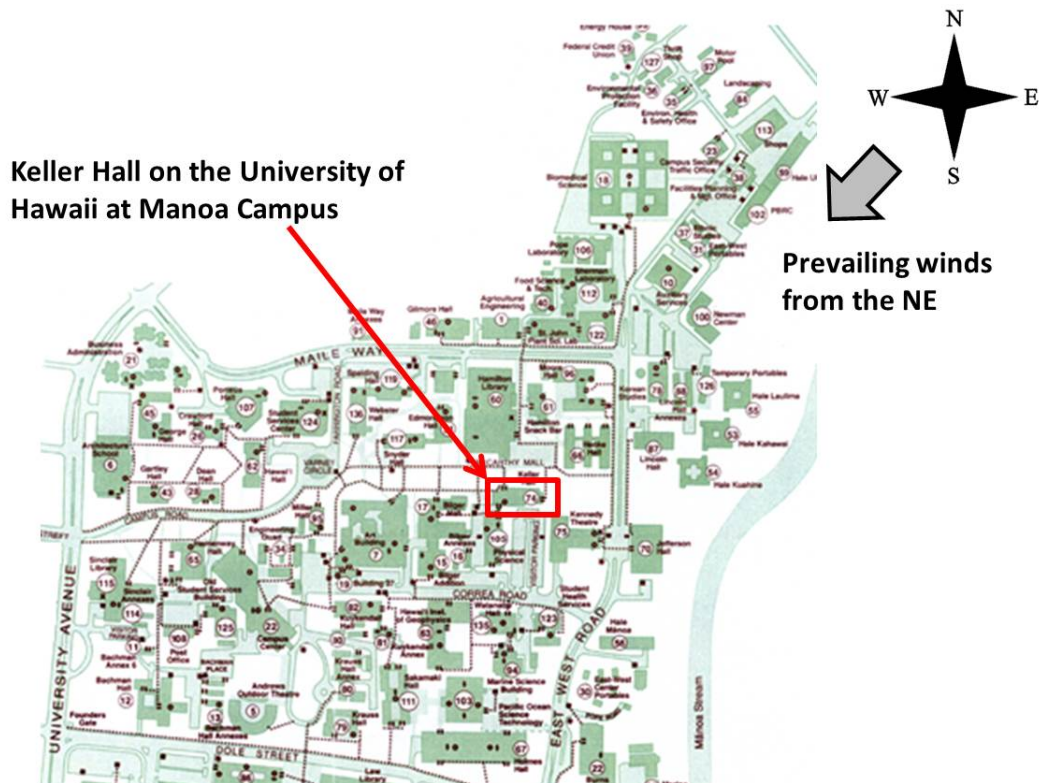


Figure 2.1.1: Location of Keller Hall within the University of Hawaii Manoa campus

Keller Hall was designed as a naturally ventilated building and a portion of the building remains naturally ventilated today. Over time, portions of the building were fitted with mechanical ventilation and cooling. The third floor of the building has several class rooms which are naturally ventilated. The class rooms are located opposite each other in North-South direction and separated by an East-West corridor, which is also naturally ventilated.

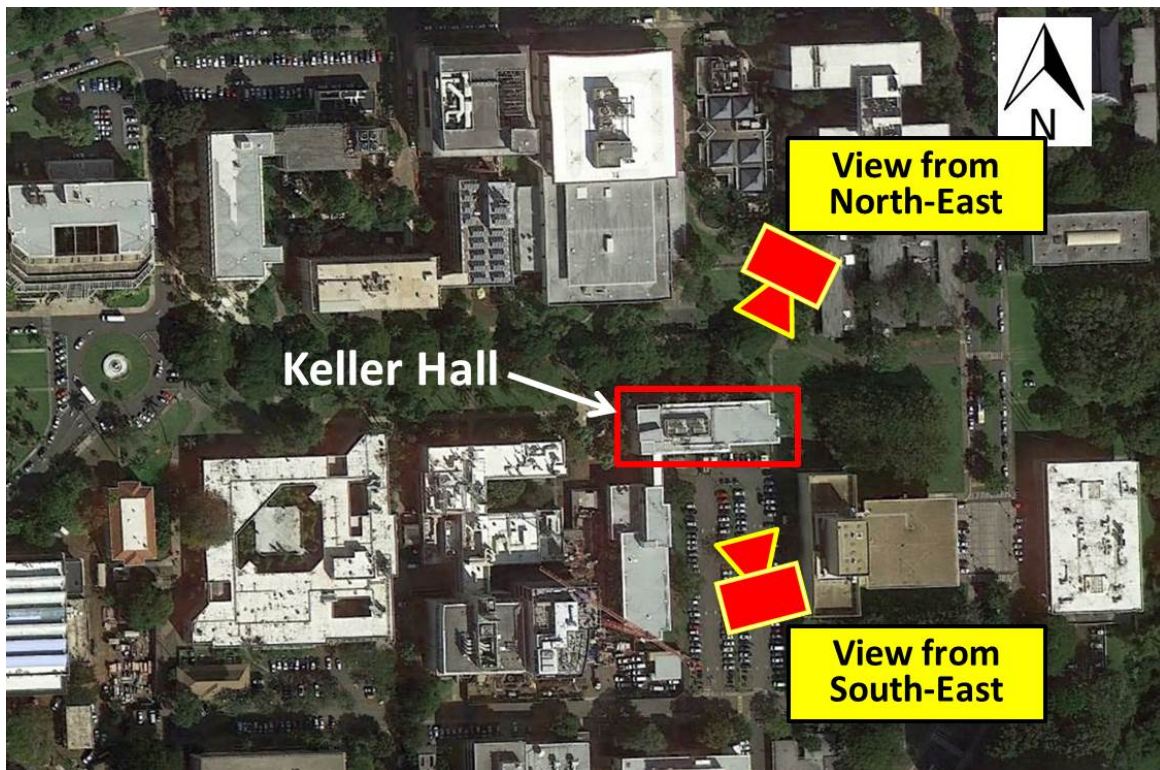


Figure 2.1.2: Vicinity Map of Keller Hall

Figures 2.1.3 through 2.1.5 show external views of Keller Hall. The views from North-East and South-East on Keller Hall are indicated in Figure 2.1.2. Figures 2.1.3 and 2.1.4 show views of Keller Hall from the North-East and Figure 2.1.5 from the South-East, respectively.



Figure 2.1.3: View of Keller Hall from the North-East

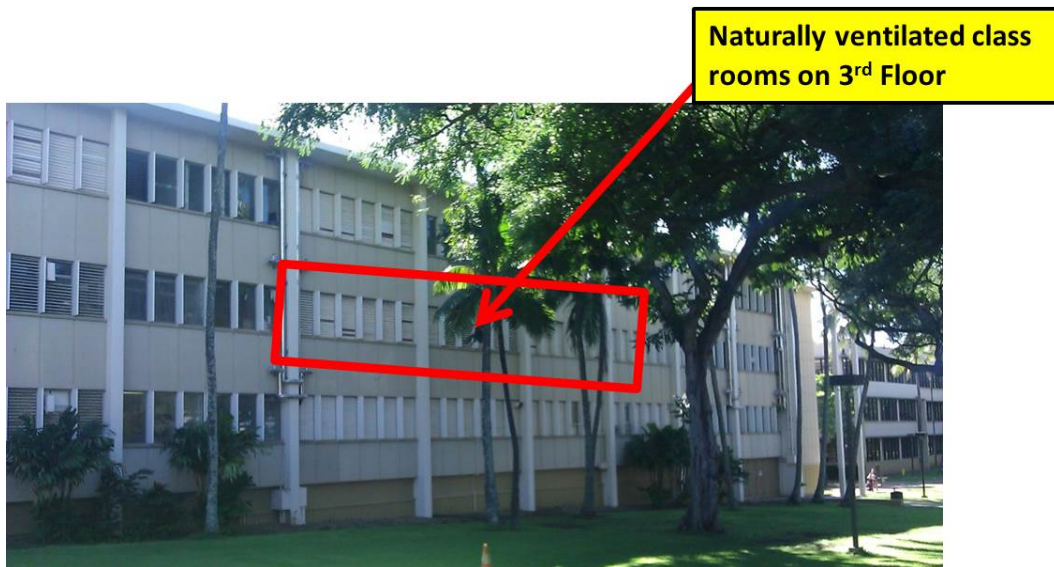


Figure 2.1.4: View of Keller Hall from the North-East, the location of the naturally ventilated classrooms on the 3rd floor of the building is indicated



Figure 2.1.5: View of Keller Hall from the South -East, the location of the naturally ventilated classrooms on the 3rd floor of the building is indicated

2.2 Initial CFD Simulations

It was determined that both wind velocity and pressure distribution on the building envelope were the two parameters that would be modeled in CFD and validated in the field.

Based on literature review it was decided to measure only wind speeds but not pressures in the wind regime surrounding the building. The pressure differentials were measured on the building envelope, within the stagnation layer in order to determine the pressure driving forces for the natural ventilation processes.

Initial CFD analysis was carried out in order to assess suitable locations for the wind speed measurements. The locations for the wind speed measurements were selected to coincide with locations that indicated higher wind speeds in the initial CFD simulations.

The initial CFD simulations used historical data for wind approach direction and wind speeds. Furthermore, the initial CFD simulations used an approximate geometry of Keller Hall, without modeling detail building envelope appurtenances. The computational domain consistent of a coarse grid which

enabled expeditious simulation runs. Several simulations were conducted to identify locations around the building that had high wind speeds and/or large wind speed differentials.

At this stage in the project work it was unimportant to determine the predicted wind speed regime around the building, since the final CFD simulations would use the prevailing wind directions and speeds.

2.3 Field Measurements

Field measurements involved the measurements of two parameters, wind speed and wind induced pressure differentials.

The field measurements of wind speed were conducted on two consecutive days, within a period of higher than normal wind speeds. Weather forecasts were tracked for several days and the decision to deploy the instrument in the field was made on relative short notice. The days when measurements were carried out had stronger than normal winds at the test site. The measurements lasted about six hours per day of measurements. Hotwire anemometers were placed at the predetermined locations to measure and record wind speed. The results of the anemometers were correlated against a portable weather station, which was deployed at ground level for the duration of the wind measurements.

The field measurements of pressures were conducted with pressure transducers that were installed on the exterior building envelope for the entire duration of tests. The duration of the pressure measurements was approximately four months, starting in April and ending in August 2014.

The field measurements included the recording of the prevailing wind direction and speed along with pertinent climatic readings, such as air temperature and relative humidity, with a weather station that was installed on the roof of Keller Hall for the duration of the tests.

2.4 Final CFD

After the completion of the test period, e.g. when pressure and other climatic readings were recorded, a set of final CFD simulation was carried out. For the final CFD analysis input values for incident wind, air temperature and humidity were used which were provided by the field measurements.

The final CFD simulations employed a detailed 3D-model of the Keller Hall building structure. Physical details such as external fins were added to the 3D-model of the building, which was used during the initial CFD simulations. The final CFD analysis used much higher grid resolutions than the initial CFD simulations.

2.5 Comparison of CFD and Field Measurements

The comparison between CFD simulations and field observations was carried out using weighted averages of incident wind direction. The weighted average approach involved determining three main approach wind directions. Multiple approach wind directions had to be used since the wind directions measurements at the site suggested prevailing winds from more than one direction. For the CFD simulation each approach wind direction was used in addition to two subset wind direction which deviated from the approach wind direction by a certain +/- value. The CFD results for the approach wind direction and two subset directions were then averaged.

3. METHODOLOGY

This section of the report provides details about the methodology chosen for the investigation.

3.1 Initial CFD Simulations

The main objective of initial CFD simulations was to get a qualitative description of the wind regime around the Keller Hall building. The results of the initial CFD simulations were used to determine preferred location to place anemometers around the building for wind speed measurements.

3.1.1 3D-Model of Keller Hall (decoupled computational domains)

The 3D-model for the initial CFD simulations was an approximation of Keller Hall building. The building envelope was modeled with an opaque surface, which means that the computational domain did not connect the internal air volume of the building to the external air volume. In doing so the building envelope was modeled as impermeable surfaces. Therefore, the approach of the external CFD simulations was a “decoupled domain”, as defined in the literature

During the earlier CFD analysis of Part 1 of the CFD research program AutoCAD Inventor was used to create the 3D-CAD models for the CFD analysis. For the CFD analysis presented in this report Google SketchUp and Rhinoceros 3D modeling applications were found to be more effective building the virtual CAD model of Keller Hall.

Another significant benefit was that by using the Google SketchUp application, it is possible to download available 3D models of buildings from the internet as well as topographic terrains for the project site. The Google SketchUp models were then imported into Rhinoceros 3D, a versatile 3D modeling software which is widely used by architecture students and professionals.

Rhinoceros 3D allows exporting the geometry files into a variety of other file formats to work with a range of applications. Exporting the files in a Stereo Lithography format worked well with STAR-CCM+ and this process is recommended as the new workflow of geometry modeling process for the remainder of the CFD research.

The process of 3D CAD modeling the external computational domain of the Keller Halls and its surrounding buildings is summarized as follows:

- 3D models of Keller Hall and neighboring buildings (Physical Science Building, Kennedy Theatre, Henke Hall, Bilger and Bilger Addition, Hawaii Institute of Geophysics, etc.) were modeled in Google SketchUp 3D modeling software. Figure 3.1.1 shows the 3D-models of Keller Hall, adjacent buildings and the terrain which were created with SketchUp. The number of buildings modeled and incorporated in the CFD investigations is a compromise between achievable accuracy and required computational resources. Adjacent buildings affect the wind regime

around the target structure, e.g. Keller Hall. Generally speaking the further away from Keller Hall adjacent buildings are located the smaller are their impacts on wind movement around Keller Hall in the computational domain for the CFD simulations. However, the CFD computational domain has to include sufficient interactions of air movement for adjacent buildings in order to produce good CFD approximations of the airflow situation. The downside of including many adjacent buildings in the computational domain is the required size of the model and the computational resources, which means the required time to run the simulations. Figure 3.1.1. shows the selected extent of buildings which were included in the computational domain and therefore were part of the CFD simulations.

- The accuracy of the Keller Hall 3D model was checked against more specific as-built information. A field reconnaissance yielded approximate measurements that were correlated against existing building plans of Keller Hall. The final product was a dimensionally concise 3D-Model that could be used both for the initial and the final CFD runs. For the initial CFD runs an early version of the 3D-model was used, which did not incorporate all external building components. A rather coarse yet dimensionally correct 3D-model was considered sufficient for the initial CFD runs. The model was then refined and more details were added for the final CFD simulations.
- The topographic terrain at the site was obtained from Google SketchUp for an area that accommodated the Keller Hall and adjacent buildings. In the benchmarking phase of the external CFD analysis of this study, several topographic extents of the terrain were considered. Using CFD simulations that incorporated a hilly terrain and select adjacent buildings to the east of Keller Hall showed that the interactions of buildings surrounding Keller Hall and the hilly areas surrounding this part of the Manoa campus the model proved to affect CFD results to a lesser extent the then using a specific wind approach direction and using a horizontal terrain model. This finding resulted in the decision of using a horizontal terrain as the bottom of the computational domain.
- After establishing the physical characteristics of the target building, Keller hall, within a group of adjacent buildings and the selected horizontal terrain the SketchUp models were imported into Rhinoceros3D modeling software. The Rhinoceros3D application allows the creation of the volume of computations domain. This volume is then used in the CFD software to create the computational volume mesh.
- As a last step in the preparation of the 3D-model the terrain of the site then was extended so that the size of the computational domain, which means the overall width, length and depth, were in conformance with dimension delineated in best practice recommendations of (Franke, 2007). Figure 3.1.2 illustrates the final extent of the computational domain for the initial CFD simulations.

As noted before, the external CFD simulations calculated the wind pattern and pressures established on the opaque building envelopes. The air volume occupied inside the computational domain is used by the

CFD program to calculate air movement and pressure distributions. The air volume does not extend into the inside of buildings, since the “decoupled domain” approach is used for this portion of the research.

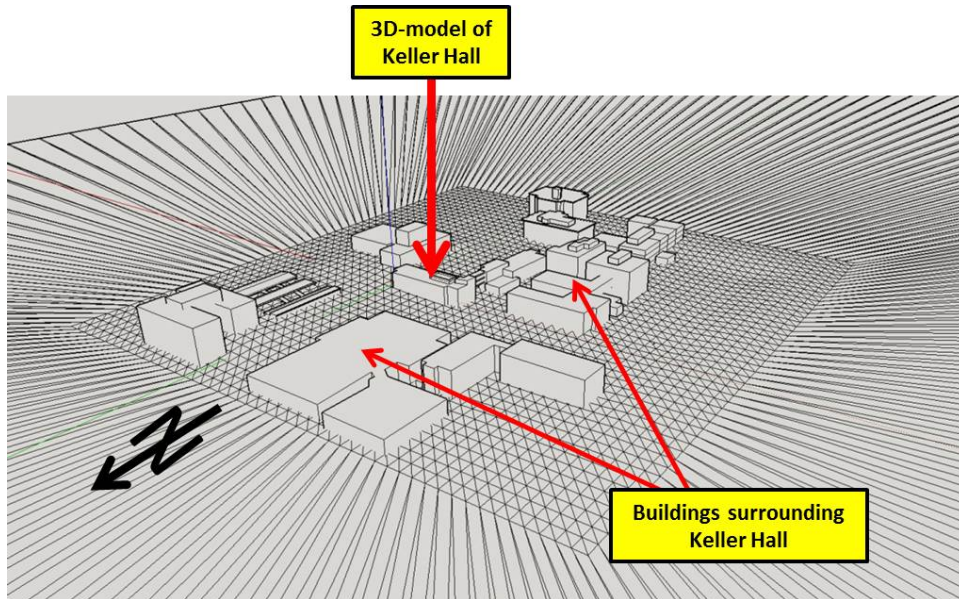


Figure 3.1.1: 3D-models of Keller Hall, adjacent buildings and terrain for the group of buildings; models created in SketchUp. The terrain then was extended horizontally to increase the size of the computational domain.

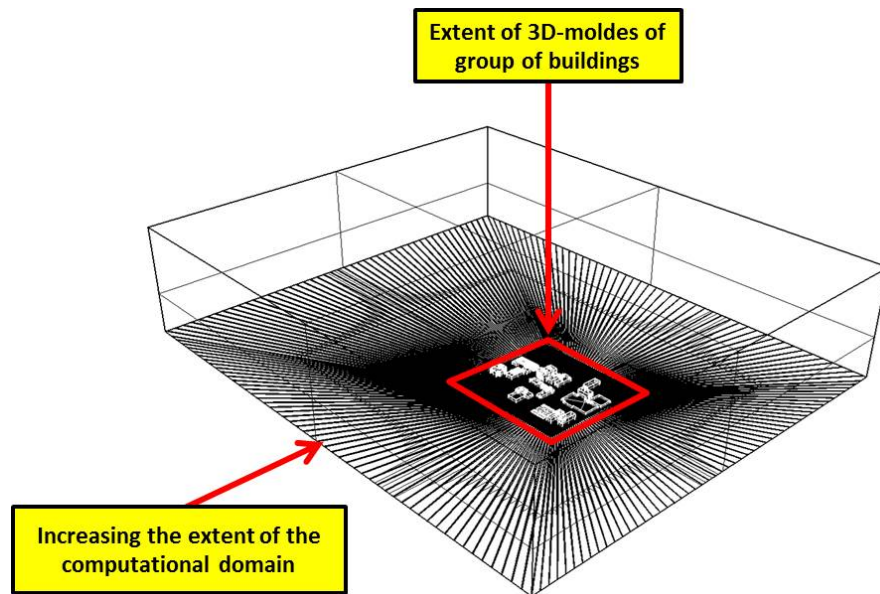


Figure 3.1.2: The 3D-model was imported into Rhinoceros 3D for creating the computational domain

3.1.2 Initial CFD Settings

The initial CFD analysis allowed a preliminary understanding the airflow patterns around Keller Hall with the influence of neighboring buildings. The results from the analysis were used to identify locations of anemometers for the field measurement portion of the study of wind movement around the building.

The CFD settings used in the initial external air flow simulations included the following:

- The reference wind direction and velocity: For the initial CFD simulation, the wind direction and wind speed reference was used based on the averaged wind data measured at the Kuykendall Hall's weather station. Based on this weather data, the wind direction and wind velocity were used for the initial CFD runs are northeast direction at 4.4 m/s (9.8mph) at the height of 25m (82 feet) above the ground. The actual weather data used for the final CFD simulations however were obtained from the weather station located at the site during the field measurement.
- The size of the computational domain for the initial CFD run is 1500m x 1500m x 300 m, the ground was assumed as flat. As approaching wind direction is northeast, the boundary condition regions for the inlet an outlet are shown in the Figure 3.1.2B
- The number of the volume cells: 2,424,267 cells (see Table 3.2.1)
- The turbulence model used: steady state Reynolds-averaged Navier-Stokes (RANS) simulation with Realizable k- ϵ (Rk- ϵ). (see Table 3.2.2)

Table 3.2.1: Number of volume cells for the initial CFD simulations

	Unit	Intial
Minimum cell size	{m}	0.10
Maximum cell size	{m}	72.00
Total volume cells	#	2,424,167

Table 3.2.2: Coefficient for the turbulence model used

Properties	
Convection	2nd-order
Curvature Correction Option	Off
Two-Layer Type	Shear Driven (Wolfstein)
Expert	
Buoyancy Production of Dissipation	Boundary Layer Orientation
C _{mu}	0.09
C _{1e}	1.44
C _{2e}	1.9
C _t	1.0
Sigma _k	1.0
Sigma _e	1.2
Sarkar	2.0
Tke Minimum	1.0E-10
Tdr Minimum	1.0E-10
Secondary Gradients	On
Normal Stress Term	<input type="checkbox"/>
Two-Layer Re _Y *	60.0
Two-Layer Delta Re _Y	10.0

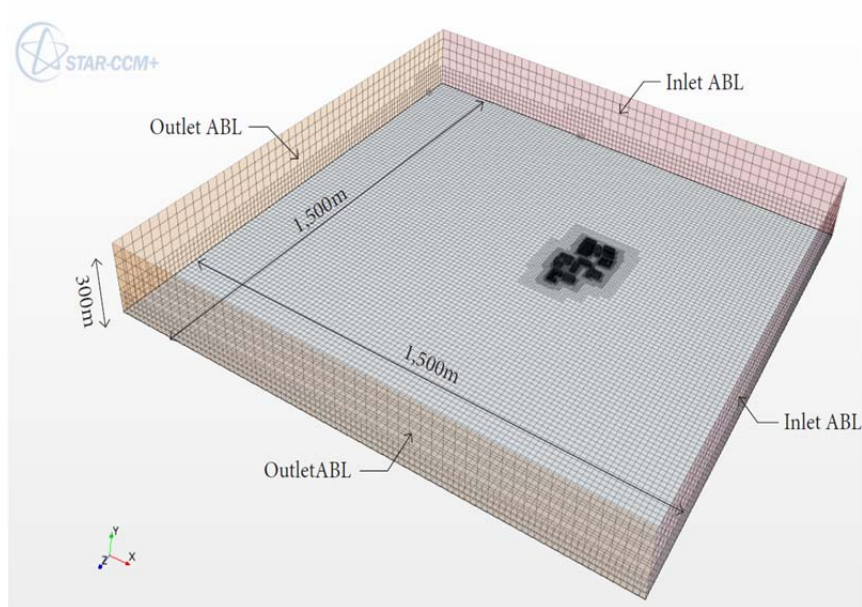


Figure 3.1.2B: 3D geometry and meshing of the computational domain for the initial CFD simulations

3.1.3 Evaluation of Initial CFD for Field Verification

In order to increase the accuracy of the field measurement, the locations of anemometers should be located in the regions where the wind directions are relatively constant and the wind speed is relatively high. Typically, wind accelerates at separation points or the edges of the buildings, which face the approaching wind, and in gaps between two buildings. Wind speeds within wake regions can also be high; however, wind directions in this leeward region can be unstable due to eddy and vortex effects.

In order to determine the proper locations for anemometer placement for field measurements, the field team was interested in the wind movement in the region around the Eastern section of Keller Hall and therefore, these field measurements focused only on this area. Based on the result from the initial CFD run, it was apparent that part of the region on the north side of Keller Hall was located within the wake region caused by the adjacent Henke building. A field reconnaissance showed high wind speeds at the gap between the Keller Hall and Kennedy Theatre and the region on the north of the Keller Hall. Figure 3.1.3 illustrates the results of initial CFD simulations.

It should be noted that several small structures and foliage were not modeled in the initial CFD. The terrain was also modeled as flat area. Settings for terrain surface roughness were done by using the equivalent sand-grain roughness height and wall function modification for the boundary condition. These types of boundary conditions were also used in the final CFD simulations, and will be discussed in more detail in the section describing the final CFD.

Figures 3.1.3 and 3.1.4 show typical results of the initial CFD simulations. Figure 3.1.3 illustrates the resulting wind speeds predicted in the vicinity of the Keller Hall and several surrounding buildings by means of a contour map. As can be seen the wind patterns around Keller Hall are complex with areas of higher wind speeds to the immediate North and South-East of the building. The gap between Keller Hall South-East corner and the adjacent Kennedy Hall suggests an accelerated wind pattern as wind funnels through the relatively narrow gap. It is also evident that the CFD simulations predict stagnation in the North-East corner of Keller Hall and separation of flow to the South of the building.

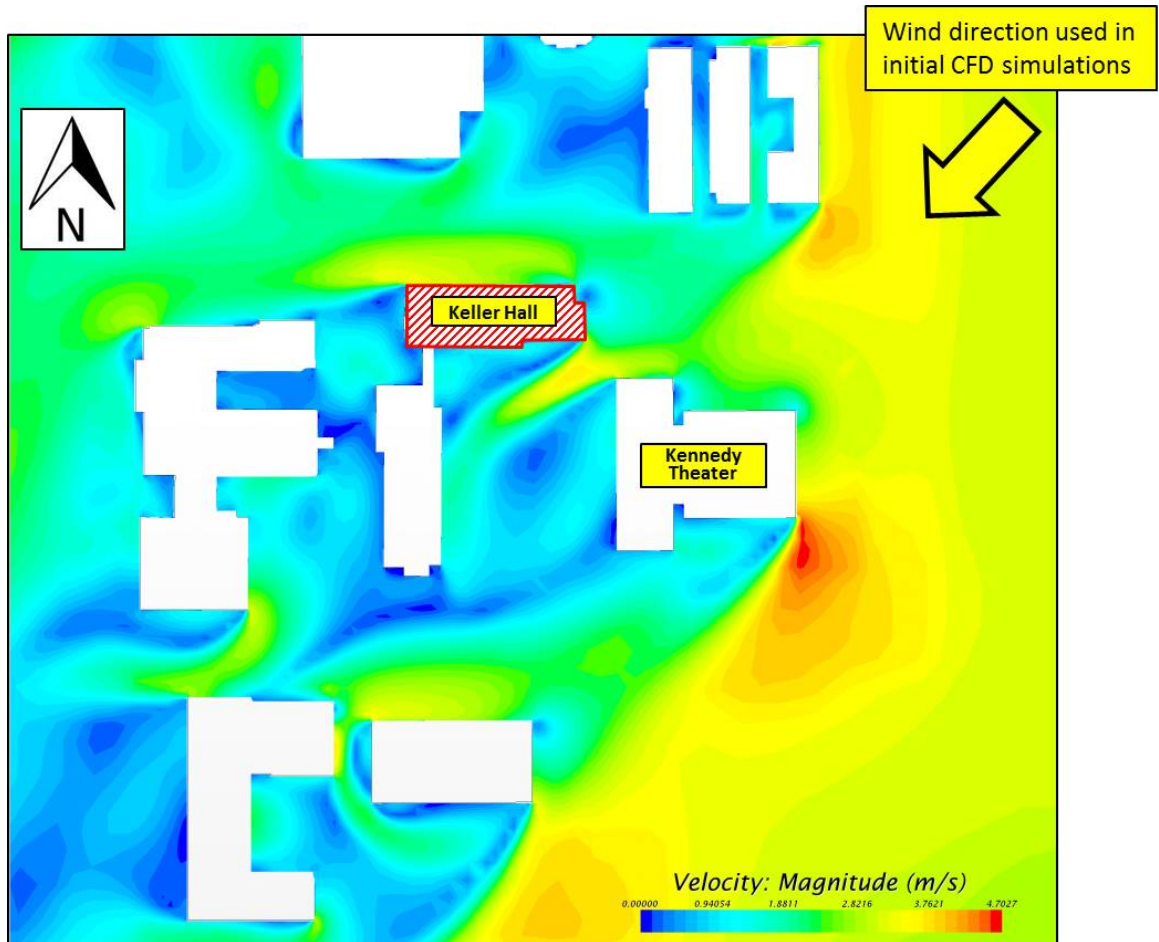


Figure 3.1.3: Results of initial CFD simulations - wind velocities at the horizontal plane at the elevation of 3'-6" above the ground for the indicated wind direction

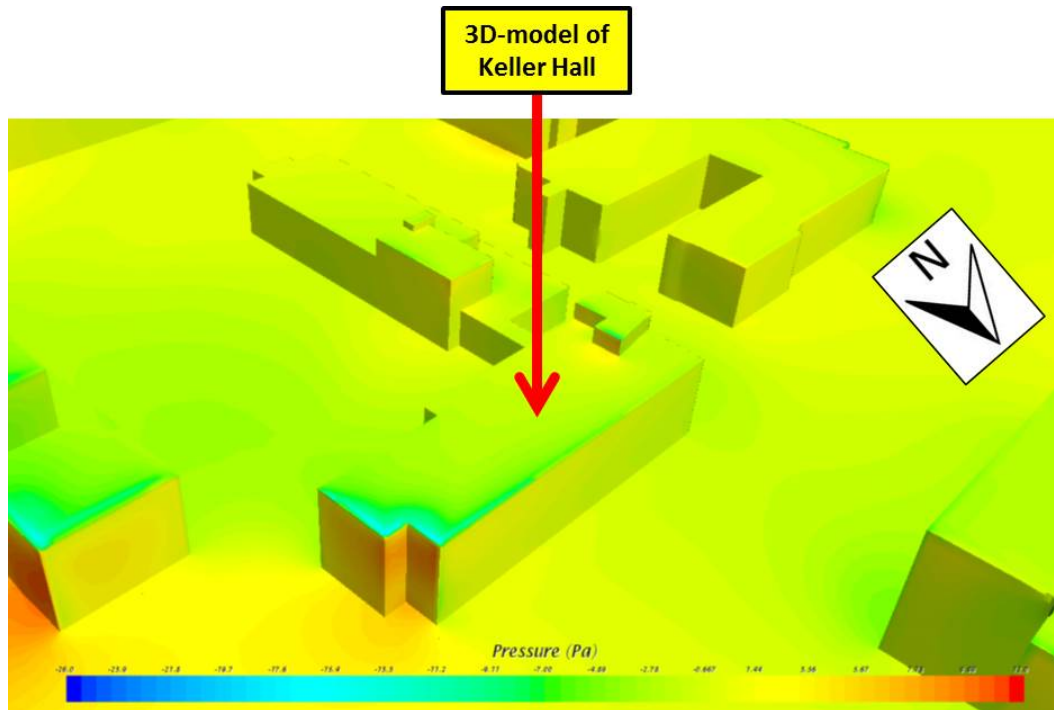


Figure 3.1.4: Results of initial CFD simulations - pressure distribution on the building facades of Keller Hall from the initial CFD run for wind direction indicated.

3.2 Field Measurements

Field measurements were conducted to evaluate the wind speed distribution around Keller Hall and the pressure differentials between several locations on the Keller Hall building envelope. The field data was used to validate the final CFD simulations.

Three types of data sets were collected:

- Weather/micro-climatic conditions at the site, including wind direction and wind speed using a weather station installed on the Keller Hall roof from April to August 2014.
- Wind speed measurements around the Keller Hall building using hotwire anemometers.
- Pressure differentials between external walls of the Keller Hall building using differential pressure transducers.

3.2.1 Weather Station on Keller Hall Roof

A weather station (Onset HOBO U30) was available to the research team to measure climatic conditions at the site over a period of five months. The weather station offered data acquisition of wind direction, instantaneous wind speed, and maximum wind gust. The sample rate was one data set per second. Figure 3.2.1 shows a picture of the Onset HOBO U30 instrument.



Figure 3.2.1: Onset HOBO U30 weather station (source Onset)

The installation of the weather station on the Keller Hall roof presented challenges. The initial CFD analysis had predicted that flow separation occurred at the edge of the roof facing oncoming wind from the North-East. Figure 3.2.2 illustrates the wind flow pattern on the Sinclair roof obtained from the initial CFD simulations. The wind flow separates and the area close to the roof has eddies. The wind measurements, however, require relatively undisturbed flow. This was achieved by placing the weather station away from areas of flow separation and eddies.

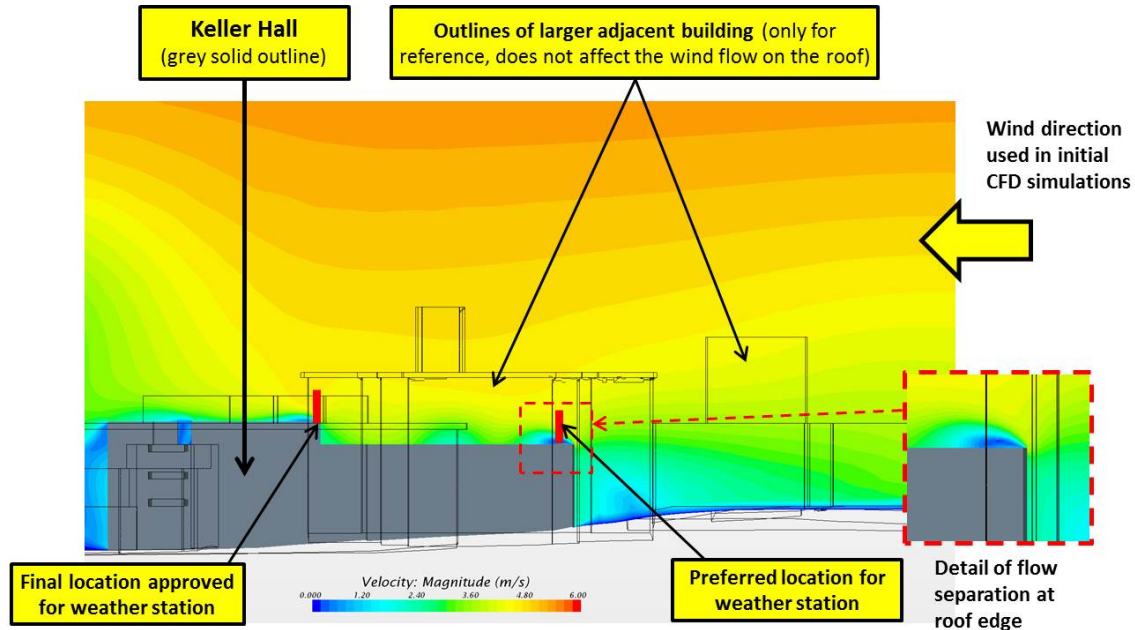


Figure 3.2.2: Wind flow condition around the roof of Keller Hall under the prevailing North-East trade winds.

The first installation approach for the weather station is illustrated in Figures 3.2.3 and 3.2.4. Figure 3.2.3 shows the location of weather station on the Keller Hall roof which was the preferred location. This preferred location was selected since the flow regime was considered the least disturbed, provided that the tripod pole extended far enough away from the roof and therefore away from the area of wind flow separation. Figure 3.2.4 shows the installation approach that was proposed to the University of Hawaii Facility department. Since the installation was considered temporary no permanent fastenings to the roof structure could be considered at this point. Instead, the proposed set-up included a tripod with a long extension pole. The tripod was supposed to be supported by counter weights placed on pallets. This approach was sufficient to ensure overturning moments from strong wind were satisfactorily compensated and the distributed and point loads of the structure and counter weights remained well under the allowable load of the roof.

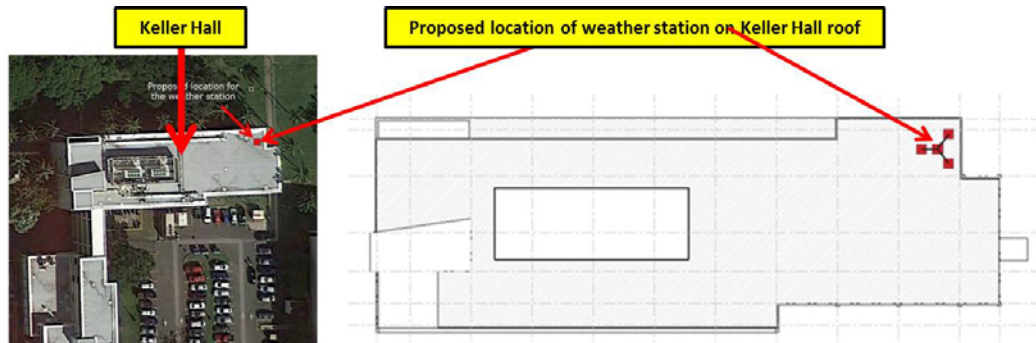


Figure 3.2.3: Preferred location for first alternative of temporary weather station installation on Keller Hall roof (this installation approach was not approved by the university facility department)

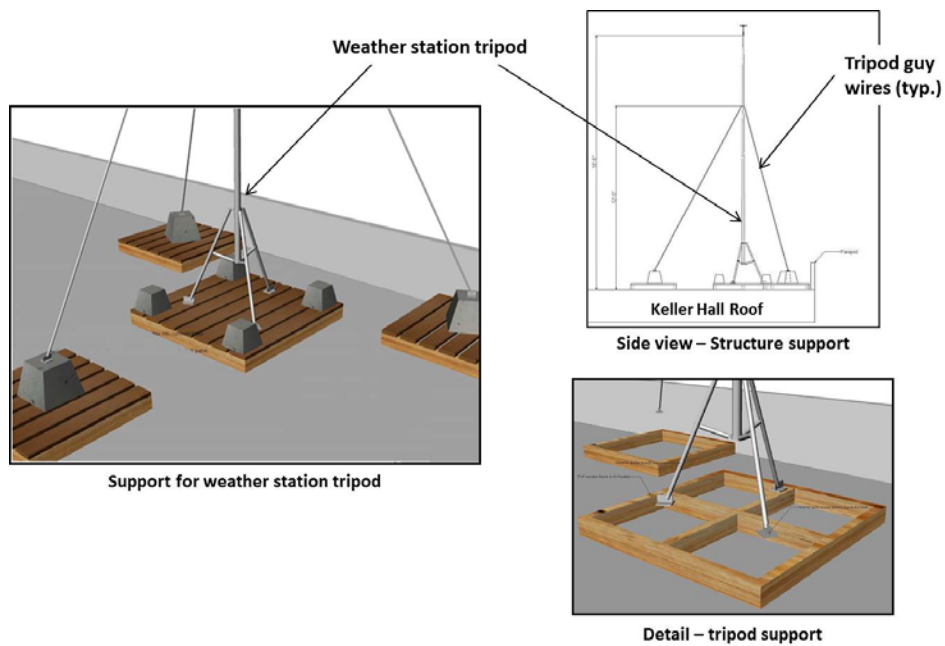


Figure 3.2.4: Proposed approach to support the temporary installation of the weather station on Keller Hall roof using counter weights (this installation approach was not approved by the university facility department)

Since the facility department did not approve the first (preferred) weather station installation approach, an alternative installation procedure was implemented. The alternative approach and location of installing the weather station was at the fenced-in HVAC compartment on the Keller Hall roof. Figure 3.2.2 illustrates that wind flow is also separating around the walls of the fenced HVAC compartment. However, with a sufficiently long extension pole the weather station wind sensors protrude into areas of relatively little disturbed flow.

The finally approved installation of the weather station is depicted in Figure 3.2.5. The 10 foot long support pole of the weather station with wind sensors was bolted to an existing structural steel beam of the HVAC fence. Figures 3.2.6 shows the wind flow conditions in the vicinity of the final attachment of weather station. The “virtual probe” depicted in Figure 3.2.6 is a function of the CFD software to determine accurate wind velocities at certain points. These points are located evenly on a probe with a certain length. The virtual probe in Figure 3.2.6 does not have any physical meaning and does not affect the airflow movement. The function of the probe is explained further in the post processing section of this report.

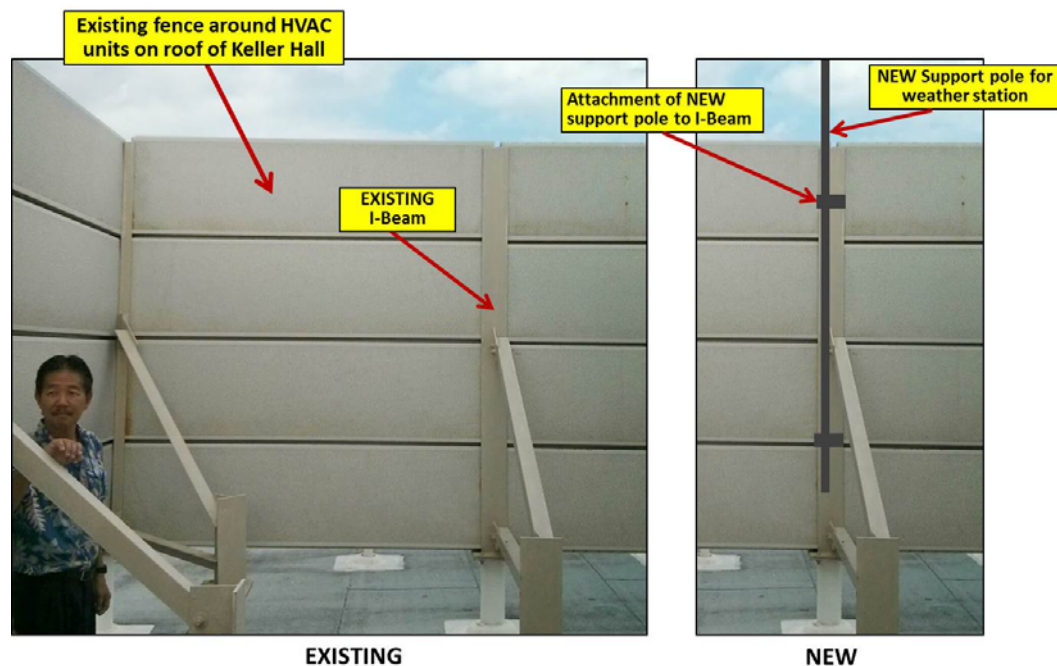


Figure 3.2.5: Attachment of the weather station support pole to I-beam of existing fence around HVAC fence on Keller Hall roof. (This was the final and approved installation approach)

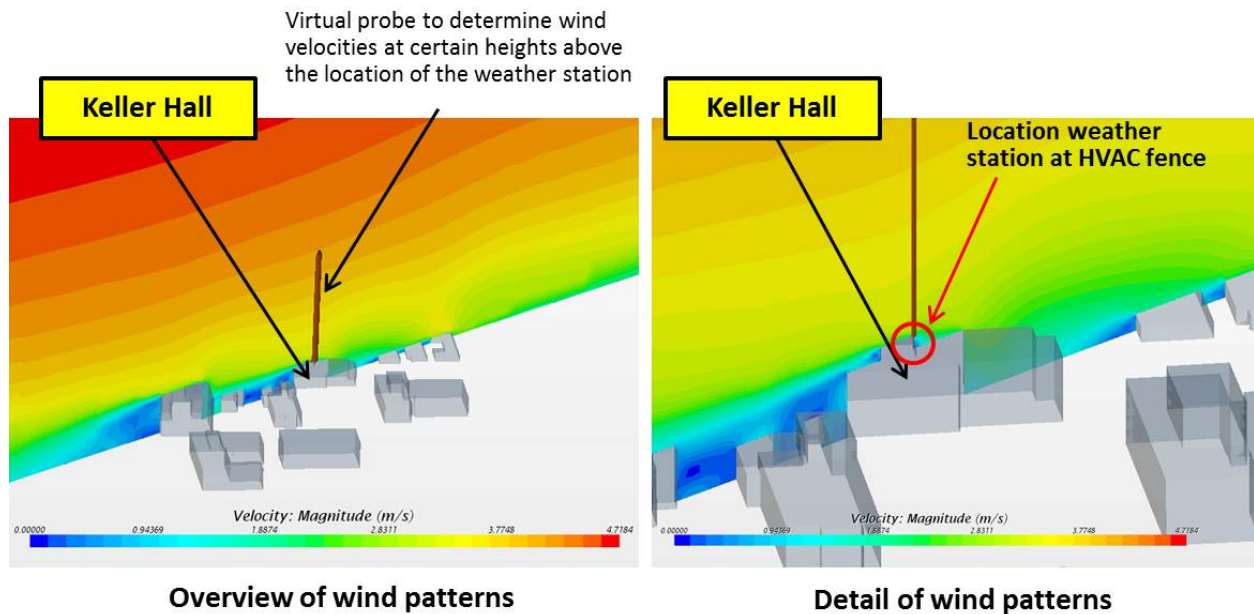


Figure 3.2.6: The wind velocity section map parallel to the North-East wind direction crossing the Keller Hall at the final weather station location. The line probe was placed to capture the wind velocity data.

3.2.2 Wind Speed Measurements around Keller Hall Building

The research team used six hotwire anemometers for the measurement of wind speed around the building. Instruments were setup on the north and east side of Keller Hall at locations that had been identified by the initial CFD simulations. The selected locations are described below. Airspeeds were measured using Degree Controls Accusense hotwire anemometers model F900-0-5-1-9-2 with the XS blade which has a range of 0 - 5 m/s air speed and an accuracy of 0.5 % of reading or 1% of full scale.

Voltages from the sensors were measured by National Instruments USB-63341 data acquisition device (multi-plexer) using National Instruments Signal Express software on a laptop computer. Anemometers were mounted on a wire extending from a vertical stand at a height of 3 feet above the ground. Table 3.2.3 shows the elevation of each anemometer in relation to second floor level. The anemometers were wire connected to the USB-63341 data acquisition device by standard AC extension cords. The three poles of the AC extension cords were used for the excitation of anemometers and sensor signals recording. This innovative way providing excitation to the anemometers and connecting the sensor output to the multiplexer proved to be very effective. The relatively long extension cords were rugged and offered a good electric connection.

Table 3.2.3: Elevations of six anemometers used in the field tests

Sensor ID	Ground elevation (±0.00 reference level is at the 2th floor)		Sensors' elevation (ground elevation + sensor height)	
	Imperial	Metric	Imperial	Metric
AI_01	+1'-9"	0.533 m	+4'-9"	1.448 m
AI_02	+0'-7"	0.178 m	+3'-7"	1.092 m
AI_03	+2'-3"	0.686 m	+5'-3"	1.600 m
AI_05	-4'-8"	-1.422 m	-1'-8"	-0.508 m
AI_06	-0'-11"	-0.279 m	+2'-1"	0.635 m
AI_07	-7'-4"	-2.235 m	-4'-4"	-1.321 m
Weather Station (WS)	+0'-7"	0.178 m	+10'-7"	3.226 m

The locations of the weather station and anemometers were chosen by interpreting the distribution of the wind speed around Keller Hall obtained in the initial CFD simulation. The initial CFD assumed northeasterly prevailing wind. As planned, the anemometers were located in the regions of assumed high wind speed and stable wind direction. The selected locations are depicted in Figure 3.2.7. During the actual field test, the wind directions were shifting and the research team experienced that wind directions were likely to fluctuate around the north direction. As a consequence, minor adjustments in the location were made which included relocating the anemometer ai_02 and the weather station (ws). The final locations of the six anemometers and the weather station, including the sensors' elevation heights and coordination are indicated in Figure 3.2.8.

Figures 3.2.9 through 3.2.15 show photos of the anemometers locations during tests. The locations of the anemometers in the photos correspond to those in Figure 3.2.8.

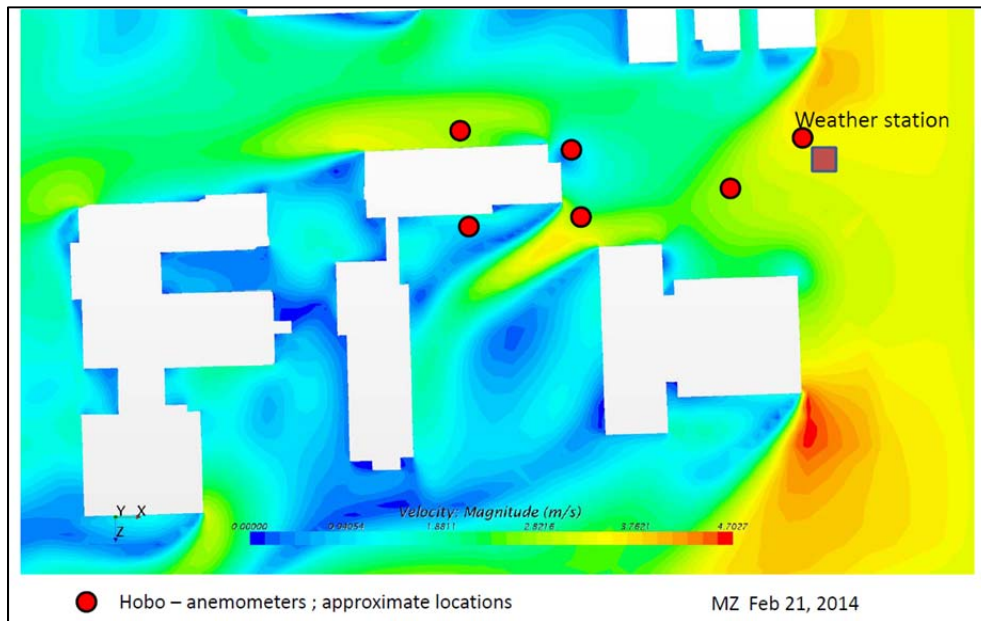


Figure 3.2.7: Selected locations of anemometers and weather stations for the initial field measurement of wind velocities around Keller Hall based on the initial CFD simulation. (planned locations for the tests)

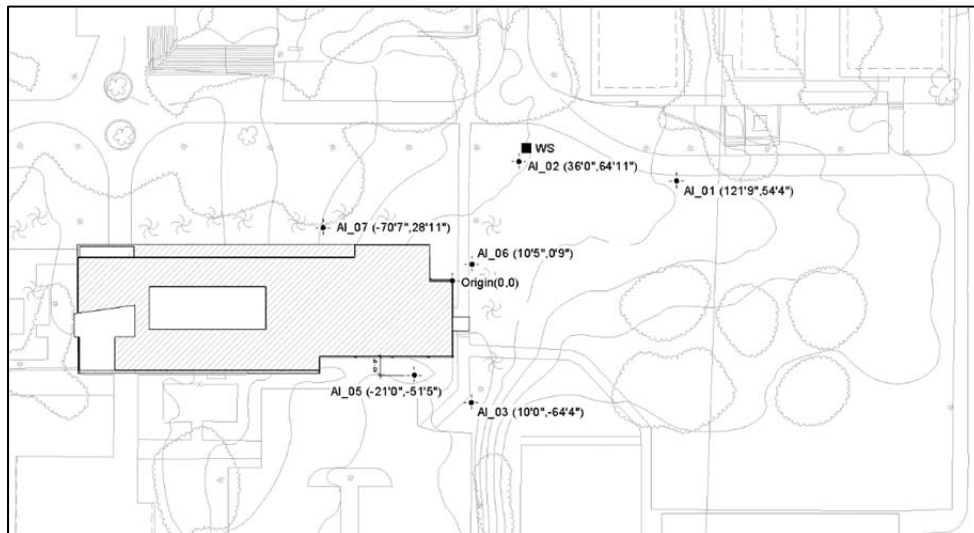


Figure 3.2.8: Actual locations of the six anemometers for wind speed measurements around the Keller Hall building

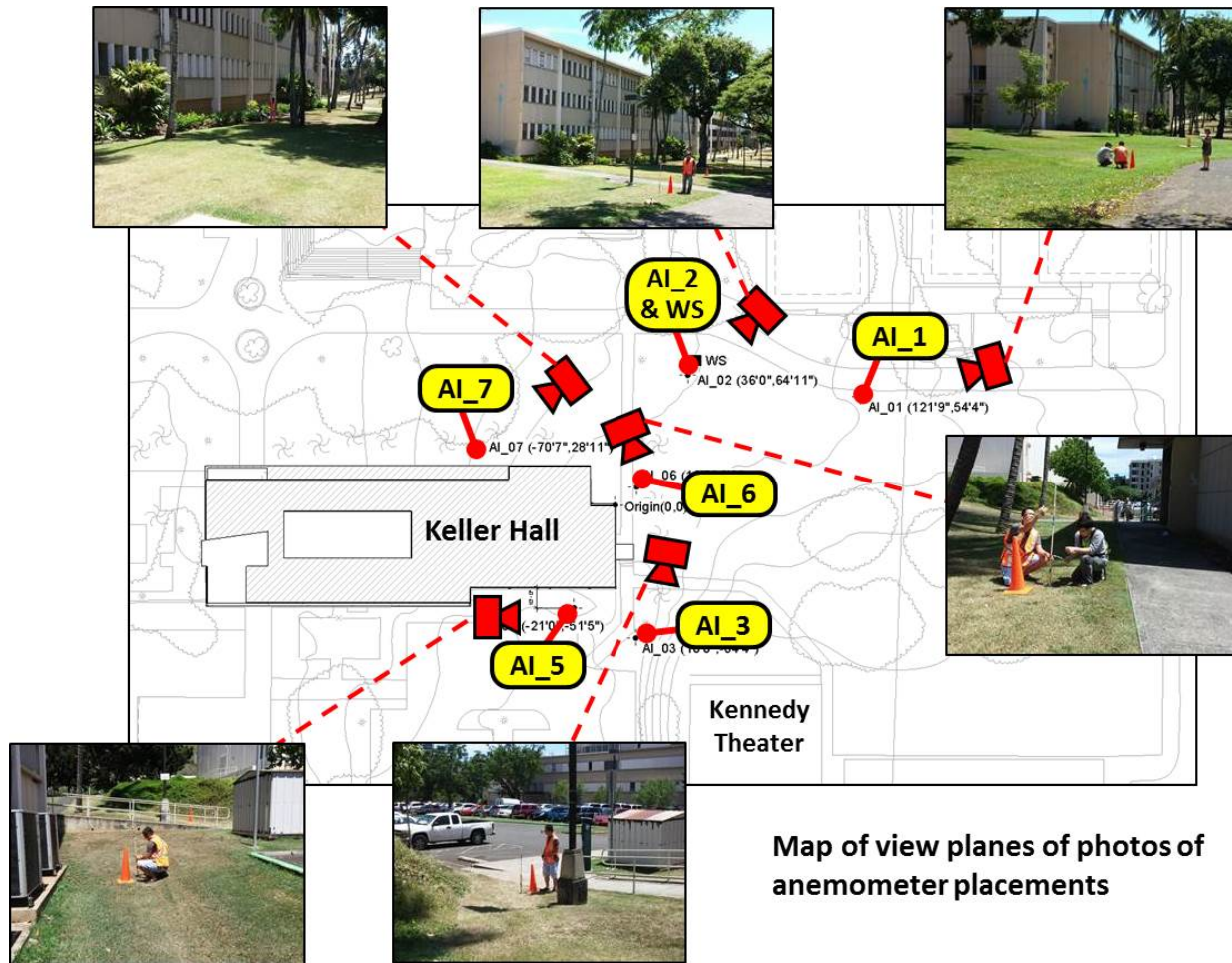


Figure 3.2.9: View planes of photos of anemometer placement around Keller Hall

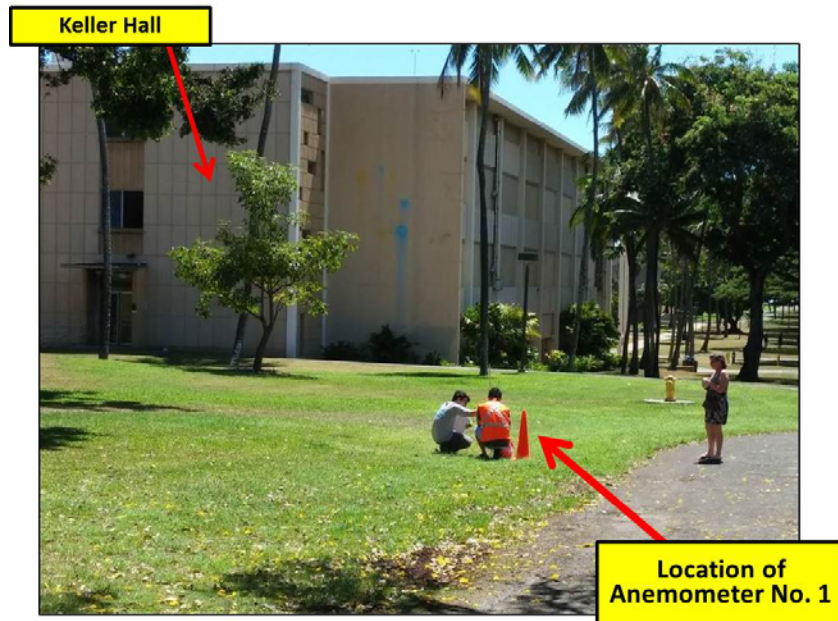


Figure 3.2.10: Test station AI-1: Location for anemometer No. 1 during measurements of external wind speed

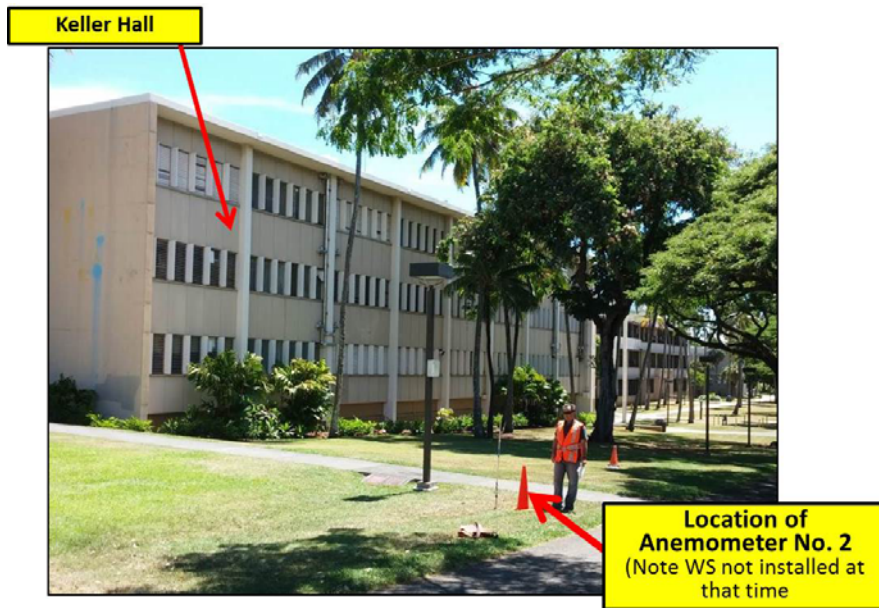


Figure 3.2.11: Test station AI-2 and WS: Location for anemometer No. 2 and WS (portable weather station) during measurements of external wind speed

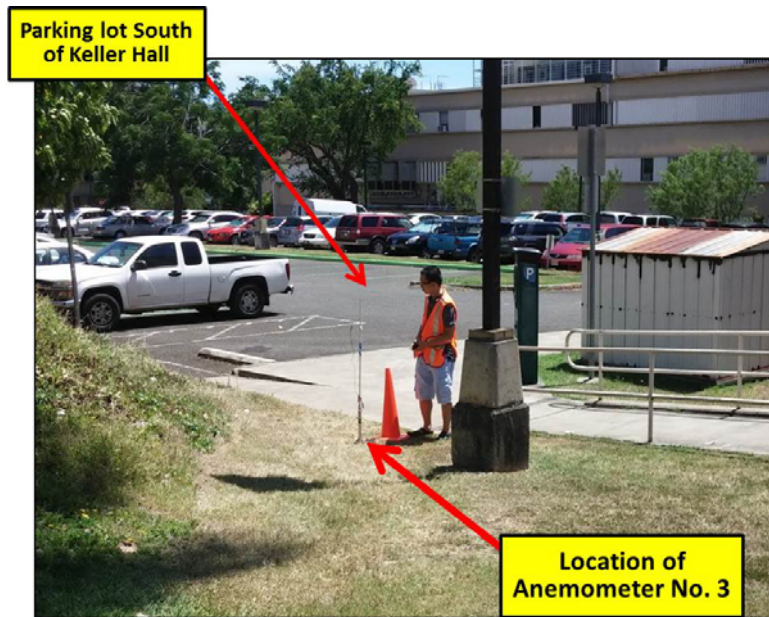


Figure 3.2.12: Test station AI-3: Location for anemometer No. 3 during measurements of external wind speed

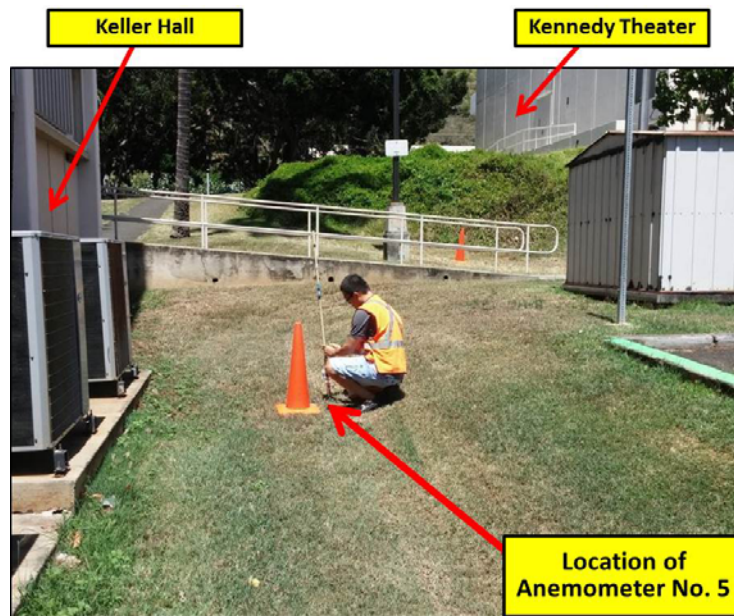


Figure 3.2.13: Test station AI-5: Location for anemometer No. 5 during measurements of external wind speed

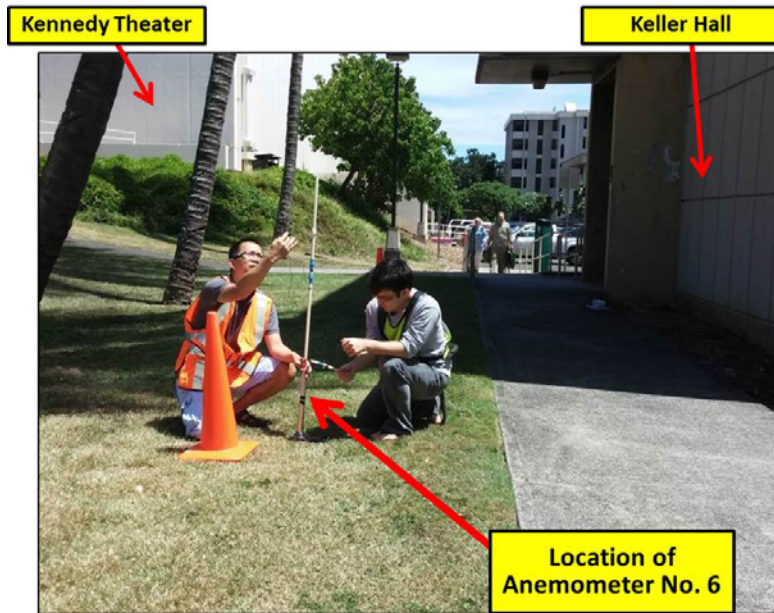


Figure 3.2.14: Test station AI-6: Location for anemometer No. 6 during measurements of external wind speed

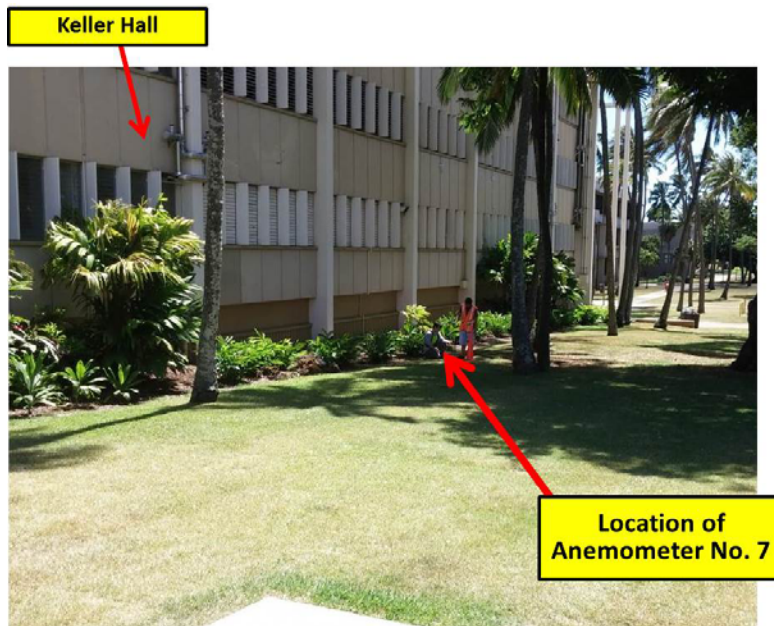


Figure 3.2.15: Test station AI-7: Location for anemometer No. 7 during measurements of external wind speed

3.2.3 External Pressure Measurements at Keller Hall Building

In the case of Keller Hall cross ventilation is the only natural ventilation method and therefore the relevant pressure properties are the differential pressures between windward and leeward side of the building. As the wind impacts on the building kinetic energy is transformed to static pressure, with the highest pressures build up at points of stagnation. Likewise on the leeward side of the building the research team encounter lower pressure as flow energy dissipated from the wind flow and flow separation occurred in conjunction with the creation large or small eddies.

Differences in pressures around the building were measured with differential pressure transducers of the type Setra Model 264 Very Low Differential Pressure Transducer. Pressure tubing of about 30 to 50 feet connected the high and low pressure ports of the pressure transducer with the location on the building facade. The difference in pressure is converted to an electronic signal. Each end of the pressure tubing was fitted with a pressure tubing terminal to ensure that no objects such as insects could enter and clog the tubing. In addition to avoiding entrainment of objects into the tubing, the pressure terminals also provided averaging of pressures at the point of detection. For this study short pipe sections with multiple small holes were used as pressure tube terminals. This design averages the pressure over a certain length of pipe and lowers the effects of local eddies on the measured pressure. Figure 3.2.16 shows the pressure tubing terminal used in this investigation.

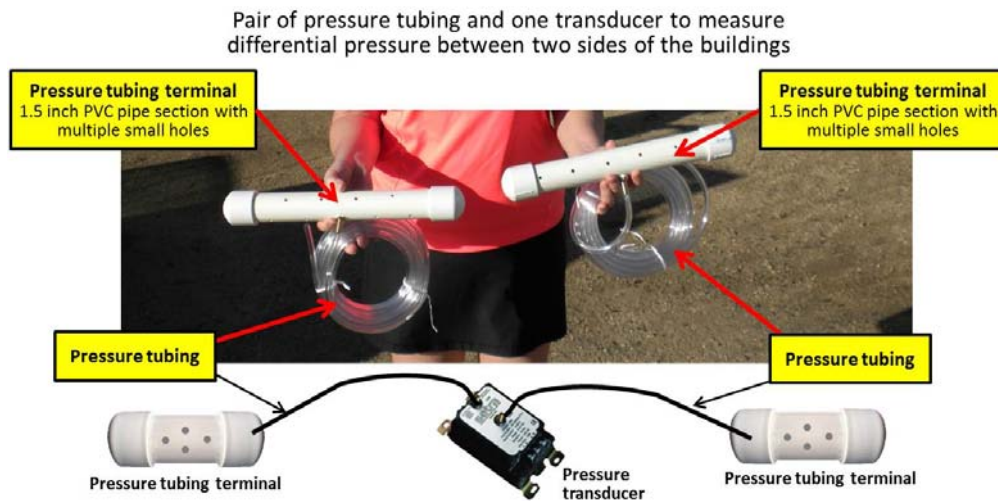


Figure 3.2.15: A pair of pressure tubing terminals – one for the high and one for the low pressure points on the building envelope

There were four differential pressure transducers equipped with one pressure tubing pair each. Figure 3.2.16 shows the location of the four pairs of pressure tubing with terminals located on the North and South side of the building. Figure 3.2.16 also indicates the ID of the differential pressure transducers.

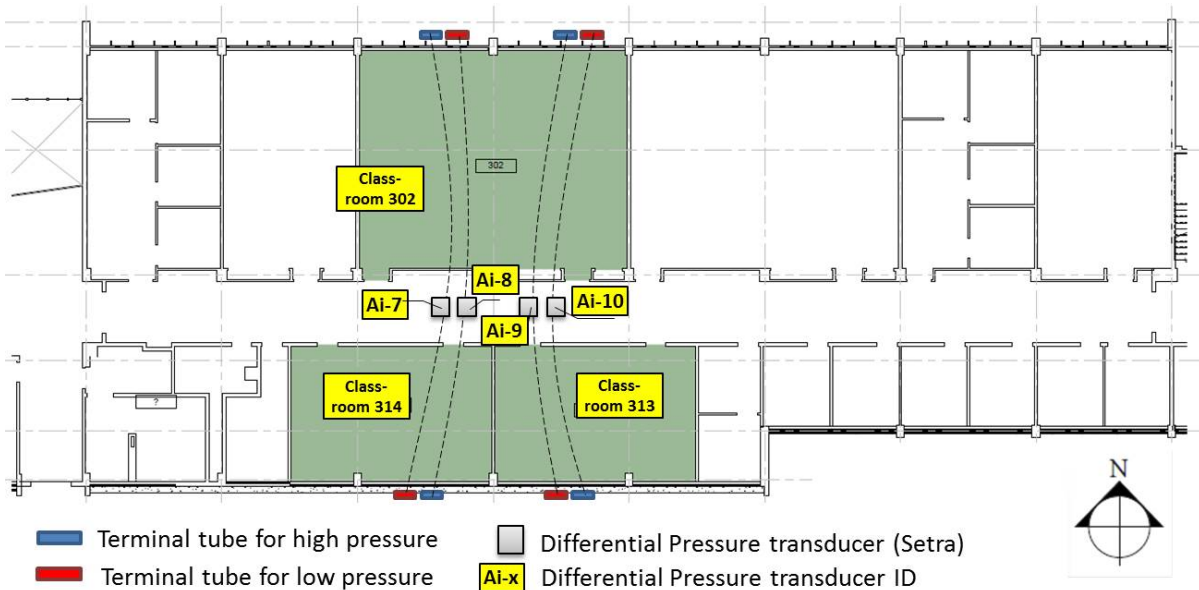


Figure 3.2.16: The four pressure tubing pairs and differential pressure transducers employed to measure long term wind induced external pressures on the Keller Hall 3rd floor

The Setra pressure differential transducer are only reliable when reading positive pressure differentials. This means the pressure tubing must be connected consistently with the higher pressure port connecting to the part of the building façade with the higher pressure and vice versa for the lower pressure port. In our case, with the anticipated prevailing wind direction approaching Keller Hall from the North the pressure tubing that connected the pressure tubing terminal on the North was connected to the High pressure port of the transducer. Consequently, in order to be able to measure differential pressures also for the wind condition with a higher pressure exerted on the South side of the Keller Hall building, a pressure transducer was required whose high-pressure port connected to the pressure tubing terminal on the South façade. Conditions that produce higher pressures on the South side are assumed as so-called “Kona” condition, which bring stronger winds from the South to the Hawaiian Islands. This double tubing strategy was deployed so that both higher pressures on the North and the South façade of Keller Hall could be detected.

Figure 3.2.17 shows the four differential pressure transducers installed in an instrumentation cabinet inside the third floor of Keller Hall. As the figure shows pairs of pressure tubing connect to the two pressure ports of each transducer. Figure 3.2.18 through 3.2.20 show the location of pressure tubing terminals installed on the North and South side of the Keller Hall building. On the South side the windows are equipped with vertical shading vertical panels. The pressure tubing terminals were placed between the windows and the shading panels. Since no air is flowing through the tubing no pressure losses occurred and therefore pressure differentials measured at the transducer does not require adjustments to account for pressure losses.

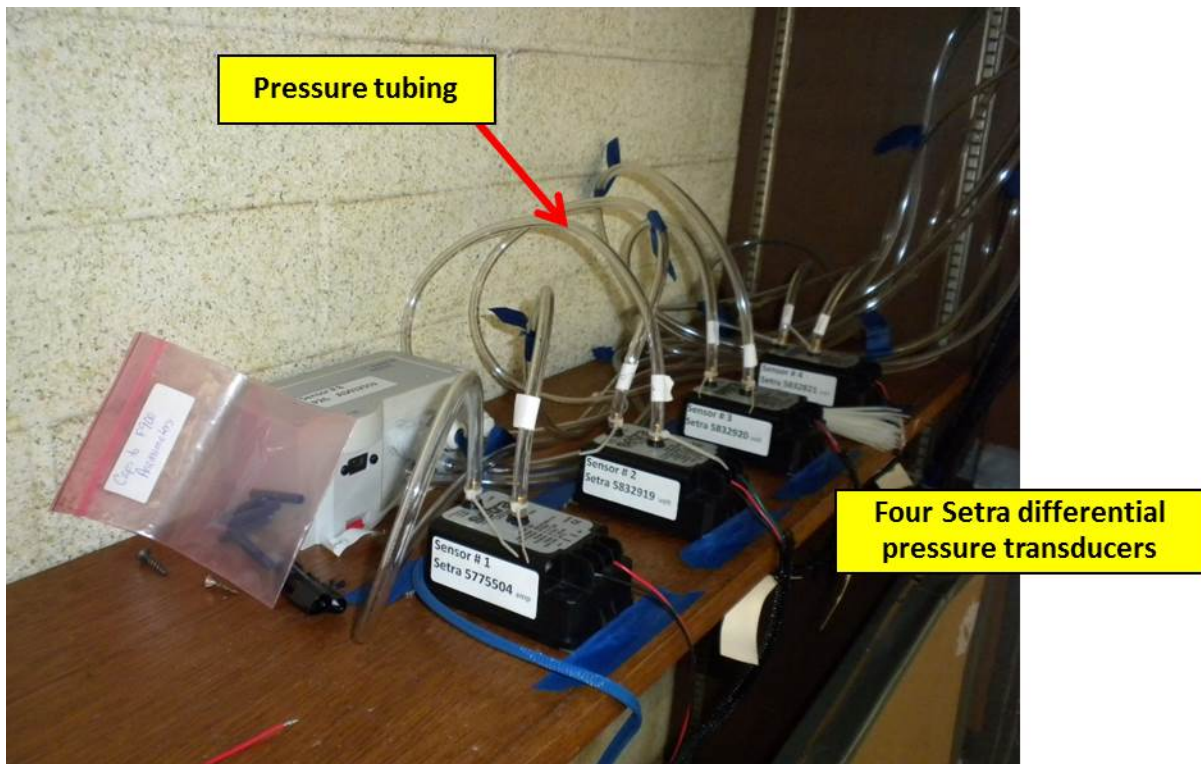


Figure 3.2.17: Four differential pressure transducers with connecting pressure tubing installed inside Keller Hall

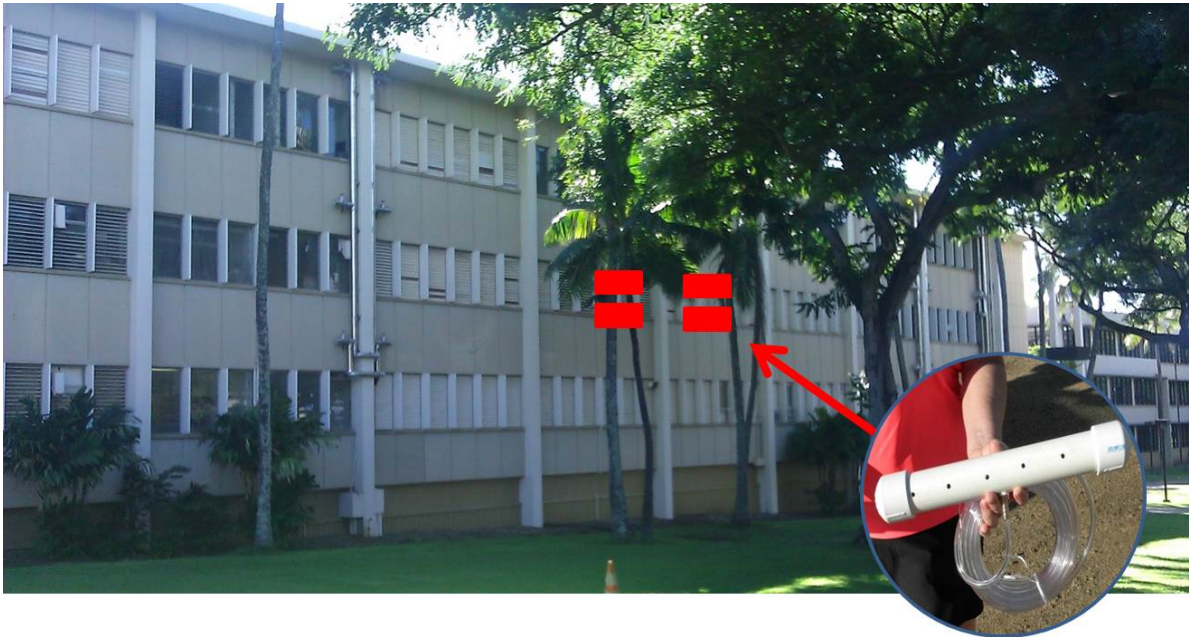


Figure 3.2.18: Location of four pressure tubing terminals installed on the North façade of Keller Hall



Figure 3.2.19: Location of four pressure tubing terminals installed on the South façade of Keller Hall – the terminals are installed behind the vertical shading panels

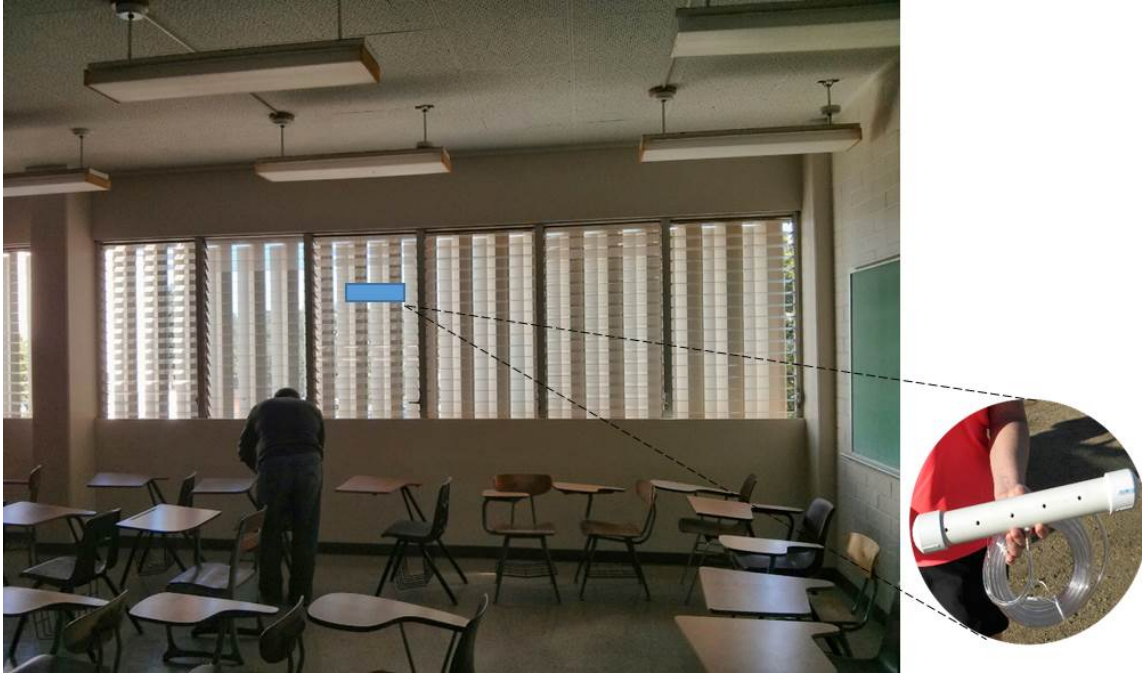


Figure 3.2.19: Location of four pressure tubing terminals installed on the South façade of Keller Hall – view from the inside with terminals being installed between the vertical shading panels and the louvered windows

3.2.4 Data Acquisition

Voltage signals were recorded at 5-hz resolution by the National Instruments Signal Express software on a laptop computer. All anemometers were initially run for 15 minutes with the caps on to obtain a calibration. Data was acquired in a text format with a starting timestamp and frequency of collection (in this case 5 times per second). The Signal Express software did not record a timestamp for each reading. A Python script was written to present the data with timestamp information, averaged the 5-hz data to 1-second resolution with a trailing timestamp, scaled it (output of 0 - 4 V DC was scaled to 0 - 5 m/s less the calibration reading) and re-shaped for upload to a PostgreSQL database (Github link to the original script is

https://github.com/csbcdAdmin/KellerInternalAutomationFiles/blob/dev/client/0_Original/extractData_r3cd.py this has since been cleaned up and automated for a later trial and that link is <https://github.com/csbcdAdmin/KellerInternalAutomationFiles/tree/dev>).

The Onset U30 weather station recorded wind direction, instantaneous wind speed, and maximum wind gust at 1-second intervals. Data was downloaded using a USB cable and a laptop computer with Hoboware software and then exported as a csv text file and uploaded to the PostgreSQL database.

3.3 Final CFD Simulations

This section of the report describes processes carried out to prepare and run the final CFD simulations

3.3.1 Refinement of the Computational Domain

The CFD input conditions and parameters were refined from initial CFD simulation runs. These refinements included:

1. A more detailed geometry of the Keller Hall building was created, with all pertinent building appurtenances. The surrounding building had the same simple geometries that was used in the initial CFD simulation runs. The use of simple 3D-geometries of these buildings was consider sufficient to adequately model the effect of these buildings on the wind movements around Keller Hall.
2. The mesh resolution, which means the number of cells in the volume mesh was increase to increase the accuracy of the solution. The mesh resolution was increase around the exterior of Keller Hall to account for more detail flow occurrences.
3. The inlet boundary condition of the computational domain was changed to account for a more precise flow distribution in vertical direction.

The improvements under points 2 and 3 above are further discussed in the following:

Increase in mesh resolution: Table 3.3.1 through 3.3.3 show the increase in mesh resolution in comparison with the mesh used in the initial CFD simulation runs. A higher mesh resolution indicates a larger number of cells and smaller minimum dimensions of cells. Figures 3.3.2 and 3.3.3 illustrate the high mesh resolution used in the final CFD simulation runs.

Table 3.3.1: Mesh sizes used in the final CFD simulations – note the comparison to the mesh used in the initial CFD runs

	Unit	Intial	Coarse	Medium	Fine
Minimum cell size	{m}	0.10	0.10	0.08	0.06
Maximum cell size	{m}	72.00	72.00	57.60	43.20
Total volume cells	#	2,424,167	3,041,620	4,441,165	7,898,730

Table 3.3.2: Parameters for near-wall cells and prism layers

	Minimum height of centroid near-wall cell ($C_p = r$) (m)	The height of each prism layer (03 layers) (m)
Upstream and downstream regions	1.08	3.650
		2.808
		2.160
Central region close to target buildings	0.36	1.217 0.936 0.720

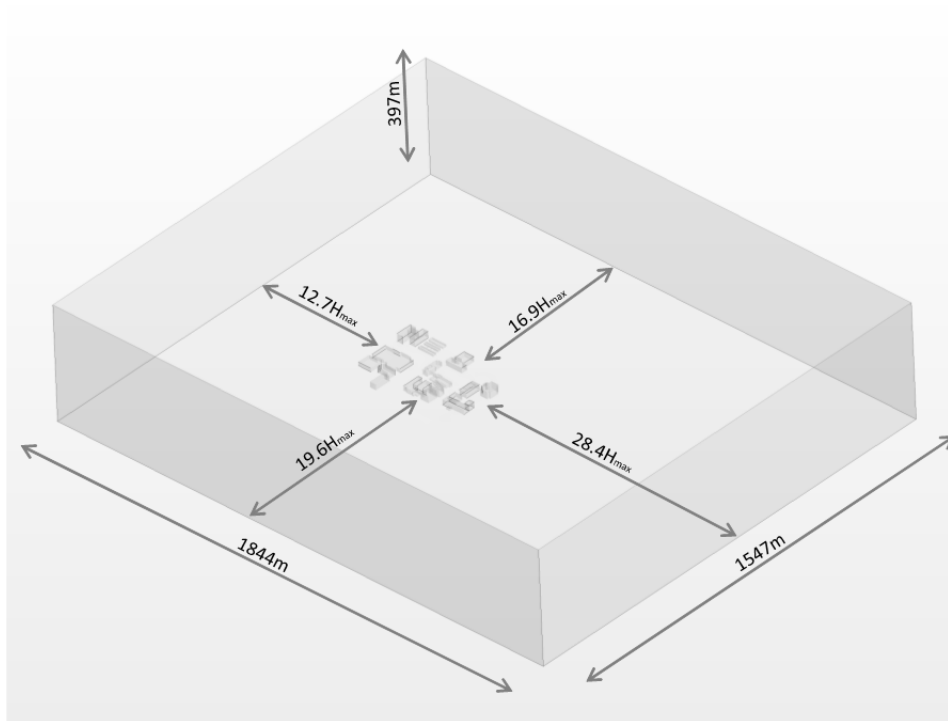


Figure 3.3.1: Computational domain dimensions

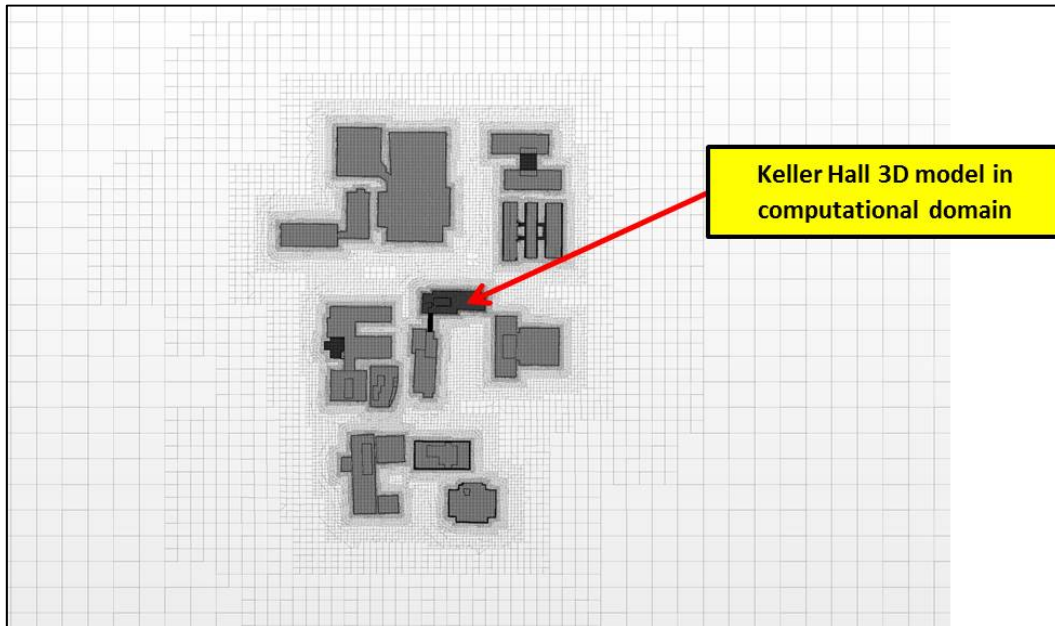


Figure 3.3.2: Using an increased mesh resolution for the Final CFD simulation runs – plan view of a section of the computational domain

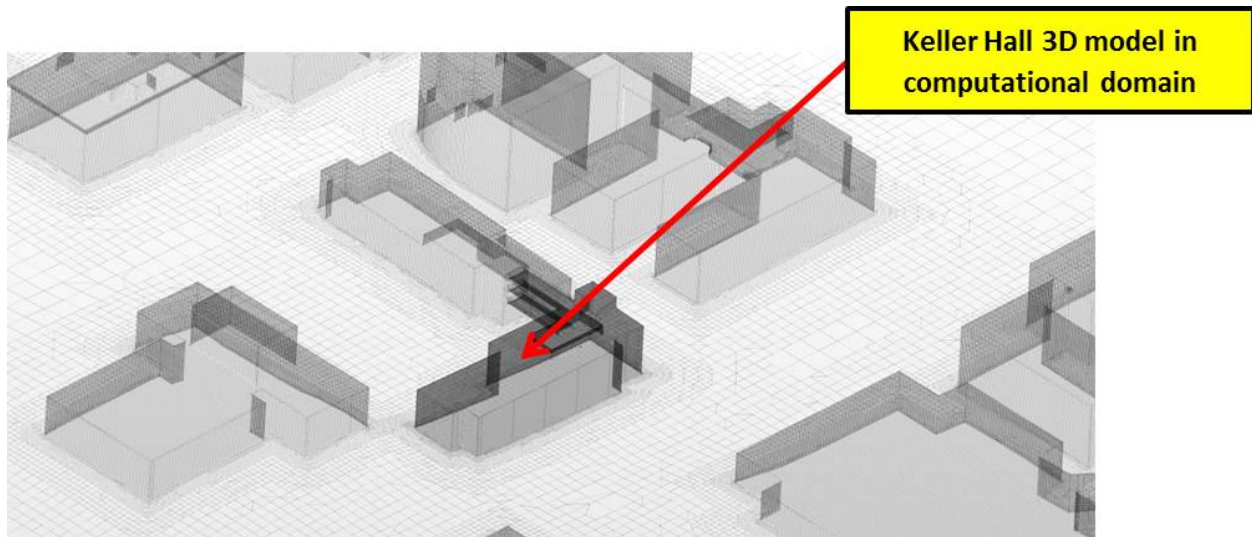


Figure 3.3.3: Using an increased mesh resolution for the Final CFD simulation runs – oblique view of a section of the computational domain

Setting up the atmosphere boundary layer: The inlet airflow boundary conditions were changed to depict a more calculation sensitive scenario. The following parameters were used in the final CFD simulation runs:

- The aerodynamic roughness length $y_o = 0.01$.
- $E = 9.0$ and $C = 0.253$ (wall functions coefficients)
- The equivalent sand-grain roughness height r :

$$r = \frac{E y_o}{C} \approx 36 y_o$$

- Far upstream and far downstream area $y_0 = 0.03$
- Closed to buildings' area $y_o = 0.01$

The terrain roughness was defined in accordance with the input variables below:

Table 3.3.3: Coefficients to define the atmosphere boundary layer

	Terrain roughness classification	The aerodynamic roughness length (y_o)	The equivalent sand-grain roughness height (r)
Upstream and downstream regions	Open field	0.03	0.9
Central region close to target buildings	smooth	0.01	0.3

Table 3.3.4: Aerodynamic roughness length based on roughness classification by Davenport (1960) and updated by Wieringa (1992)

	y_0 (m)	Landscape description
1	0.0002 Sea	Open sea or lake (irrespective of the wave size), tidal flat, snow-covered flat plain, featureless desert, tarmac, concrete, with a free fetch of several kilometres.
2	0.005 Smooth	Featureless land surface without any noticeable obstacles and with negligible vegetation; e.g. beaches, pack ice without large ridges, morass, and snow-covered or fallow open country.
3	0.03 Open	Level country with low vegetation (e.g. grass) and isolated obstacles with separations of at least 50 obstacle heights; e.g. grazing land without windbreaks, heather, moor and tundra, runway area of airports.
4	0.10 Roughly open	Cultivated area with regular cover of low crops, or moderately open country with occasional obstacles (e.g. low hedges, single rows of trees, isolated farms) at relative horizontal distances of at least 20 obstacle heights.
5	0.25 Rough	Recently-developed "young" landscape with high crops or crops of varying height, and scattered obstacles (e.g. dense shelterbelts, vineyards) at relative distances of about 15 obstacle heights.
6	0.50 Very rough	"Old" cultivated landscape with many rather large obstacle groups (large farms, clumps of forest) separated by open spaces of about 10 obstacle heights. Also low large vegetation with small interspaces such as bush land, orchards, young densely-planted forest.
7	1.0 Closed	Landscape totally and quite regularly covered with similar-size large obstacles, with open spaces comparable to the obstacle heights; e.g. mature regular forests, homogeneous cities or villages.
8	≥ 2.0 Chaotic	Centres of large towns with mixture of low-rise and high-rise buildings. Also irregular large forests with many clearings.

3.3.2 CFD Settings According to Measured Wind Conditions

The actual wind direction and speed conditions found at the site were used for the final CFD simulation. Since the wind direction and speed fluctuate due to gusts and other short term wind occurrences, a statistically representative descriptor of wind direction and speed was determined. Due to the random nature of the wind fluctuation, a normal distribution was used in the analysis of the measured wind direction and speed at the test site. Table 3.3.3 shows the resulting average wind speed along with the standard deviation for three representative wind directions. From the analysis of the data record, time periods of the tests were identified when these three representative wind directions prevailed.

Table 3.3.3: Estimation of reference wind speed for final CFD simulations

Wind direction	North (0°)	East (90°)	Northeast (45°)
Measurement Time	12:27:00 PM – 12:37:00 PM	12:19:00 PM – 12:29:00 PM	12:23:00 PM – 12:33:00 PM
Sensor ID	Averages and (Standard Deviations) of Wind Speeds (m/s)		
AI_01	1.644 (0.592)	1.678 (0.584)	1.709 (0.613)
AI_02	2.119 (0.716)	1.861 (0.691)	1.762 (0.633)
AI_03	3.581 (0.703)	3.650 (0.644)	1.841 (0.804)
AI_05	1.638 (0.501)	1.564 (0.319)	3.242 (0.679)
AI_06	2.125 (0.656)	2.352 (0.823)	1.827 (0.584)
AI_07	2.280 (0.802)	2.583 (0.823)	2.301 (1.027)
Weather Station (WS)	1.519 (0.352)	1.436 (0.444)	1.709 (0.613)

Note: The averages and standard deviations of wind speeds from the measurement whose data were filtered out for particular wind directions (North, East and Northeast) including a range $\pm 15^\circ$.

The reference wind speed for the inlet's wind profile in CFD boundary condition settings, was determined by the following local wind speed formula (ASHRAE Fundamentals 2005):

$$u_z = u_{met} \left(\frac{\delta_{met}}{z_{met}} \right)^{\alpha_{met}} \left(\frac{z}{\delta} \right)^\alpha$$

With the following parameters:

- z = the height above ground
- u_z = the wind speed at the height of z
- α = wind speed profile exponent at the site
- δ = wind speed profile boundary layer thickness at the site
- u_{met} = the wind speed measured at the meteorological station
- α_{met} = wind speed profile exponent at the meteorological station
- δ_{met} = wind speed profile boundary layer thickness at the meteorological station

The profile coefficients α , δ , α_{met} , δ_{met} are variables dependent on the roughness characteristics of the sounding terrain (ASHRAE Fundamentals 2005).

Table 3.3.1: Wind speed profile coefficients (ASHRAE Fundamentals 2005)

Terrain Description	Exponent, α	Boundary Layer Thickness, δ (m)
Flat, open country	0.14	270
Rough, wooded country	0.22	370
Towns and cities	0.33	460
Ocean	0.10	210
Urban, industrial, forest	0.22	370

The reference wind speed for the inlet profile can be readily obtained by using this formula with the meteorological station located close to the test site. Terrain characteristics of the surrounding of this weather station were assumed to be classified as “towns and cities”. Thus, wind profile exponents and boundary layer thicknesses to be equal to 0.33 and 460 m, respectively. The approaching wind is assumed to be passing the urban area, with a wind profile exponent and boundary layer thickness of 0.22 [-] and 370 [m], respectively.

With $z_{\text{met}} = 3.226\text{m}$, $\alpha_{\text{met}} = 0.33$, $\delta_{\text{met}} = 460\text{m}$, $\alpha = 0.22$, $\delta_{\text{met}} = 370\text{m}$, $z = 10\text{m}$, the reference wind speeds, which were used for the inlet boundary conditions of the final CFD simulation, are shown as follows:

Table 3.3.3: Results obtained for terms U_{met} and U_z (m/s)

Wind direction	U_{met} (m/s)	U_z (m/s)
North	1.519	3.527
East	1.436	3.334
North-East	1.709	3.968

The surface roughness chosen for the model affects the size of the mesh. According to our literature review, wall-function treatments suggest that the centroid of the first prism layer C_p has to be larger

than the equivalent grain roughness height (r). With three prism layers selected to describe effects surfaces in the CFD model, the heights of each prism layer cell were set as is indicated in Table 3.3.4.

Table 3.3.3: Height of prism layer selected in accordance to recommendations in the literature for wall-function treatment

	Minimum height of centroid near-wall cell ($C_p > r$)	The height of each prism layer (three layers total)
Upstream and downstream regions	1.08 m	3.650 m
		2.808 m
		2.160 m
Central region close to target buildings	0.36 m	1.217 m
		0.936 m
		0.720 m

3.3.3 Post Processing

Typical CFD post processing involves creating contoured graphs or streamlined plots to illustrate pertinent parameters from the huge CFD data sets that have been created in the simulations. The post processing procedure of contoured parameter maps is used for this report since it provides an intuitive understanding of the predicted wind induced fluid dynamic mechanisms.

For the validation of CFD simulations with real world data an exact determination of wind speed and wind induced pressures at exact given locations is required. Rather than interpolating the numerical values from colored contour maps a procedure is adopted to extract exact simulated data from presentation grids for validation against field data.

The following describes the process of preparing and extracting simulated data for specific locations from calculated data in the computational domain. Once the specific CFD data has been obtained for the location in the computational domain, this data can be compared with actually measured data from the field observation that corresponds to the location in the computational grid. In order to obtain representative values from the CFD domain, a small virtual presentation grid of 6 by 6 data points located on a 1 foot by 1 foot square is created. This presentation grid is placed at the location in the computational domain that corresponds with the actual location of the sensors used in the field measurements. Presentation grids were used to validate the wind speed measurements.

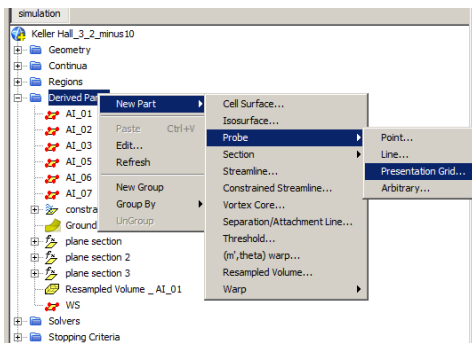
Specifically, six presentation grids in the CFD domain, named as virtual anemometer (e.g. AI_01, AI_02, AI_03, etc.) were placed at the corresponding anemometer locations using exact coordinates

determined in the field tests. Each 1'x1' square CFD presentation grid is represented by a 6 x 6 point matrix to extrapolate data at all of the 36 point. The 36 data points were averaged to obtain a representative value.

The procedure with main steps is described below:

Step 1: Create Presentation Grid:

- Derived Part > New Part > Probe > Presentation Grid...
- Name the presentation grid as the anemometer id (e.g. AI_01, etc.)
- Input Parts: choose the computational domain (air).
- Create 6x6 point presentation grids to extract the averaged simulated air velocity



Screenshot of CFD application (STAR-CCM+):

Creating a presentation grid for the evaluation of wind speed and pressure values.

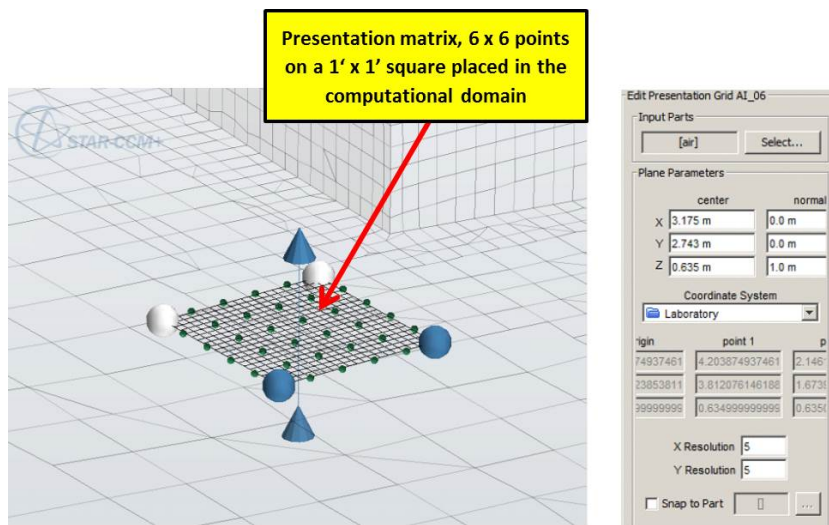
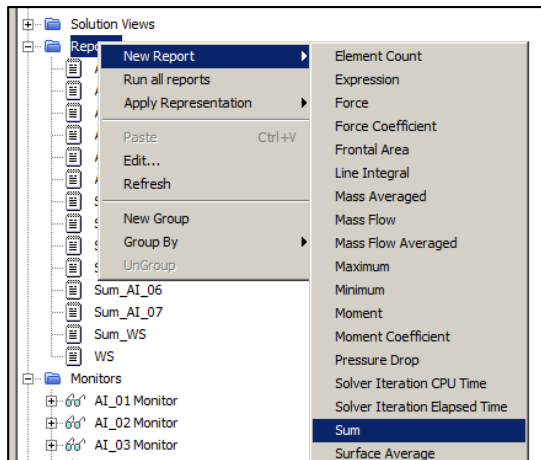


Illustration of presentation grid for the evaluation of wind speed and pressure values. *Note: the presentation grid is only a post processing function and does not affect air movement*

Step 2: Create the report and monitoring functions

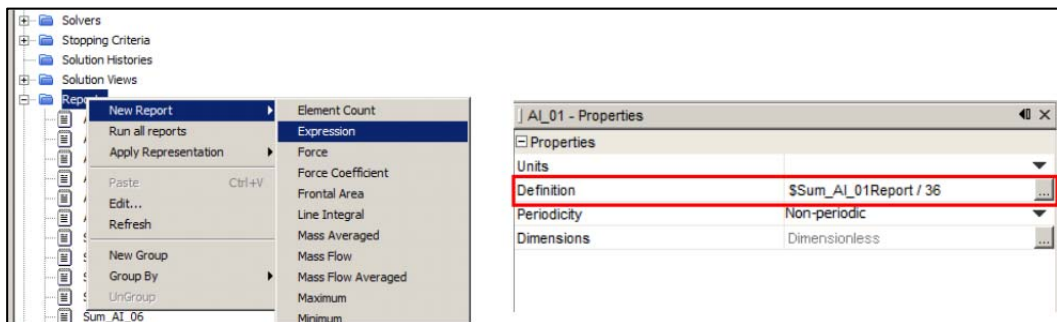
- Create a Sum report which calculate the total value based on all data extracted from 5x5 point presentation grid. Rename the sum report as Sum_AI_01, etc.



Screenshot of CFD application (STAR-CCM+):

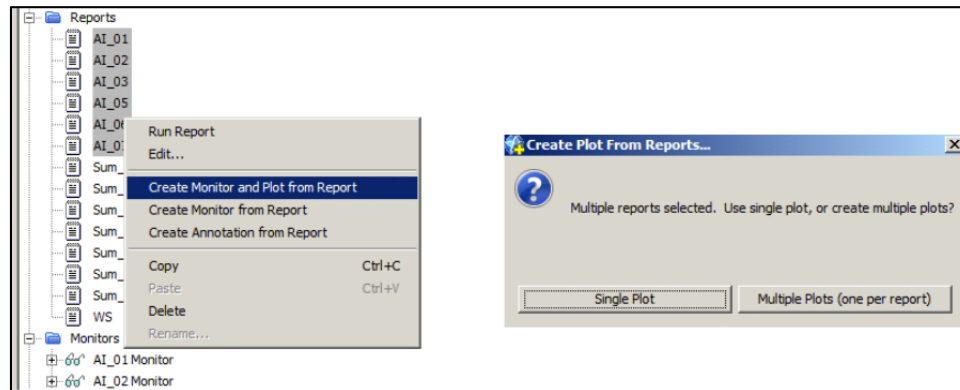
Creating a “Sum” report for the evaluation of wind speed and pressure values.

- Create an Expression report: in the definition box, add the following script `$Sum_AI_01Report/36` and so on.



Screenshot of CFD application (STAR-CCM+): Creating an “Expression” report for the evaluation of wind speed and pressure values.

- Create Monitor and Plot from reports: group select (hold SHIFT key) all reports (AI_01, AI_2, etc.) and right-click to open the pop-up menu and select Create Monitor and Plot from Report. Select Sing Plot on the next dialogue.



Screenshot of CFD application (STAR-CCM+): Creating a “Monitor and Plot” report for the evaluation of wind speed and pressure values.

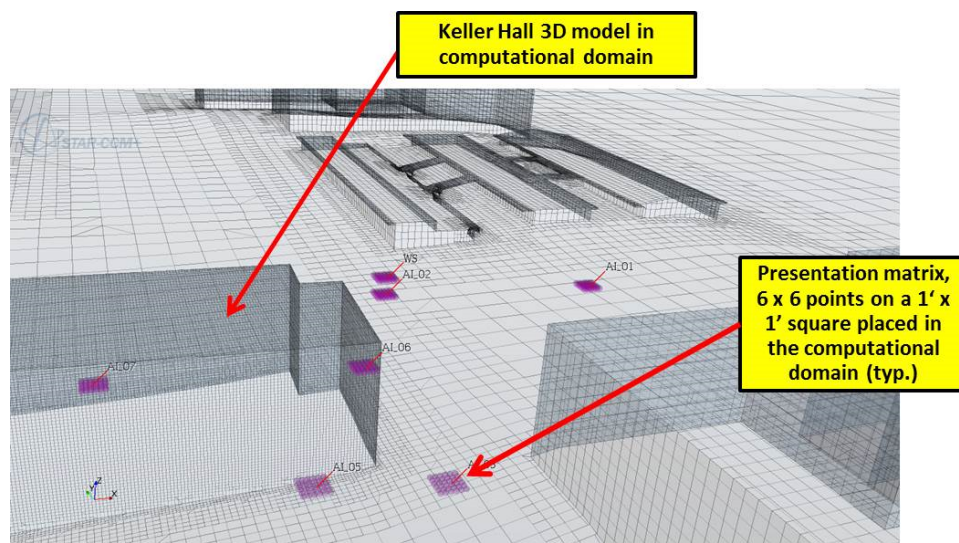


Figure 3.3.4: Screenshot of CFD application (STAR-CCM+): Depiction of all presentation grids for wind speed assessment at locations of anemometer in the field tests

Figure 3.3.5 shows an example of the wind speed values for the “virtual” anemometers (e.g. the presentation grids for the locations of the actual anemometers in the field measurements).

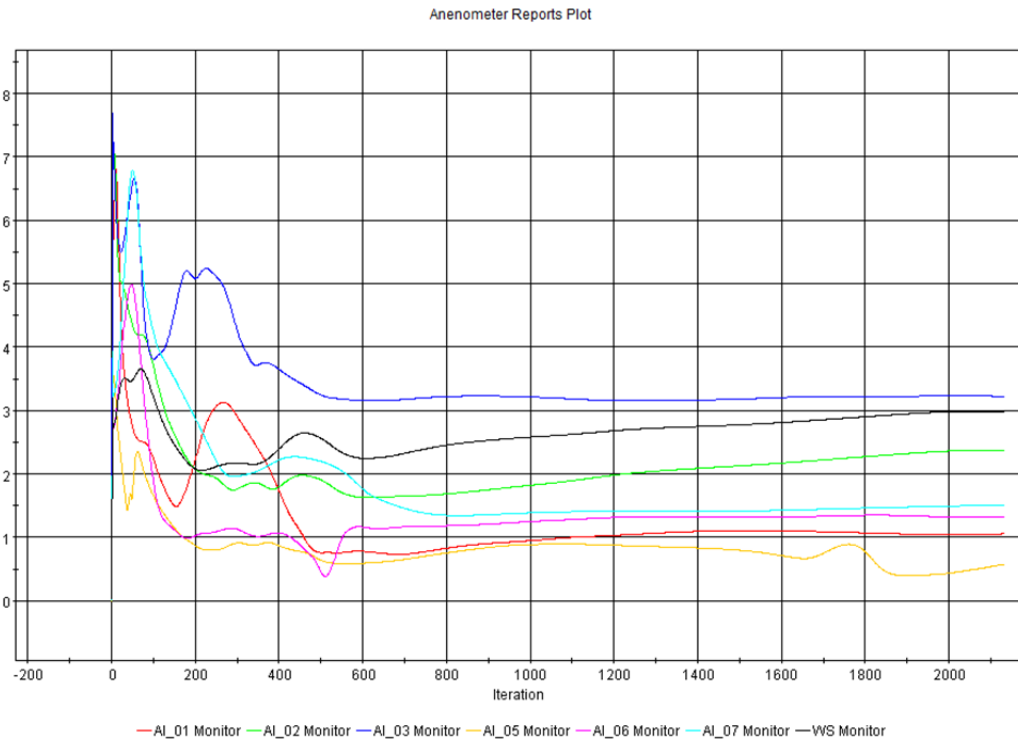


Figure 3.3.5: Example of wind speeds for presentation grids (=“virtual anemometers) obtained from CFD simulations; a sample monitor plot of the anemometer’s simulated data during the simulation

4. RESULTS AND DISCUSSION

This section of the report presents the main results of the CFD simulations and data obtained in the field tests. The results of the CFD simulations and actual field tests were used to compare theoretical and actual results and thus validate CFD predictions of relevant wind induced occurrences around buildings that affect natural ventilation performance. It must be kept in mind, though, that the correlation between CFD results and field observations uses two different time domains.

The type of steady-state CFD simulations used in this investigation represents snapshots in time and produces a prediction of instantaneous fluid dynamic occurrence within the computational domain. There are more advanced non-steady state CFD simulations, which require much more powerful computation resources than those available to the research team at the time of the research work. Even with non-steady state CFD simulations, the time periods that are simulated are relatively short, maybe several seconds or minutes. Therefore practical CFD applications at this point in time are limited to predict instantaneous fluid dynamic behavior for the performances of natural ventilation.

Natural wind flow occurrences, on the other hand, are intermittent by nature. Both wind speed and directions vary with site specific circumstances; for example, short-time gusts and longer-term variations from large scale eddies contribute to unsteadiness. The determination of the representative actual wind speed and direction at the site, on which the basis final CFD simulations are carried out, can only be done with statistical means.

Therefore the correlation of steady-state CFD wind predictions and site specific measured wind measurement require consideration of this obvious diversion of observation and analysis principles. The present discussion of result and correlation of CFD and measurement results is addressing these diverging principles.

4.1 Results of Field Measurements of Wind Speed and Directions

The data obtained in the field tests represents a significant number of data points. The data is held in a relational database with the data reduced in PostgreSQL and visualized/presented using Tableau. For this investigation, statically representative values were reduced from the raw data of wind speed and pressure measurements.

Figure 4.1.1 shows a wind rose diagram for the entire data sets, including all recorded wind speeds and wind directions. Figures 4.1.2 through 4.1.4 present sample groups, which show only data for wind speeds larger than a certain threshold. Figures 4.1.2, 4.1.3 and 4.2.4 show only data points with wind speed exceeding 2 m/s, 3 m/s and 4 m/s, respectively. It is important to note that the data analysis could not distinguish between instantaneous gusts and shorter periods of steady high winds.

From these graphs three representative wind directions were selected, which were used as input parameters for the CFD simulation runs. The selected wind directions are wind approaching from the North, East and North-East. Specific representative values were extracted for pertinent data analysis. Figures 4.1.5 through 4.1.7 provide some examples of field data representation of wind speed and direction.

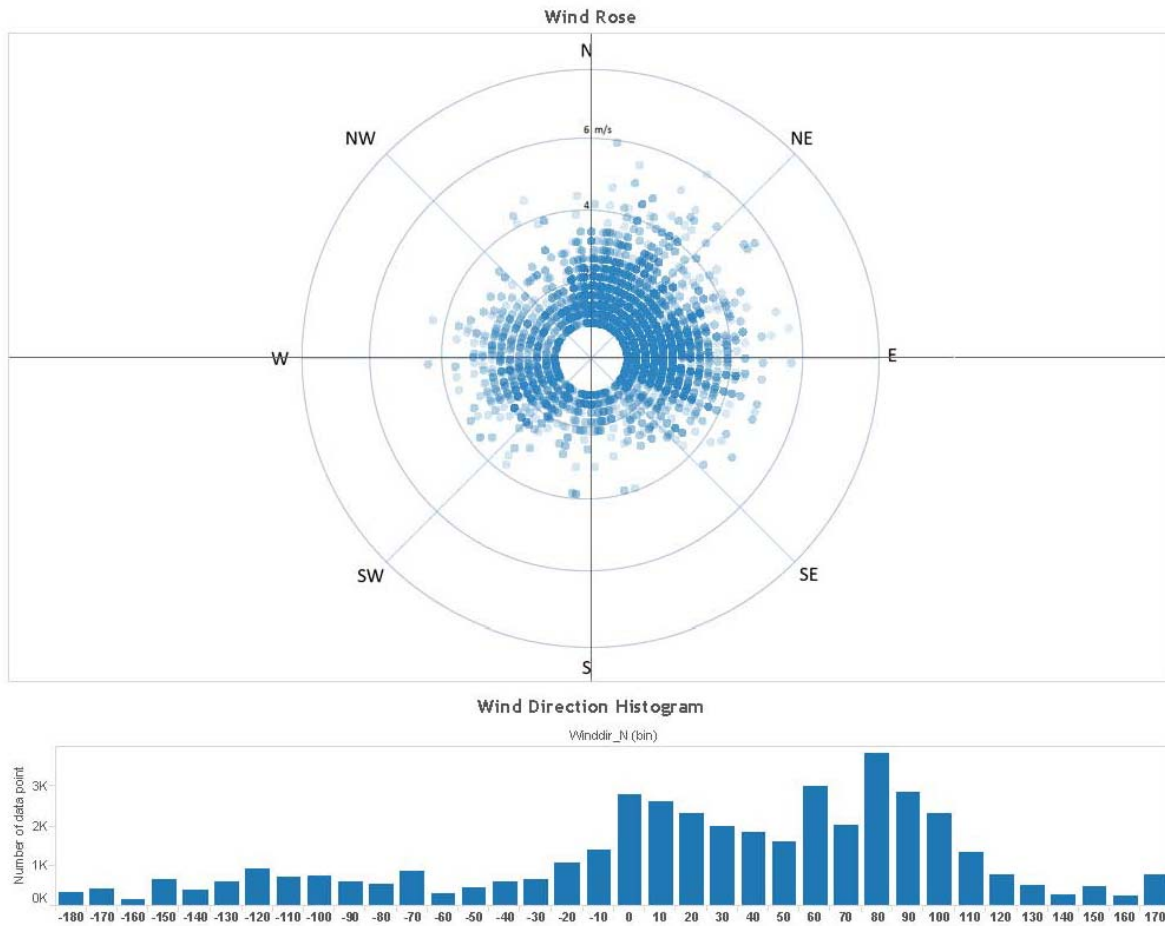


Figure 4.1.1: Wind representative observations for the entire data set (North corresponds to “0” degree)

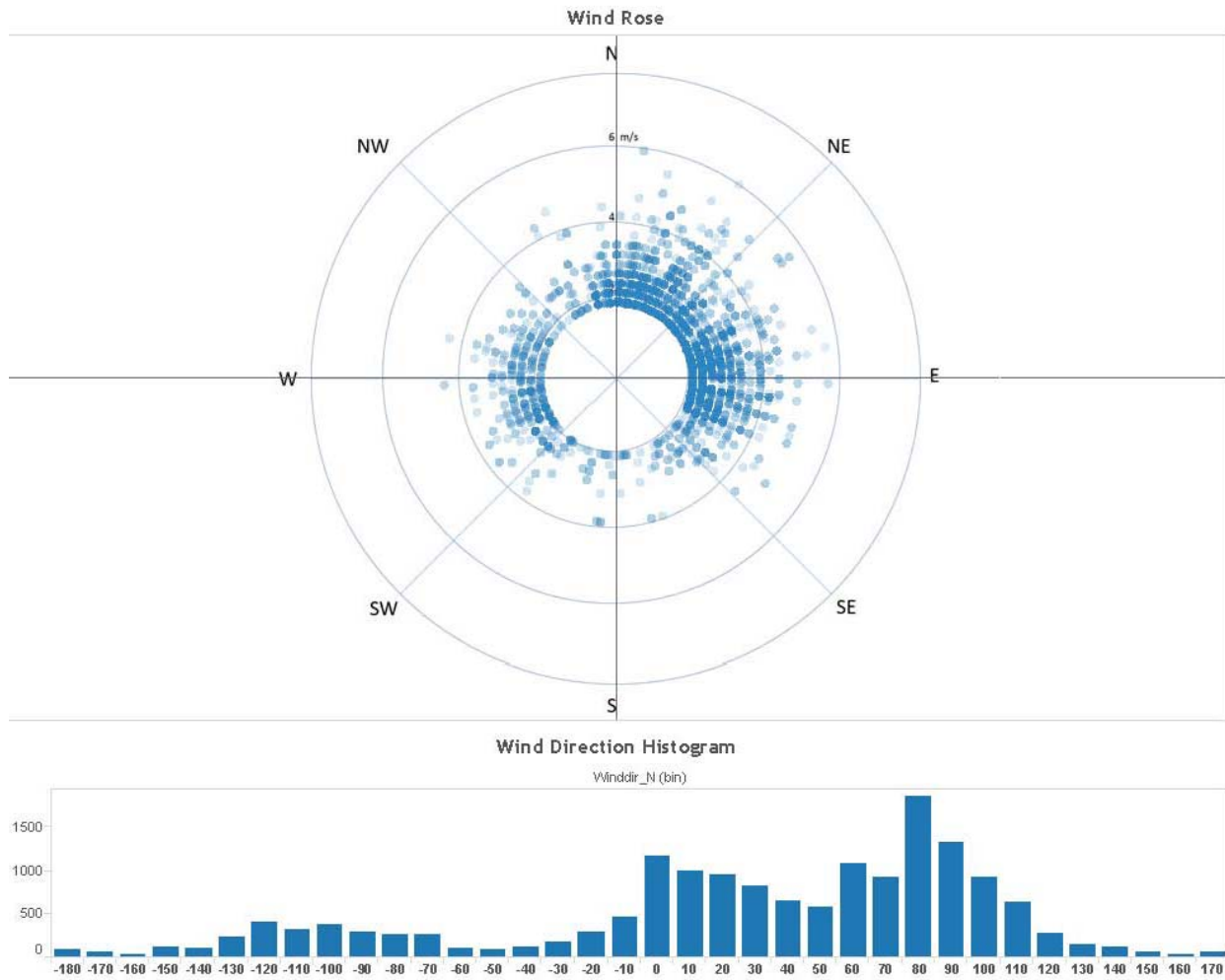


Figure 4.1.2: Observations of wind speeds and directions for the entire data set with an applied filter to present only those wind velocities above or equal to 2 m/s. (North corresponds to "0" degree)

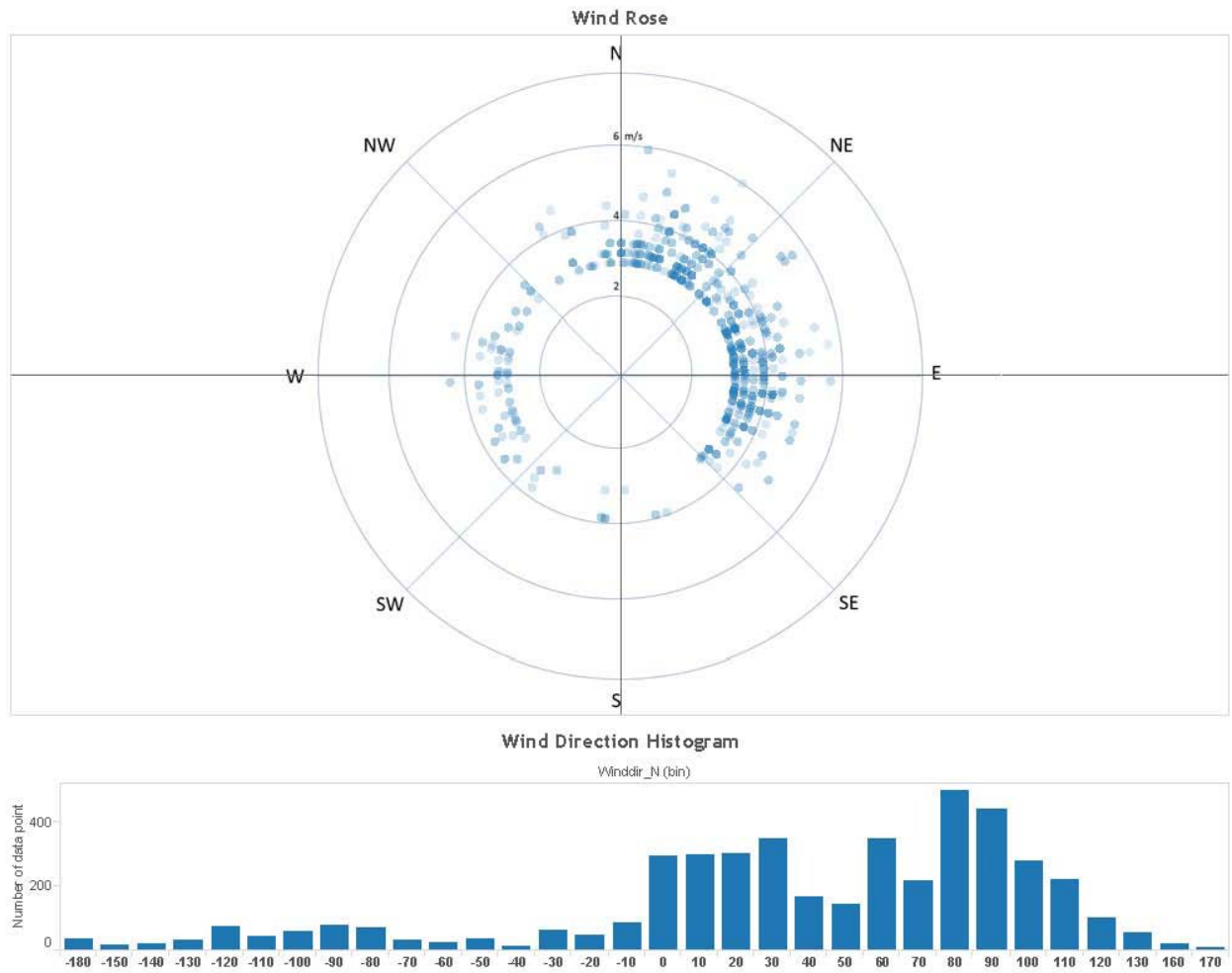


Figure 4.1.3: Observations of wind speeds and directions for the entire data set with an applied filter to present only those wind velocities above or equal to 3 m/s. (North corresponds to “0” degree)

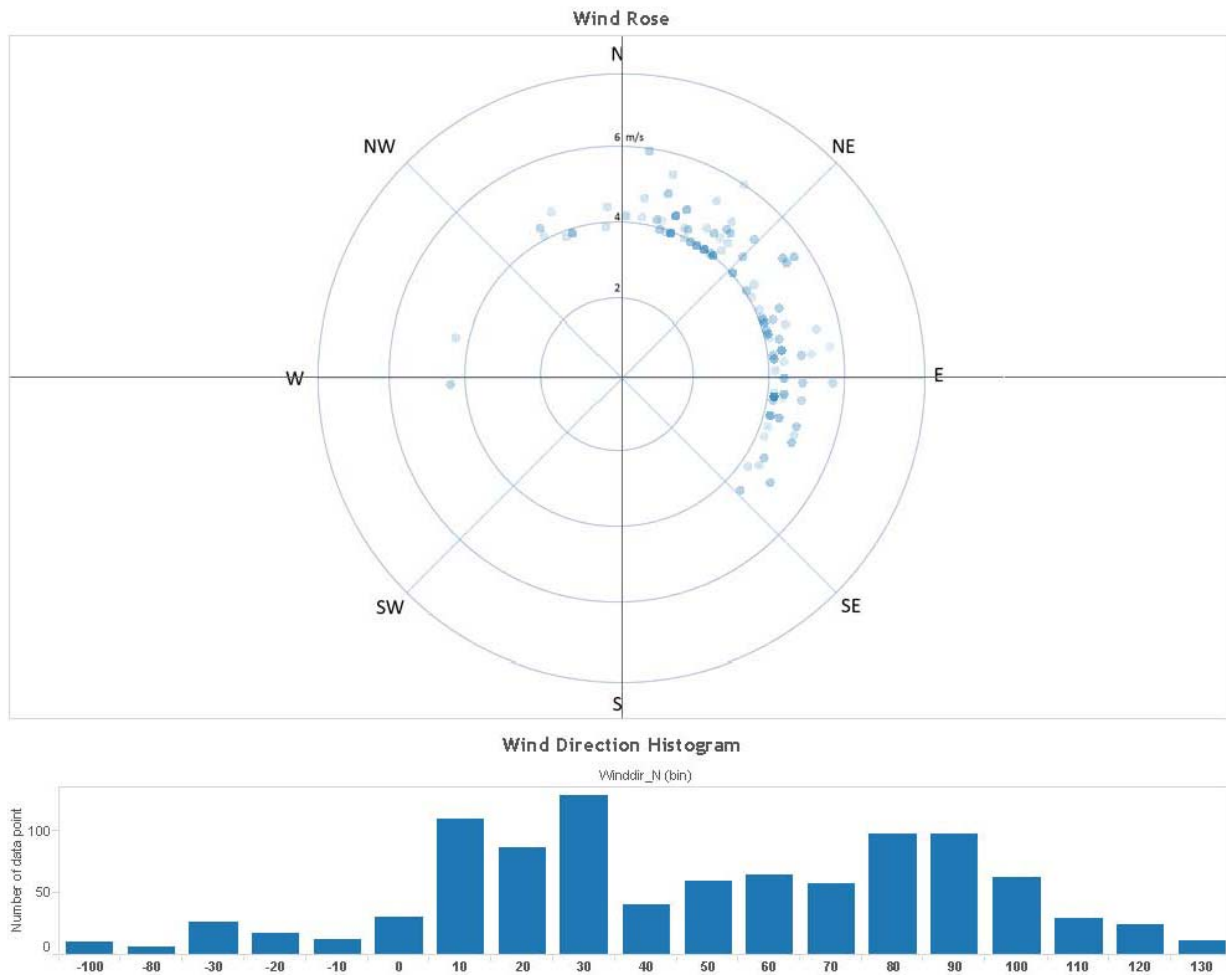


Figure 4.1.4: Observations of wind speeds and directions for the entire data set with an applied filter to present only those wind velocities above or equal to 4 m/s. (North corresponds to “0” degree)

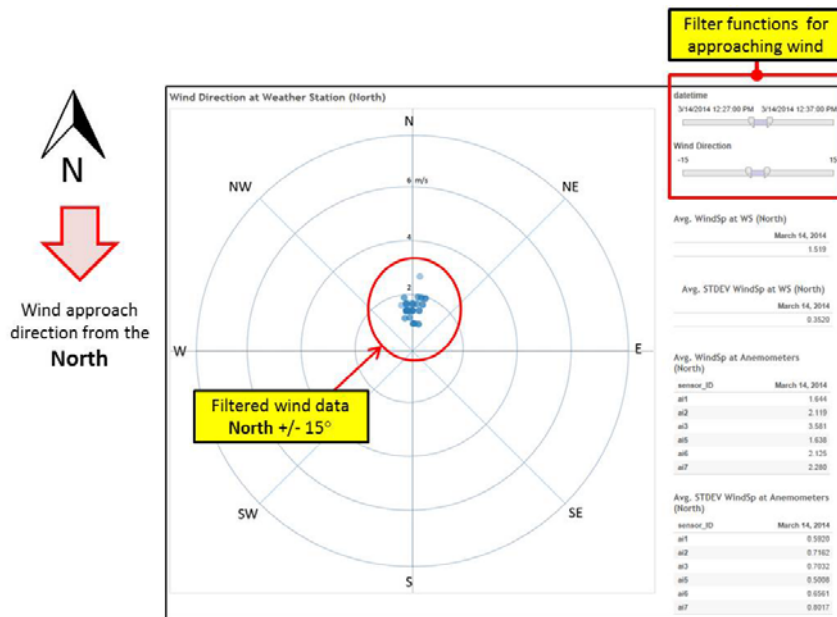


Figure 4.1.5: Filtered wind representative observations for wind from the North

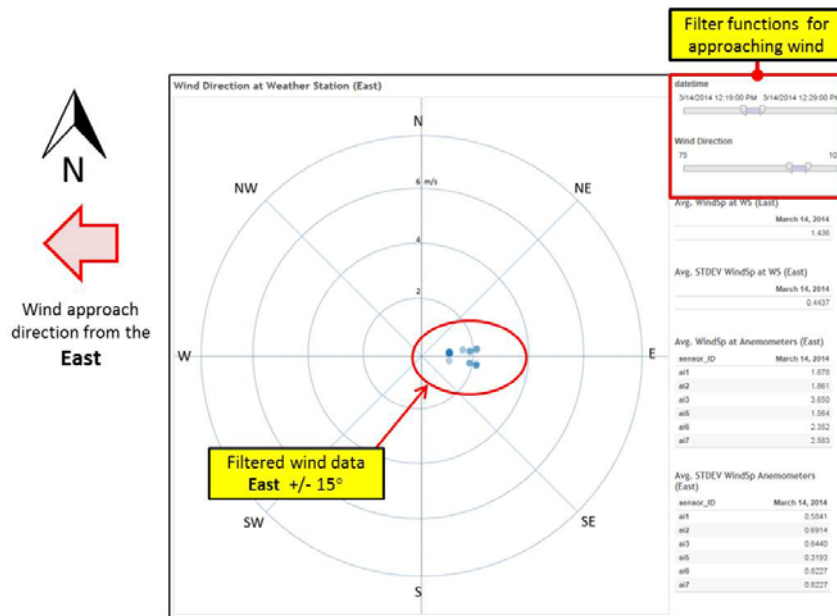


Figure 4.1.6: Filtered wind representative observations for wind from the East

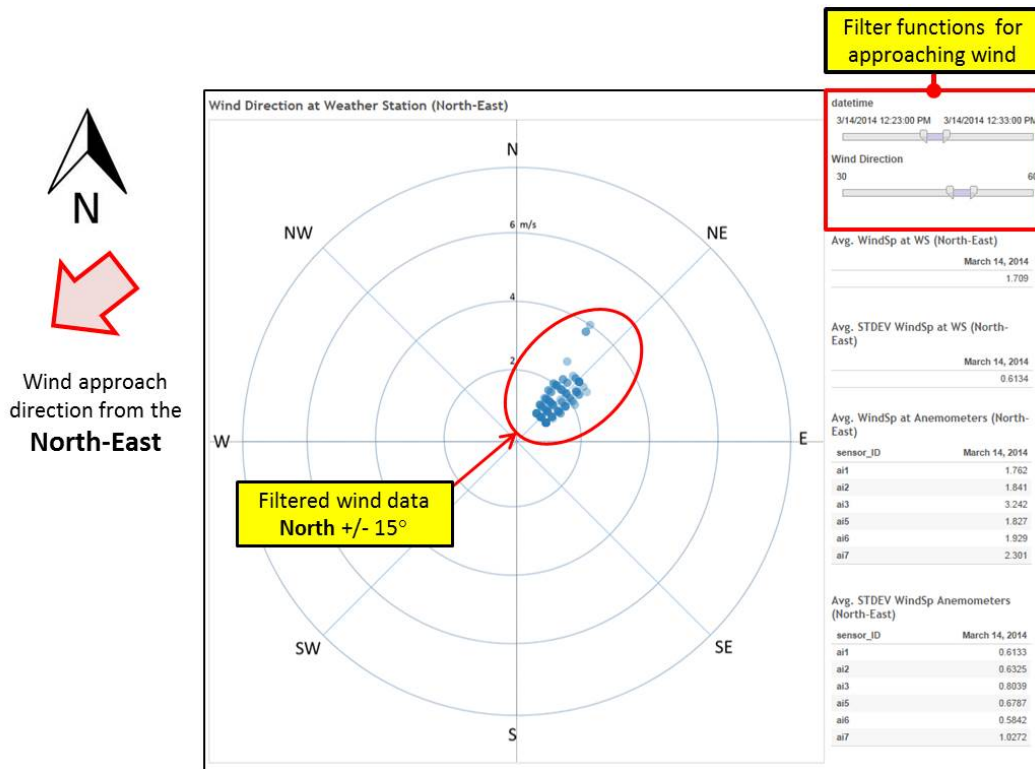


Figure 4.1.7: Filtered wind representative observations for wind from the North-East

4.2 Results of Field Measurements of for Wind Induced Pressure

Examples of pressures recorded are presented in Figure 4.2.1 and 4.2.2. The figures show differential pressures measured between the North and the South for the two opposing classrooms, 302 and 313/314, on the third floor of Keller Hall. The differential pressures are depicted for a time period of approximately one hour.

4. RESULTS AND DISCUSSION

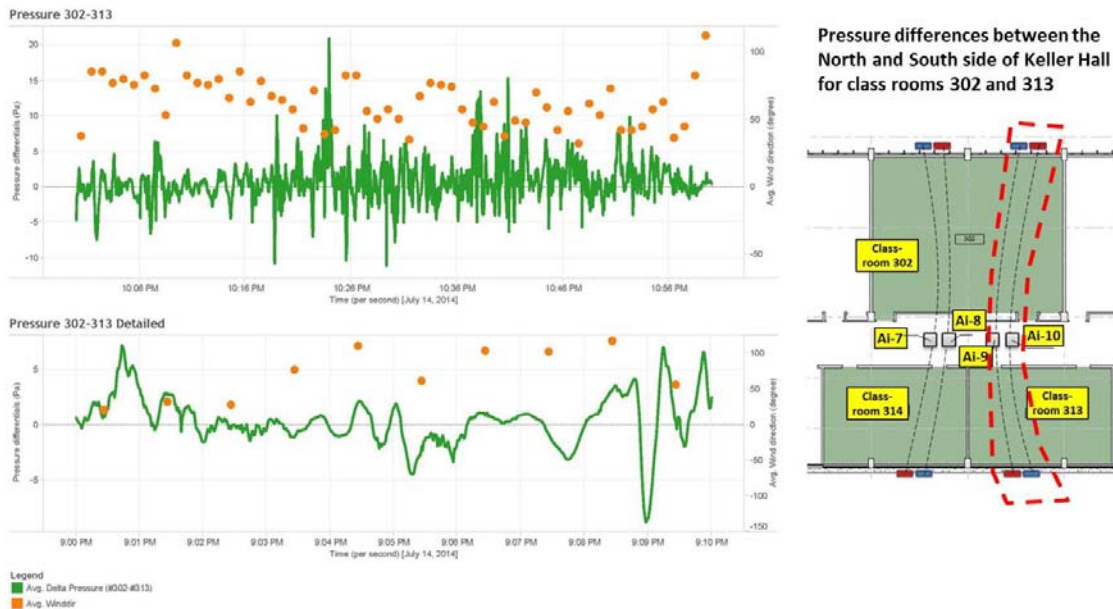


Figure 4.2.1: Differential pressure measured over a period of one hour – for opposing classrooms 302 and 313

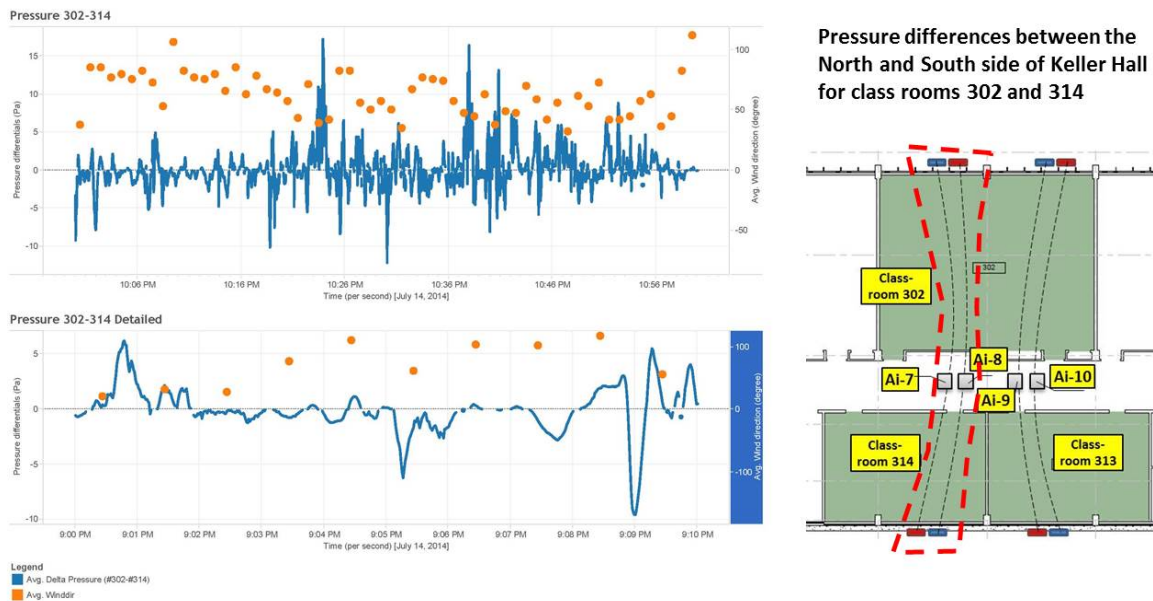


Figure 4.2.2: Differential pressure measured over a period of one hour – for opposing classrooms 302 and 314

4.3 Results of CFD Simulations

As stated previously, the steady-state CFD simulations carried out in our study provide assessments of instantaneous wind and pressure occurrences around the building. Since the wind measurements revealed significant variations of wind directions around several main wind directions, it was decided to emulate a broader representation of this range in the wind direction for CFD simulation.

The selected procedure was to carry out 27 CFD simulation runs based on a 3x3x3 parameter matrix. Figure 4.3.1 illustrates the selected parameters for the 3x3x3 matrix, which are as follows:

- The three main wind directions used for the CFD simulations, which have been identified by the field measurements as the approach wind directions; e.g. wind coming from North, East and North-East.
- The three grid resolutions used in the final CFD simulations were low, medium and high. These grid resolutions correspond to coarse, medium and fine computational grids, respectively.
- The variations from the main wind directions; +/- 10% away from the three main wind directions.

The variations of the three main wind directions were used in order to establish averages of CFD simulation results for the specific grid resolution and main wind directions. Consequently, a 3x3 parameter matrix was used for the presentation of CFD simulation results. The resulting nine CFD simulation scenarios are combinations of wind direction and grid resolutions. These nine CFD simulation scenarios are identified in Figure 4.3.2.

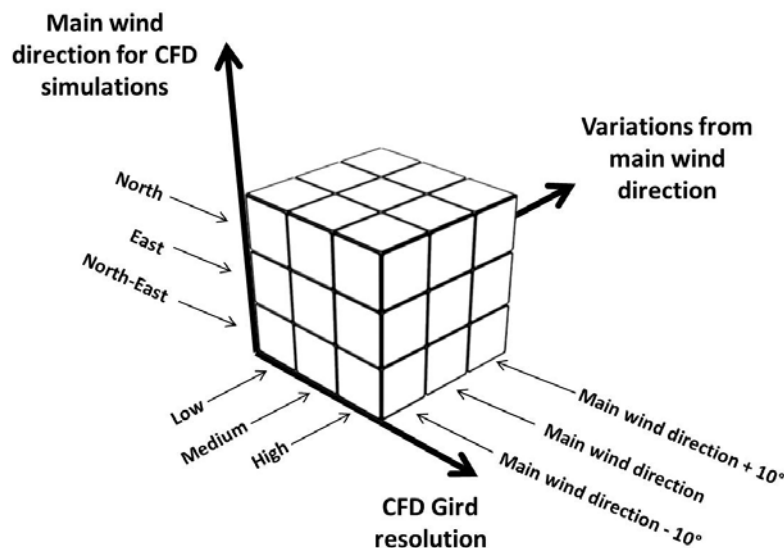


Figure 4.3.1:
Definition of the 3x3x3
parameter matrix used
for the Final CFD
simulation runs

CFD SCENARIO RUN MATRIX

Grid resolution	Approaching Wind Direction		
	North	East	Northeast
Coarse	N-C	E-C	NE-C
Medium	N-M	E-M	NE-M
Fine	N-F	E-F	NE-F

Figure 4.3.2: Definition of the 3x3 parameter matrix used for most of the CFD results presentation

Appendix A shows post processing graphs of all nine CDS scenarios, as defined in Figure 4.3.2. All nine scenarios have the same structure of illustration, which means each of them are presented by 12 post processing figures. The 12-figure structure of the “image reports” is delineated in Table 4.3.1.

Table 4.3.1.: 12-Figure Structure of the image report which is used for all nine CFD run scenarios

LIST OF IMAGE REPORT PER CFD SCENARIO RUN

Fig. No	Figure brief descriptions	View plane	View range descriptions
1	Convergence Residuals	N/A	
2	Convergence Anemometers	N/A	
3	Velocity; contours slice	oblique	over view from NE
4	Velocity; contours slice	Plan view	detail around Keller Hall
5	Velocity, streamlines	Plan view	over view
6	Velocity, streamlines	Plan view	details around Keller Hall
7	Velocity, sections	cross-section	along long axis of Keller Hall
8	Velocity, sections	cross-section	along short axis of Keller Hall
9	Pressure; contours	oblique	overview from NE
10	Pressure; contours	oblique	overview from SE
11	Pressure; contours	oblique	details of Keller Hall NE envelope, larger PA scale
12	Pressure; contours	oblique	details of Keller Hall SE envelope, larger PA scale

The following explains the significance of the 12 figures of the image report per CFD scenario run. The figures presented as samples for all scenarios depict the N-F scenario, which means “N” for wind from North and “F” using a fine grid resolution

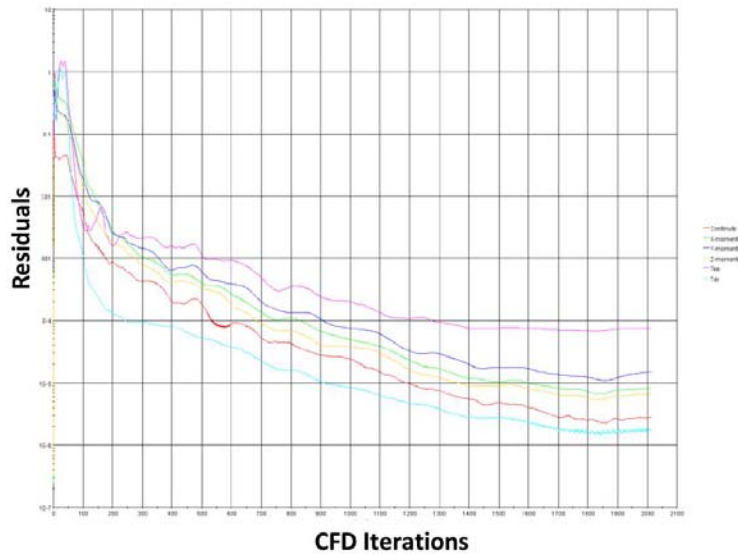


Figure 4.3.3: Type Figure 1 = Convergence Residual Plot

The convergence residual plot in Figure 4.3.3 indicates the performance of the CFD simulation, which means how well the simulation is approaching good convergence. Typically, the lower the residuals, the better the results and the more stable is the simulation.

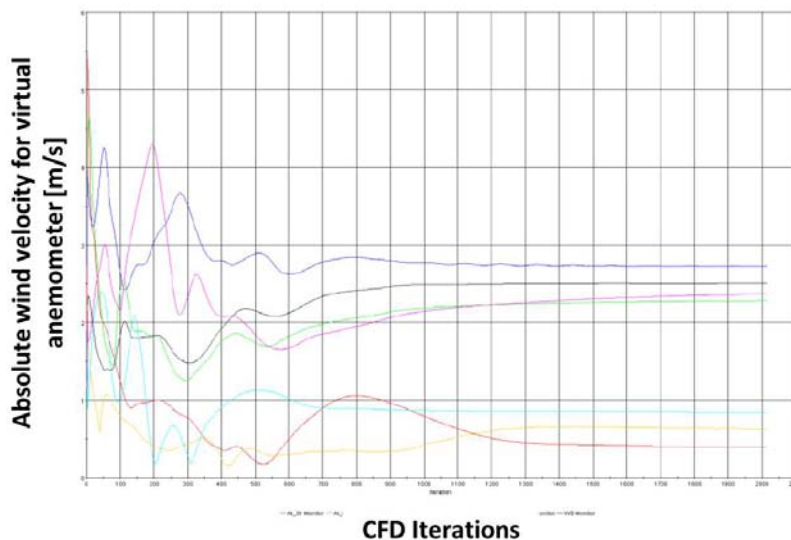


Figure 4.3.4: Type Figure 2 = Convergence Anemometers' Simulated Wind Velocity Plot

The convergence of anemometer's simulated wind plot in Figure 4.3.4 indicates when the wind velocity calculated in the CFD run converges toward the final velocity for the specific virtual anemometer. The earlier the wind velocity approaches the final value the better is the quality of the simulation.

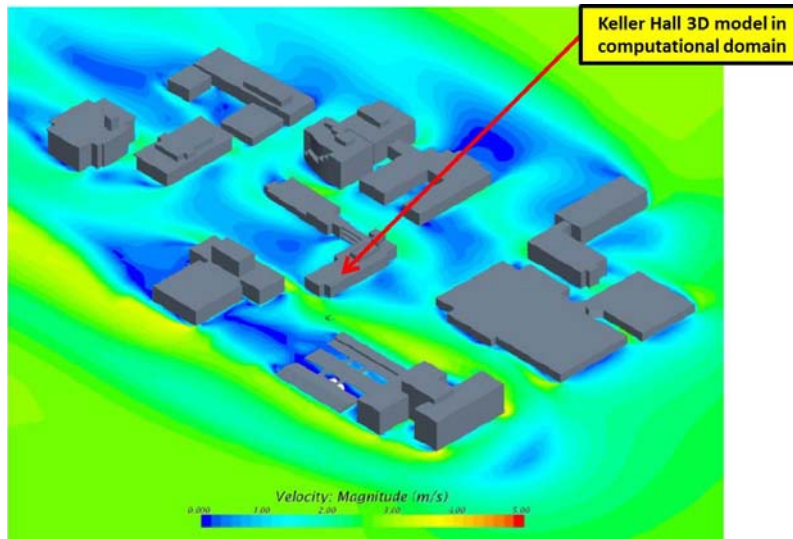


Figure 4.3.5: Type Figure 3 = Overall Isometric View (from NE) of Wind Velocity Contour Map

The colored contour map in Figure 4.3.5 indicates the wind speed around Keller Hall and surrounding buildings for wind approaching from the North. The horizontal slice (e.g. colored contour map) is referenced to the horizontal plane at 1m height above finishing level of the 1st floor of Keller Hall.

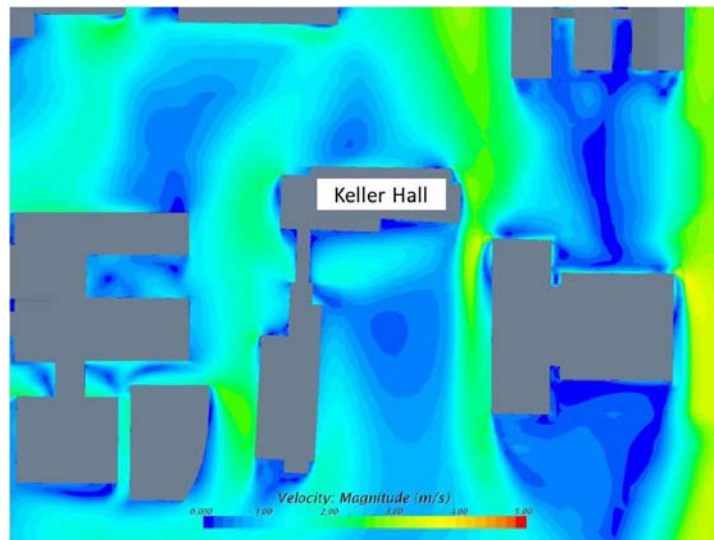


Figure 4.3.6: Type Figure 4 = Plan View of Detailed Wind Velocity Contour Map around Keller Hall

The colored contour map in Figure 4.3.6 indicates the wind speed around the Keller Hall and surrounding buildings for wind approaching from the North. The horizontal slice (e.g. contour map) is referenced to the horizontal plane at 1m height above finishing level of the 1st floor of Keller Hall.



Figure 4.3.7: Type Figure 5 = Plan View of Overall Wind Velocity Streamline Map

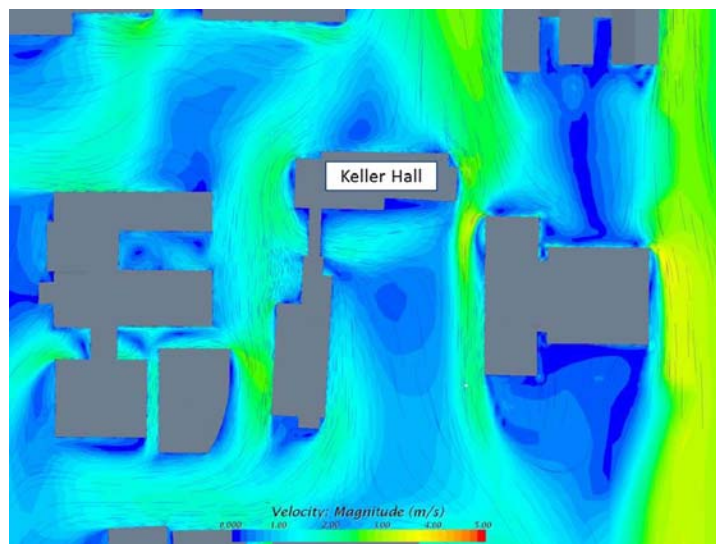


Figure 4.3.8: Type Figure 6 = Plan View of Detailed Wind Velocity Stream Map around Keller Hall

The streamlined plots in Figures 4.3.7 and 4.3.8 combine colored contour maps (e.g. indicators of the wind velocity) and wind flow streamlines (e.g. directional information of the wind flow). The plots provide a good illustration of the wind speed and streamline conditions around Keller Hall and the surrounding buildings. Wind approach is from the North.

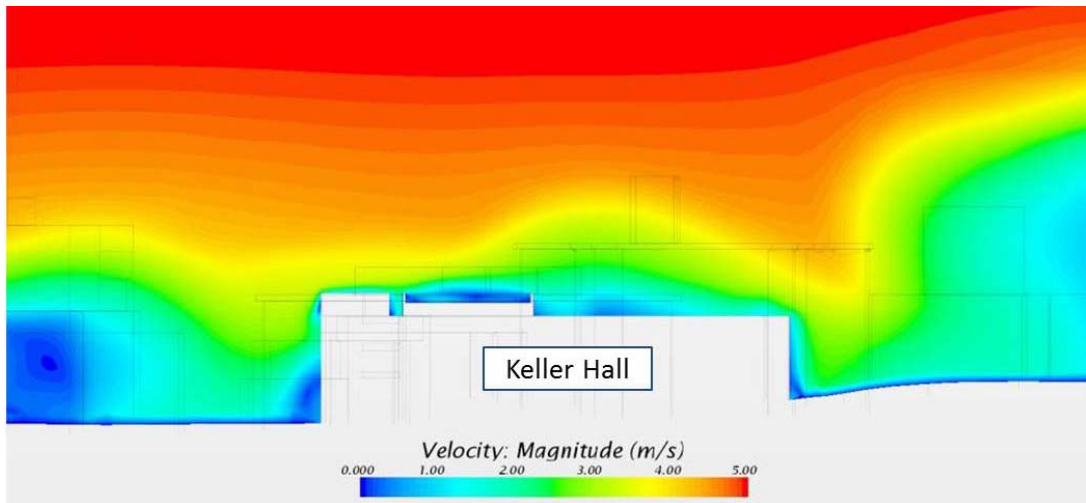


Figure 4.3.9: Type Figure 7 = Detailed Wind Velocity Contour Map on Cross Section Along Long Axis of Keller Hall (East and West is right and left in the picture)

The colored contour map in Figure 4.3.9 indicates the wind speed around the Keller Hall for wind approach from the North. The horizontal slice (e.g. contour map) is referenced to the East – West centerline of the Keller Hall building.

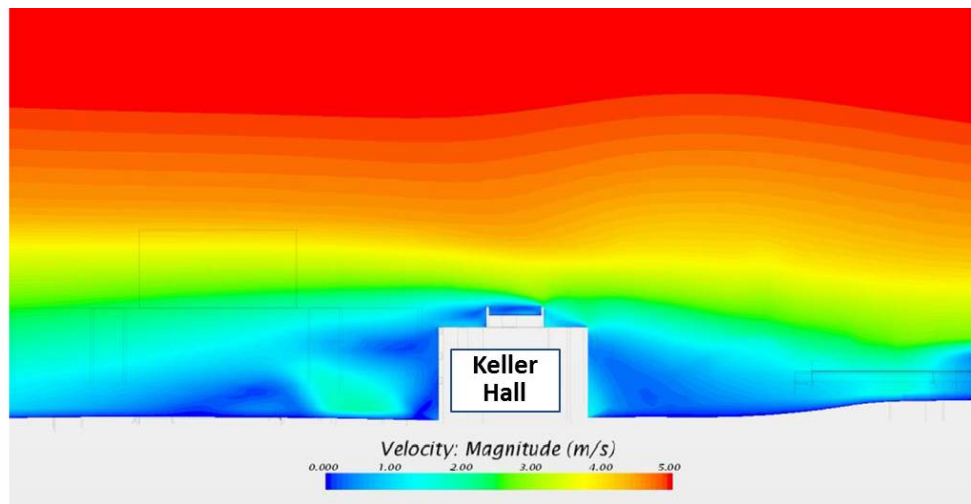


Figure 4.3.10: Type Figure 8 = Detailed Wind Velocity Contour Map on Cross Section Along Short Axis of Keller Hall (North and South is left and right in the picture)

The colored contour map in 4.3.10 indicates the wind speed around the Keller Hall for wind approach from the North. The horizontal slice (e.g. contour map) is referenced to the North-South centerline of the Keller Hall building.

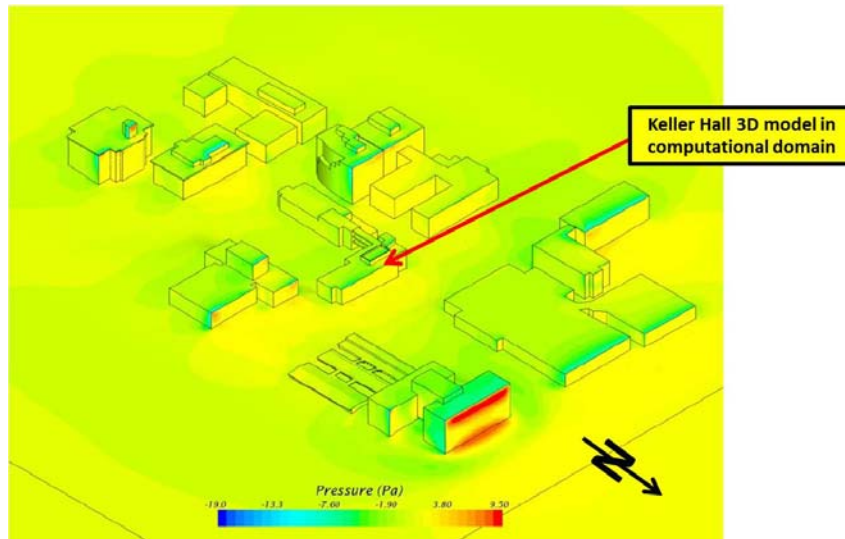


Figure 4.3.11: Type Figure 9 = Overall Isometric View (from NE) of Wind-Induced Pressure Distribution on Building Facades

The colored contour map in Figure 4.3.11 provides an overview of absolute pressure from the Northeast on the Keller Hall buildings and surrounding buildings. Wind approach is from the North.

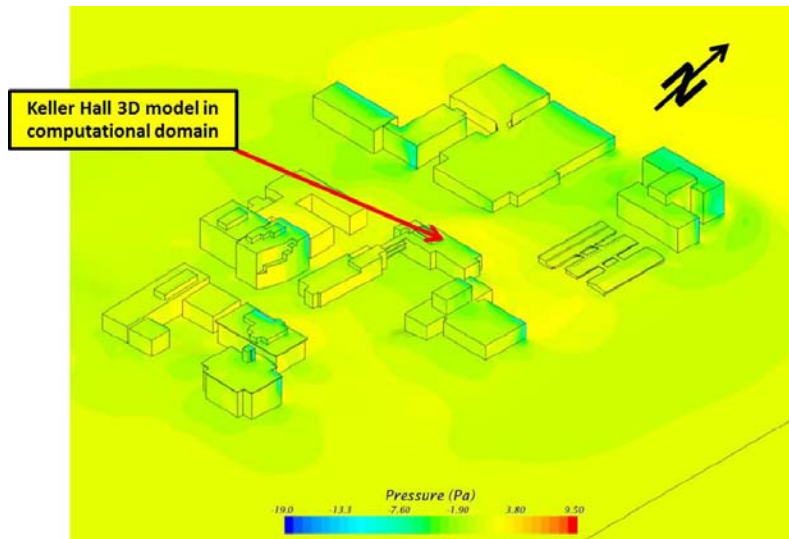


Figure 4.3.12: Type Figure 10 = Overall Isometric View (from SE) of Wind-Induced Pressure Distribution on Building Facades

This contour map in 4.3.12 provides an overview from the Southeast of absolute pressure on the Keller Hall buildings and surrounding buildings. Wind approach is from the North.

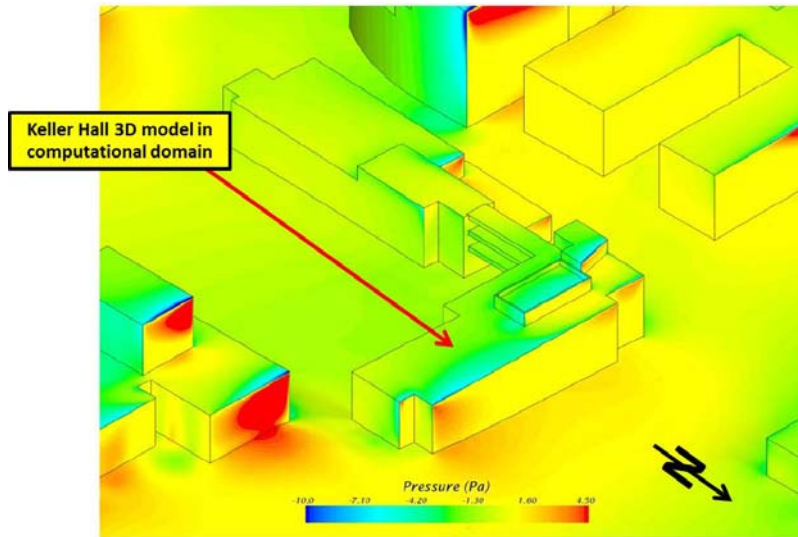


Figure 4.3.13: Type Figure 11 = Detailed Isometric View (from NE) of Wind-Induced Pressure Distribution on Keller Hall's Facades

The colored contour map in Figure 4.3.13 provides a detailed view from the Northeast of absolute pressures on the Keller Hall buildings. Wind approach is from the North.

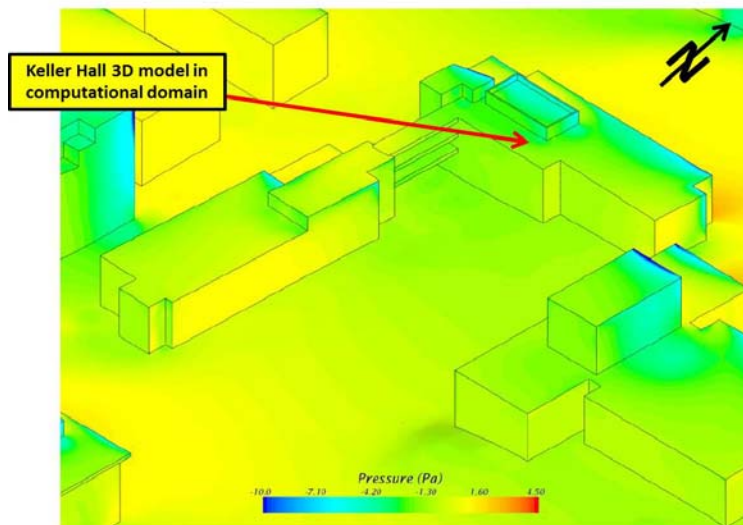


Figure 4.3.14: Type Figure 12 = Detailed Isometric View (from SE) of Wind-Induced Pressure Distribution on Keller Hall's Facades

The colored contour map in Figure 4.3.14 provides a detailed view from the Southeast of absolute pressures on the Keller Hall buildings. Wind approach is from the North.

4.4 Discussion of Results

This section discusses the comparison of measured wind and pressures values and values derived from the various CFD simulations.

Table 4.4.1 provides the main characteristics for the three computational grids used in the simulations. Table 4.4.2 shows wind speeds at the virtual anemometers positions calculated for nine CFD scenarios. As can be seen for each scenario the wind speed has been calculated for the main wind direction as well as for two wind direction variations, e.g. +10° and -10° direction variation from the main wind directions. For the scenarios, the wind speeds obtained at the +/- 10° wind direction variations differ from the main wind direction. The arithmetic mean of the three values is the representative value considered for the CFD scenario. The values in Table 4.4.2 indicate that the calculated wind velocities between the mean direction and the two 10° direction variations differ most for the scenarios with North wind. The smallest differences are obtained for winds from the East.

Table 4.4.3 depicts pressure differentials between the North and South facades of the building for the nine CFD scenarios. Within each scenario, values differ between the main wind direction and the two wind direction variations. There is no clear trend recognizable and average values for differential pressure for each scenario are obtained by the arithmetic mean of the values for main wind direction and two wind direction variations. Figures 4.4.1 and 4.4.2 indicate sensitivity of calculated values to the resolution of CFD grids used in the simulations. The resolution of the grid refers to the number of cells that are used in the computational domain. The number of cells increases as the cell sizes is decreased close to the target object, which means close to the flow obstruction that is under observation. Table 4.4.1 indicates the grid characteristics for the three grid resolutions used in the final CFD analysis.

Table 4.4.1: Characteristics for three different types of CFD grids (e.g. meshes)

	Unit	Coarse	Medium	Fine
Minimum cell size	{m}	0.10	0.08	0.06
Maximum cell size	{m}	72.00	57.60	43.20
Total volume cells	#	3,041,620	4,441,165	7,898,730

The sensitivity analysis in Figures 4.4.1 and 4.4.2 suggests that calculated wind velocities obtained with grids of different resolutions diverge more at lower than at higher wind speed. Explanations for these trends could include indications that transport terms in the CFD codes are more congruent at higher mass transport velocity, which means higher momentum transfer at higher wind speeds. Explanations could also indicate that vortex shedding and turbulent energy at lower wind velocities can affect resulting wind velocities more at lower wind speeds. The previous literature review suggested that typically CFD results of wind movement around buildings using higher wind speeds are more consistent with observed wind speeds than CFD results using lower wind speeds.

Table 4.4.2: Results of CFD simulations to determine wind velocities (m/s) at given anemometers' locations at given approaching wind directions simulated at different grid resolutions (coarse, medium and fine).

Resolution		North						East						North East					
		AI_01	AI_02	AI_03	AI_05	AI_06	AI_07	AI_01	AI_02	AI_03	AI_05	AI_06	AI_07	AI_01	AI_02	AI_03	AI_05	AI_06	AI_07
Coarse	-10	1.96	1.53	1.97	0.62	1.37	1.89	3.21	3.07	2.72	0.97	1.50	0.58	2.74	1.71	3.67	1.06	1.21	1.15
	0	0.39	2.28	2.72	0.62	2.36	0.84	3.31	3.19	2.78	0.99	1.72	1.15	1.94	2.64	3.77	0.65	0.57	2.39
	+10	1.46	0.79	3.04	0.51	0.75	0.99	3.38	3.33	1.80	0.81	0.98	0.79	1.18	2.16	3.26	0.81	1.38	1.55
	Avg.	1.27	1.53	2.58	0.59	1.49	1.24	3.30	3.19	2.43	0.93	1.40	0.84	1.95	2.17	3.57	0.84	1.05	1.70
Medium	-10	2.02	1.58	1.94	0.56	1.47	1.81	3.19	3.05	2.72	0.93	1.49	0.65	2.75	1.66	3.58	0.99	1.24	1.41
	0	0.48	2.22	2.73	0.67	2.23	0.82	3.29	3.16	2.76	0.98	1.69	1.01	1.90	2.76	3.75	0.71	0.72	2.38
	+10	1.36	0.68	2.98	0.52	0.90	0.93	3.36	3.30	1.80	0.89	0.99	0.64	1.04	2.36	3.23	0.43	1.32	1.49
	Avg.	1.29	1.49	2.55	0.58	1.53	1.19	3.28	3.17	2.43	0.93	1.39	0.77	1.90	2.26	3.52	0.71	1.09	1.76
Fine	-10	1.99	1.50	1.93	0.52	1.51	1.87	3.20	3.03	2.71	0.93	1.51	0.69	2.78	1.65	3.63	1.07	1.25	1.17
	0	0.53	2.24	2.70	0.61	2.27	0.82	3.31	3.19	2.78	0.99	1.72	1.15	1.94	2.72	3.57	0.60	0.55	2.43
	+10	1.47	0.51	3.07	0.52	1.15	0.91	3.38	3.32	1.79	0.91	0.95	0.67	1.08	2.42	3.28	0.79	1.32	1.57
	Avg.	1.33	1.42	2.57	0.55	1.65	1.20	3.30	3.18	2.43	0.94	1.39	0.84	1.93	2.27	3.49	0.82	1.04	1.72

Table 4.4.3: Results of CFD simulations to determine pressure differential comparison (Pa) between three different grid resolutions (coarse, medium and fine) at given approaching wind directions.

Grid Resolution	Pressure differential terminal ID	North				East				North East			
		-10	due North	+ 10	Avg.	-10	due East	+ 10	Avg.	-10	due NorthEast	+ 10	Avg.
Coarse	AI_08	2.314	1.654	4.765	2.911	-0.480	-1.058	-1.552	-1.030	0.336	0.764	0.650	0.583
	AI_09	3.560	1.849	4.216	3.209	-0.631	-0.985	-1.472	-1.030	0.334	0.466	0.357	0.386
	AI_10	-1.934	-1.704	-1.099	-1.579	-0.820	0.190	0.526	-0.035	-2.135	-2.743	-2.614	-2.497
	AI_11	-2.089	-1.787	-1.126	-1.668	-0.462	0.417	1.926	0.627	-3.272	-3.761	-2.771	-3.268
Medium	AI_08	2.233	1.635	4.634	2.834	-0.455	-1.083	-1.698	-1.079	0.317	0.744	0.632	0.564
	AI_09	3.388	1.795	4.062	3.082	-0.581	-1.020	-1.609	-1.070	0.306	0.442	0.334	0.361
	AI_10	-1.919	-1.723	-1.123	-1.588	-0.940	0.190	0.482	-0.089	-2.219	-2.763	-2.587	-2.523
	AI_11	-2.060	-1.806	-1.175	-1.680	-0.516	0.442	1.762	0.563	-3.333	-3.703	-2.775	-3.270
Fine	AI_08	2.316	1.660	4.666	2.881	-0.401	-1.058	-1.708	-1.056	0.316	0.774	0.689	0.593
	AI_09	3.567	1.835	4.126	3.176	-0.538	-0.985	-1.625	-1.049	0.308	0.471	0.376	0.385
	AI_10	-1.912	-1.711	-1.119	-1.581	-1.018	0.190	0.440	-0.129	-2.087	-2.783	-2.585	-2.485
	AI_11	-2.060	-1.789	-1.166	-1.672	-0.573	0.417	1.712	0.519	-3.235	-3.746	-2.724	-3.235

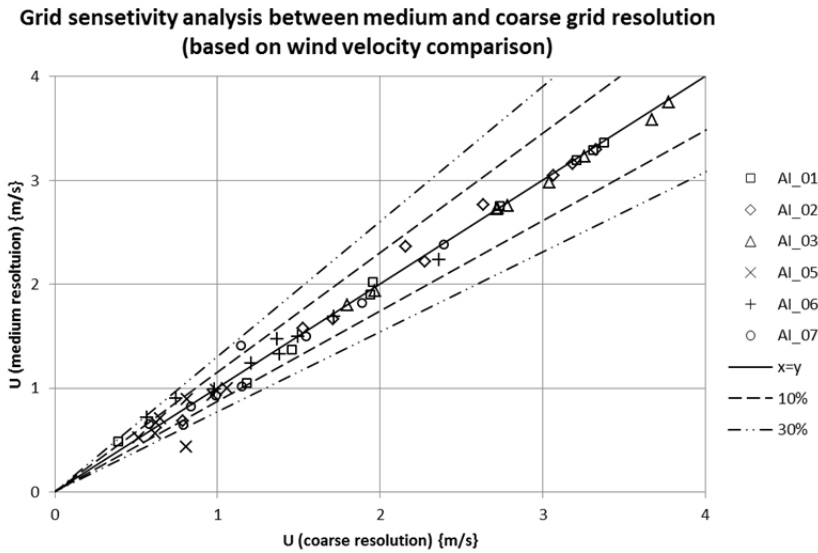


Figure 4.4.1: Comparison of wind velocities obtained through CFD simulation using a coarse and fine grid – for all wind approach directions

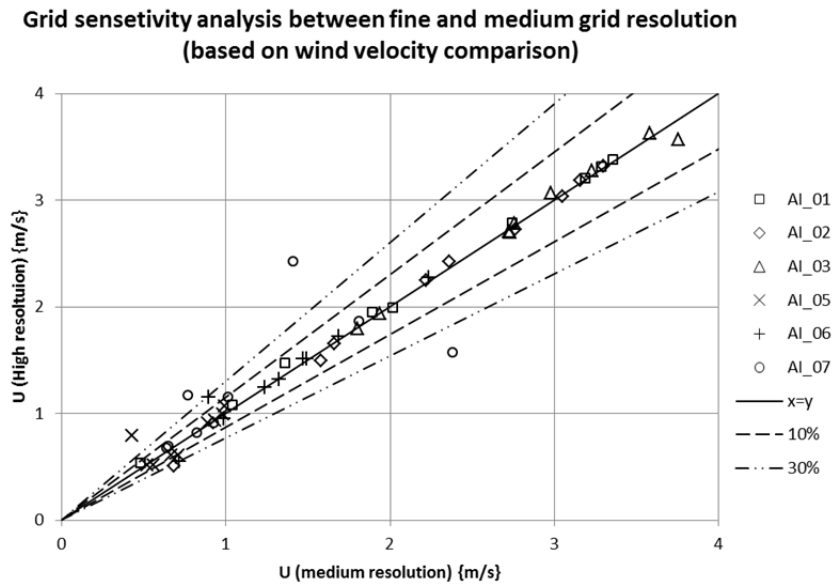


Figure 4.4.2: Comparison of wind velocities obtained through CFD simulation using a medium and fine grid – for all wind approach directions

Table 4.4.3 presents a summary of wind velocities obtained through data reduction of actual field measurements and CFD calculated values for all anemometer locations. The CFD values were obtained with a medium grid resolution.

Figures 4.4.3, 4.4.4 and 4.4.5 show comparisons of measured and CFD predicted wind velocities for wind approach directions from the North, East and North-East, respectively. Figure 4.4.6 shows the divergence of measured and CFD simulated (medium grid resolution) values for the three wind directions. The comparison of representative values obtained by CFD simulation and field measurements depict the most consistent tend for wind approaching the building from the North.

The comparison of averaged measured data and calculated CFD results suggest that values show reasonable and less reasonable correlations for selected wind setting and anemometer locations. Figure 4.4.7 shows the probability density of the velocity divergence ratios V_d falling into certain ranges. The range of diverging values shown in Figure 4.4.7 indicate that about two thirds of the data points that correlate between measured and CD calculated values show less than 50% divergence. Compared with other studies presented in the literature these diverging values are not uncommon.

Table 4.4.3: Wind velocities obtained through field measurement and CFD simutaions, for all anemometer locations

Approaching wind direction		AI_01	AI_02	AI_03	AI_05	AI_06	AI_07
Measurement							
North	avg.	1.644	2.119	3.581	1.638	2.125	2.280
	stdev	0.592	0.716	0.703	0.501	0.656	0.802
East	avg.	1.678	1.861	3.650	1.564	2.352	2.583
	stdev	0.584	0.691	0.644	0.319	0.823	0.823
North East	avg.	1.709	1.762	1.841	3.242	1.827	2.301
	stdev	0.613	0.633	0.804	0.679	0.584	1.027
Simulation							
North	avg.	1.289	1.493	2.550	0.583	1.534	1.187
East	avg.	3.279	3.167	2.427	0.935	1.389	0.769
North East	avg.	1.895	2.263	3.523	0.712	1.093	1.761

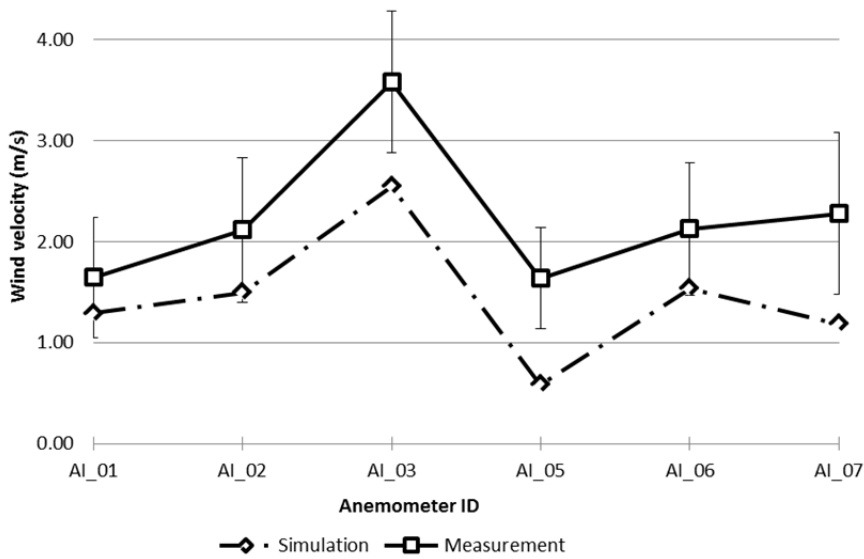


Figure 4.4.3: Comparison between averaged wind velocity for field measurements and simulation (medium grid resolution) wind is approaching from the North.

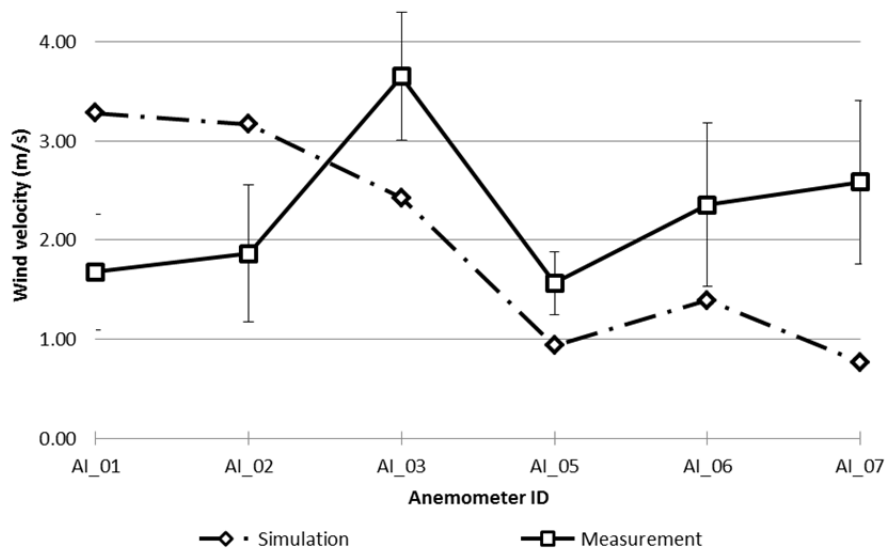


Figure 4.4.4: Comparison between averaged wind velocity for field measurements and simulation (medium grid resolution) wind is approaching from the East.

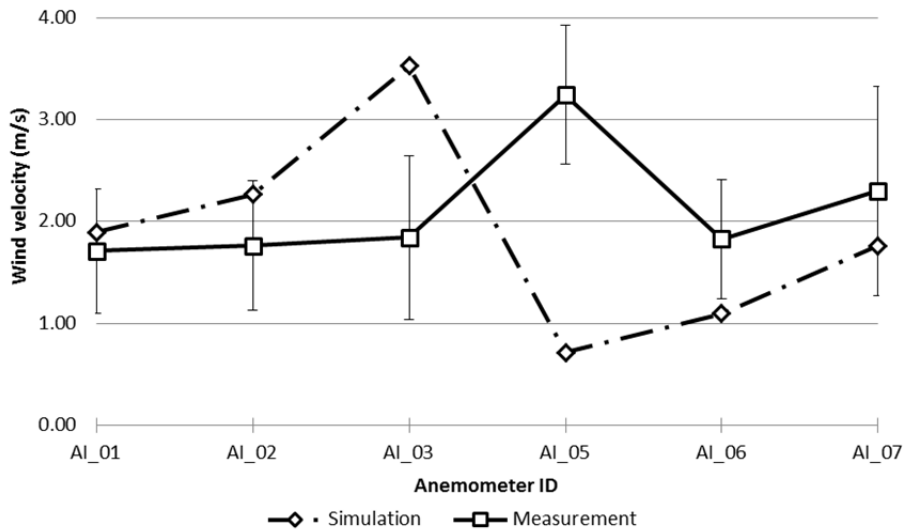


Figure 4.4.5: Comparison between averaged wind velocity for field measurements and simulation (medium grid resolution) wind is approaching from the North-East.

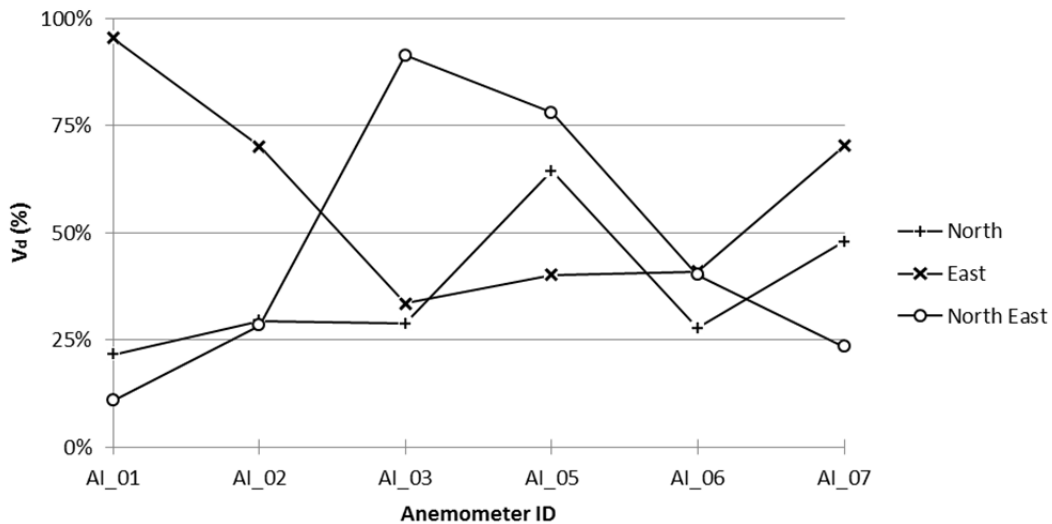


Figure 4.4.6: Wind velocity divergence ratios V_d (%) between measurement and simulation (medium grid resolution) at given approaching wind directions ($V_d = ABS((V_s - V_m)/V_m)$), where V_s is simulated wind velocity and V_m is measured wind velocity).

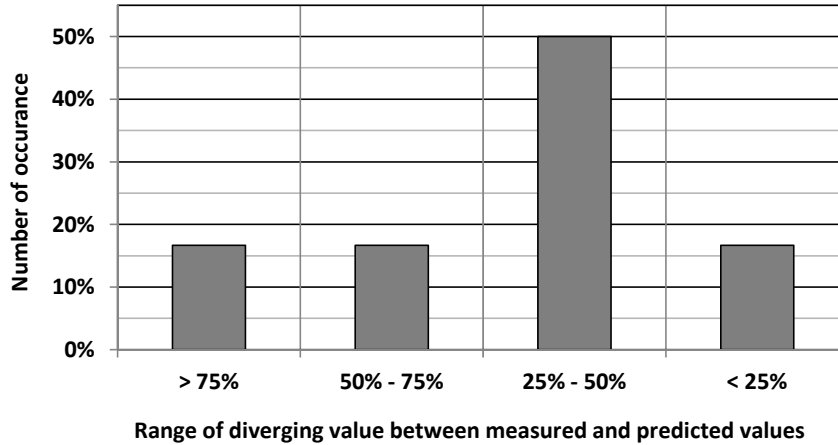


Figure 4.4.7: Probability density of velocity divergence ratios V_d (from Figure 4.4.6)

Table 4.4.4 presents the sensitivity of grid resolution on results of CFD simulations for the main three wind directions. A low percentage value indicates good correlation between the different grid resolutions. The values in Table 4.4.4 suggest that the highest divergences between CFD simulations using different grid resolutions occur with wind coming from the East. The smallest divergences are observed with wind coming from the North. These results are consistent with assumptions of winds from the North having the least effects on uncertain flow separation and leeward eddies. Winds from the East would bring approaching winds parallel the North and South facades which promotes large-scale and small scale eddy generation (e.g. created by the vertical fins on the North and South facades) and therefore possible non converging characteristics for near façade points. The pressure tubing terminals were installed in close proximity to the South and North walls.

Table 4.4.5 and Figure 4.4.8 indicate differences of values for differential pressures obtained through measurements and CFD simulations. The results suggest that the CFD simulations over predict pressure differentials for wind approaching from the North and the North-East. Measured and calculated values for wind coming from the East suggest that a higher pressure is produced on the South façade. This results in negative values for East winds in Table 4.4.5 and Figure 4.4.8. It should be noted how small the pressure differentials are between the North and South façade. Reliable measurements of such small pressures are quite difficult and reasons for the diverging measured and calculated values could be pressure transducer limitations at such small pressure differentials.

Table 4.4.4: Grid sensitivity analysis for differential pressures between North and South façade of Keller Hall

Grid resolution	Pressure differential terminal ID	North	East	Northeast
Medium vs. Coarse	Ai_7	2.7%	4.5%	3.4%
	Ai_8	4.1%	3.8%	7.0%
	Ai_9	0.6%	61.2%	1.0%
	Ai_10	0.8%	11.4%	0.1%
Fine vs. Medium	Ai_7	1.6%	2.2%	4.8%
	Ai_8	3.0%	2.0%	6.4%
	Ai_9	0.5%	30.8%	1.5%
	Ai_10	0.5%	8.5%	1.1%

Table 4.4.5: Grid sensitivity analysis for differential pressures between North and South façade of Keller Hall

Wind direction		North		East		North East	
The location where pressure differentials measured		Delta P. btw #302-#313 (North)	Delta P. btw #302-#314 (North)	Delta P. btw #302-#313 (East)	Delta P. btw #302-#314 (East)	Delta P. btw #302-#313 (North-East)	Delta P. btw #302-#314 (North-East)
Measurement	Average	1.721	1.190	-0.832	-0.792	1.589	1.194
Simulation (Pa)	Coarse	4.490	4.876	-0.996	-1.657	3.080	3.654
	Medium	4.422	4.762	-0.989	-1.633	3.087	3.631
	Fine	4.461	4.848	-0.927	-1.568	3.078	3.620

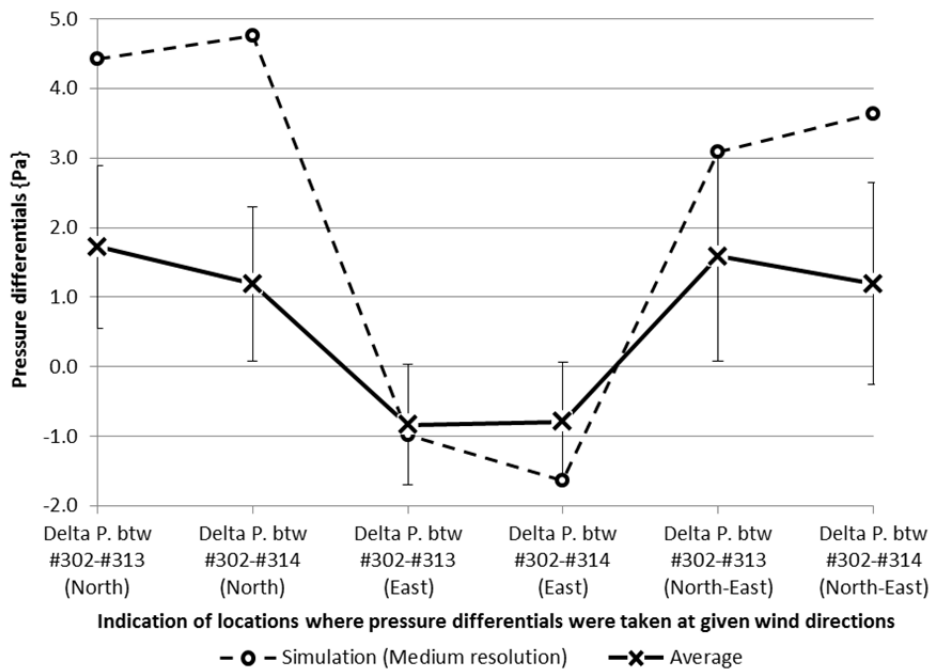


Figure 4.4.8: Comparison between averaged values of differential pressures across the North and South façade of Keller Hall obtained from measurements and CFD calculations (Higher pressure on the North façade indicate positive values)

A final discussion point touches on a pressure fluctuation phenomenon, which was observed from the data analysis and also during the validation tests. Figure 4.4.9 presents a short term differential pressure record. A positive pressure differential indicates higher pressures in on the North façade. The record in Figure 4.4.9 shows a correlation between fluctuation of differential pressures and the observed instantaneous recorded wind direction. The data for wind direction indicates changes in the order of 100 degrees within 10 minutes of recorded time. The resulting pressure differentials indicate that wind pressures build up on opposite sides of the building with periods between 10 and 60 seconds. The interpretation of the differential pressure variations is supported by internal air movement observations when the research team encountered air flow reversal from northward to southward inside Keller hall. The causes for these pressure variations and resulting air flow reversal observations inside the building is not conclusive at this point in time. Since fluctuations of external differential pressures and the somehow related air flow reversals observed inside buildings could have an effect on natural ventilation performance of buildings, further investigation is needed to study this phenomenon.

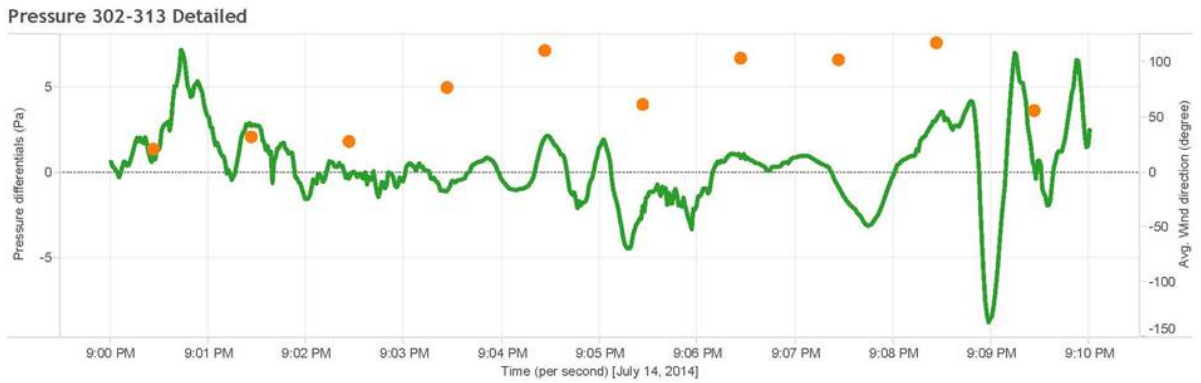


Figure 4.4.9: Fluctuations in measured differential pressures (positive differential pressures indicate pressure is higher on the North façade of Keller Hall building)

5. CONCLUSION AND RECOMMENDATIONS

This section of the report presents main conclusions and recommendations of the research study summarized in categories of related issues.

1. CFD Applications:

- 1.1. The CFD software STAR-CCM+ provided an efficient and powerful platform for advanced CFD analysis of wind induced air movement and pressure phenomena around the selected building as well as surrounding buildings. The technical support of the developer of STAR CCM+ provided helpful input for a couple of application issues.
- 1.2. For this study the research team applied a process of generating 3D-CAD geometries of flow obstructions inside and boundaries around the computation domain, which was different from previous processes. The newly developed process uses the CAD functions of SketchUp and Rhino to produce 3D-geometries and import these geometries into STAR-CCM+. The new process is more effective than the previous process of creating geometry with the CAD software AutoCAD Inventor and importing it into the STARR-CCM+ CFD application.
- 1.3. Benchmarking simulations were conducted early in the study to ascertain the required scope of surrounding buildings and type of topography to be included in the computational domain so that simulations would yield reliable results . Surrounding building and topography can significantly affect the air movement and pressure distribution around the target building, Keller Hall. The decision how much of the surrounding buildings and topography is included in the model has to balance two conflicting consideration of the simulation procedure. First, , extending the reach of the surrounding geometry of buildings and topography can improve the quality of the simulation by including more interactions and second, increase air flow obstructions in the computational domain increases the required computational resources, which means simulation running time. It basically comes down to a balancing act between high probability of simulation accuracy and length of time of simulation runs. The research team came up with a viable and effective choice of the extent and geometry of surrounding buildings and topography.
- 1.4. Foliage was not included in the geometry model of the domain. The literature reports on various approaches to include vegetation objects in the CFD simulations. The research team is aware that there are multiple trees in the vicinity of Keller Hall which will affect wind pattern to a certain extent. Foliage, however, was not included for this study since other influences to the wind pattern around the target buildings were considered more significant. For other

building situations including foliage might be a more important consideration as for prevailing wind movement around Keller Hall.

- 1.5. The terrain surrounding Keller Hall used in the CFD simulations was taken as flat and horizontal. Benchmarking (see point 1.3 above) suggested that using more complicated topography for the case of Keller Hall would not increase accuracy of the flow prediction appreciatively to warrant the significantly higher demand on computational time and effort in modeling. The goal of this study is to identify and test CFD procedures that aid in the design process and the assessment of multiple performance criteria. Including complicated topography involves significant 3D-geometry data import and manipulation and is usually beyond the practical use of CFD to assess wind movement around buildings.
- 1.6. Four different mesh resolutions were used in this study. Initial CFD investigations used a rather coarse grid. This simplification for the initial CFD served the desired level of complexity since the initial CFD simulations also use simpler geometries and assumed (from historical weather files) speeds and direction of the approaching wind. The purpose of the initial CFD runs was to gain a basic understanding of the wind pattern around the target building and select preferred locations of wind speed measurements around the building. For future CFD investigations the same procedure of initial CFD runs will be used to determine preferred locations to place sensors for CFD validations of advanced CFD models.
- 1.7. Benchmarking with three different grid resolutions was conducted for a sensitivity analysis of the final CFD simulations. A coarse, medium and fine grid was used with a total number of cells of 3.0, 4.4 and 7.9 million cells, respectively. Using higher grid resolutions typically increases the accuracy of predicting relevant flow occurrence close to the target and at areas of higher flow property gradients. This means that in areas where an accurate prediction of flow phenomena is required, such as at areas with flow separation or flow stagnation, more and smaller cells in the computational grid are preferred. The disadvantage of higher grid resolution is the required computational resources. From benchmarking conducted in this study it was observed that for identical setting and boundary conditions a coarse, medium and fine grid resolution required an average 6 hours, 12 hours and 36 hours simulation run times, respectively. Results suggested that a medium grid was sufficient and, apart from reasonable run times, also showed good convergence.
- 1.8. As a way of improving the accuracy of the CFD simulation solution, the literature proposes the process of so-called “adaptive mesh refinement” (Blocken, 2007). The research team benchmarked this process against the normal procedure of setting the grid resolution through inbuilt CFD software functions. For external CFD analysis, the results suggested that adaptive mesh refinement did not result in significantly improved performance to warrant the extra

5. CONCLUSION AND RECOMMENDATIONS

time and effort. For the internal CFD analysis adaptive mesh refinement could, however, be a relevant procedure to increase performance of the simulation.

- 1.9. An important consideration for the cell dimensions of the mesh is the required number and size of prism layers. The process used in this study used sizing of prism layers in accordance of the selected surface roughness and recommended wall-function treatment procedures.
- 1.10. It was found that in addition to CFD simulation residuals, the behavior of absolute wind speeds detected for the (virtual) anemometer monitors proved an effective means to assess level of convergence of the simulations.
- 1.11. A typical CFD simulation run required up to 3,000 iterations for residuals to achieve the convergence criterion for properties such as momentum or turbulence. As pointed out under point 1.10 the absolute wind velocities for (virtual) anemometers converged to a final value much earlier.
- 1.12. The building façade was modeled as opaque or impermeable in the CFD model. This is consistent with the “decoupled” CFD simulation approach of the study. With assuming an opaque wall the wind impinges on the façade as a true stagnation and the resulting pressures are calculated accordingly. The pressure tubing terminals, however, were installed close to the open windows of the naturally ventilated spaces on the third floor of Keller Hall. This was done for logistical reasons since installation of terminals from the inside the class rooms through the louvered windows was the only practical way to access the building façade. Open windows, however, permit air movement to the inside which could change the air flow pattern in the vicinity of the windows. Air flow in the vicinity of the pressure tubing terminals can affect the absolute and time dependent values of the pressure measurements. The research team believes that this effect was not significant in magnitude, but this aspect might need further consideration for future CFD work of the team.
- 1.13. The presentation grid approach used to determine the absolute wind velocities in CFD post processing was effective in providing good representative values for wind velocities at locations of interest, e.g. the locations where the virtual anemometers were located. The use of presentation grids is not widely addressed in the literature that describes validation of CFD with field measurements. The good performance of presentation grids in this study, however, justifies the extra effort in post processing. In the future, the research team might use a 3D rather than a 2D presentation grid to make the determination of properties in the CFD domains even more effective.

2. Instrumentation and Data Handling:

- 2.1. The anemometers that were used for the measurements had some limitations since their sensitivity is a function of their face orientation towards the approach wind direction. The type of anemometers used for the wind measurements around the Keller Hall building have a preferred measurement sensitivity of $\pm 30^\circ$ of the direction towards which the face of the sensor is pointing. Any measurements of wind coming from a direction outside of this optimum range of about 60° will be affected. The research team did not find a reliable correlation how to adjust the data in accordance to the direction of the wind which was selected when the anemometers were deployed in their stands. The effect on the recording, therefore, cannot be ruled out and could also not be quantified. The preferred direction towards which the instruments were pointed was selected from the initial CFD runs. These initial CFD runs considered a wind approach from the North. Therefore it can be assumed that wind recording for wind approaching the building from North should be most consisted with the CFD simulation predictions. As a matter of fact, the results of measurements support this conjecture.
- 2.2. A further limitation of the anemometers used in the investigations is that they cannot identify the wind approach direction. The anemometers basically only measure a property changes in conductance that is caused by a cooling effect of the passing wind. Hence, the anemometer can only determine the wind speed but not the direction. A good, albeit expensive, alternative to the type of anemometers used in the study are 3D ultra-sonic anemometers, which are highly accurate and can identify wind direction. An internal discussion with an European leading expert in CFD application in the urban environment suggested the use of two ultra-sonic anemometers, one for reference at a fixed location and one moveable that can be deployed in a patterns of sequential measurements at different predetermined locations.
- 2.3. The differential pressure ranges detected in the field measurements are quite small, with ranges well under 10 Pascal. The recorded pressure differentials compared well with those reported in the literature for other natural ventilation investigations. The differential pressure transducers had a full range of 10Pa and 25 Pa for the Halstrup-Walcher P-26 and Setra Model 264, respectively. In their performance the Setra transducers showed a very good cost benefit ratio. The Setra transducer will be the differential pressure transducer of choice for future investigations.
- 2.4. The Tableau software for data analysis was very effective. The use of software allowed for expeditious data analysis, including display of data in accordance to filtering of parameters.
- 2.5. The data acquisition using a combination of web based instruments, with a wireless signal conditioning, and hard wired instruments proved to be very effective and resulted in stable and

consistent recording. The time and effort, however that went into developing robust deployment procedures and data capturing and conditioning should not be underestimated. The time and effort was in fact considerable. The procedures and experience were recorded for future reference. With changing of the research assistants being a regular event at ERDL this is an important task and serves to capture important experiences for future research.

- 2.6. The procedure of filtering data in accordance with certain governing parameters such as approach wind direction or time was a powerful analysis process. The software Tableau proved to be an indispensable analysis tool.

3. Wind and Pressure Pattern:

Since wind and pressure measurements have been adequately addressed in the report there are a few general observations that will have to be considered for future comparable applied research efforts at ERDL.

- 3.1. The use of wind speeds to validate CFD simulation results appears to yield better results than using pressures as indicators of wind induced air movement phenomena around buildings. The determination of pressures, however, is nevertheless important since the driving force for natural ventilation is the pressure differential between sides, or more precise between air intake and discharge of the building.
- 3.2. A surprising observation of the differential pressure measurements is the fluctuations of differential pressures around the building. These appear to be periodic in nature and significant periods in the range between 30 and 60 seconds have been identified. It is not surprising that eddies have a significant effect on the pressure distribution of the building. The fact, however, that such significant wind direction change occur in relatively quick succession and can be correlated with short period differential pressure reversals could have a significant effect on the natural ventilation performance of buildings. Further investigation in this phenomenon seems prudent.

REFERENCES

American Society of Heating, Refrigerating and Air-Conditioning Engineers. (2005). 2005 ASHRAE Handbook: Fundamentals - SI edition. Atlanta, Ga: American Society of Heating Refrigerating and Air-Conditioning.

Blocken B., Stathopoulos T., Carmeliet J. (2007). "CFD simulation of the atmospheric boundary layer – wall function problems". Atmospheric Environment 41(2):238-252

Franke J. et al. (2007) "Best Practice Guideline for the CFD Simulation of Flows in the Urban Environment", "COST", May 2007

Davenport, A.G. (1960) "Rationale for determining design wind velocities". Journal of Structural Division, American Society of Civil Engineers. 86, 39-68.

Wieringa, J. (1992) "Updating the Davenport roughness classification", Journal of Wind Engineering and Industrial Aerodynamics. 41, 357-368.

CD Adapco (2008), User Guide STAR CCM+ Version 8.02

Precious research reports and notes elaborated under this research program have been used in the report without giving reference.

ACRONYMS

3D	Three Dimensional
3D-Cad	Three Dimensional Computer Aided Design
ABL	Atmospheric Boundary Layer
CFD	Computational Fluid Dynamics
ERDL	Environmental Research and Design Laboratory
HNEI	Hawaii Natural Energy Institute
HVAC	Heating, Ventilating, and Air Conditioning
ID	Identification Index of Descriptor
LES	Large Eddy Simulation
V	Velocity
WS	Weather Station

Units:

DC	Direct Current
ft	Foot or feet
hz	Hertz
m	Meter
m/s	Meter per second
mph	Miles per Hour
Pa	Pascal
sqft	Square Feet

APPENDIX A: RESULTS OF CFD SIMULATIONS

APPENDIX A

RESULTS FROM CFD RUNS

This appendix showed the results of 09 CFD scenario runs which were based on the combination of 03 approaching wind directions (North, East and Northeast) as well as 03 different grid resolutions for grid sensitivity analysis.

CFD SCENARIO RUN MATRIX

Grid resolution	Approaching Wind Direction		
	North	East	Northeast
Coarse	N-C	E-C	NE-C
Medium	N-M	E-M	NE-M
Fine	N-F	E-F	NE-F

Each scenario includes 12 outputs named as from Figure 01 to Figure 12 as the following descriptions:

LIST OF IMAGE REPORT PER CFD SCENARIO RUN

Fig. No	Figure brief descriptions	View plane	View range descriptions
1	Convergence Residuals	N/A	
2	Convergence Anemometers	N/A	
3	Velocity; contours slice	oblique	over view from NE
4	Velocity; contours slice	Plan view	detail around Keller Hall
5	Velocity, streamlines	Plan view	over view
6	Velocity, streamlines	Plan view	details around Keller Hall
7	Velocity, sections	cross-section	along long axis of Keller Hall
8	Velocity, sections	cross-section	along short axis of Keller Hall
9	Pressure; contours	oblique	overview from NE
10	Pressure; contours	oblique	overview from SE
11	Pressure; contours	oblique	details of Keller Hall NE envelope, larger PA scale
12	Pressure; contours	oblique	details of Keller Hall SE envelope, larger PA scale

N-C	Approaching Wind Direction	Grid Resolution
	North	Coarse

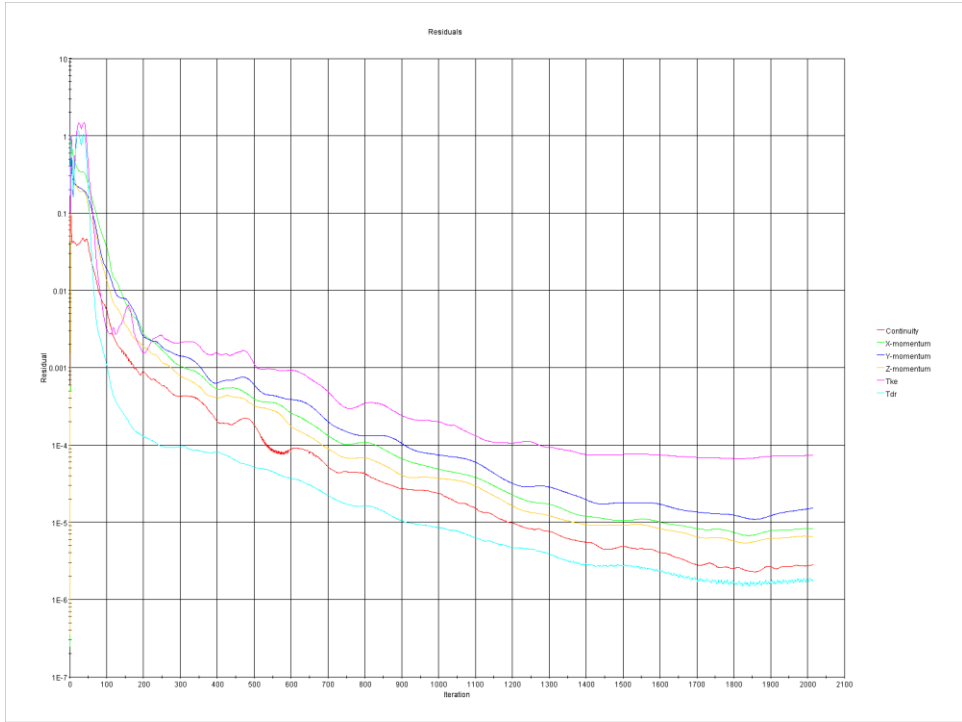


Figure 1: Convergence Residual Plot

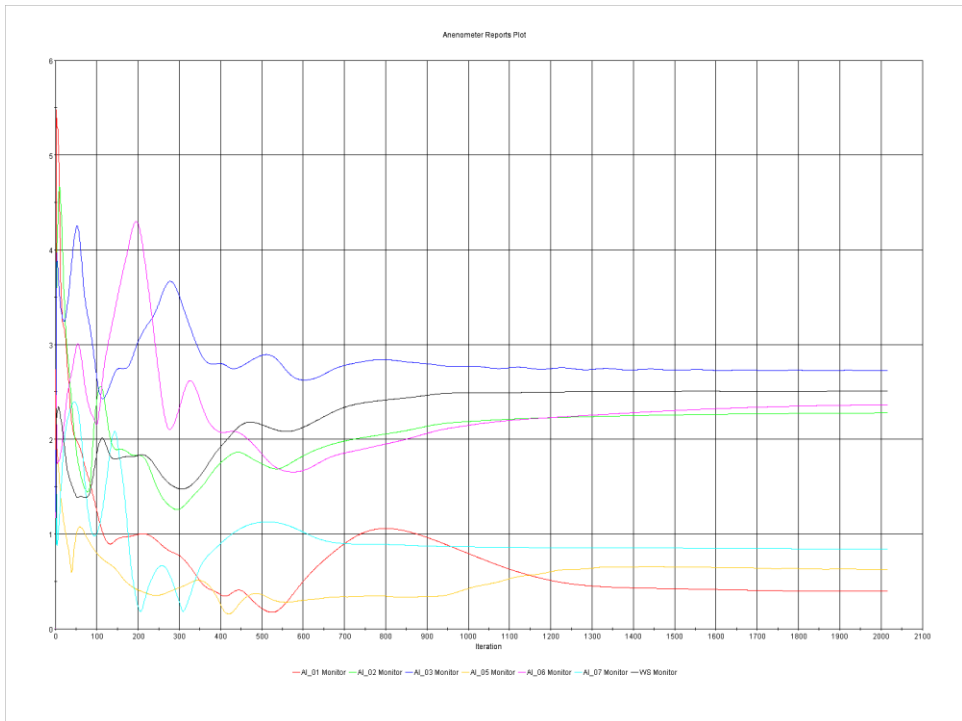


Figure 2: Convergence Anemometers' Simulated Wind Velocity Plot

N-C	Approaching Wind Direction	Grid Resolution
	North	Coarse

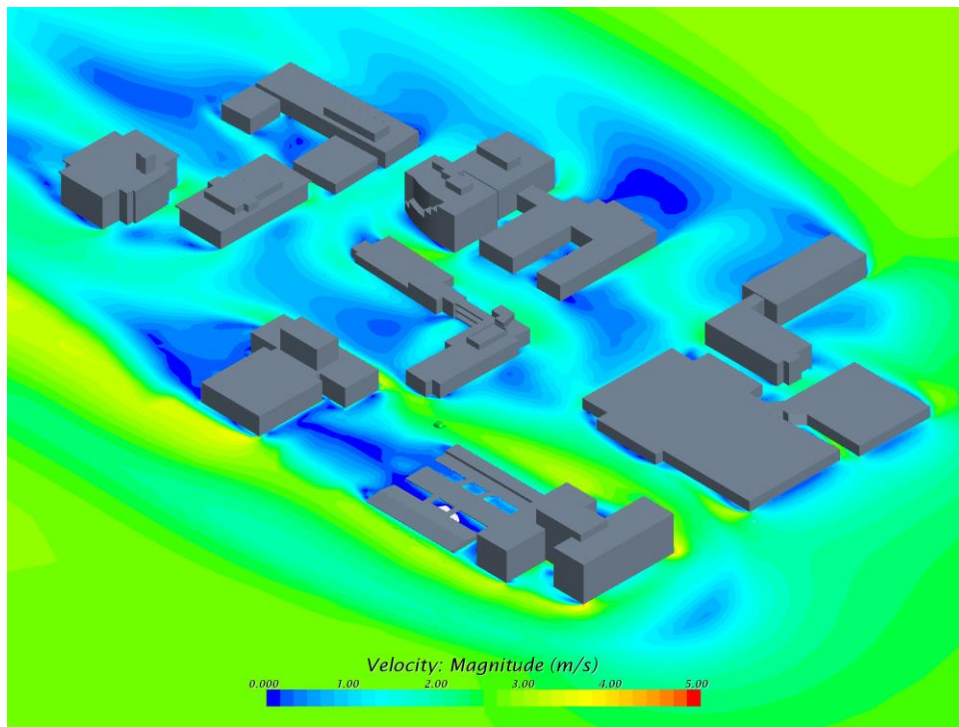


Figure 3: Overall Isometric View (from NE) of Wind Velocity Contour Map*,**

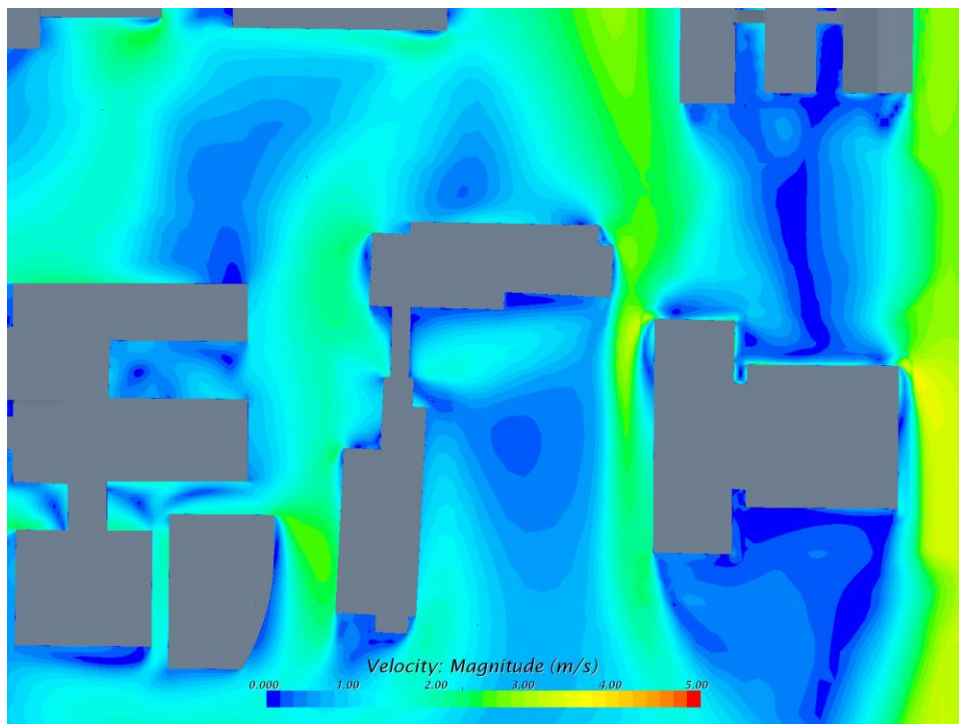


Figure 4: Plan View of Detailed Wind Velocity Contour Map*,** around Keller Hall
 *On the horizontal plane at 1m height above finishing level of the 1st floor.
 ** The minimum and maximum value of the above legend ranges do not indicate the minimum and maximum values of those maps.

N-C	Approaching Wind Direction	Grid Resolution
	North	Coarse

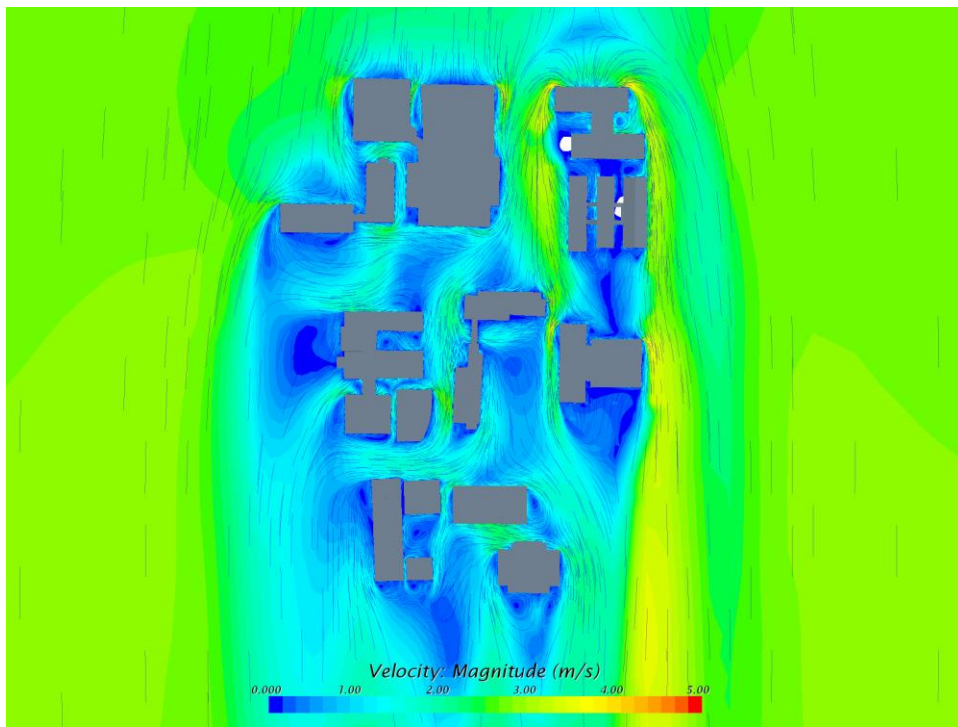


Figure 5: Plan View of Overall Wind Velocity Streamline Map*,**

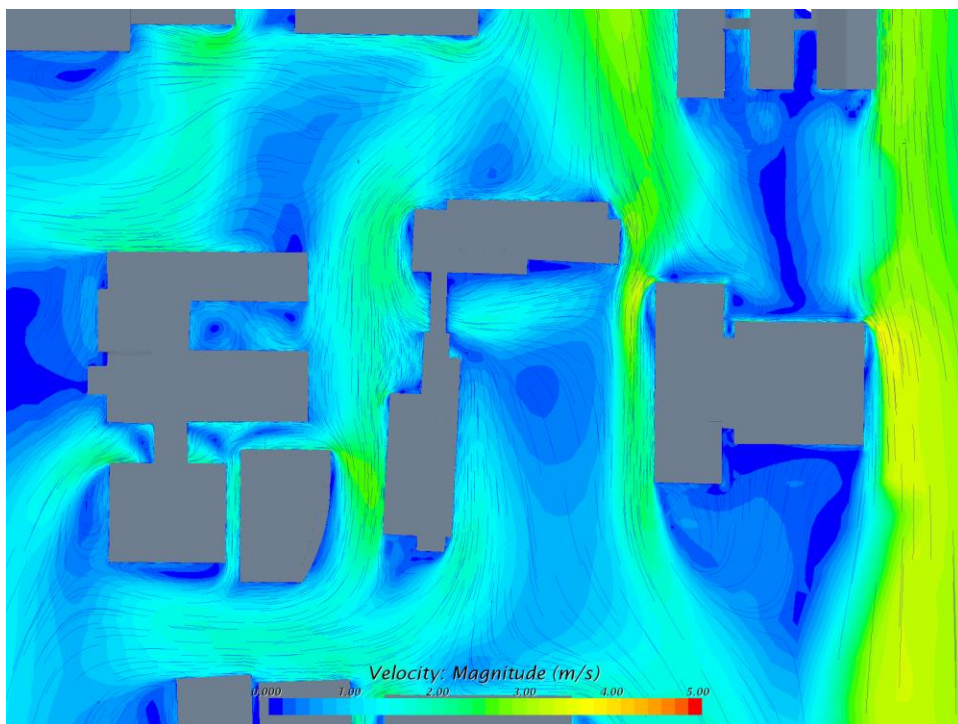


Figure 6: Plan View of Detailed Wind Velocity Stream Map*,** around Keller Hall

*On the horizontal plane at 1m height above finishing level of the 1st floor.

** The minimum and maximum value of the above legend ranges do not indicate the minimum and maximum values of those maps.

N-C	Approaching Wind Direction	Grid Resolution
	North	Coarse

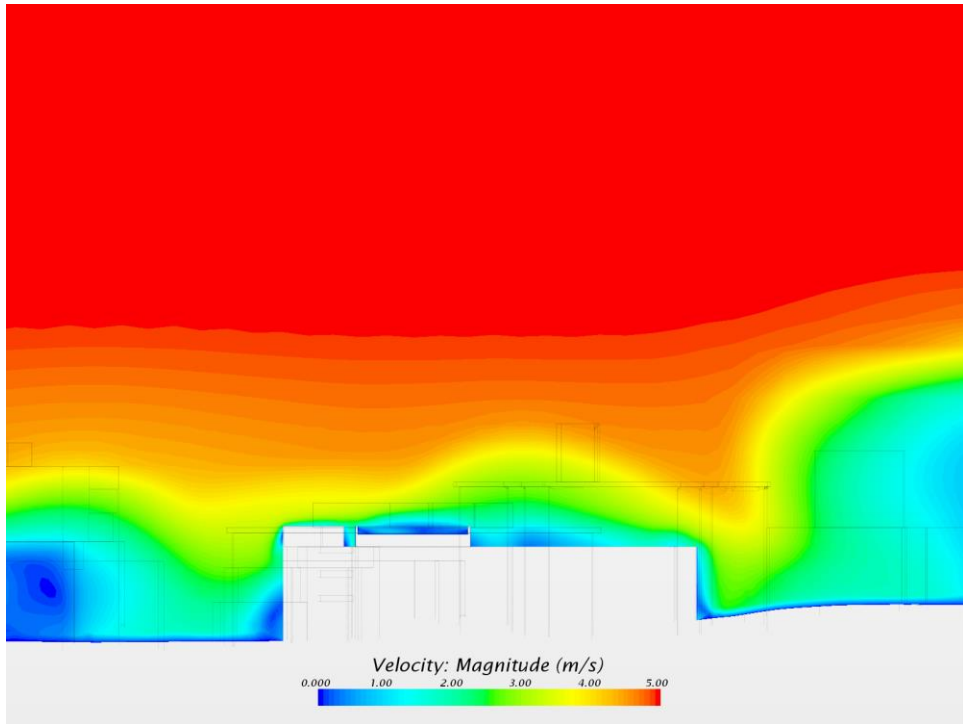


Figure 7: Detailed Wind Velocity Contour Map* on Cross Section Along Long Axis of Keller Hall

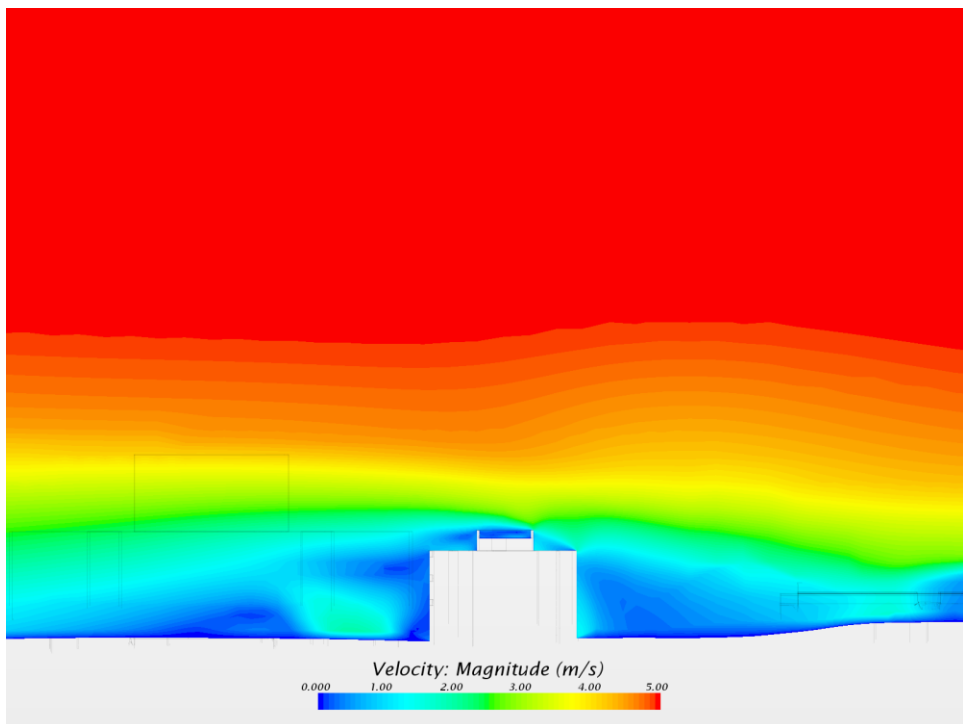


Figure 8: Detailed Wind Velocity Contour Map* on Cross Section Along Short Axis of Keller Hall

* The minimum and maximum value of the above legend ranges do not indicate the minimum and maximum values of those maps.

N-C	Approaching Wind Direction	Grid Resolution
	North	Coarse

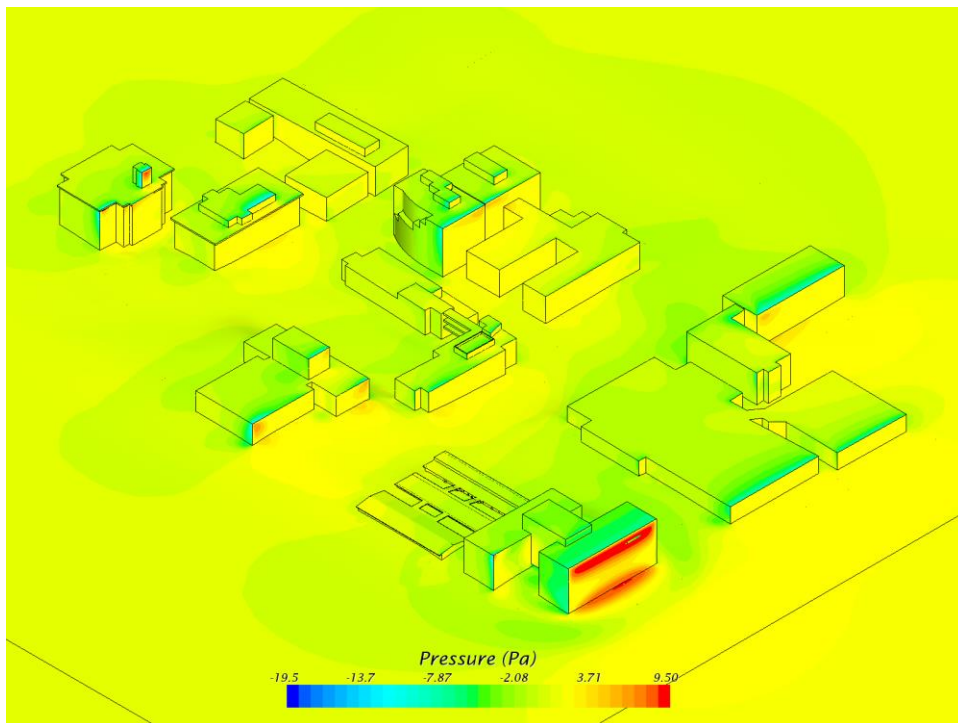


Figure 9: Overall Isometric View (from NE) of Wind-Induced Pressure Distribution* on Building Facades

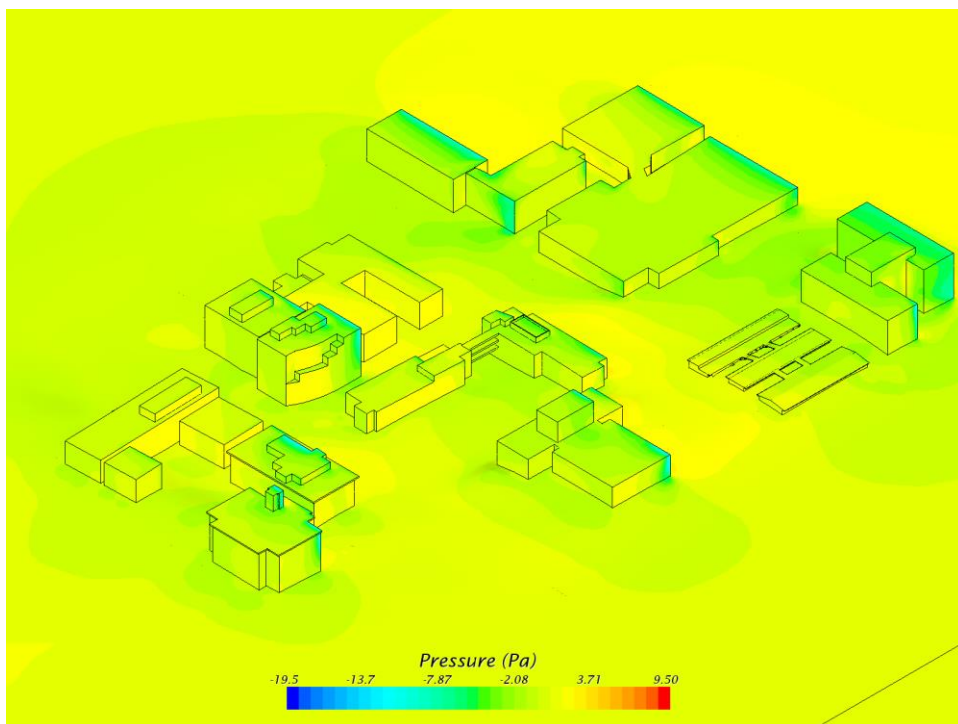


Figure 10: Overall Isometric View (from SE) of Wind-Induced Pressure Distribution* on Building Facades

* The minimum and maximum value of the above legend ranges do not indicate the minimum and maximum values of those maps.

N-C	Approaching Wind Direction	Grid Resolution
	North	Coarse

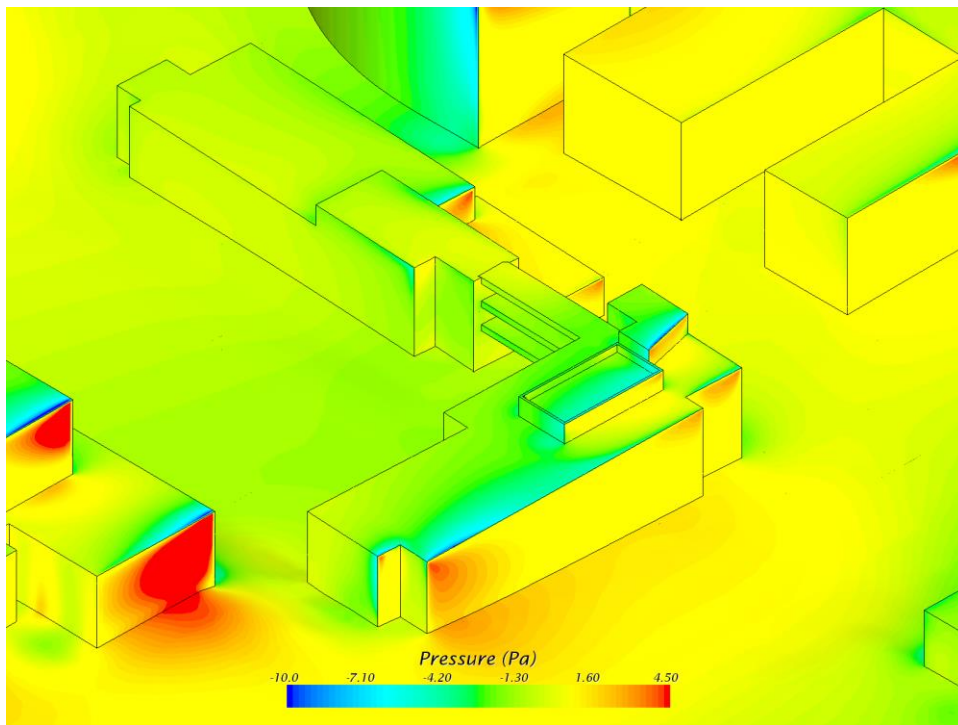


Figure 11: Detailed Isometric View (from NE) of Wind-Induced Pressure Distribution* on Keller Hall's Facades

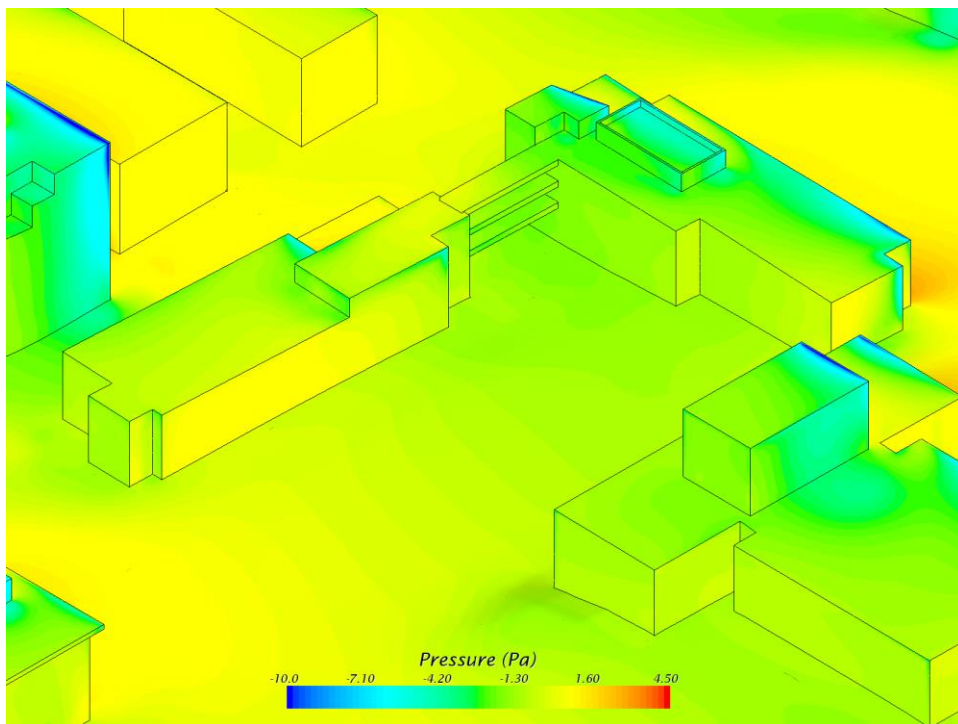


Figure 12: Detailed Isometric View (from SE) of Wind-Induced Pressure Distribution* on Keller Hall's Facades

* The minimum and maximum value of the above legend ranges do not indicate the minimum and maximum values of those maps.

N-M	Approaching Wind Direction	Grid Resolution
	North	Medium

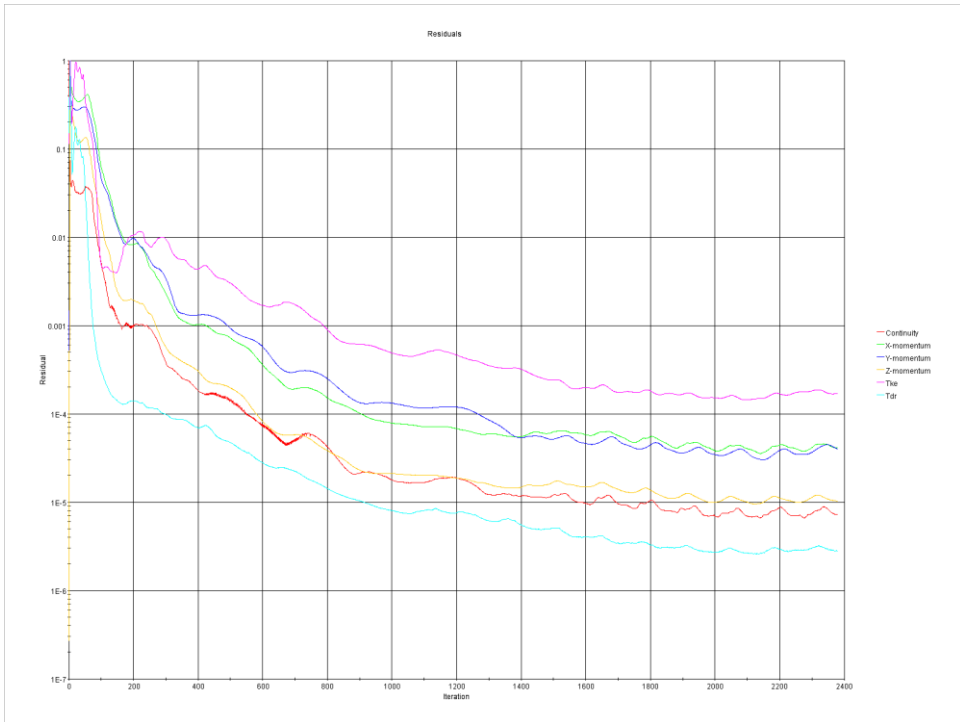


Figure 1: Convergence Residual Plot

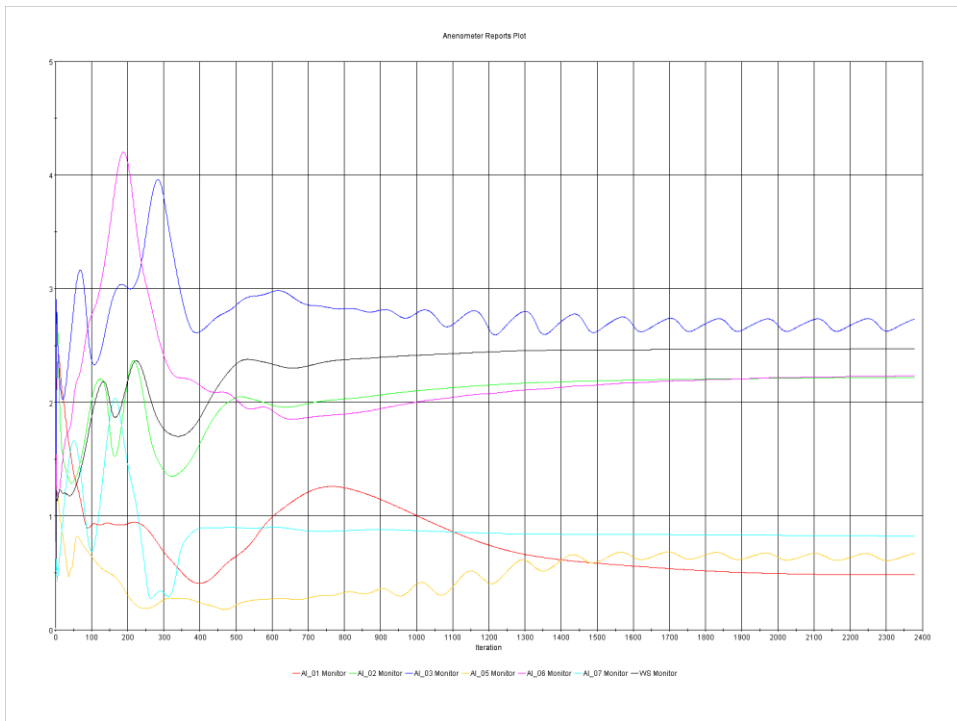


Figure 2: Convergence Anemometers' Simulated Wind Velocity Plot

N-M	Approaching Wind Direction	Grid Resolution
	North	Medium

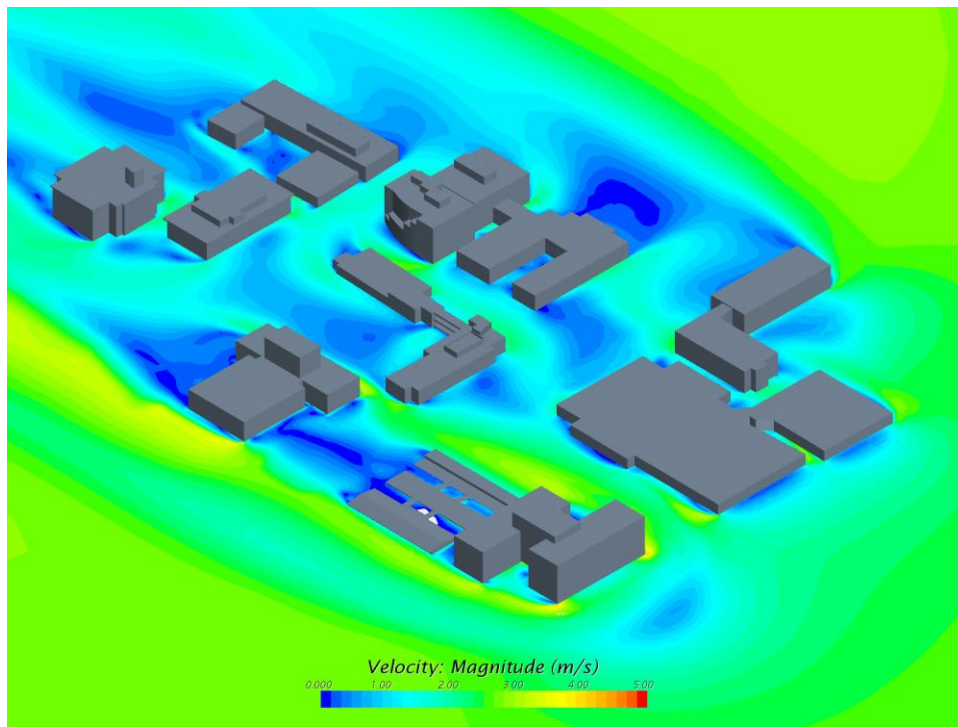


Figure 3: Overall Isometric View (from NE) of Wind Velocity Contour Map*,**

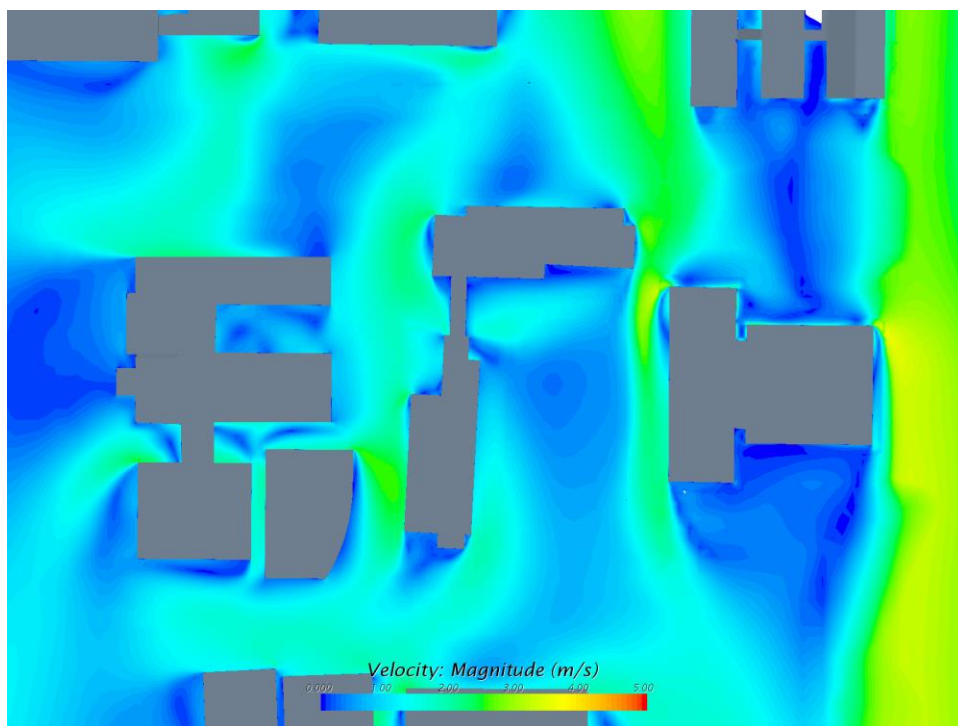


Figure 4: Plan View of Detailed Wind Velocity Contour Map*,** around Keller Hall
 *On the horizontal plane at 1m height above finishing level of the 1st floor.
 ** The minimum and maximum value of the above legend ranges do not indicate the minimum and maximum values of those maps.

N-M	Approaching Wind Direction	Grid Resolution
	North	Medium

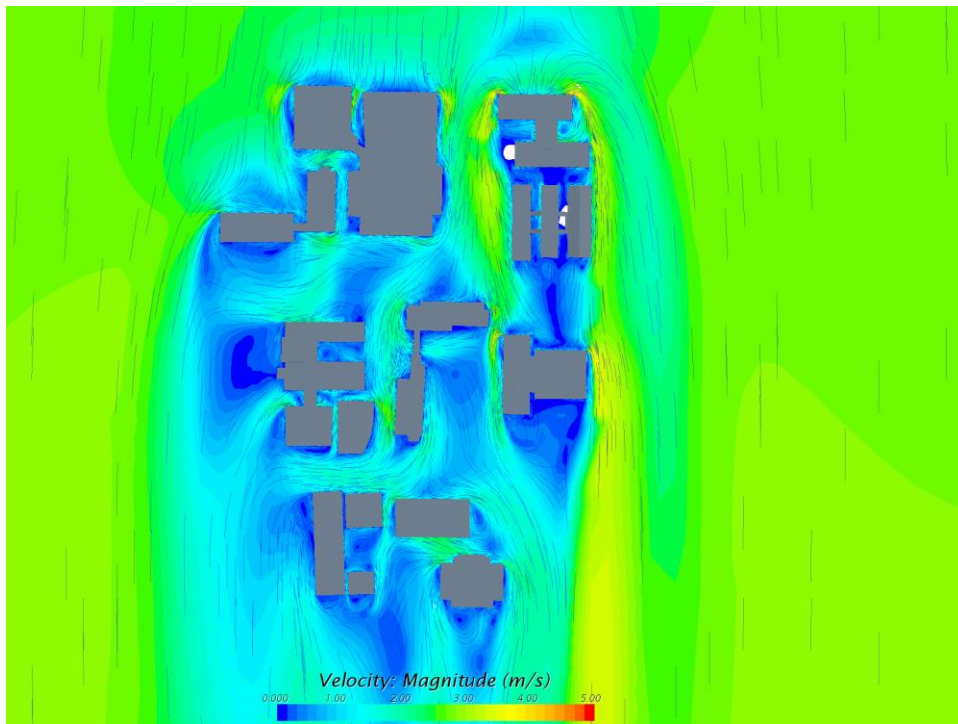


Figure 5: Plan View of Overall Wind Velocity Streamline Map*,**

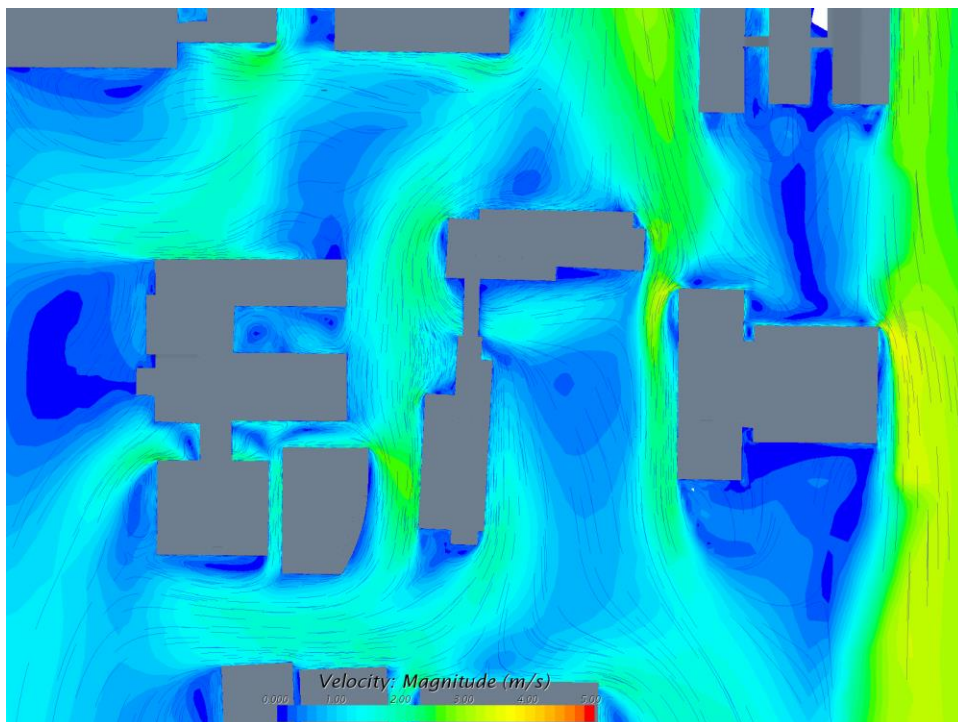


Figure 6: Plan View of Detailed Wind Velocity Stream Map*,** around Keller Hall

*On the horizontal plane at 1m height above finishing level of the 1st floor.

** The minimum and maximum value of the above legend ranges do not indicate the minimum and maximum values of those maps.

N-M	Approaching Wind Direction	Grid Resolution
	North	Medium

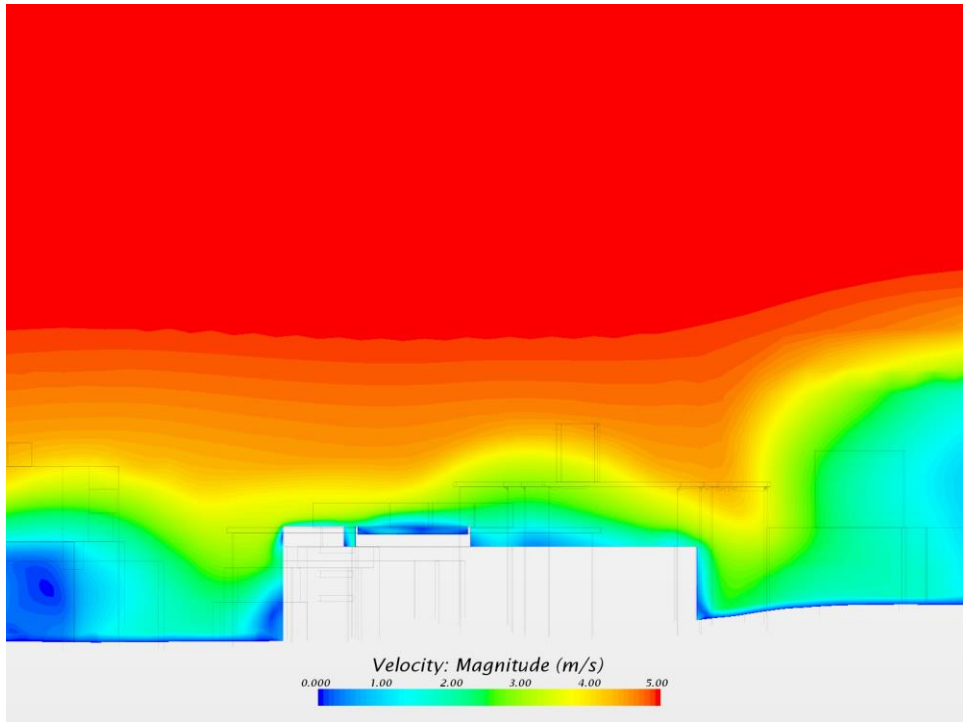


Figure 7: Detailed Wind Velocity Contour Map* on Cross Section Along Long Axis of Keller Hall

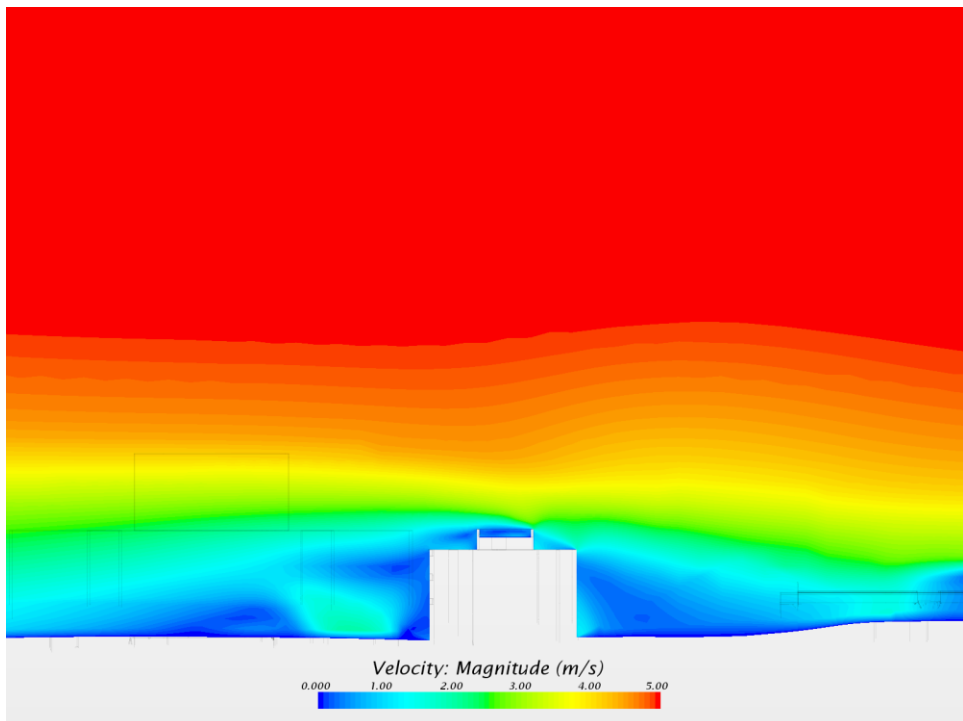


Figure 8: Detailed Wind Velocity Contour Map* on Cross Section Along Short Axis of Keller Hall

* The minimum and maximum value of the above legend ranges do not indicate the minimum and maximum values of those maps.

N-M	Approaching Wind Direction	Grid Resolution
	North	Medium

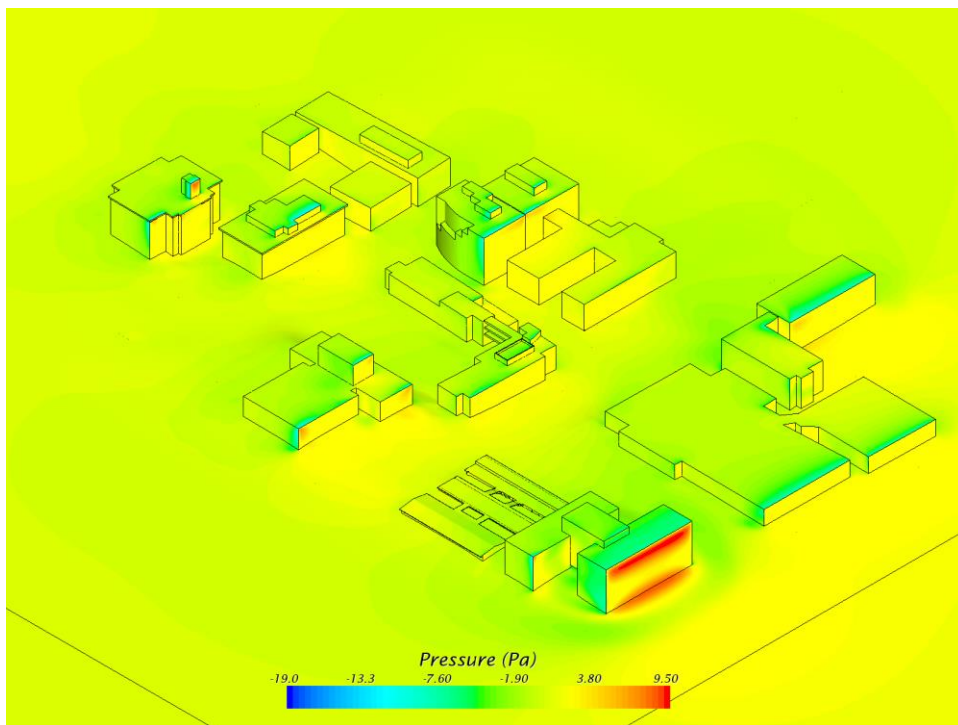


Figure 9: Overall Isometric View (from NE) of Wind-Induced Pressure Distribution* on Building Facades

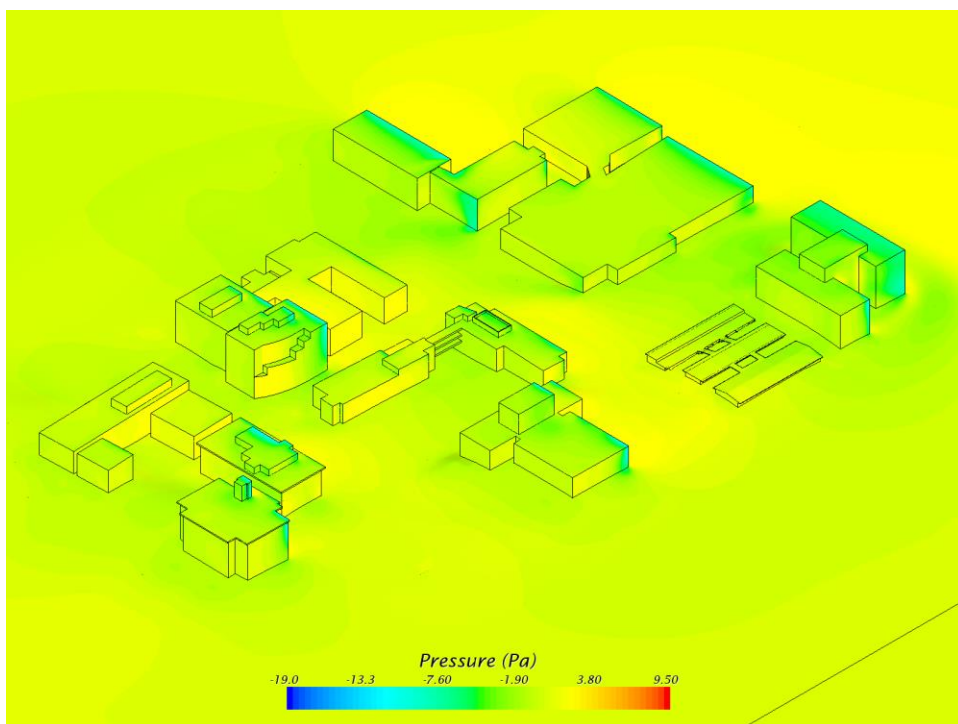


Figure 10: Overall Isometric View (from SE) of Wind-Induced Pressure Distribution* on Building Facades

* The minimum and maximum value of the above legend ranges do not indicate the minimum and maximum values of those maps.

N-M	Approaching Wind Direction	Grid Resolution
	North	Medium

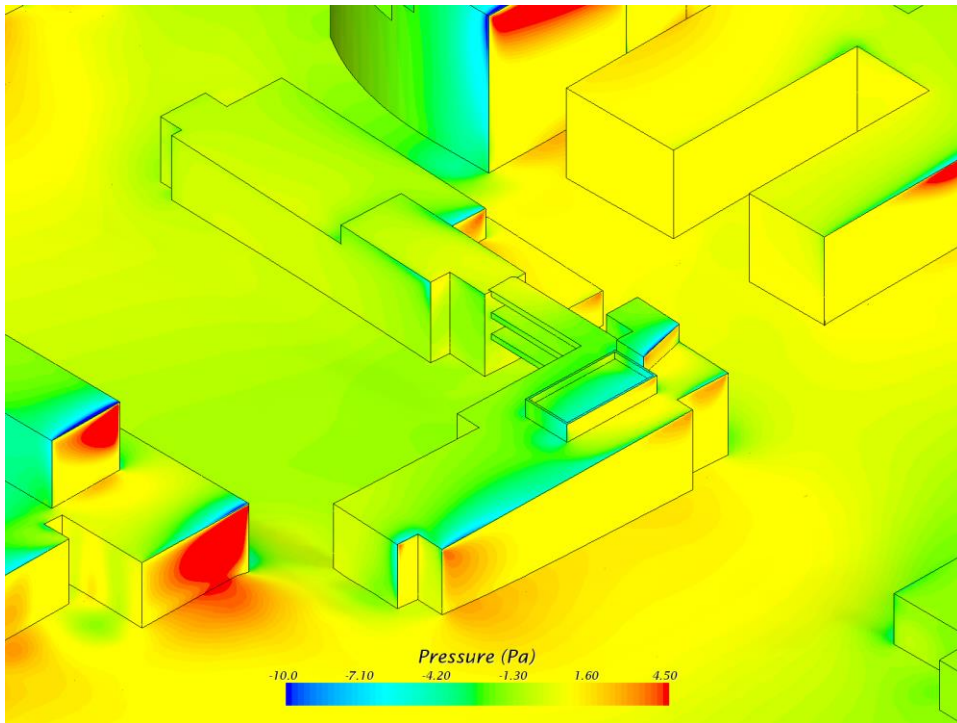


Figure 11: Detailed Isometric View (from NE) of Wind-Induced Pressure Distribution* on Keller Hall's Facades

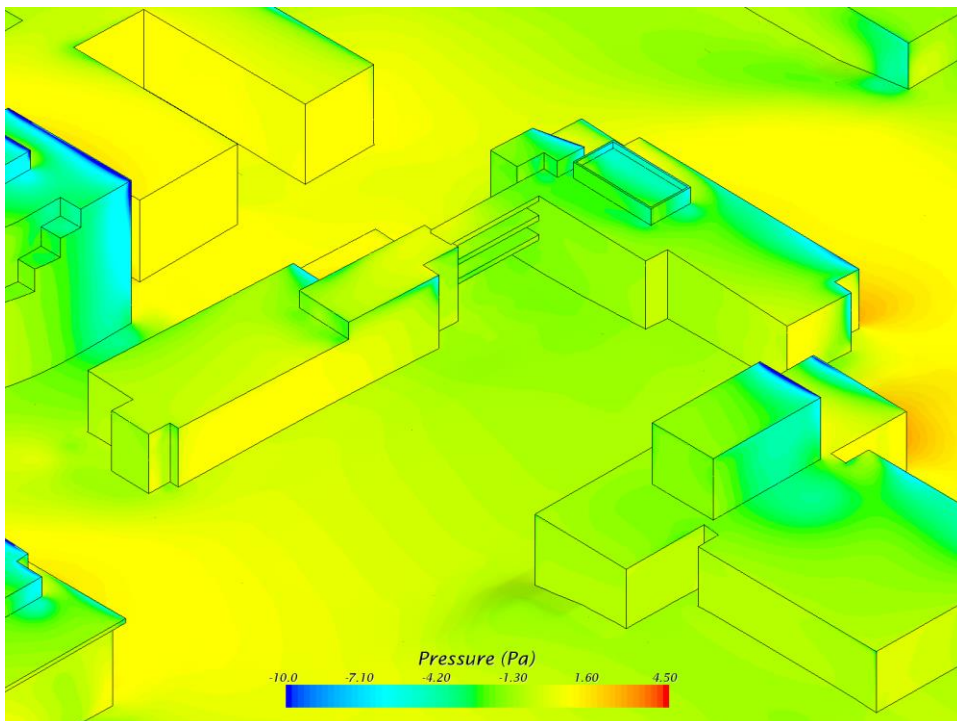


Figure 12: Detailed Isometric View (from SE) of Wind-Induced Pressure Distribution* on Keller Hall's Facades

* The minimum and maximum value of the above legend ranges do not indicate the minimum and maximum values of those maps.

N-F	Approaching Wind Direction	Grid Resolution
		North

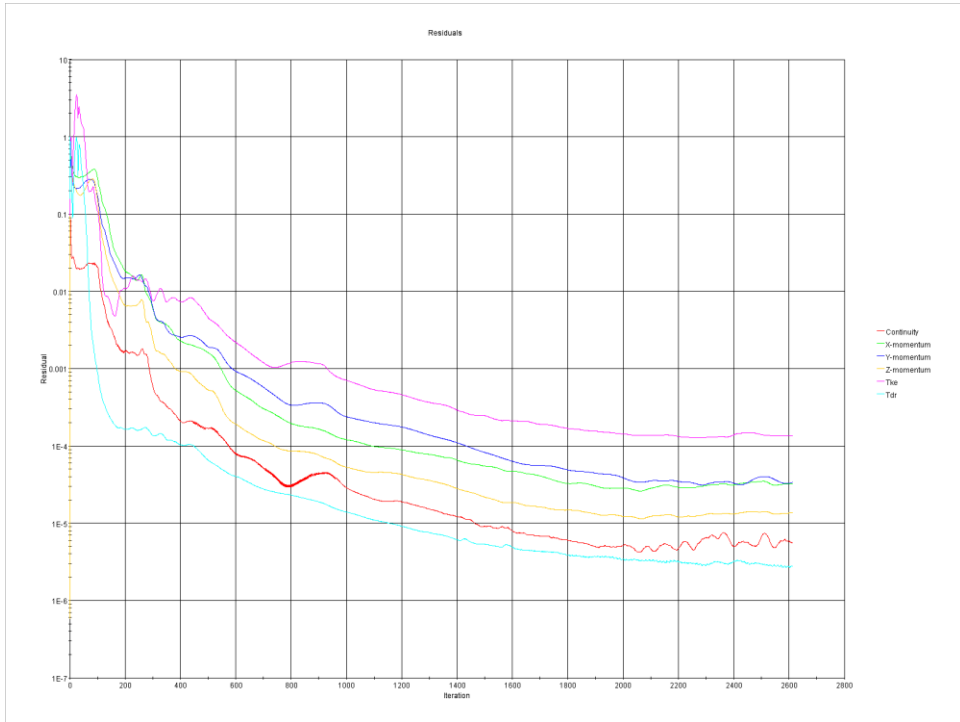


Figure 1: Convergence Residual Plot

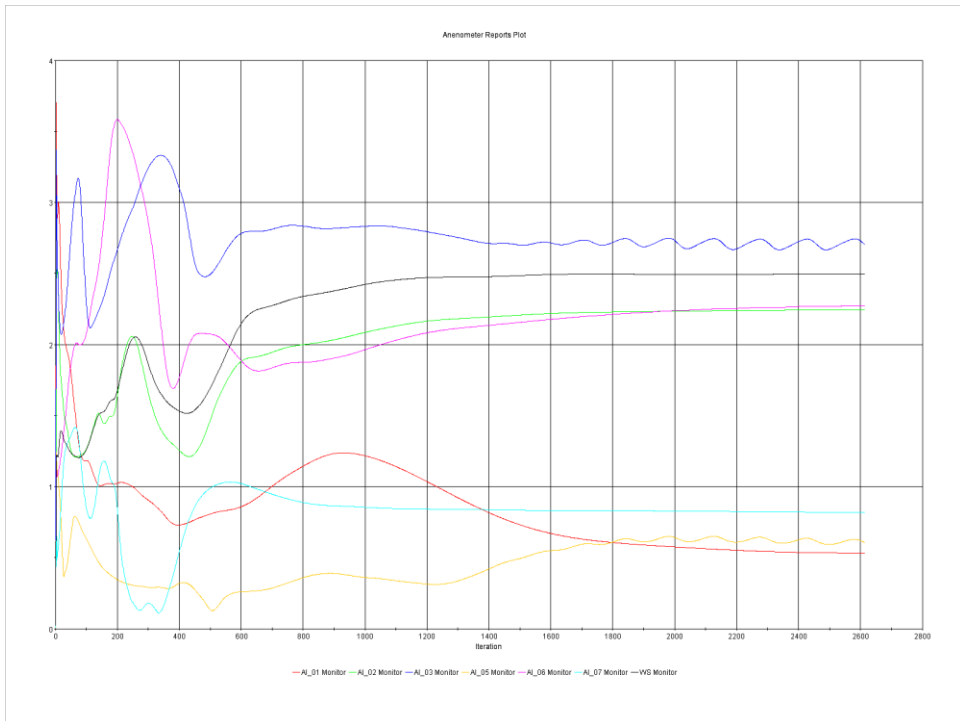


Figure 2: Convergence Anemometers' Simulated Wind Velocity Plot

N-F	Approaching Wind Direction	Grid Resolution
	North	Fine

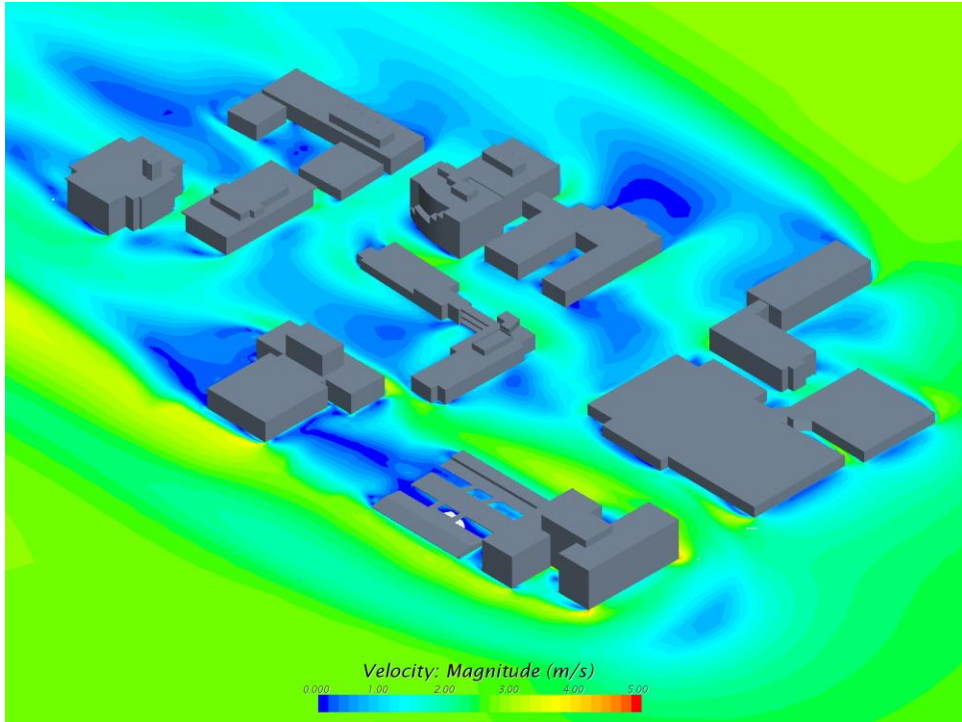


Figure 3: Overall Isometric View (from NE) of Wind Velocity Contour Map*,**

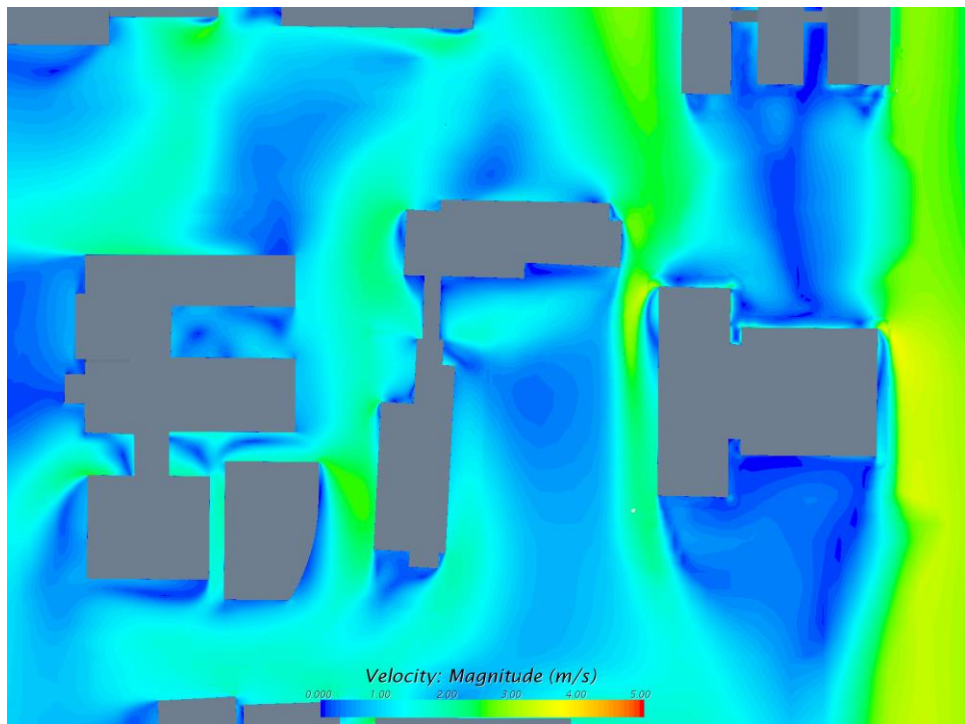


Figure 4: Plan View of Detailed Wind Velocity Contour Map*,** around Keller Hall

*On the horizontal plane at 1m height above finishing level of the 1st floor.

** The minimum and maximum value of the above legend ranges do not indicate the minimum and maximum values of those maps.

N-F	Approaching Wind Direction	Grid Resolution
	North	Fine

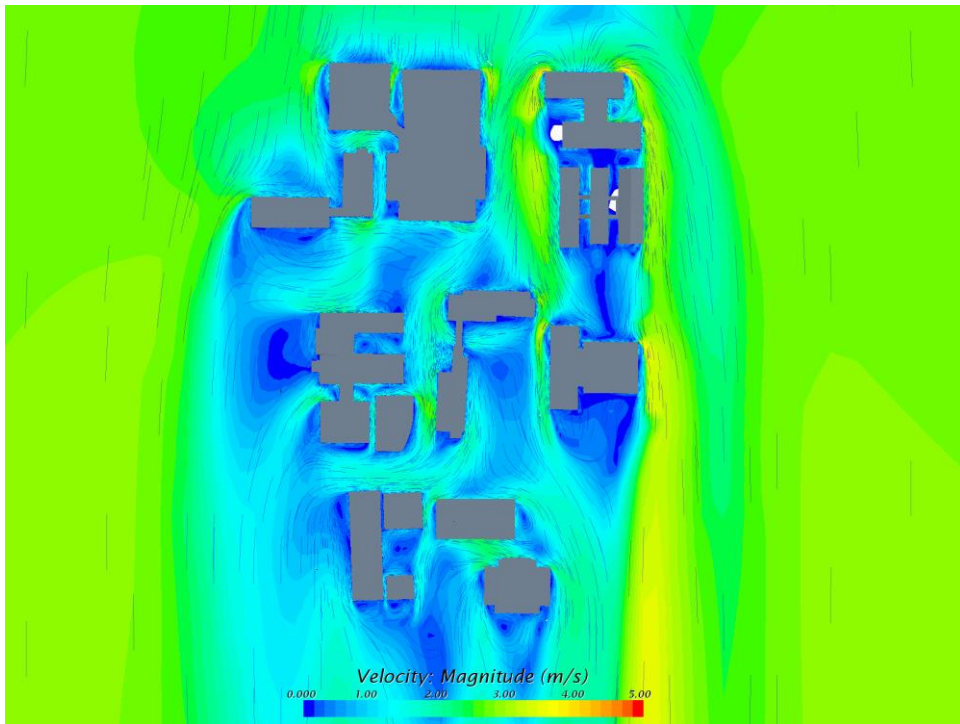


Figure 5: Plan View of Overall Wind Velocity Streamline Map*,**

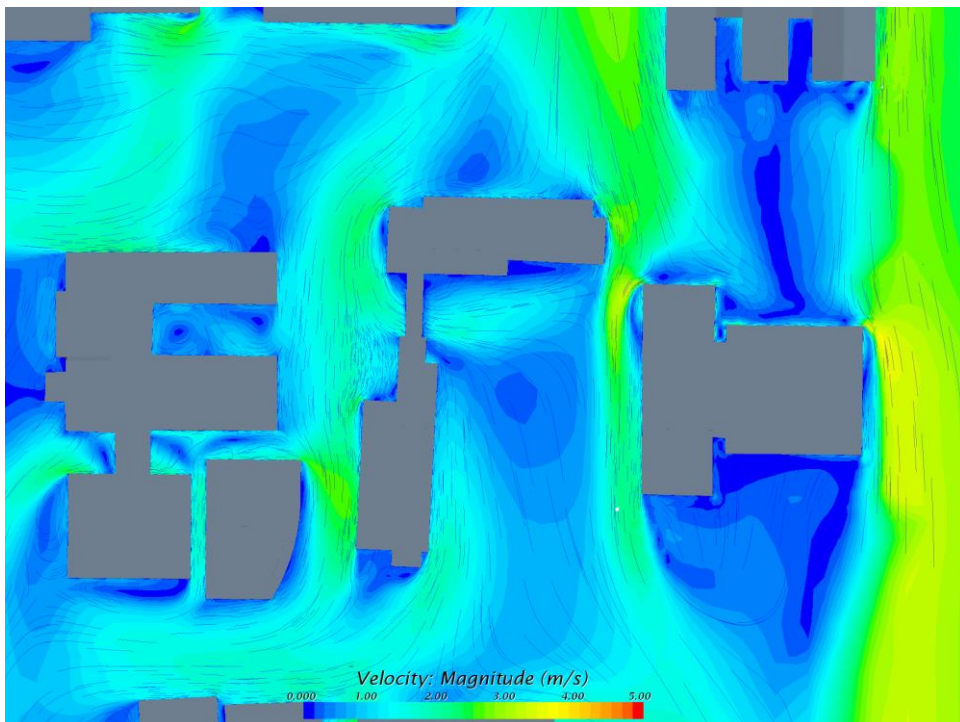


Figure 6: Plan View of Detailed Wind Velocity Stream Map*,** around Keller Hall

*On the horizontal plane at 1m height above finishing level of the 1st floor.

** The minimum and maximum value of the above legend ranges do not indicate the minimum and maximum values of those maps.

N-F	Approaching Wind Direction	Grid Resolution
	North	Fine

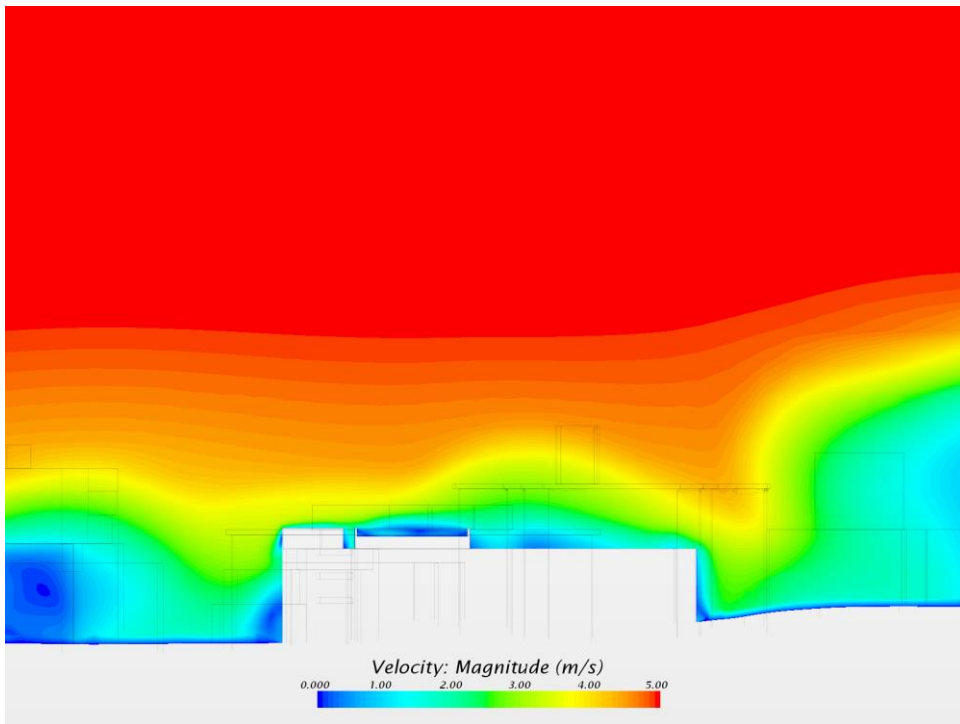


Figure 7: Detailed Wind Velocity Contour Map* on Cross Section Along Long Axis of Keller Hall

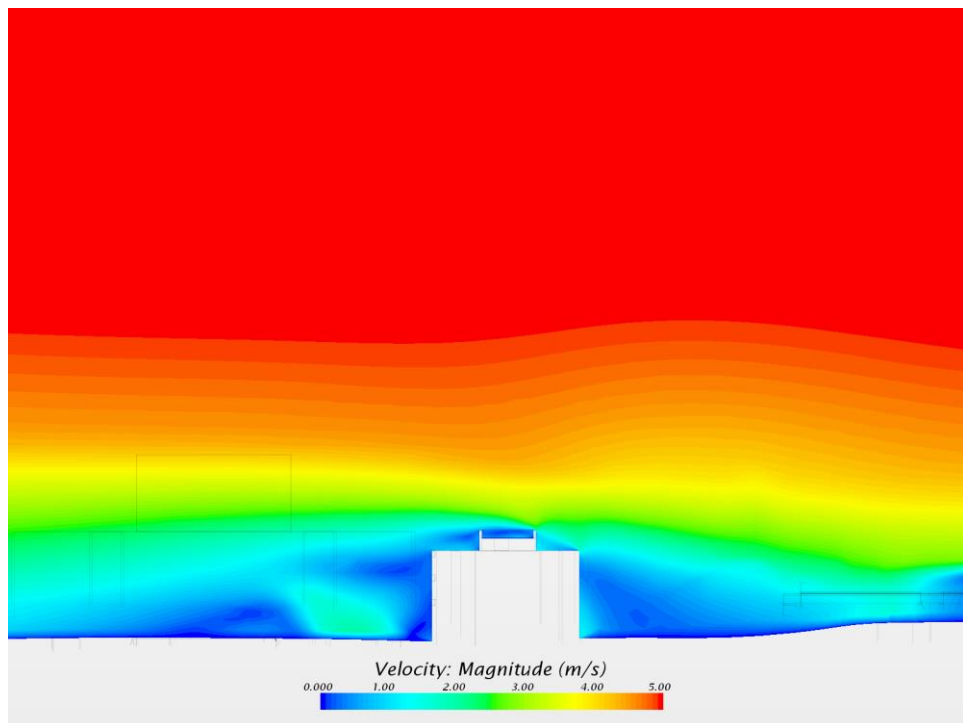


Figure 8: Detailed Wind Velocity Contour Map* on Cross Section Along Short Axis of Keller Hall

* The minimum and maximum value of the above legend ranges do not indicate the minimum and maximum values of those maps.

N-F	Approaching Wind Direction	Grid Resolution
	North	Fine

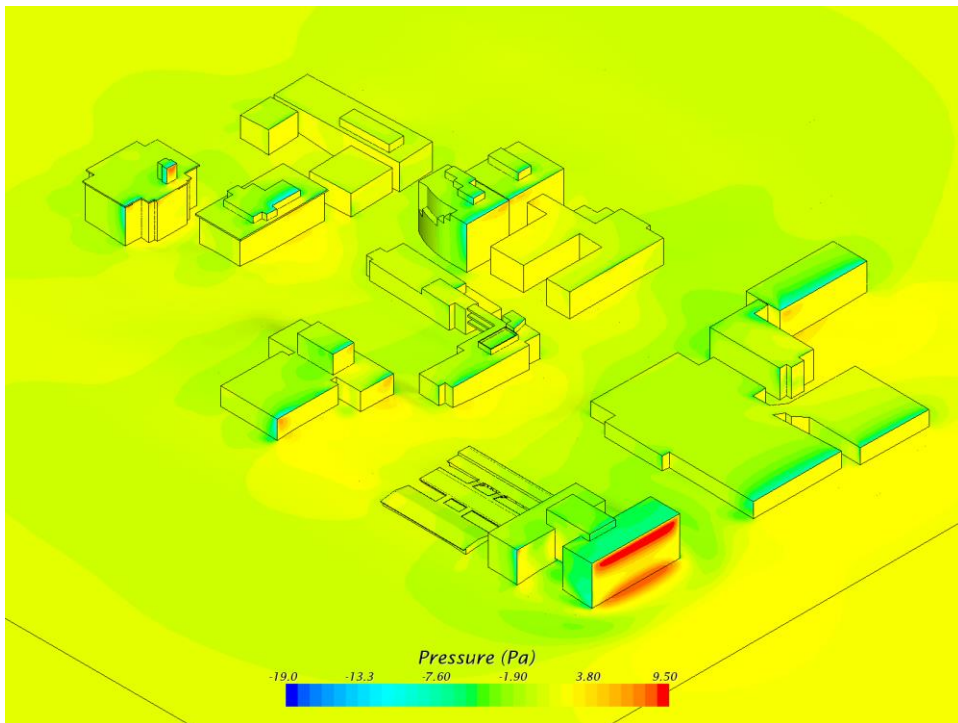


Figure 9: Overall Isometric View (from NE) of Wind-Induced Pressure Distribution* on Building Facades

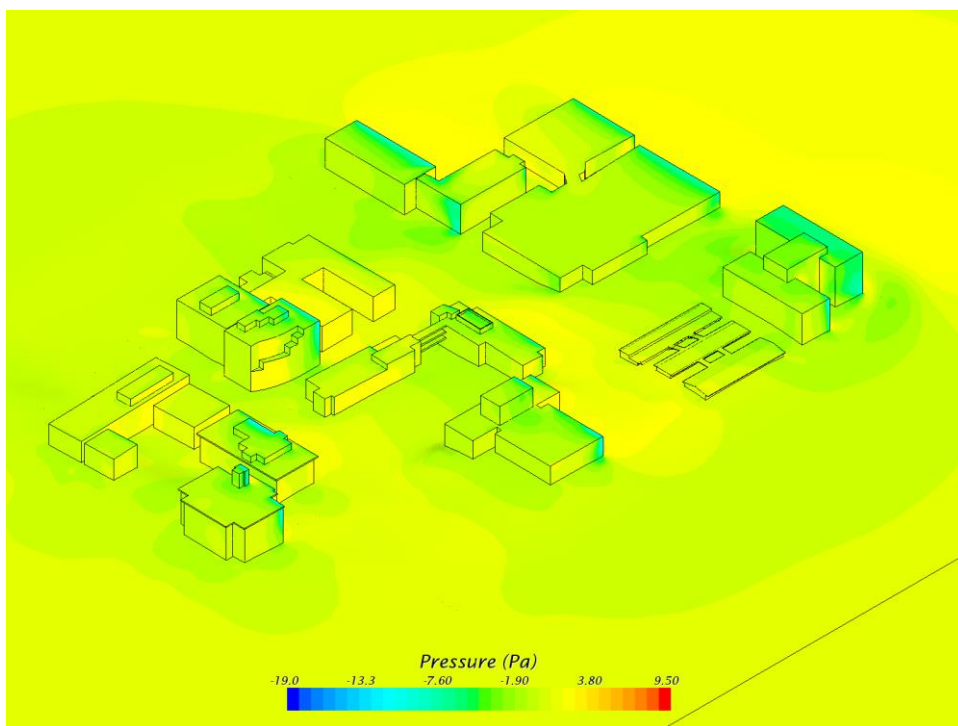


Figure 10: Overall Isometric View (from SE) of Wind-Induced Pressure Distribution* on Building Facades

* The minimum and maximum value of the above legend ranges do not indicate the minimum and maximum values of those maps.

N-F	Approaching Wind Direction	Grid Resolution
	North	Fine

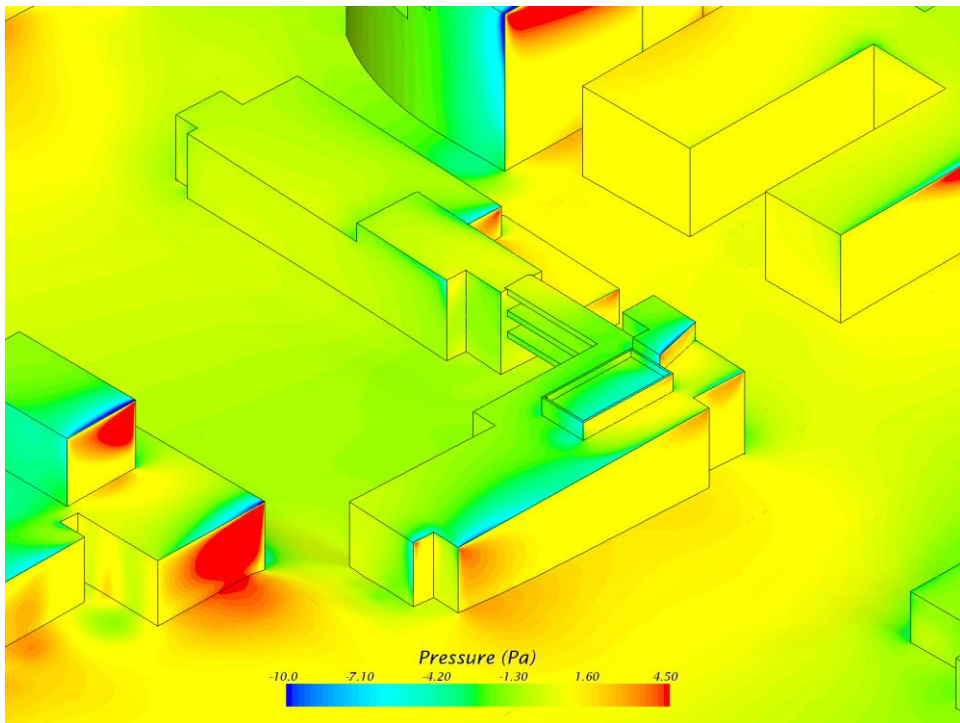


Figure 11: Detailed Isometric View (from NE) of Wind-Induced Pressure Distribution* on Keller Hall's Facades

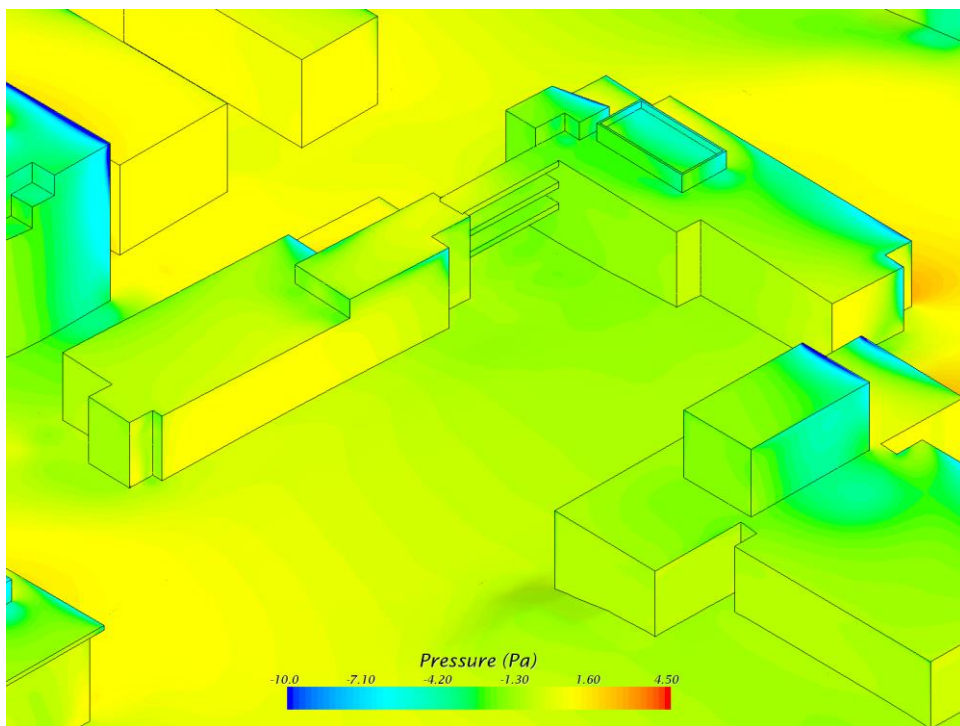


Figure 12: Detailed Isometric View (from SE) of Wind-Induced Pressure Distribution* on Keller Hall's Facades

* The minimum and maximum value of the above legend ranges do not indicate the minimum and maximum values of those maps.

E-C	Approaching Wind Direction	Grid Resolution
	East	Coarse

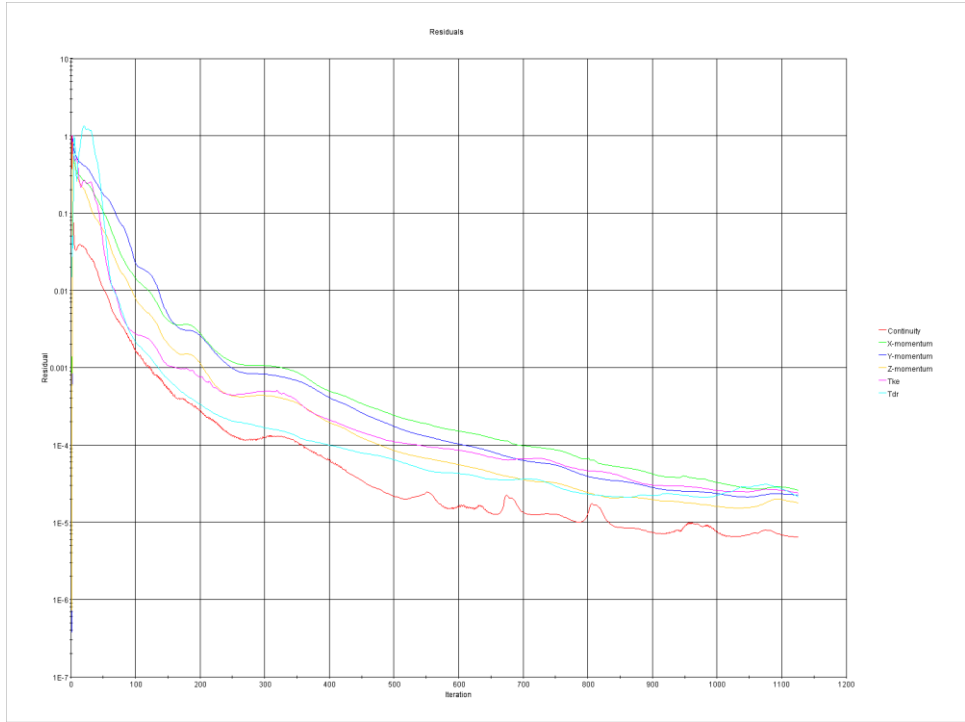


Figure 1: Convergence Residual Plot

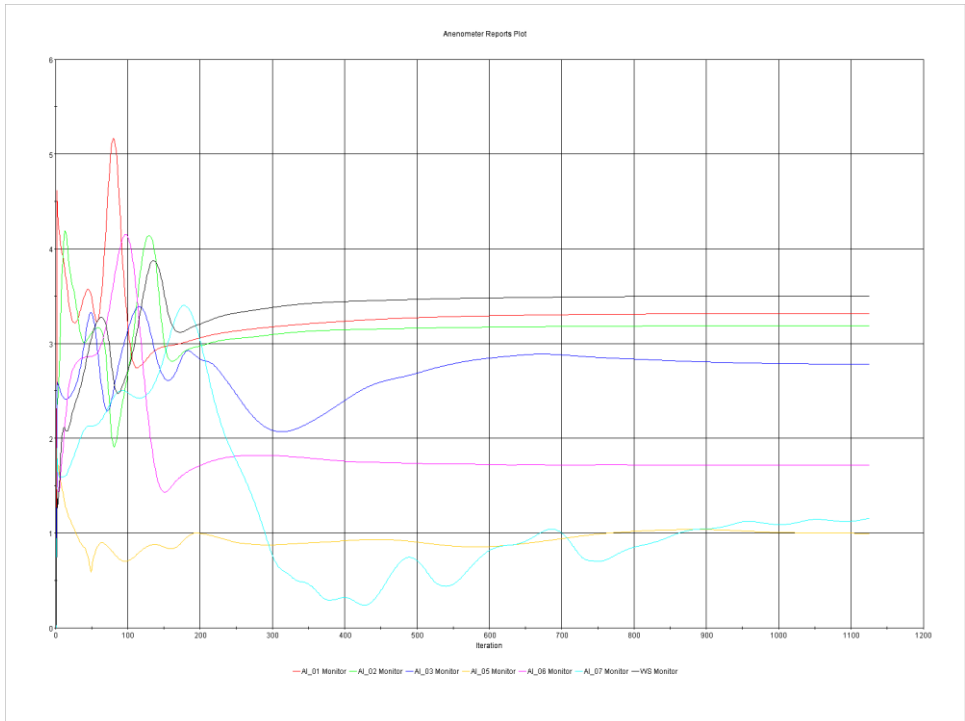


Figure 2: Convergence Anemometers' Simulated Wind Velocity Plot

E-C	Approaching Wind Direction	Grid Resolution
	East	Coarse

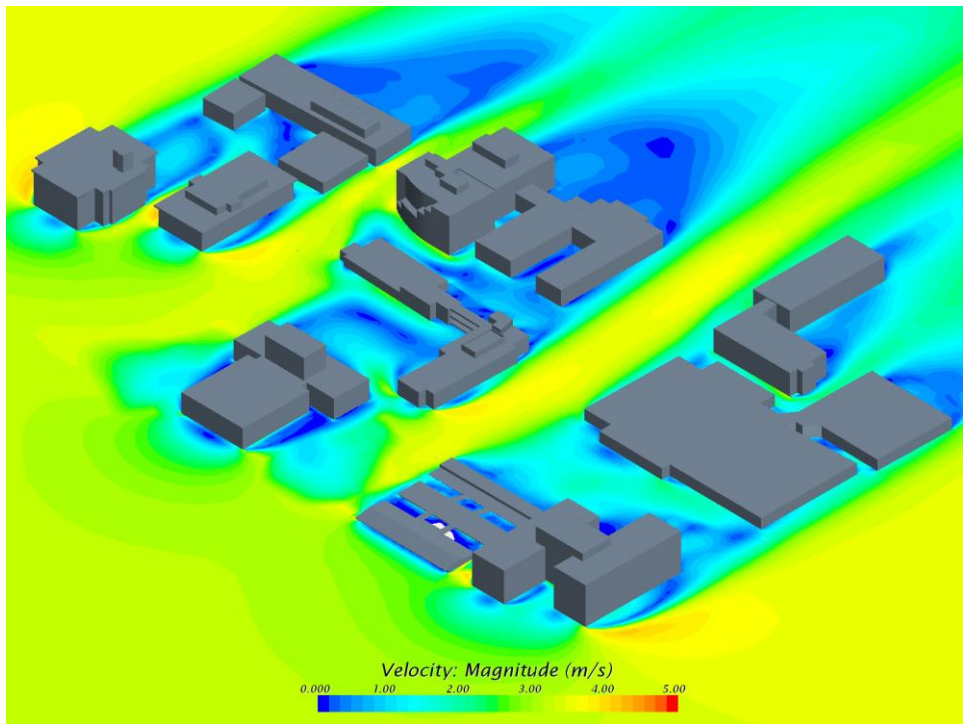


Figure 3: Overall Isometric View (from NE) of Wind Velocity Contour Map*,**

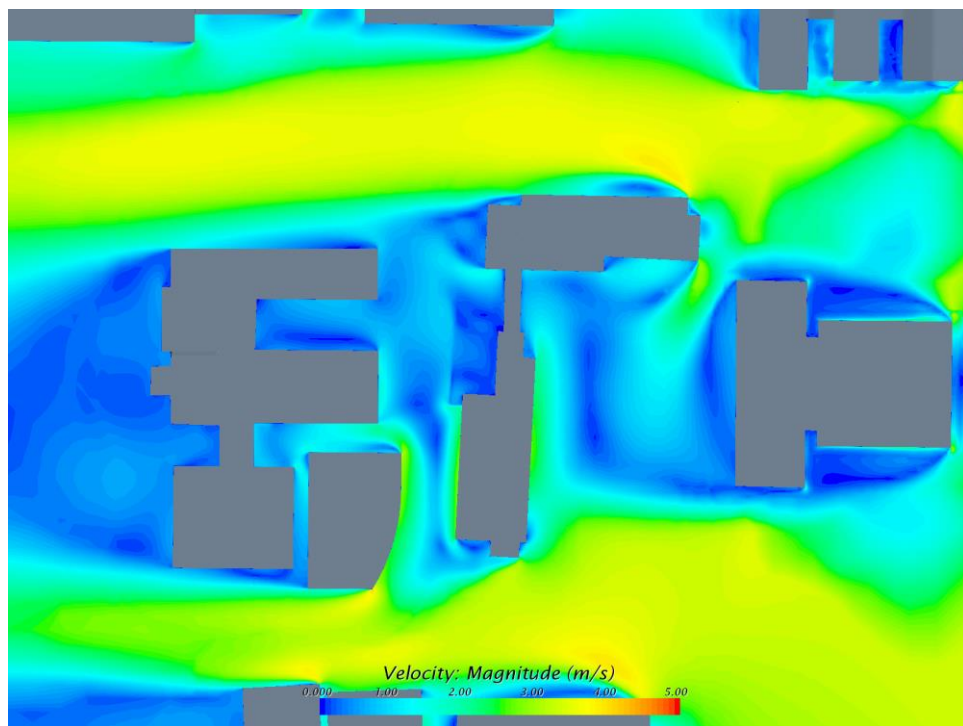


Figure 4: Plan View of Detailed Wind Velocity Contour Map*,** around Keller Hall

*On the horizontal plane at 1m height above finishing level of the 1st floor.

** The minimum and maximum value of the above legend ranges do not indicate the minimum and maximum values of those maps.

E-C	Approaching Wind Direction	Grid Resolution
	East	Coarse

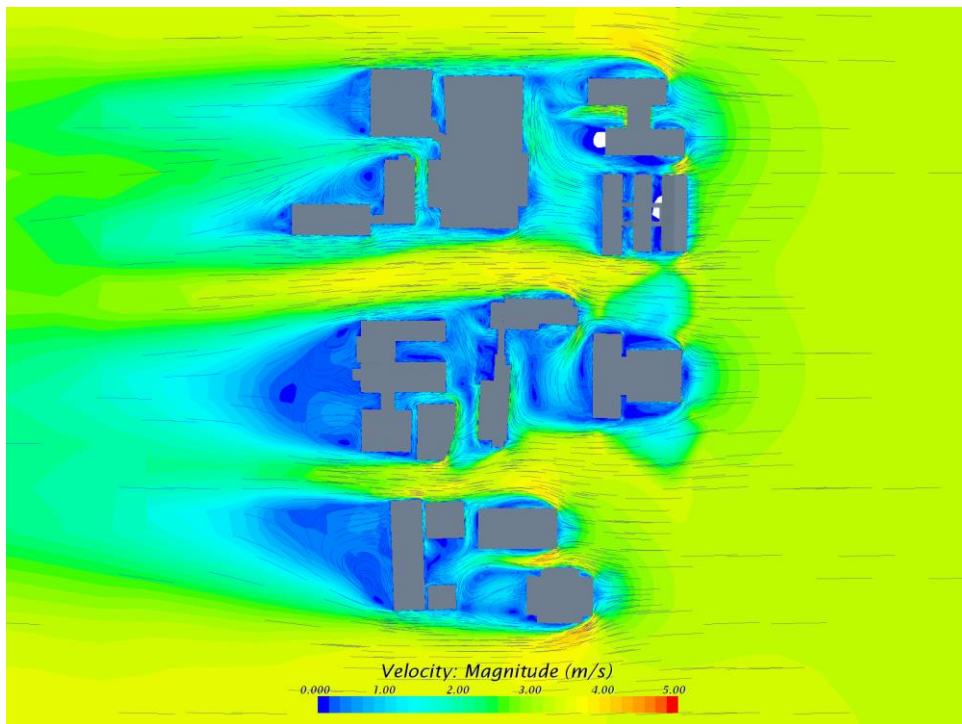


Figure 5: Plan View of Overall Wind Velocity Streamline Map*,**

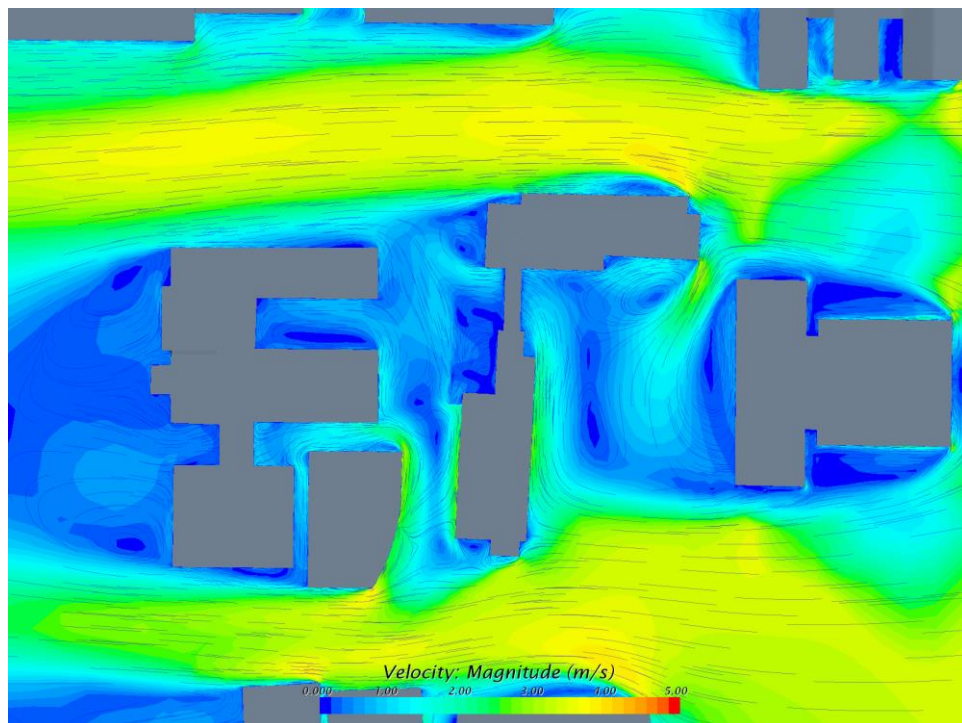


Figure 6: Plan View of Detailed Wind Velocity Stream Map*,** around Keller Hall

*On the horizontal plane at 1m height above finishing level of the 1st floor.

** The minimum and maximum value of the above legend ranges do not indicate the minimum and maximum values of those maps.

E-C	Approaching Wind Direction	Grid Resolution
	East	Coarse

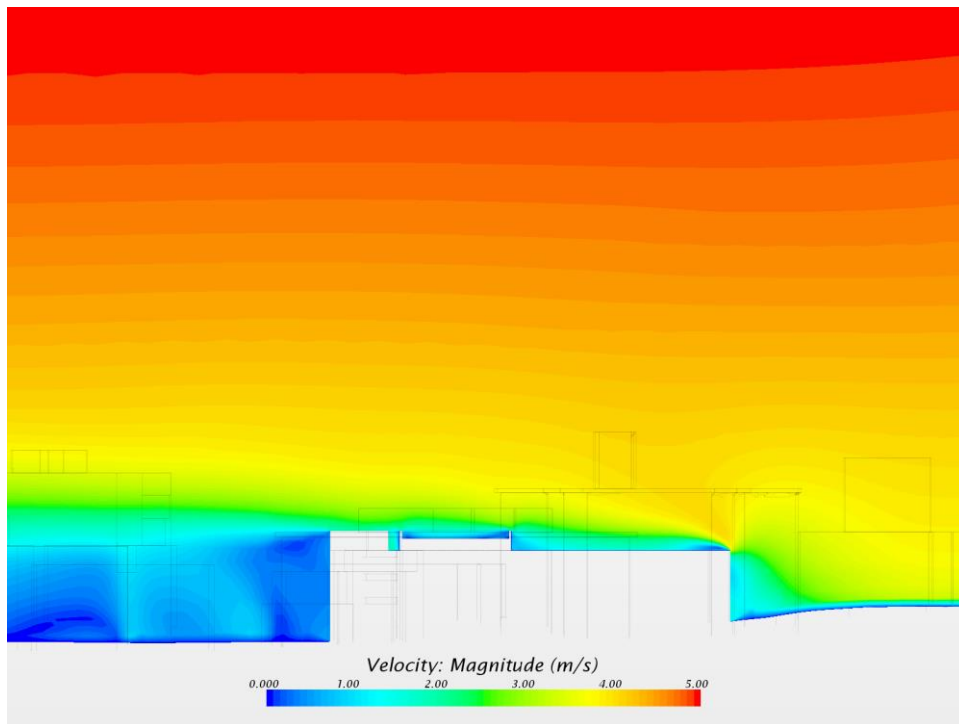


Figure 7: Detailed Wind Velocity Contour Map* on Cross Section Along Long Axis of Keller Hall

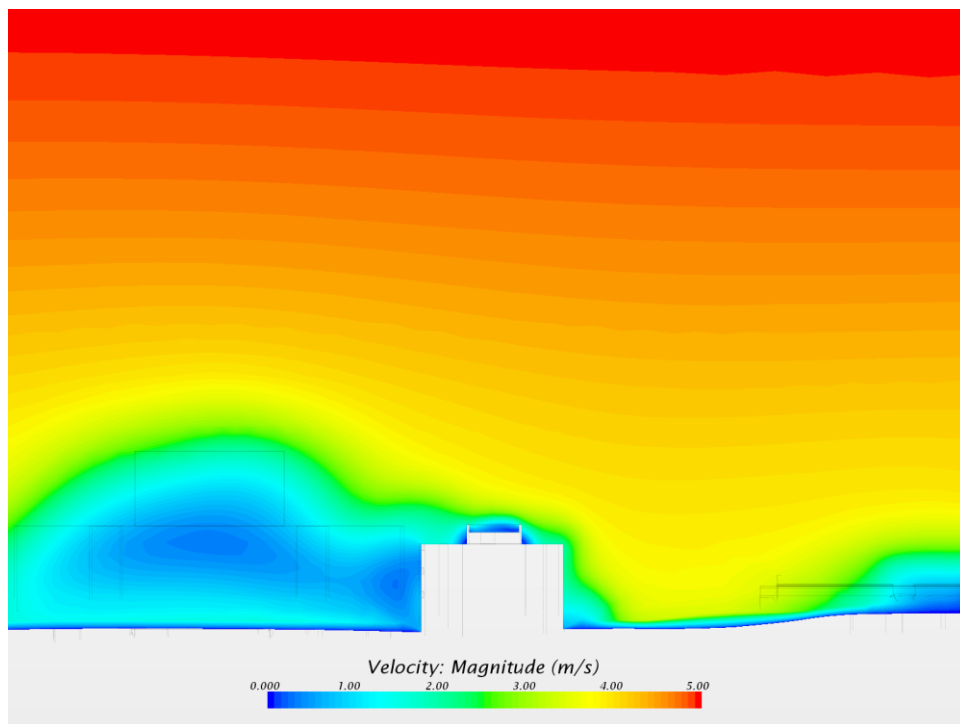


Figure 8: Detailed Wind Velocity Contour Map* on Cross Section Along Short Axis of Keller Hall

* The minimum and maximum value of the above legend ranges do not indicate the minimum and maximum values of those maps.

E-C	Approaching Wind Direction	Grid Resolution
	East	Coarse

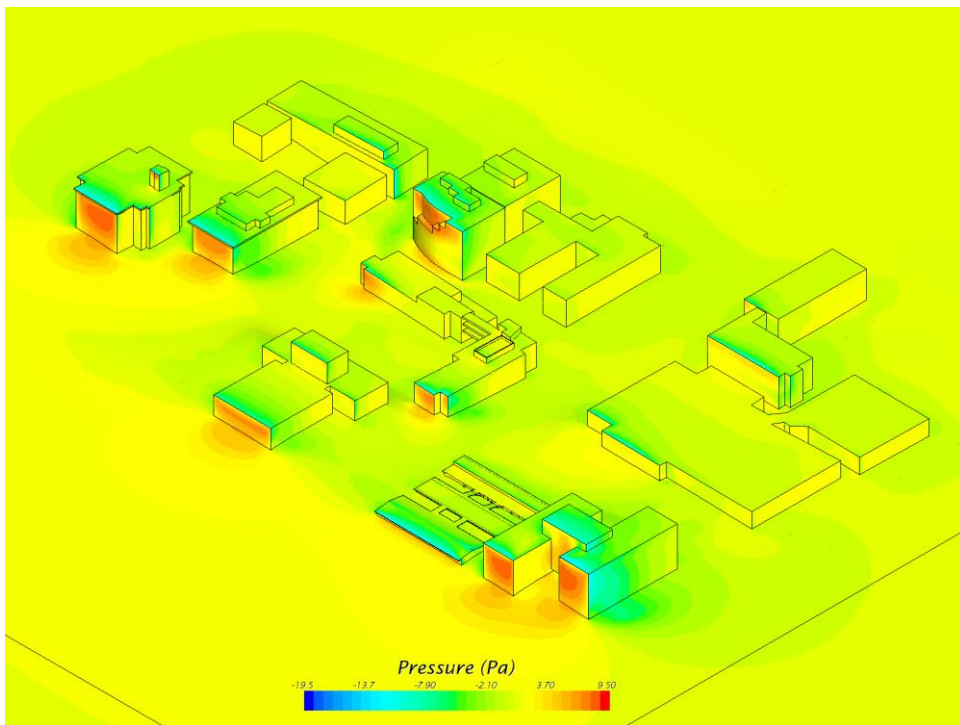


Figure 9: Overall Isometric View (from NE) of Wind-Induced Pressure Distribution* on Building Facades

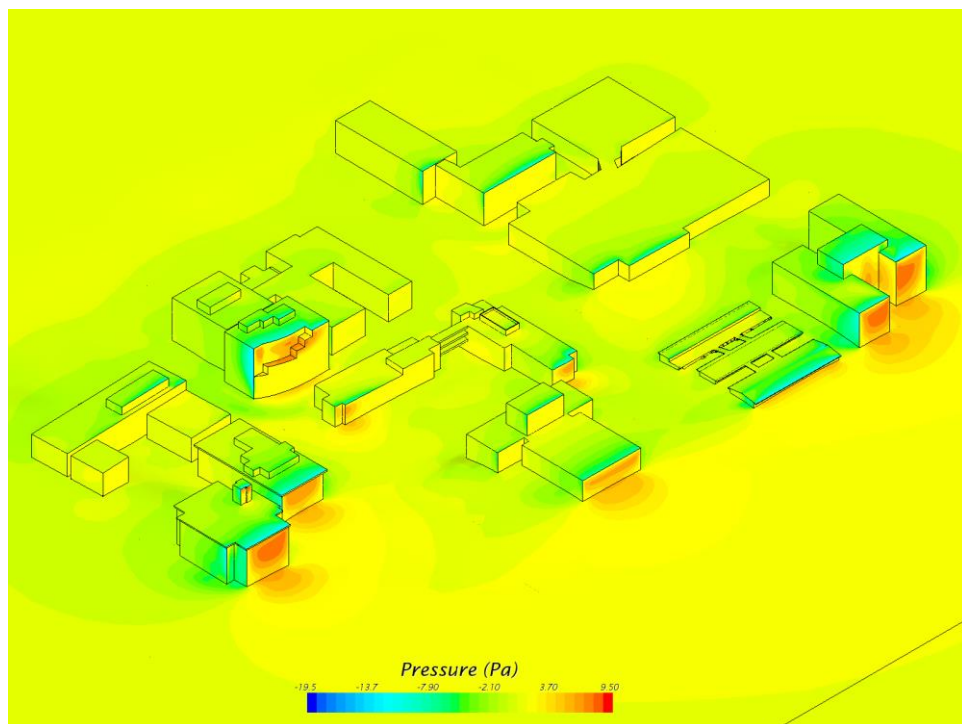


Figure 10: Overall Isometric View (from SE) of Wind-Induced Pressure Distribution* on Building Facades

* The minimum and maximum value of the above legend ranges do not indicate the minimum and maximum values of those maps.

E-C	Approaching Wind Direction	Grid Resolution
	East	Coarse

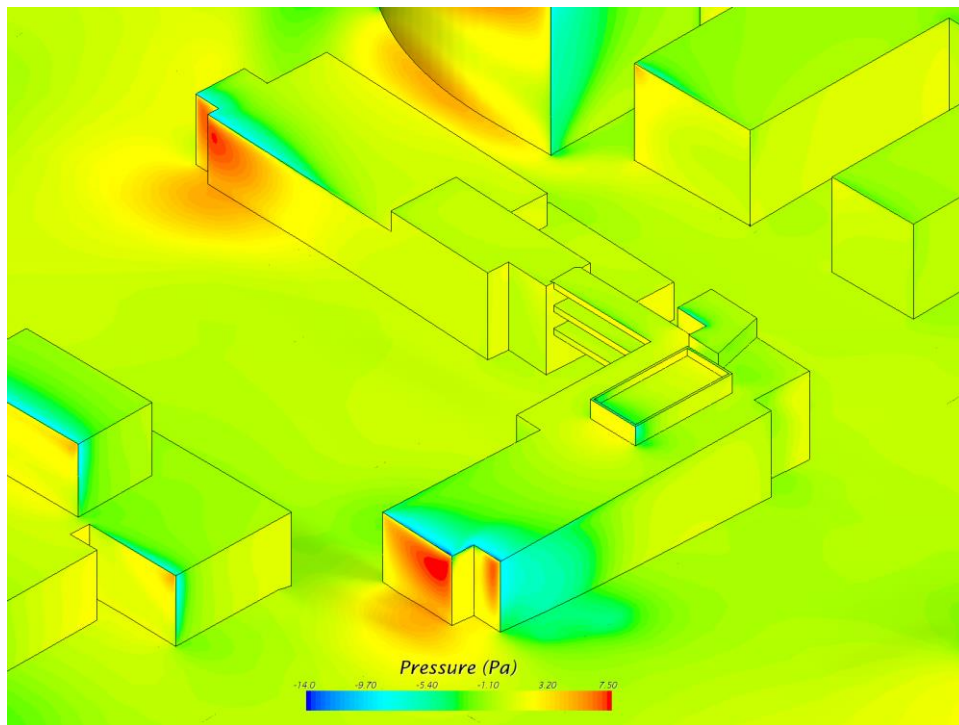


Figure 11: Detailed Isometric View (from NE) of Wind-Induced Pressure Distribution* on Keller Hall's Facades

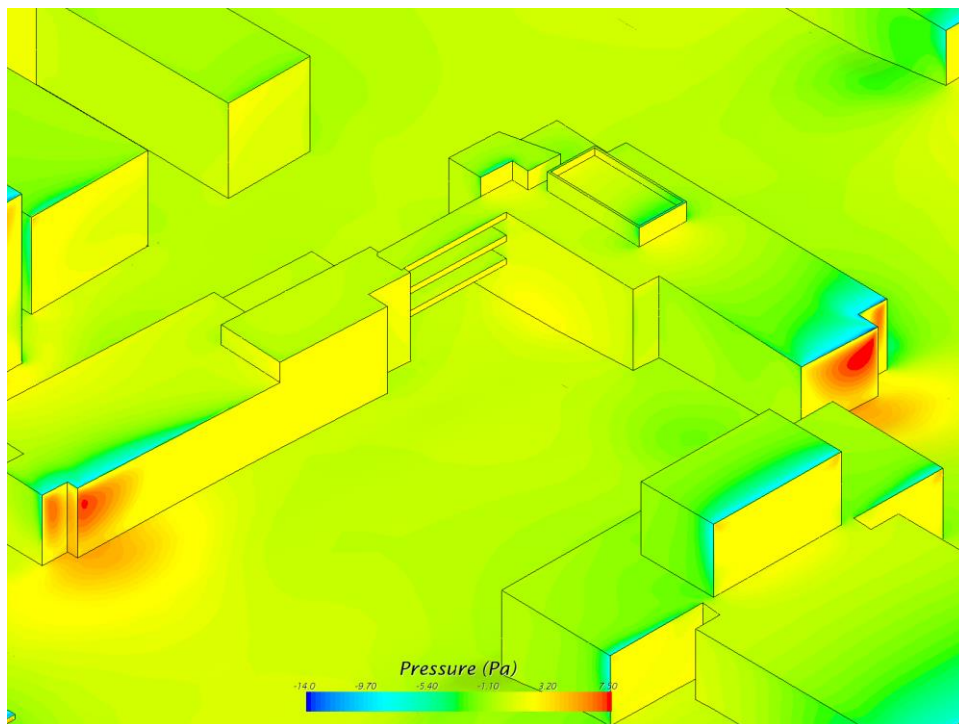


Figure 12: Detailed Isometric View (from SE) of Wind-Induced Pressure Distribution* on Keller Hall's Facades

* The minimum and maximum value of the above legend ranges do not indicate the minimum and maximum values of those maps.

E-M	Approaching Wind Direction	Grid Resolution
	East	Medium

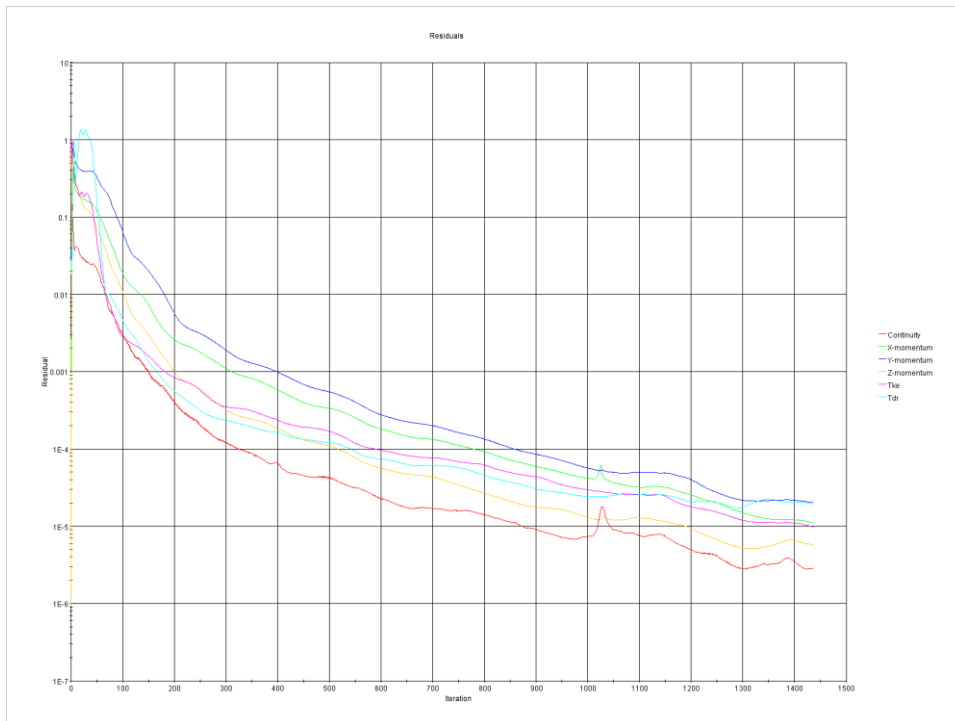


Figure 1: Convergence Residual Plot

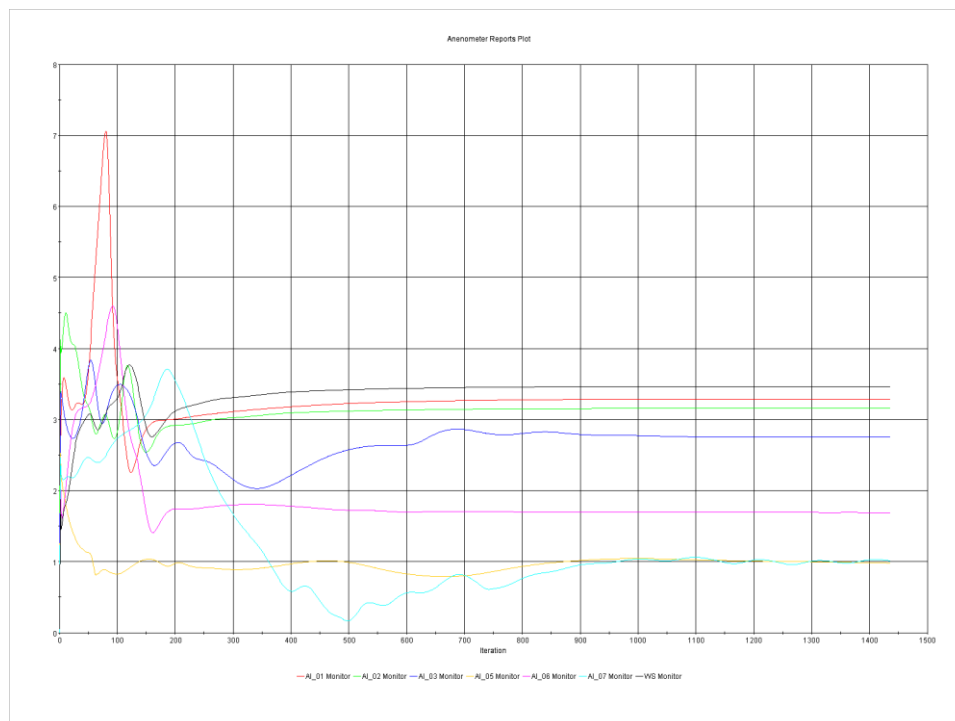


Figure 2: Convergence Anemometers' Simulated Wind Velocity Plot

E-M	Approaching Wind Direction	Grid Resolution
	East	Medium

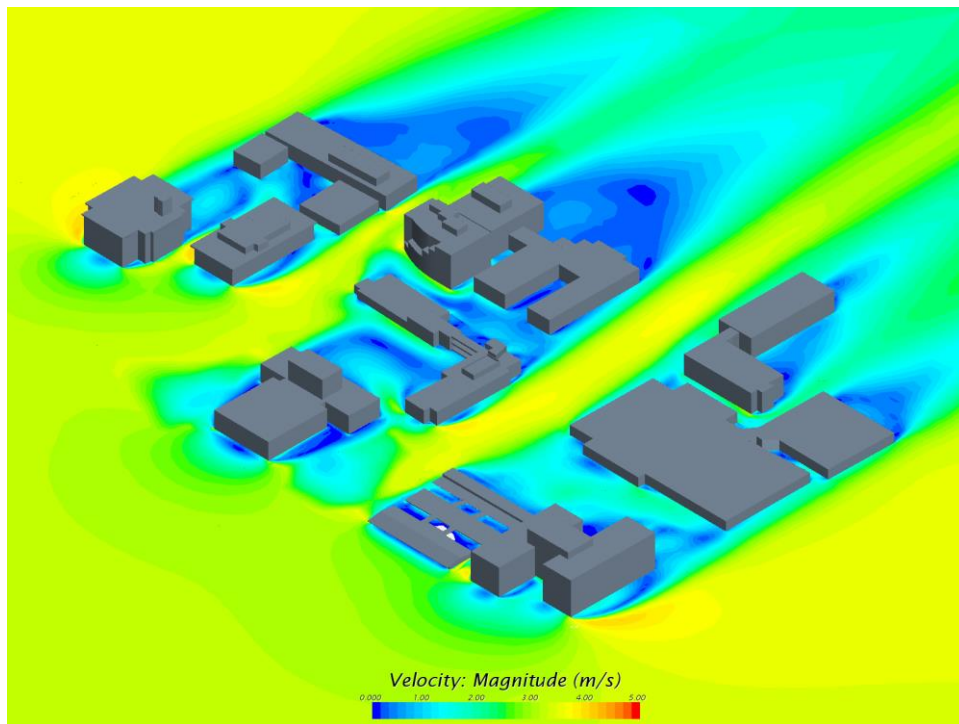


Figure 3: Overall Isometric View (from NE) of Wind Velocity Contour Map*,**

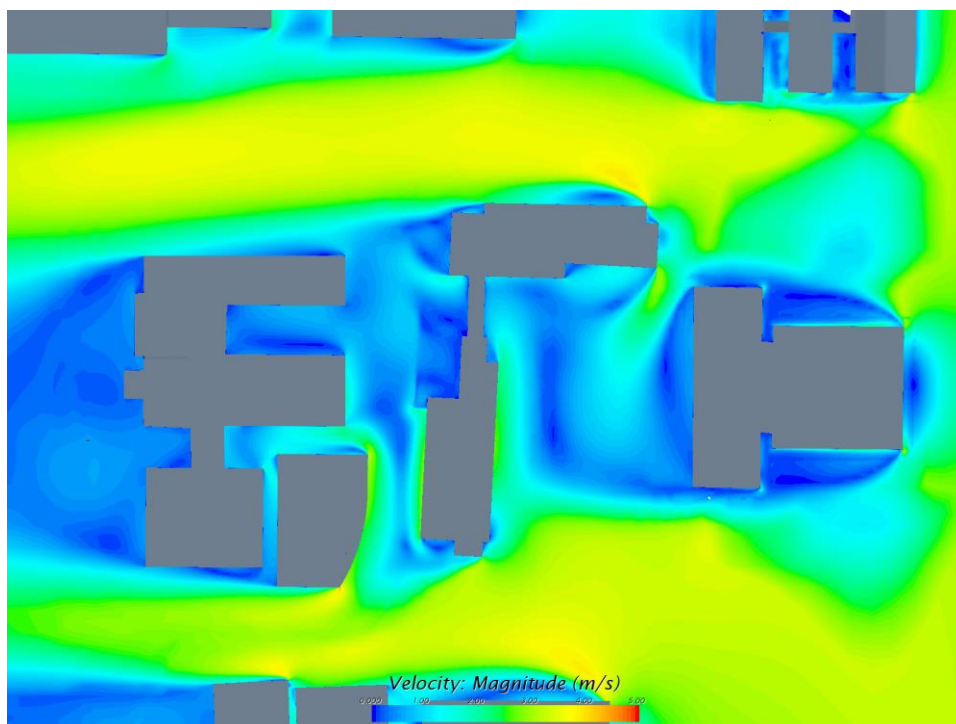


Figure 4: Plan View of Detailed Wind Velocity Contour Map*,** around Keller Hall
 *On the horizontal plane at 1m height above finishing level of the 1st floor.
 ** The minimum and maximum value of the above legend ranges do not indicate the minimum and maximum values of those maps.

E-M	Approaching Wind Direction	Grid Resolution
	East	Medium

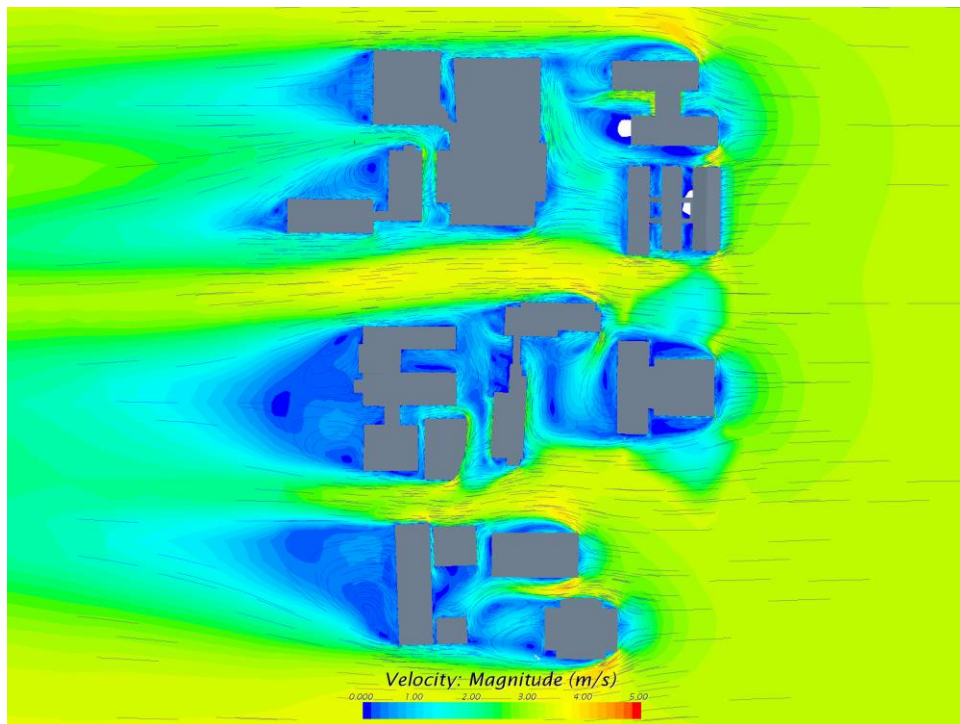


Figure 5: Plan View of Overall Wind Velocity Streamline Map*,**

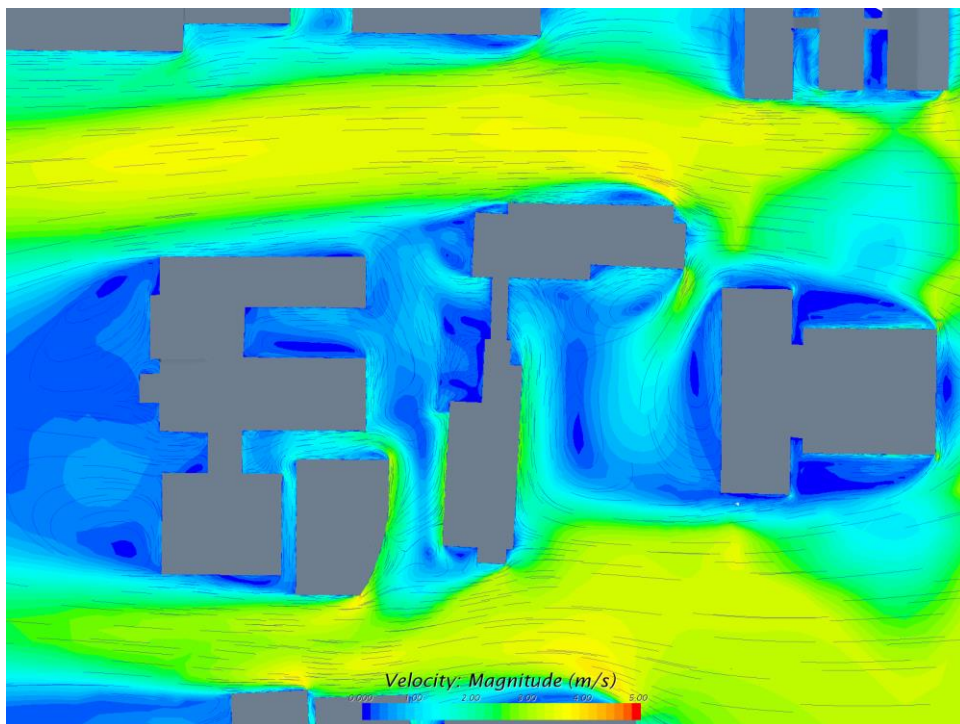


Figure 6: Plan View of Detailed Wind Velocity Stream Map*,** around Keller Hall

*On the horizontal plane at 1m height above finishing level of the 1st floor.

** The minimum and maximum value of the above legend ranges do not indicate the minimum and maximum values of those maps.

E-M	Approaching Wind Direction	Grid Resolution
	East	Medium

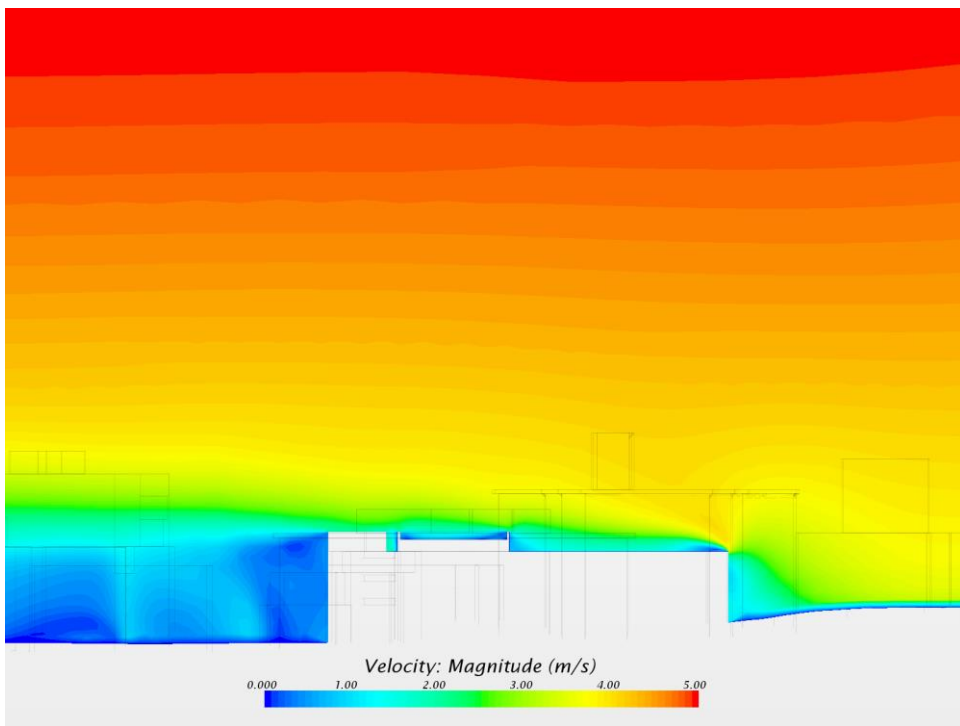


Figure 7: Detailed Wind Velocity Contour Map* on Cross Section Along Long Axis of Keller Hall

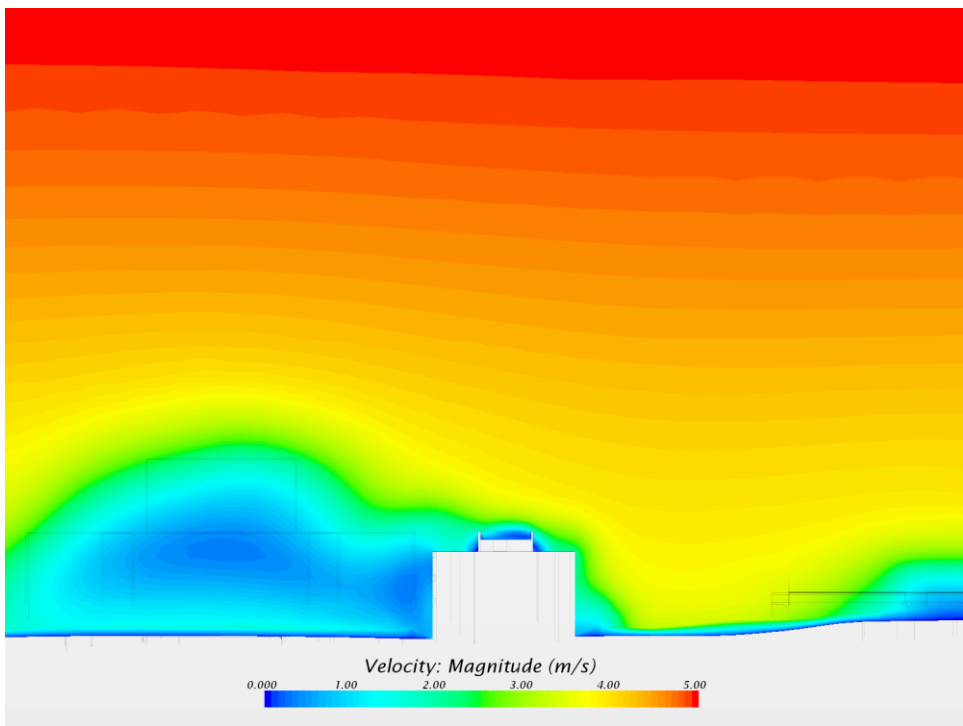


Figure 8: Detailed Wind Velocity Contour Map* on Cross Section Along Short Axis of Keller Hall

* The minimum and maximum value of the above legend ranges do not indicate the minimum and maximum values of those maps.

E-M	Approaching Wind Direction	Grid Resolution
	East	Medium

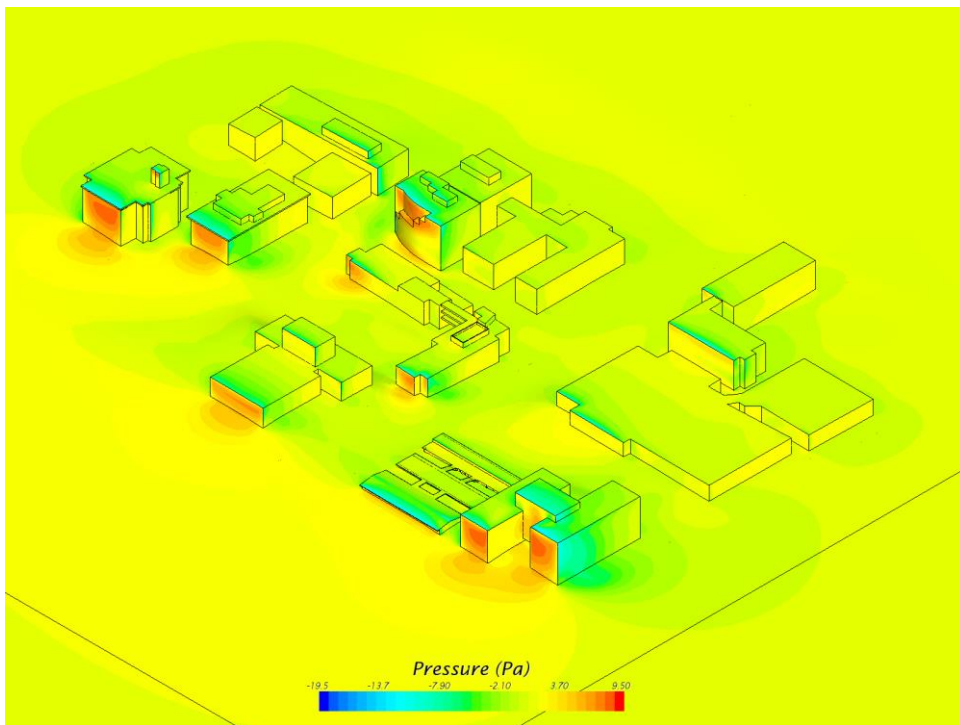


Figure 9: Overall Isometric View (from NE) of Wind-Induced Pressure Distribution* on Building Facades

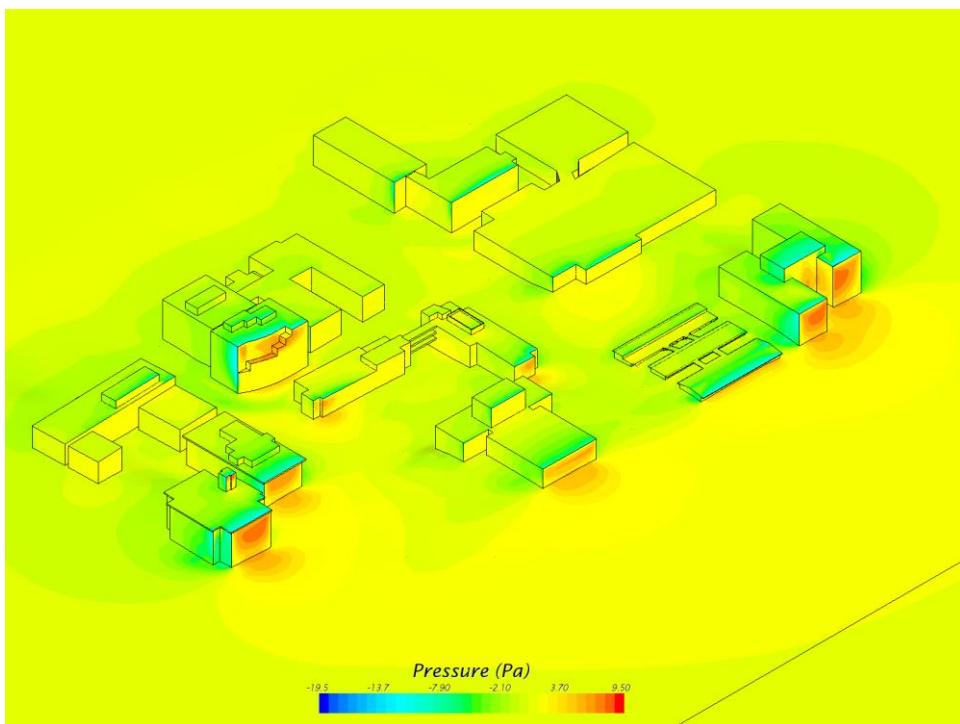


Figure 10: Overall Isometric View (from SE) of Wind-Induced Pressure Distribution* on Building Facades

* The minimum and maximum value of the above legend ranges do not indicate the minimum and maximum values of those maps.

E-M	Approaching Wind Direction	Grid Resolution
	East	Medium

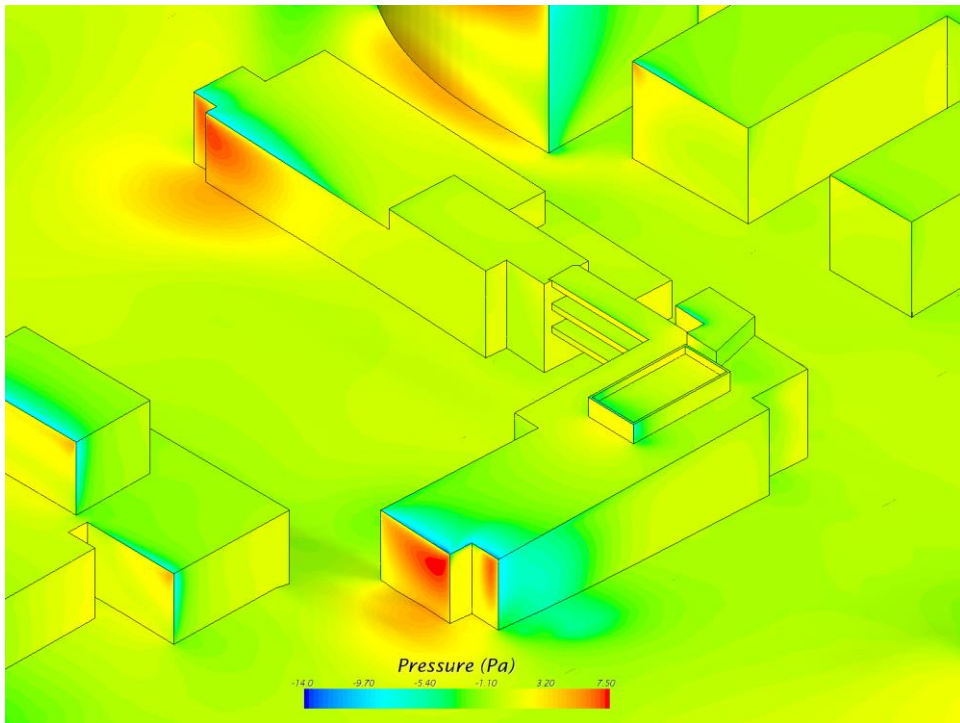


Figure 11: Detailed Isometric View (from NE) of Wind-Induced Pressure Distribution* on Keller Hall's Facades

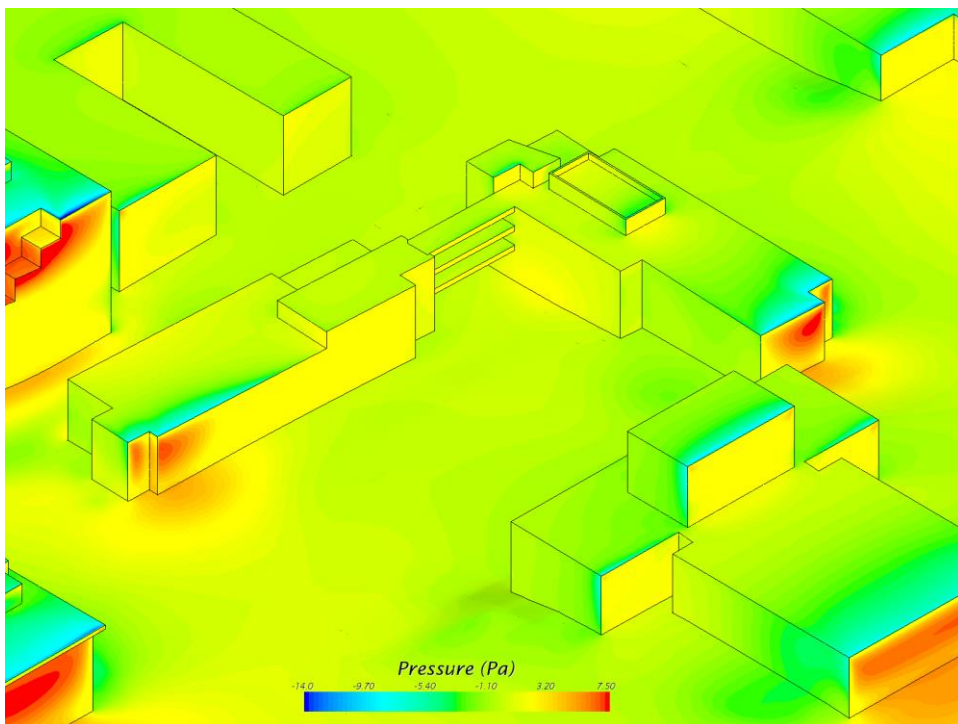


Figure 12: Detailed Isometric View (from SE) of Wind-Induced Pressure Distribution* on Keller Hall's Facades

* The minimum and maximum value of the above legend ranges do not indicate the minimum and maximum values of those maps.

E-F	Approaching Wind Direction	Grid Resolution
		East

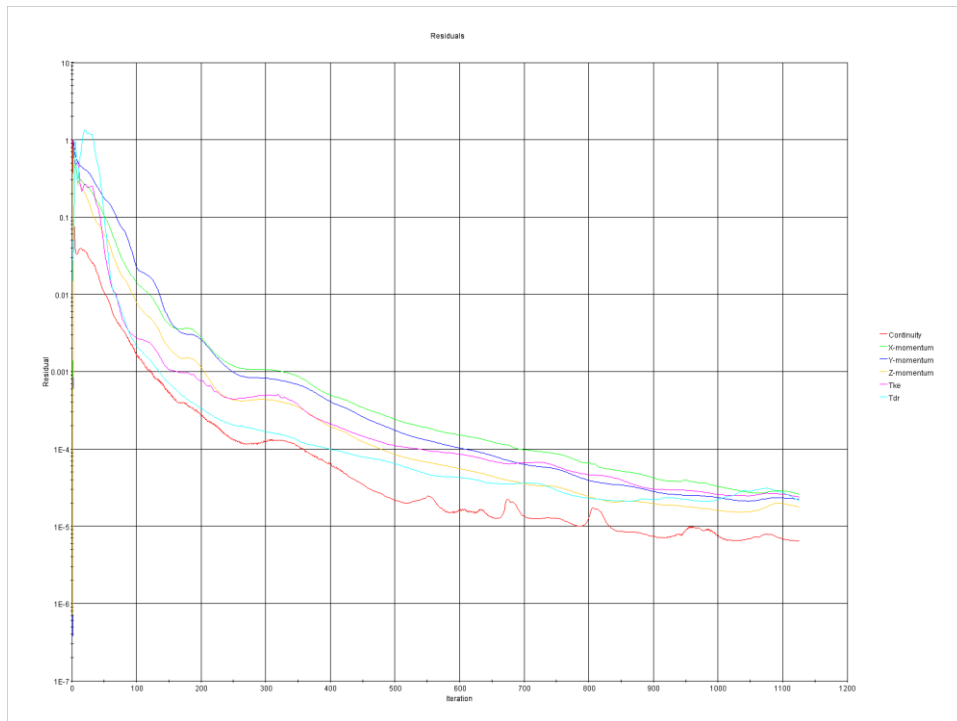


Figure 1: Convergence Residual Plot

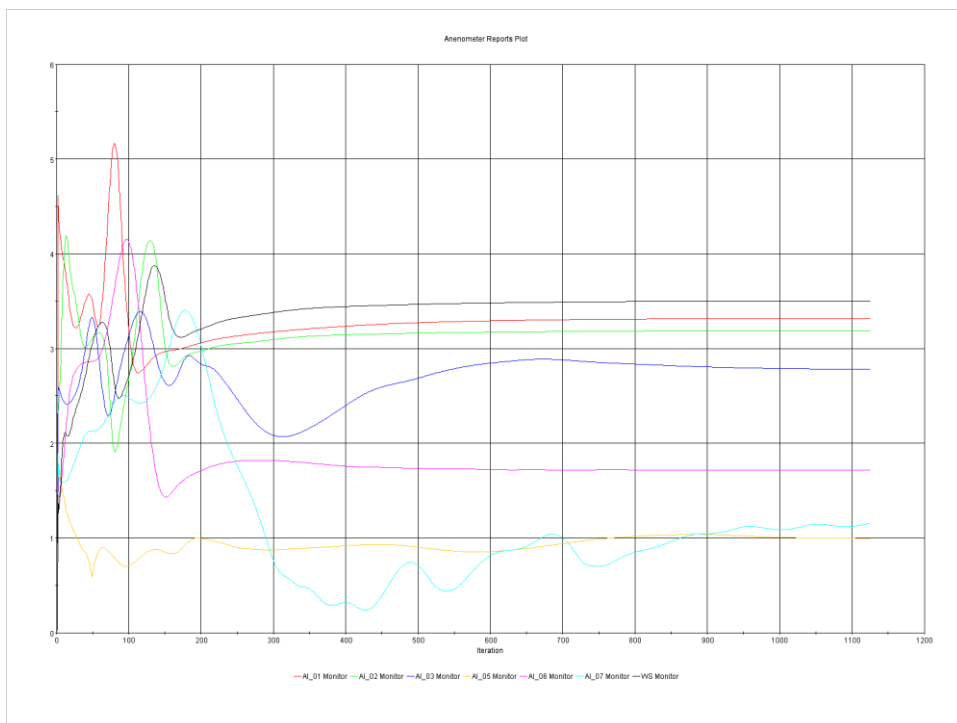


Figure 2: Convergence Anemometers' Simulated Wind Velocity Plot

E-F	Approaching Wind Direction	Grid Resolution
	East	Fine

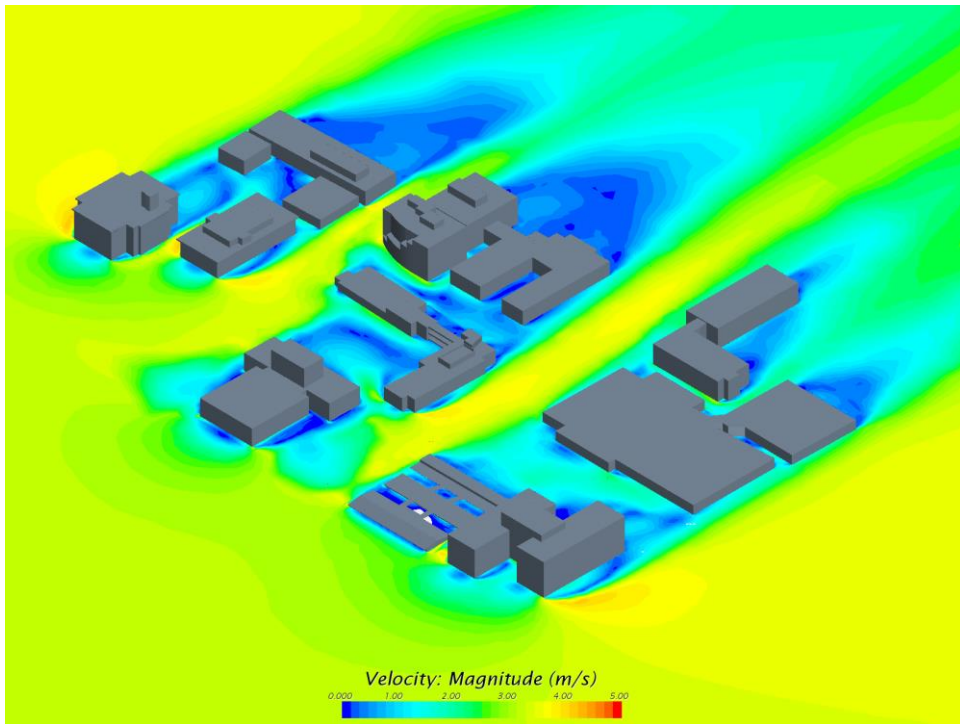


Figure 3: Overall Isometric View (from NE) of Wind Velocity Contour Map*,**

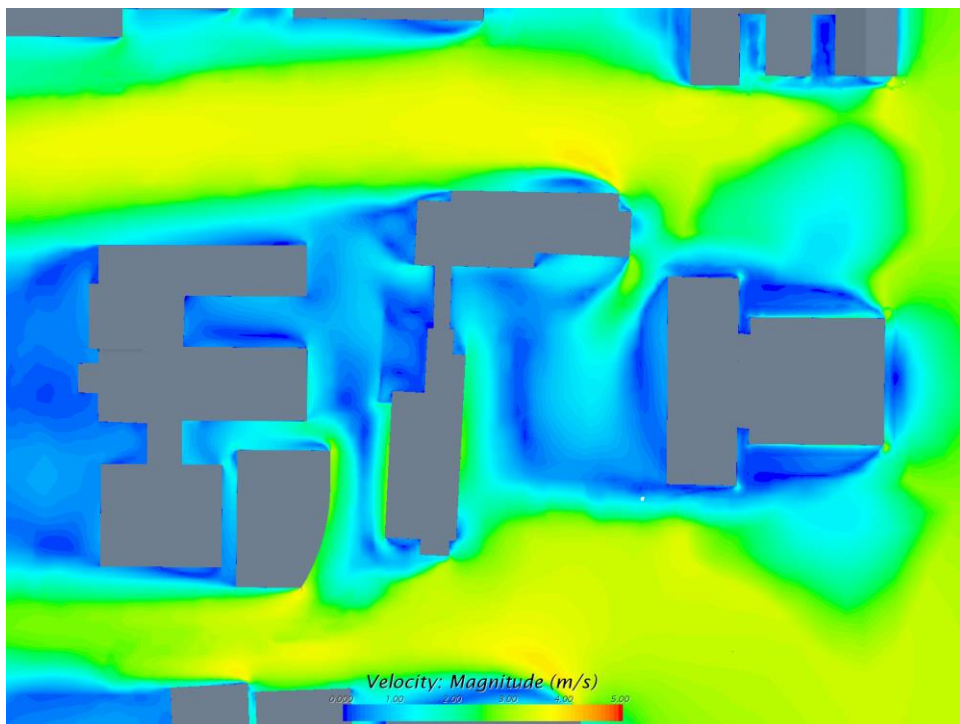


Figure 4: Plan View of Detailed Wind Velocity Contour Map*,** around Keller Hall

*On the horizontal plane at 1m height above finishing level of the 1st floor.

** The minimum and maximum value of the above legend ranges do not indicate the minimum and maximum values of those maps.

E-F	Approaching Wind Direction	Grid Resolution
	East	Fine

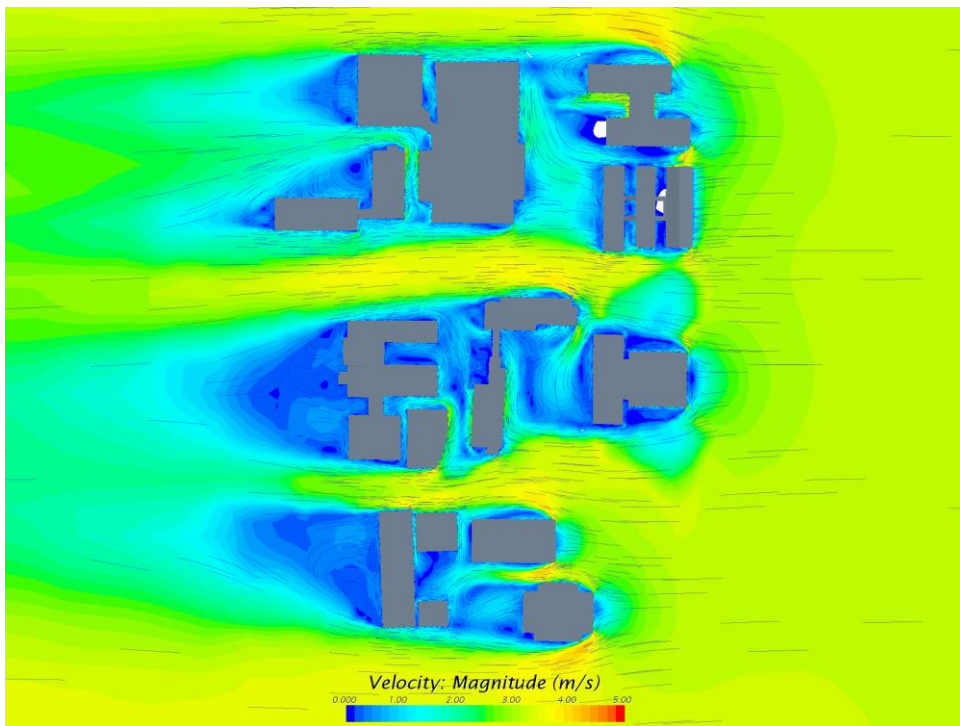


Figure 5: Plan View of Overall Wind Velocity Streamline Map*,**

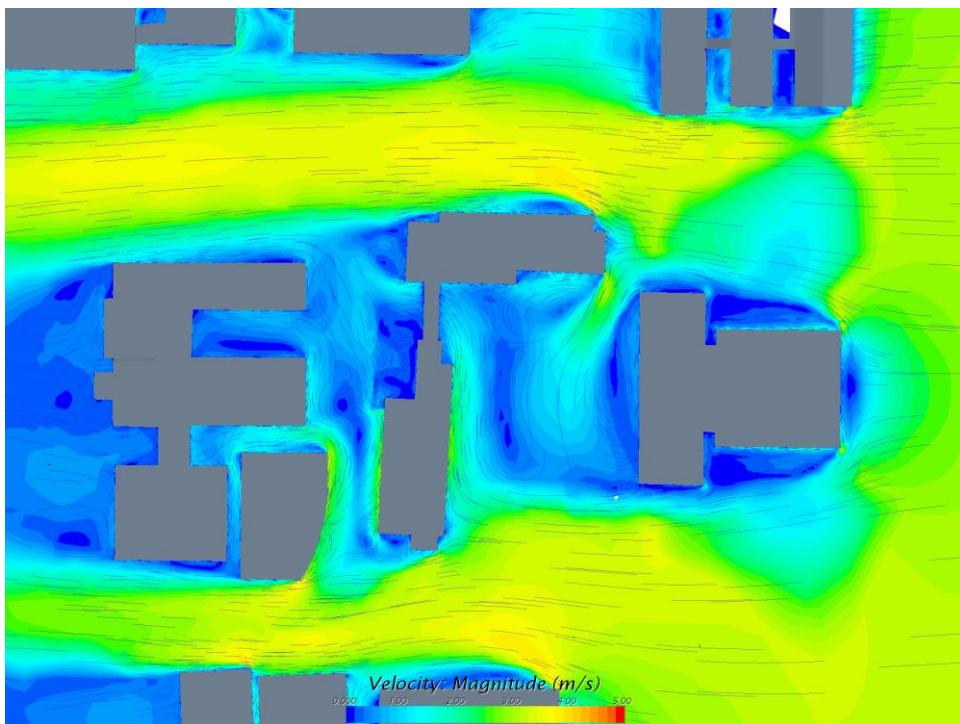


Figure 6: Plan View of Detailed Wind Velocity Stream Map*,** around Keller Hall

*On the horizontal plane at 1m height above finishing level of the 1st floor.

** The minimum and maximum value of the above legend ranges do not indicate the minimum and maximum values of those maps.

E-F	Approaching Wind Direction	Grid Resolution
	East	Fine

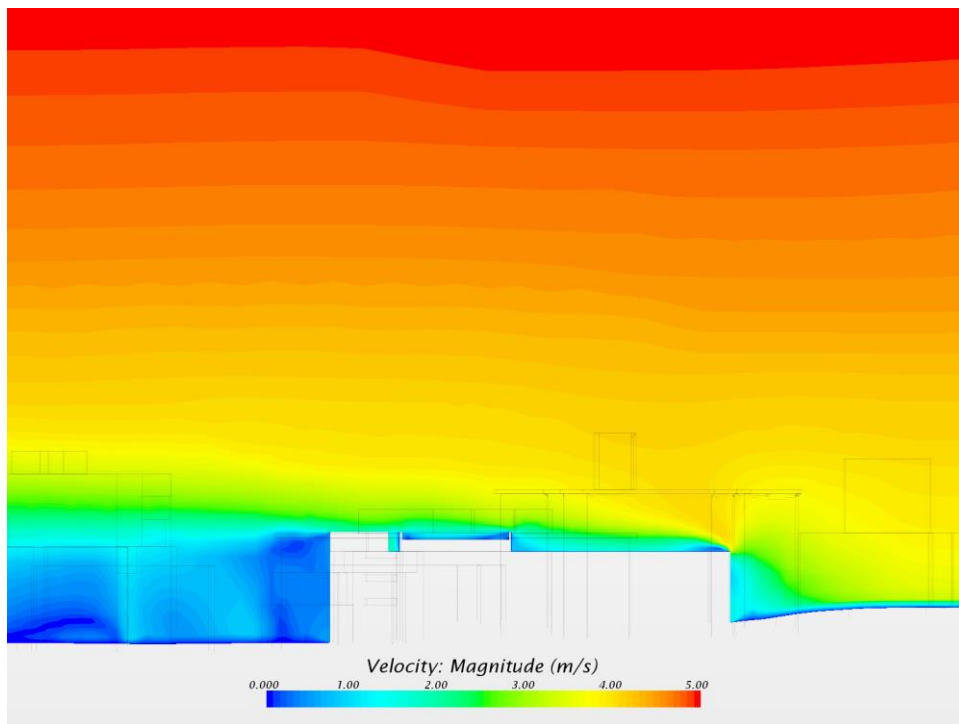


Figure 7: Detailed Wind Velocity Contour Map* on Cross Section Along Long Axis of Keller Hall

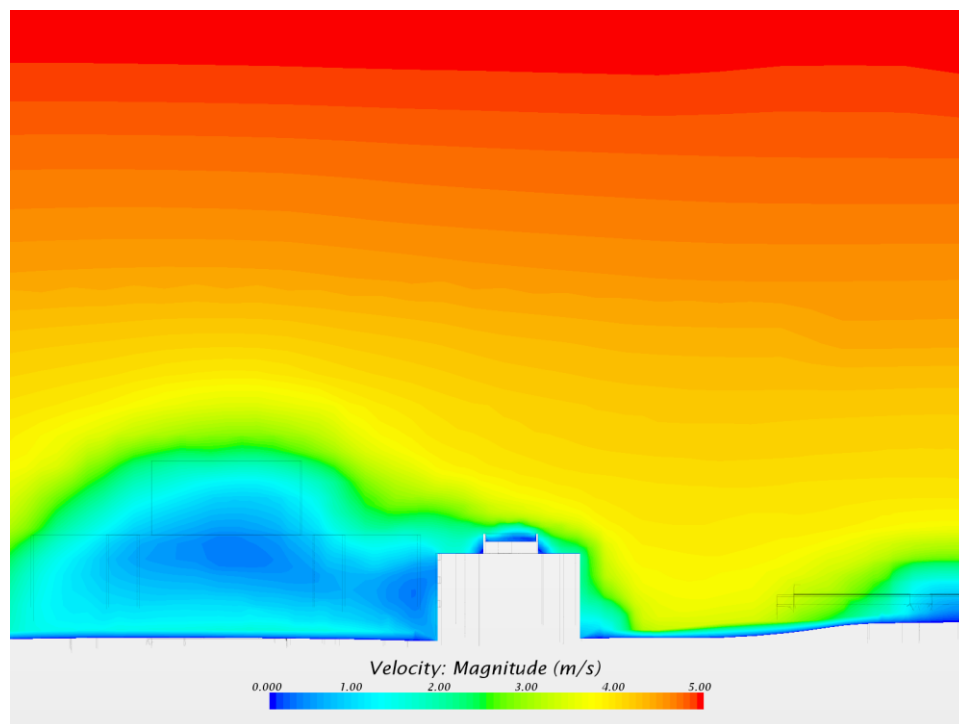


Figure 8: Detailed Wind Velocity Contour Map* on Cross Section Along Short Axis of Keller Hall

* The minimum and maximum value of the above legend ranges do not indicate the minimum and maximum values of those maps.

E-F	Approaching Wind Direction	Grid Resolution
	East	Fine

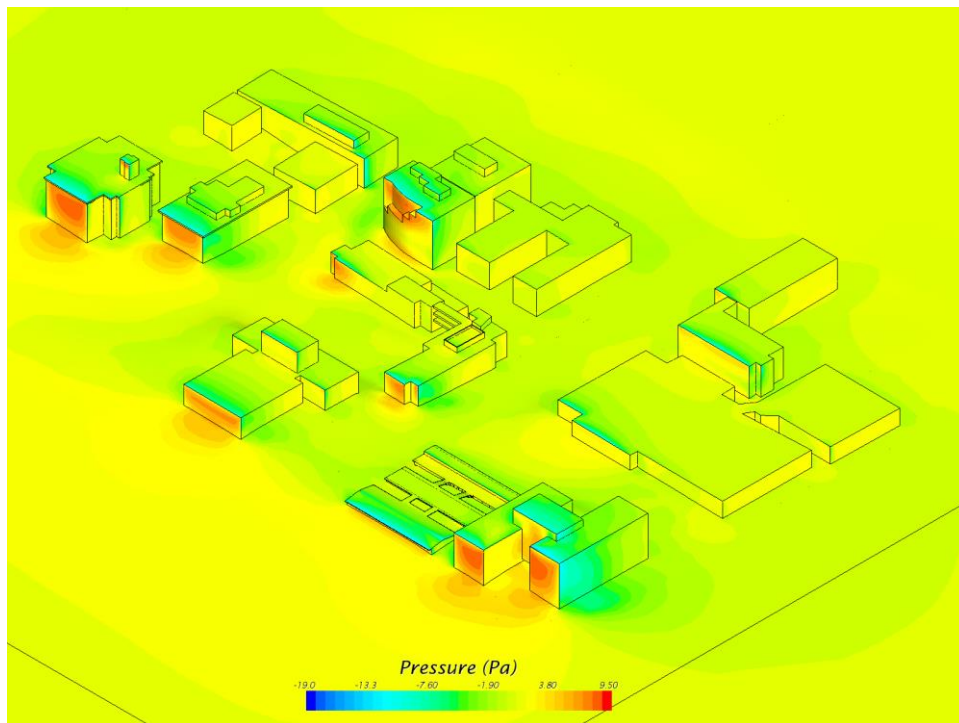


Figure 9: Overall Isometric View (from NE) of Wind-Induced Pressure Distribution* on Building Facades

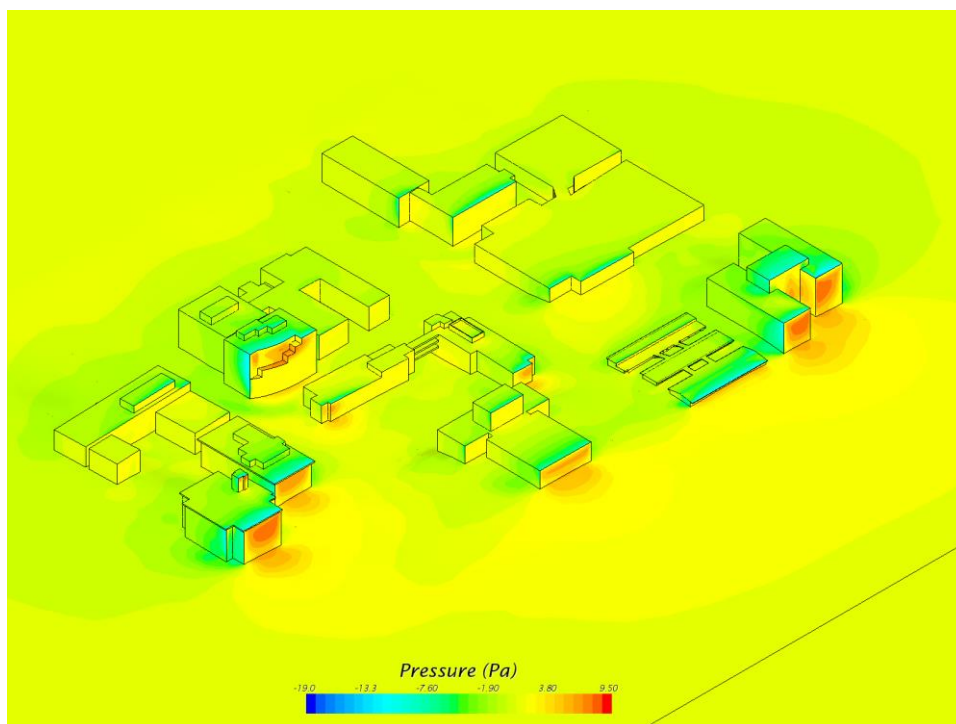


Figure 10: Overall Isometric View (from SE) of Wind-Induced Pressure Distribution* on Building Facades

* The minimum and maximum value of the above legend ranges do not indicate the minimum and maximum values of those maps.

E-F	Approaching Wind Direction	Grid Resolution
	East	Fine

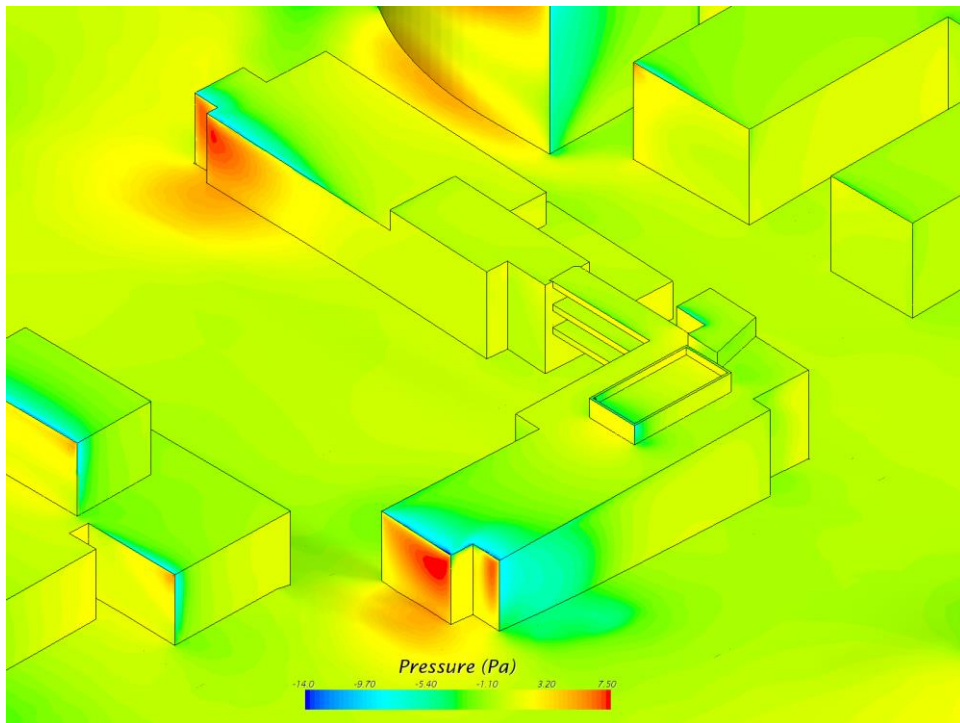


Figure 11: Detailed Isometric View (from NE) of Wind-Induced Pressure Distribution* on Keller Hall's Facades

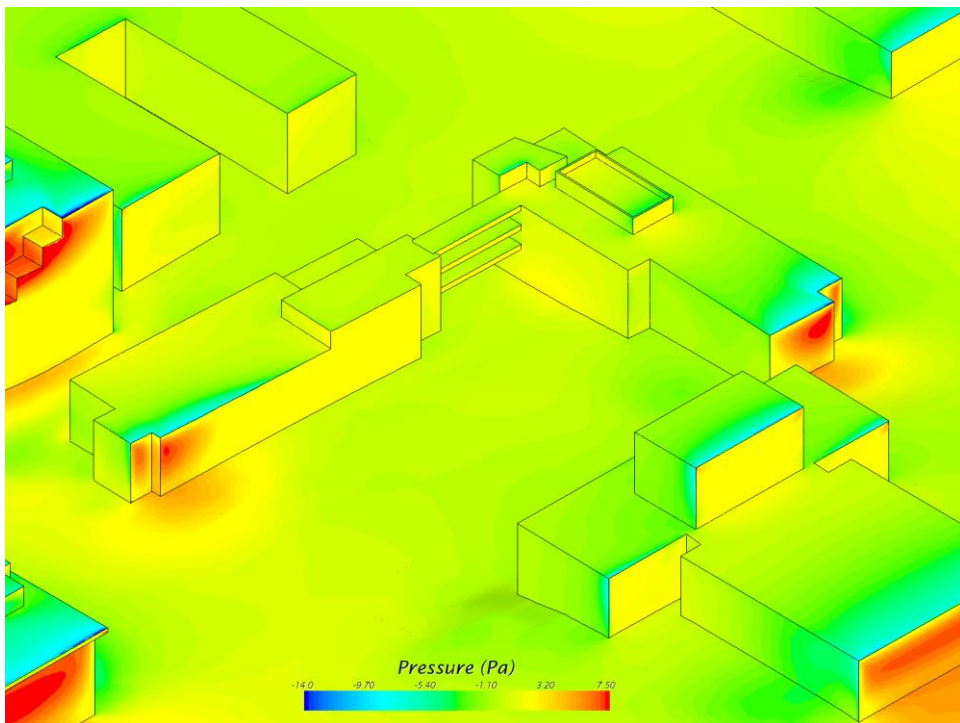


Figure 12: Detailed Isometric View (from SE) of Wind-Induced Pressure Distribution* on Keller Hall's Facades

* The minimum and maximum value of the above legend ranges do not indicate the minimum and maximum values of those maps.

NE-C	Approaching Wind Direction	Grid Resolution
	Northeast	Coarse

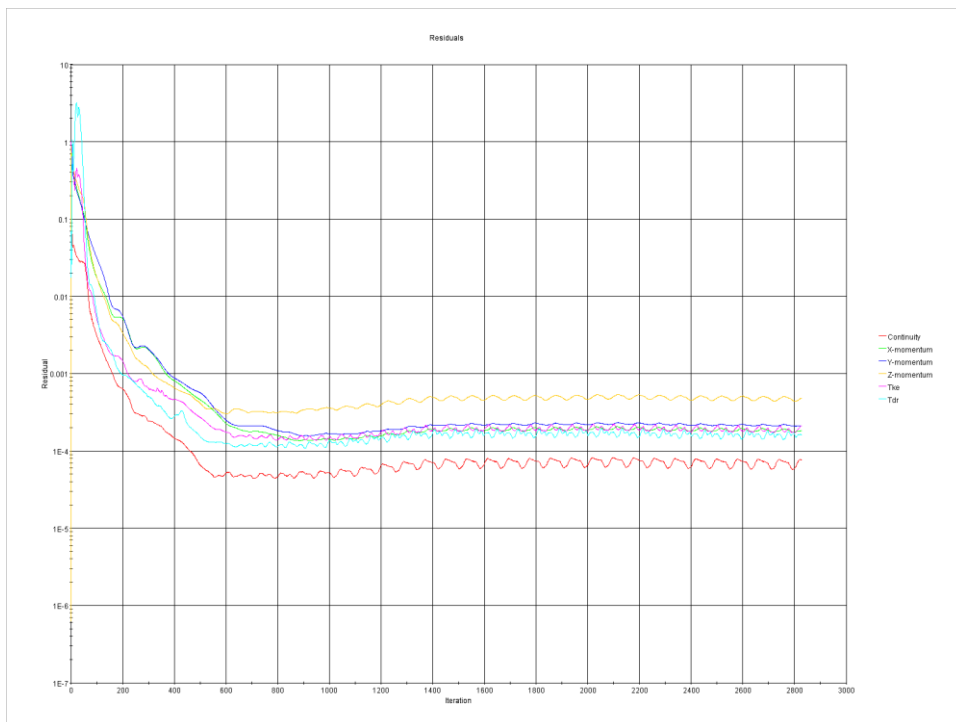


Figure 1: Convergence Residual Plot

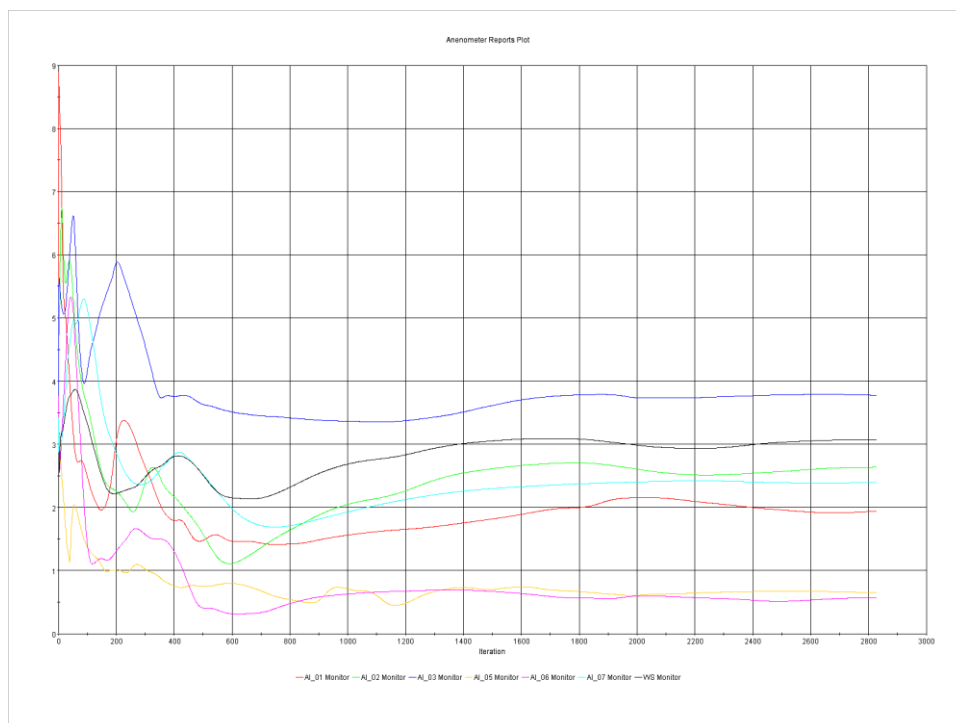


Figure 2: Convergence Anemometers' Simulated Wind Velocity Plot

NE-C	Approaching Wind Direction	Grid Resolution
	Northeast	Coarse

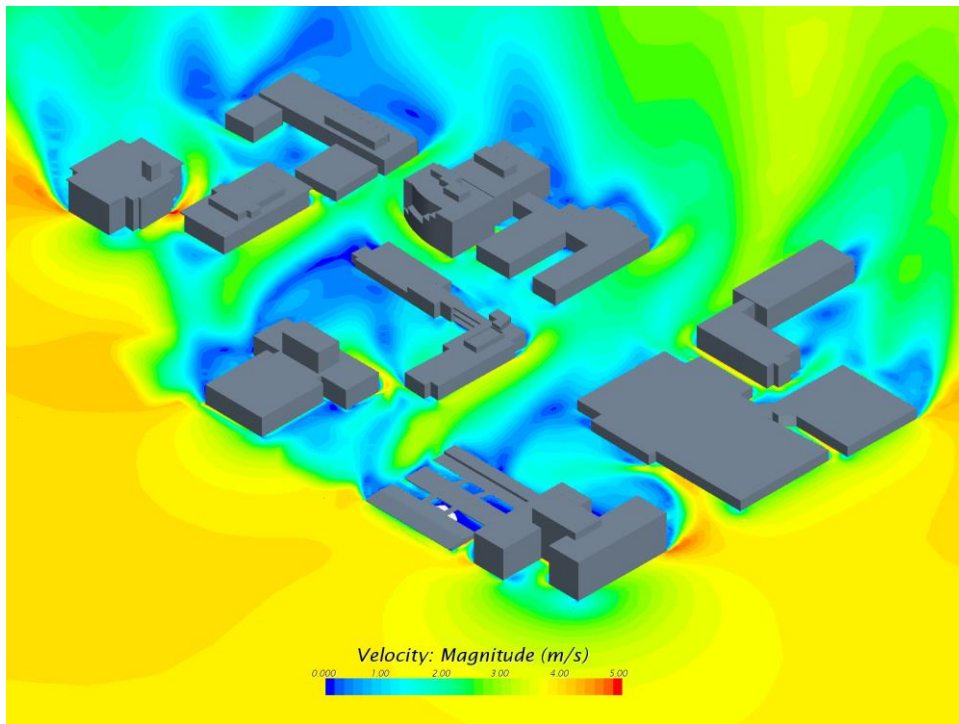


Figure 3: Overall Isometric View (from NE) of Wind Velocity Contour Map*,**

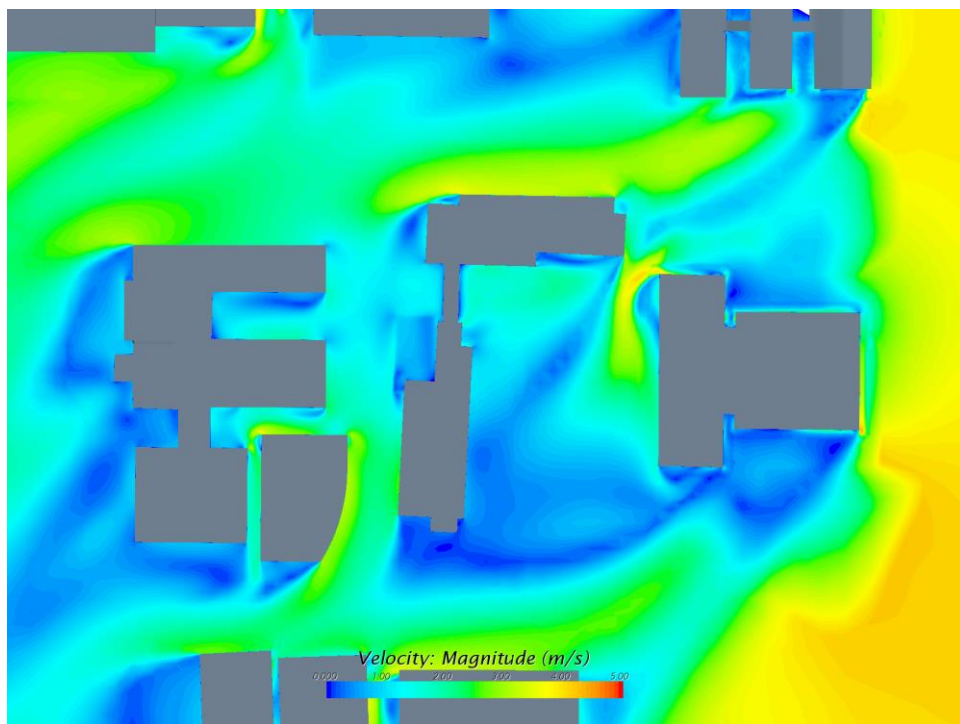


Figure 4: Plan View of Detailed Wind Velocity Contour Map*,** around Keller Hall
 *On the horizontal plane at 1m height above finishing level of the 1st floor.
 ** The minimum and maximum value of the above legend ranges do not indicate the minimum and maximum values of those maps.

NE-C	Approaching Wind Direction	Grid Resolution
	Northeast	Coarse

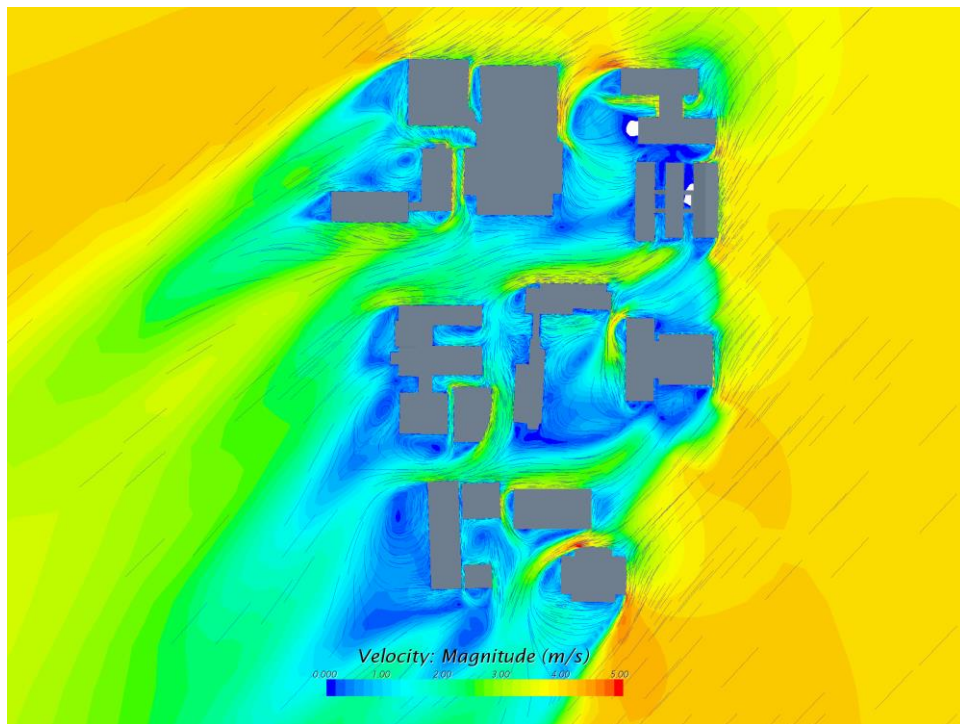


Figure 5: Plan View of Overall Wind Velocity Streamline Map*,**

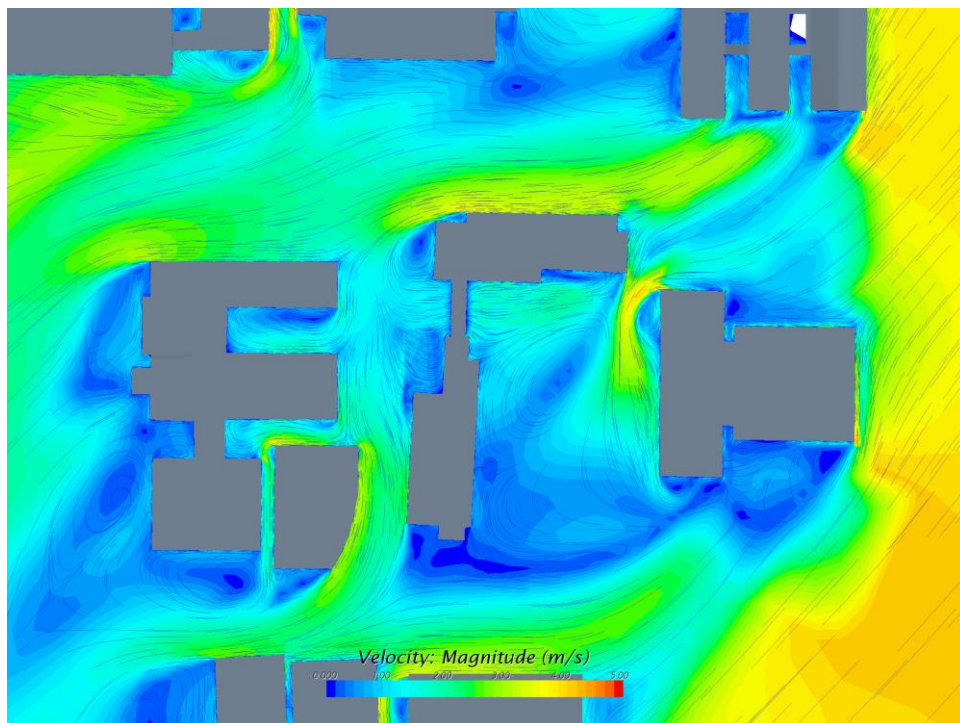


Figure 6: Plan View of Detailed Wind Velocity Stream Map*,** around Keller Hall

*On the horizontal plane at 1m height above finishing level of the 1st floor.

** The minimum and maximum value of the above legend ranges do not indicate the minimum and maximum values of those maps.

NE-C	Approaching Wind Direction	Grid Resolution
	Northeast	Coarse

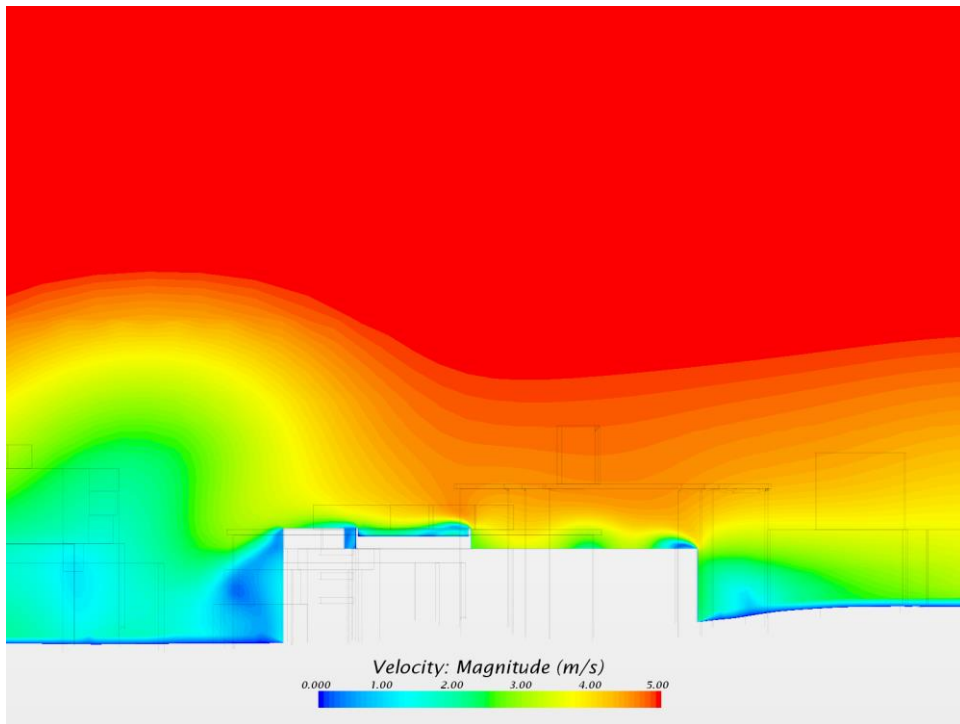


Figure 7: Detailed Wind Velocity Contour Map* on Cross Section Along Long Axis of Keller Hall

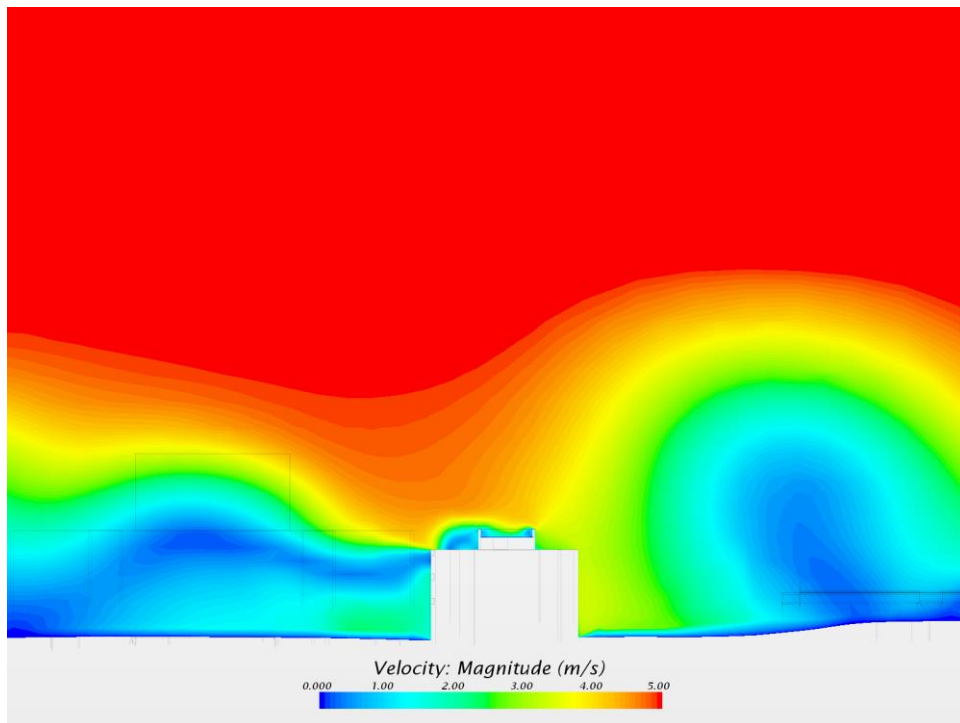


Figure 8: Detailed Wind Velocity Contour Map* on Cross Section Along Short Axis of Keller Hall

* The minimum and maximum value of the above legend ranges do not indicate the minimum and maximum values of those maps.

NE-C	Approaching Wind Direction	Grid Resolution
	Northeast	Coarse

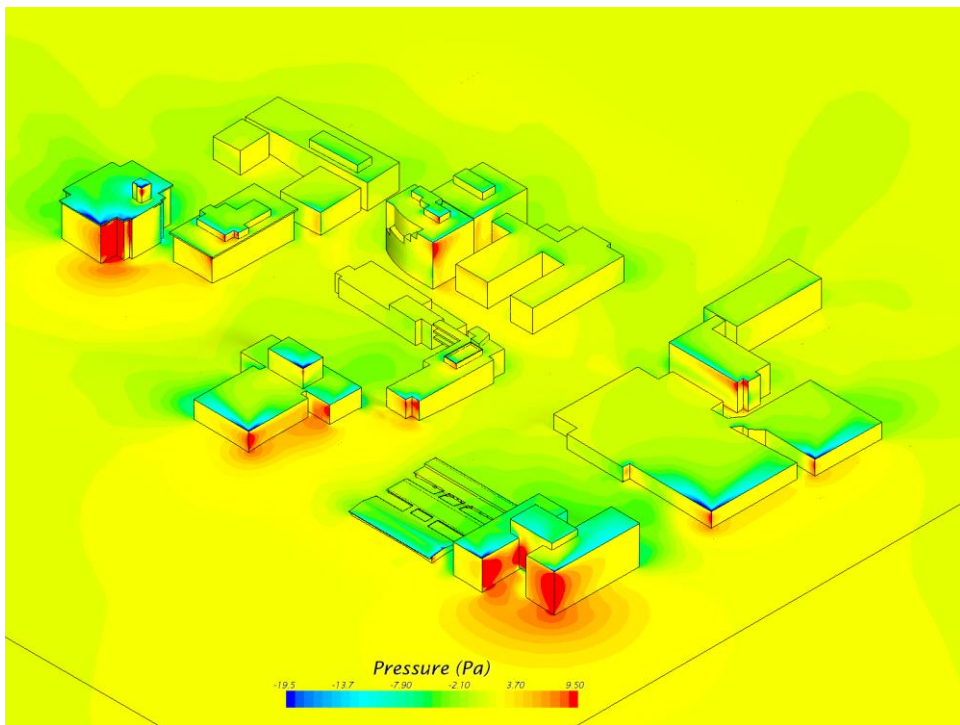


Figure 9: Overall Isometric View (from NE) of Wind-Induced Pressure Distribution* on Building Facades

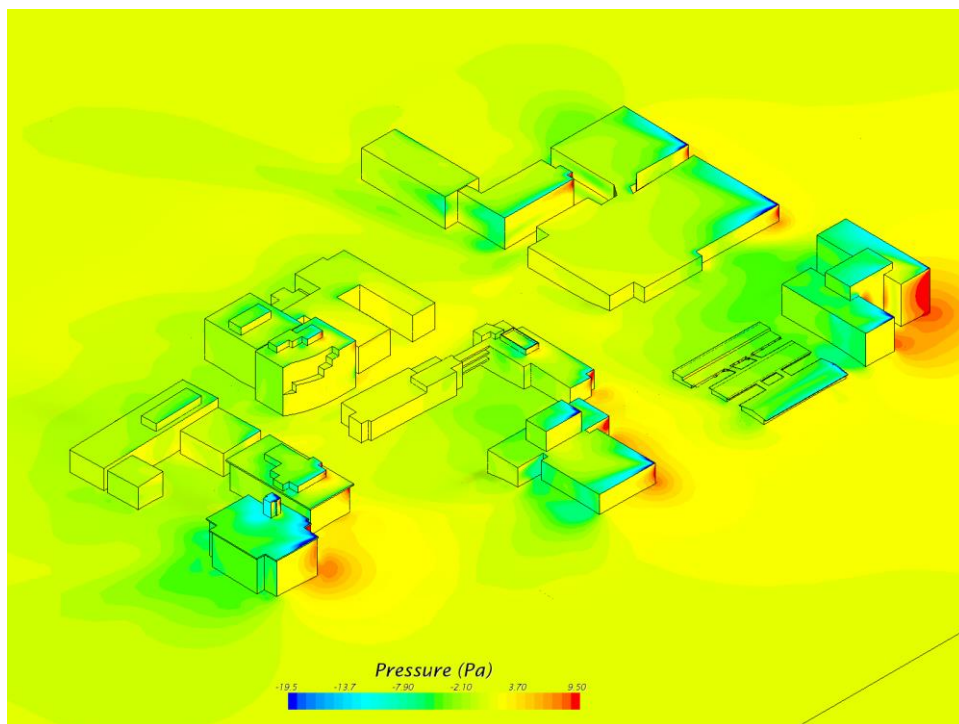


Figure 10: Overall Isometric View (from SE) of Wind-Induced Pressure Distribution* on Building Facades

* The minimum and maximum value of the above legend ranges do not indicate the minimum and maximum values of those maps.

NE-C	Approaching Wind Direction	Grid Resolution
	Northeast	Coarse

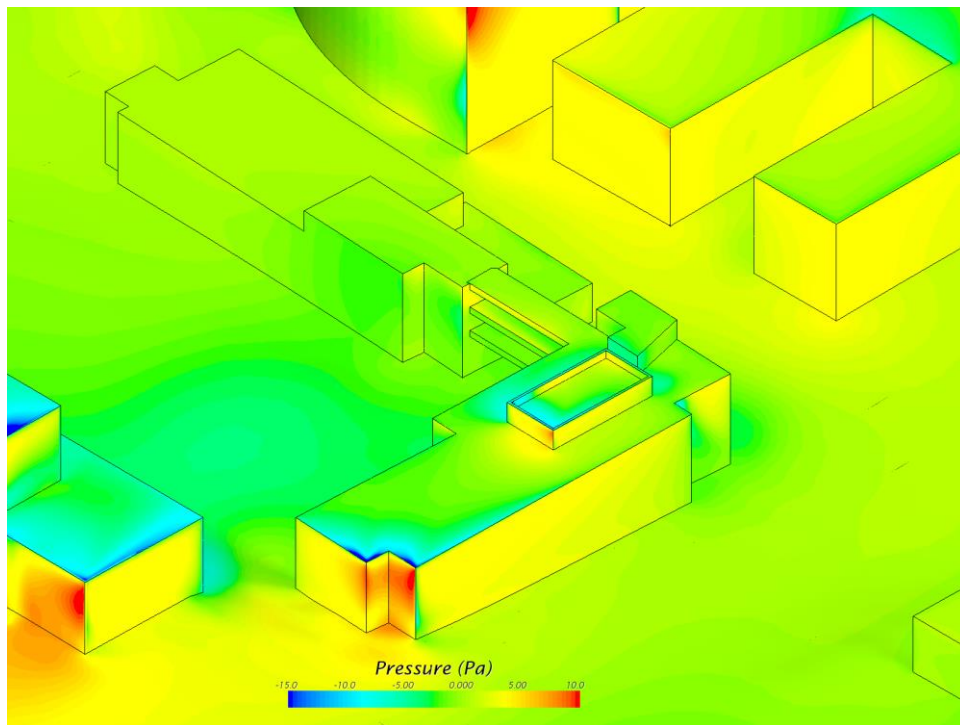


Figure 11: Detailed Isometric View (from NE) of Wind-Induced Pressure Distribution* on Keller Hall's Facades

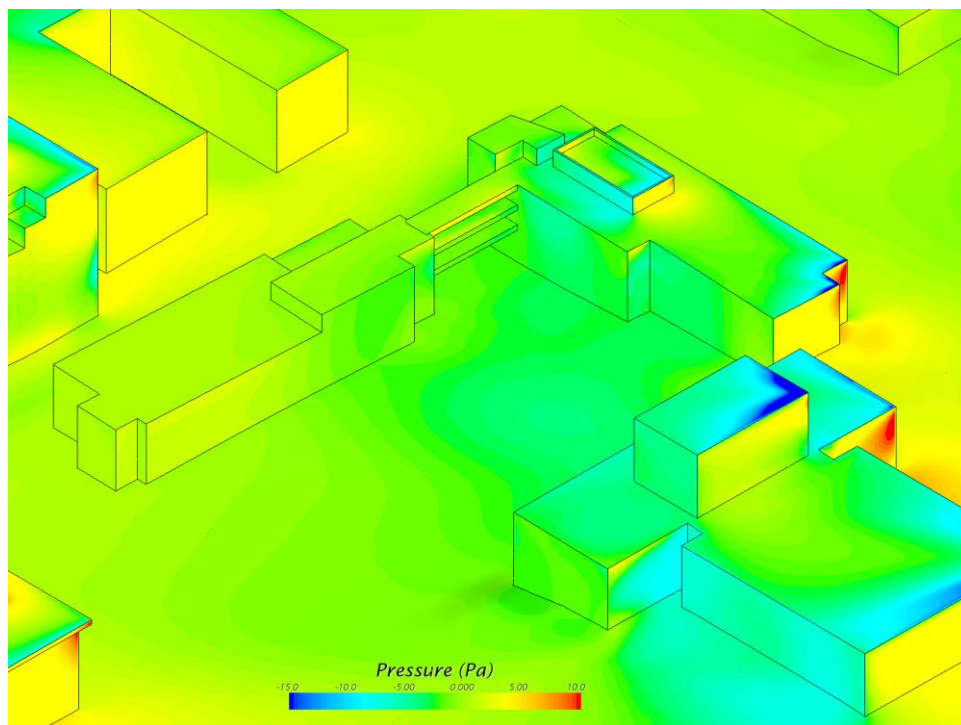


Figure 12: Detailed Isometric View (from SE) of Wind-Induced Pressure Distribution* on Keller Hall's Facades

* The minimum and maximum value of the above legend ranges do not indicate the minimum and maximum values of those maps.

NE-M	Approaching Wind Direction	Grid Resolution
	Northeast	Medium

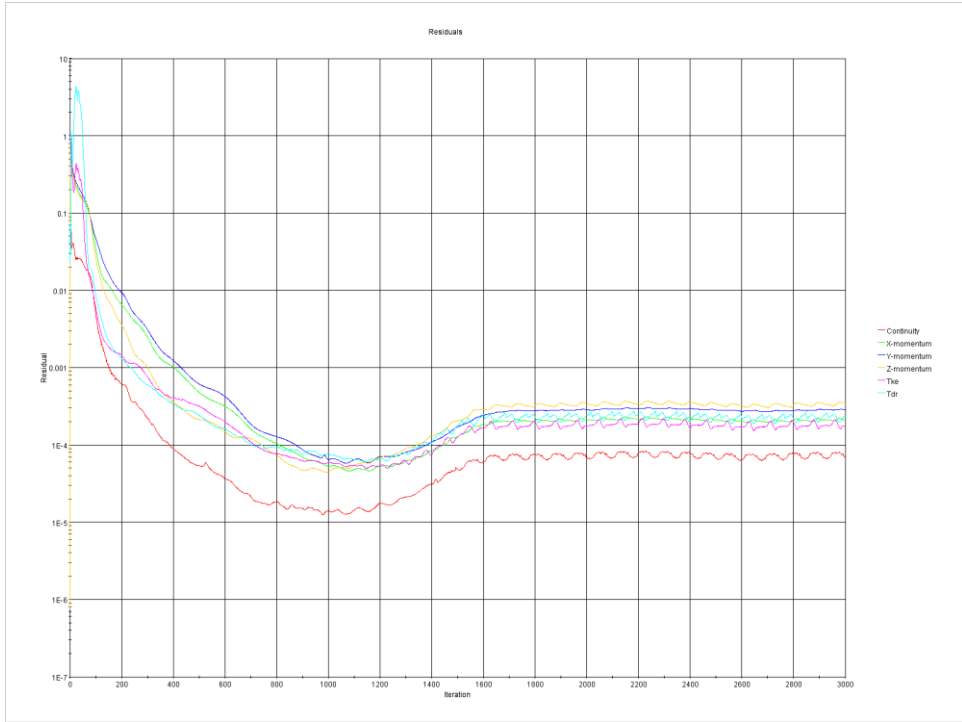


Figure 1: Convergence Residual Plot

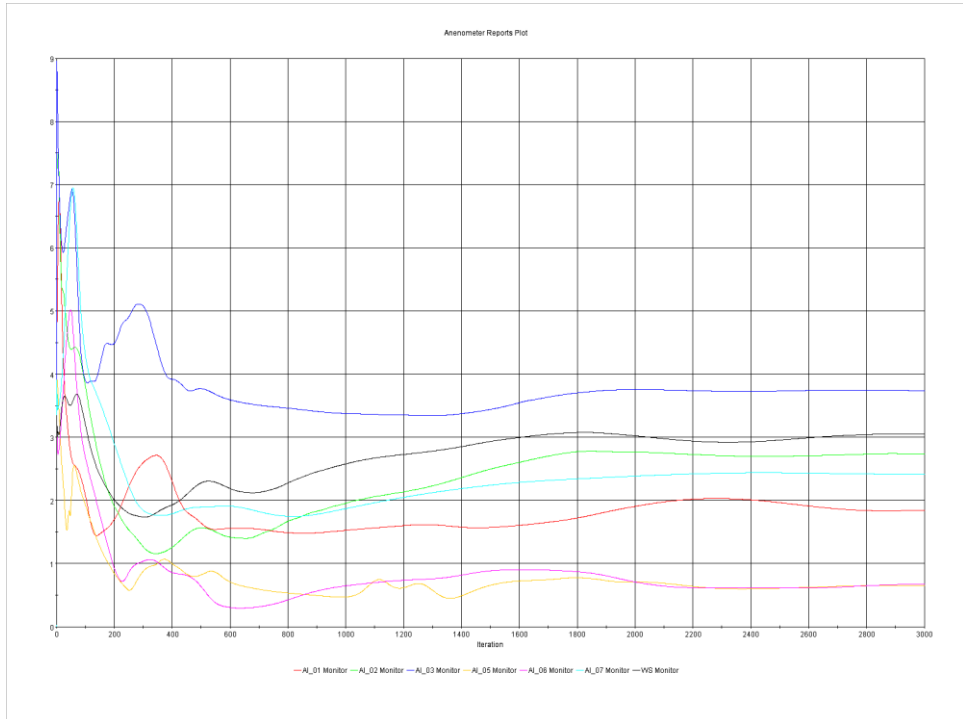


Figure 2: Convergence Anemometers' Simulated Wind Velocity Plot

NE-M	Approaching Wind Direction	Grid Resolution
	Northeast	Medium

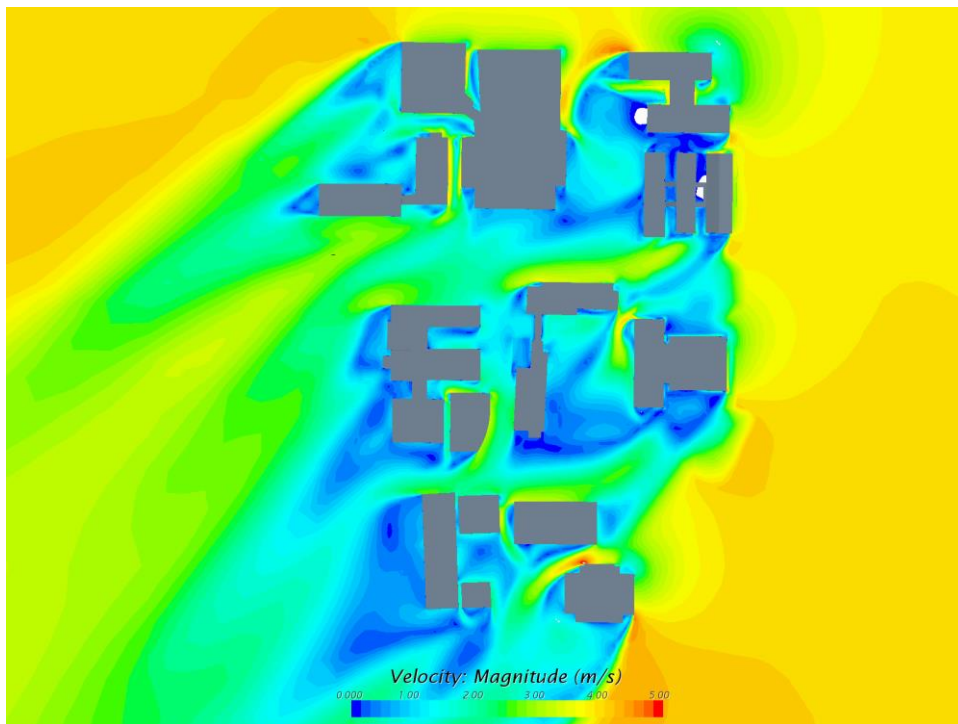


Figure 3: Overall Isometric View (from NE) of Wind Velocity Contour Map*,**

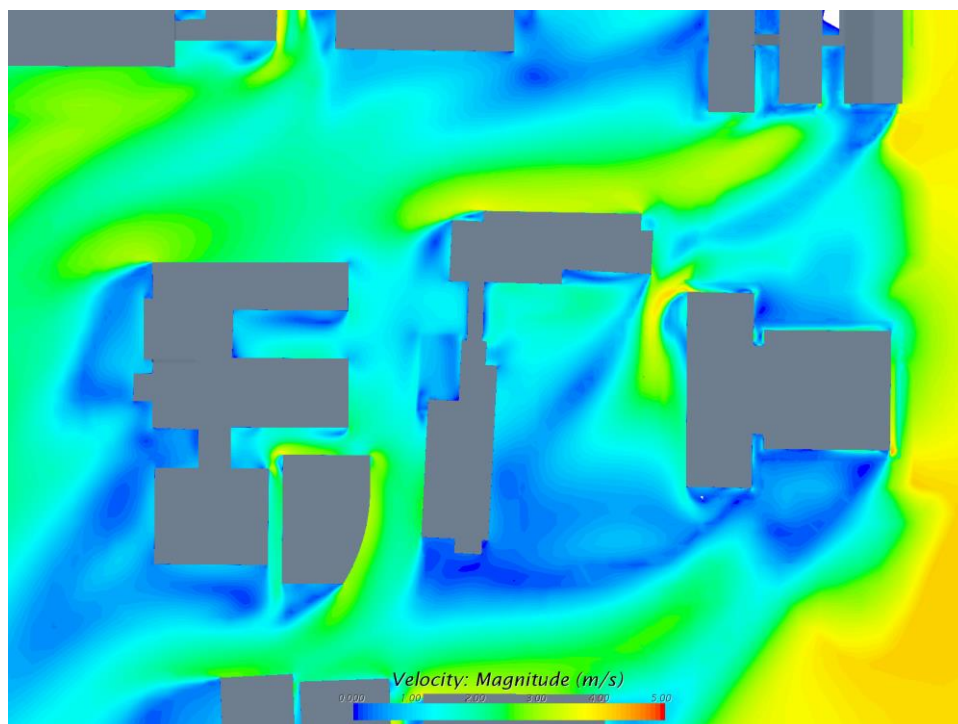


Figure 4: Plan View of Detailed Wind Velocity Contour Map*,** around Keller Hall

*On the horizontal plane at 1m height above finishing level of the 1st floor.

** The minimum and maximum value of the above legend ranges do not indicate the minimum and maximum values of those maps.

NE-M	Approaching Wind Direction	Grid Resolution
	Northeast	Medium

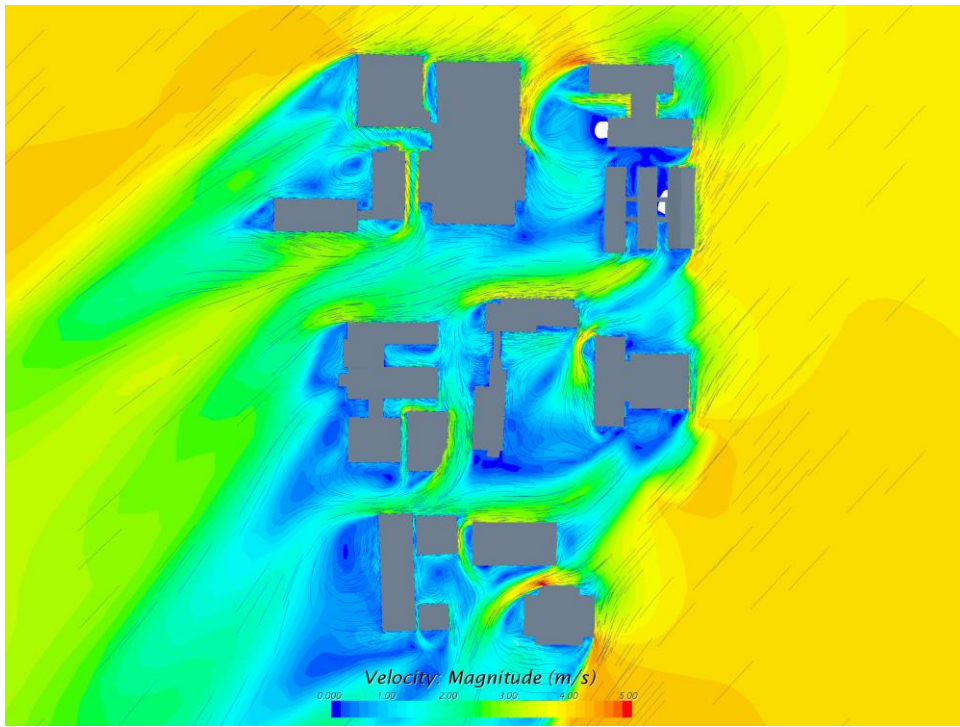


Figure 5: Plan View of Overall Wind Velocity Streamline Map*,**

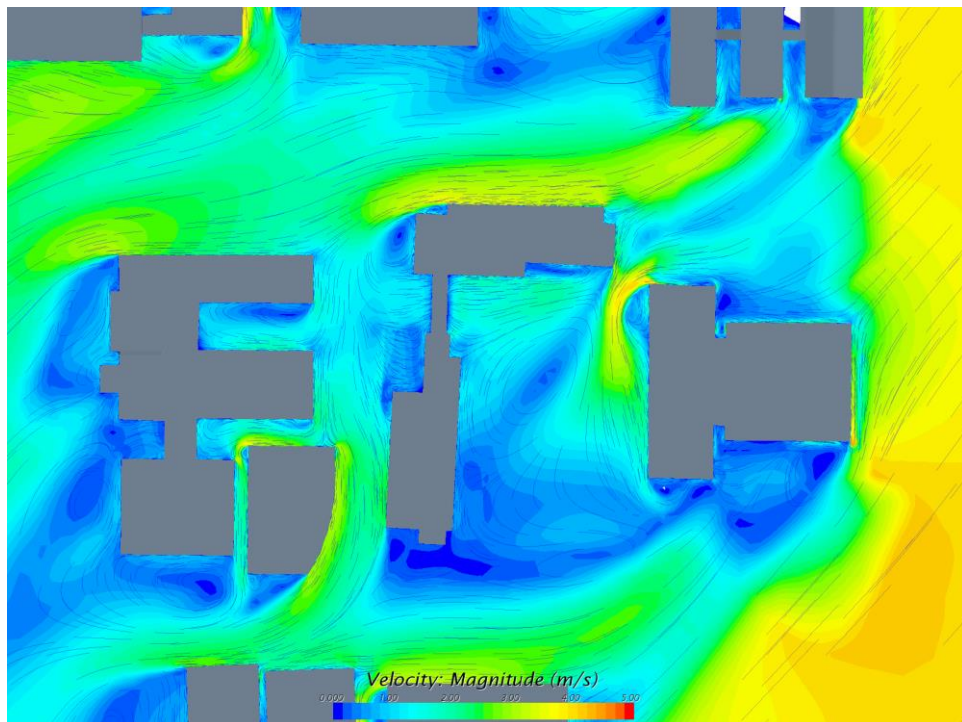


Figure 6: Plan View of Detailed Wind Velocity Stream Map*,** around Keller Hall

*On the horizontal plane at 1m height above finishing level of the 1st floor.

** The minimum and maximum value of the above legend ranges do not indicate the minimum and maximum values of those maps.

NE-M	Approaching Wind Direction	Grid Resolution
	Northeast	Medium

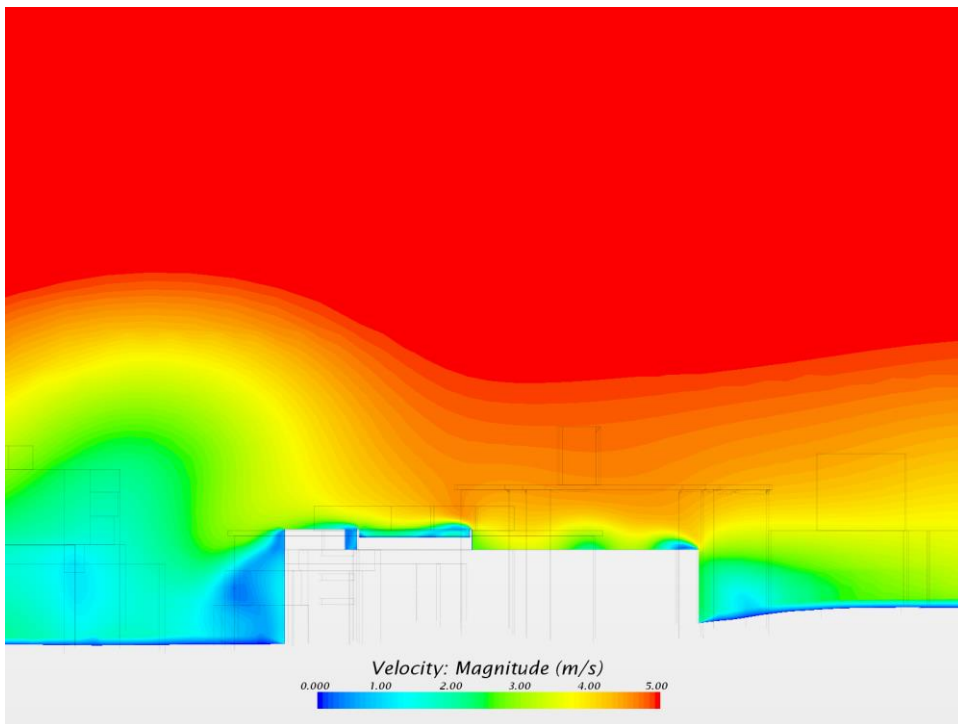


Figure 7: Detailed Wind Velocity Contour Map* on Cross Section Along Long Axis of Keller Hall

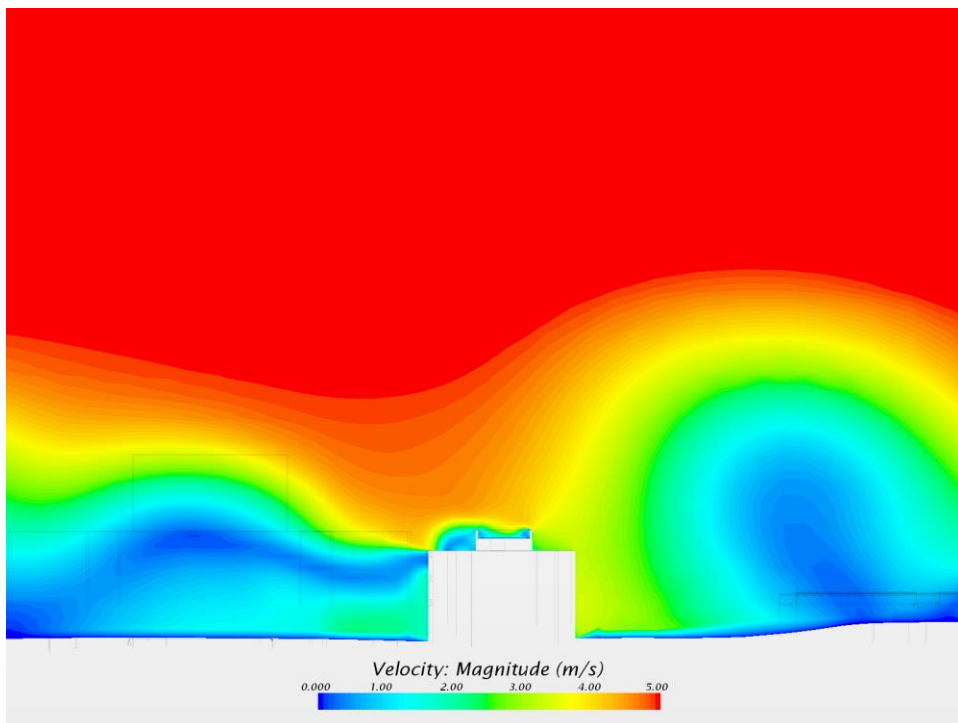


Figure 8: Detailed Wind Velocity Contour Map* on Cross Section Along Short Axis of Keller Hall

* The minimum and maximum value of the above legend ranges do not indicate the minimum and maximum values of those maps.

NE-M	Approaching Wind Direction	Grid Resolution
	Northeast	Medium

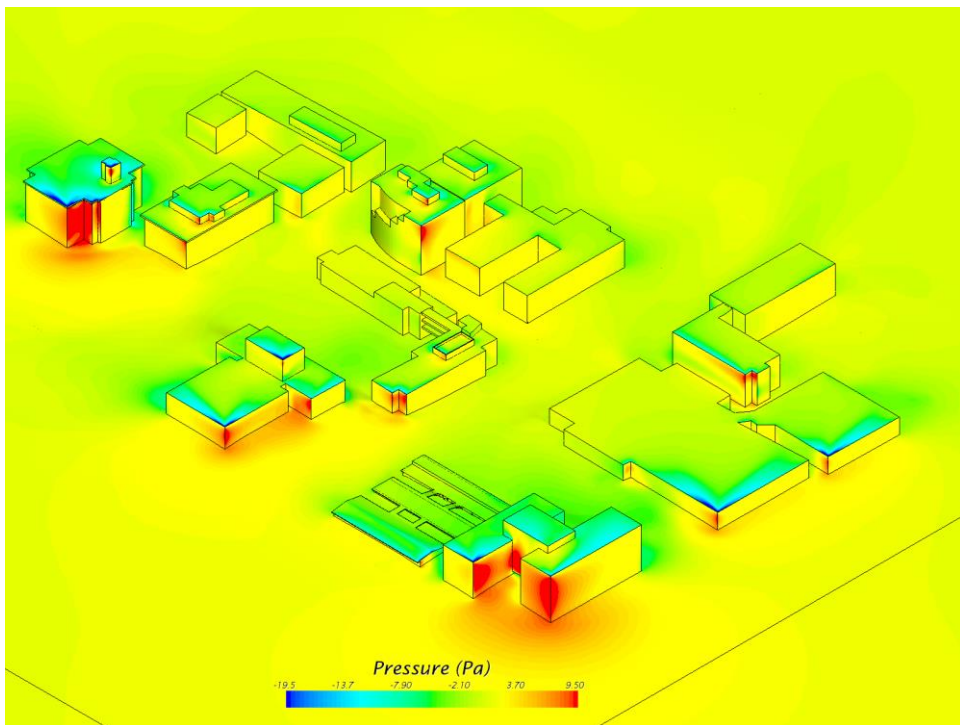


Figure 9: Overall Isometric View (from NE) of Wind-Induced Pressure Distribution* on Building Facades

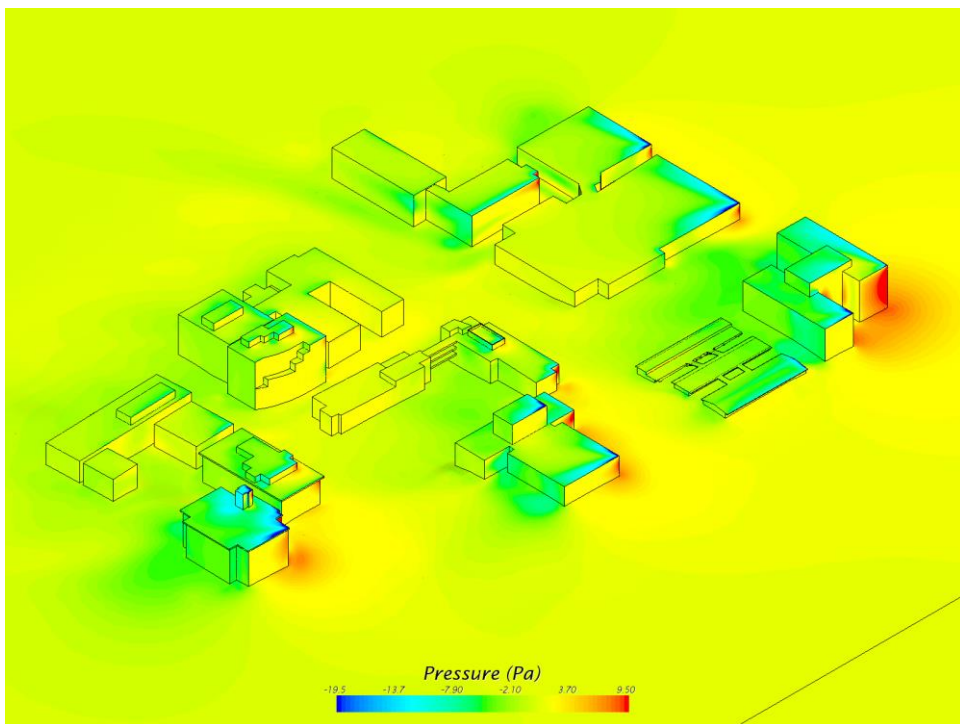


Figure 10: Overall Isometric View (from SE) of Wind-Induced Pressure Distribution* on Building Facades

* The minimum and maximum value of the above legend ranges do not indicate the minimum and maximum values of those maps.

NE-M	Approaching Wind Direction	Grid Resolution
	Northeast	Medium

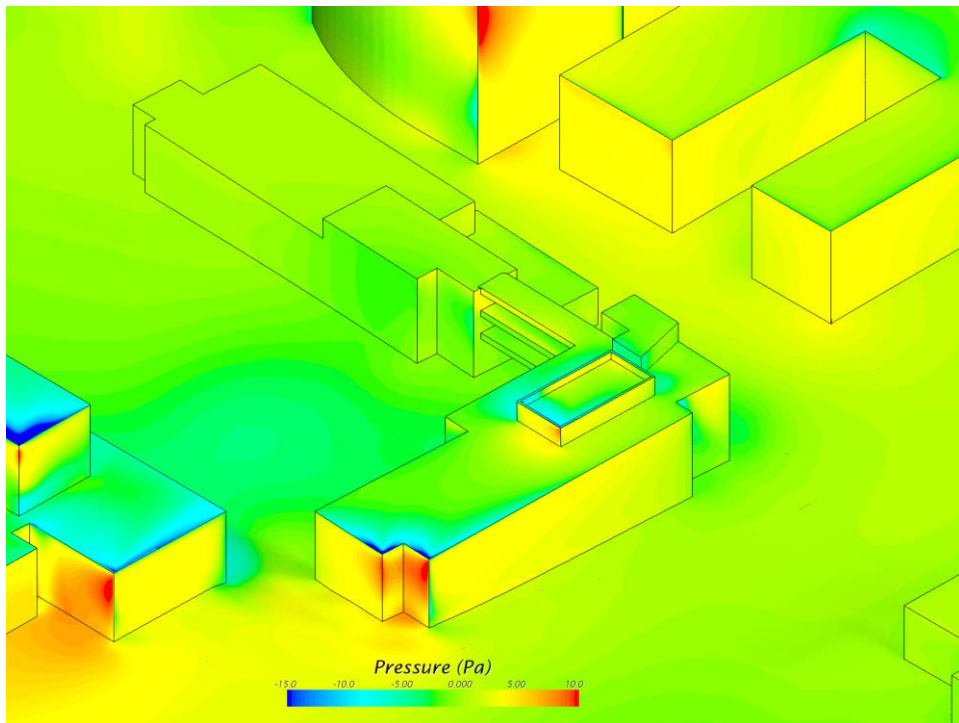


Figure 11: Detailed Isometric View (from NE) of Wind-Induced Pressure Distribution* on Keller Hall's Facades

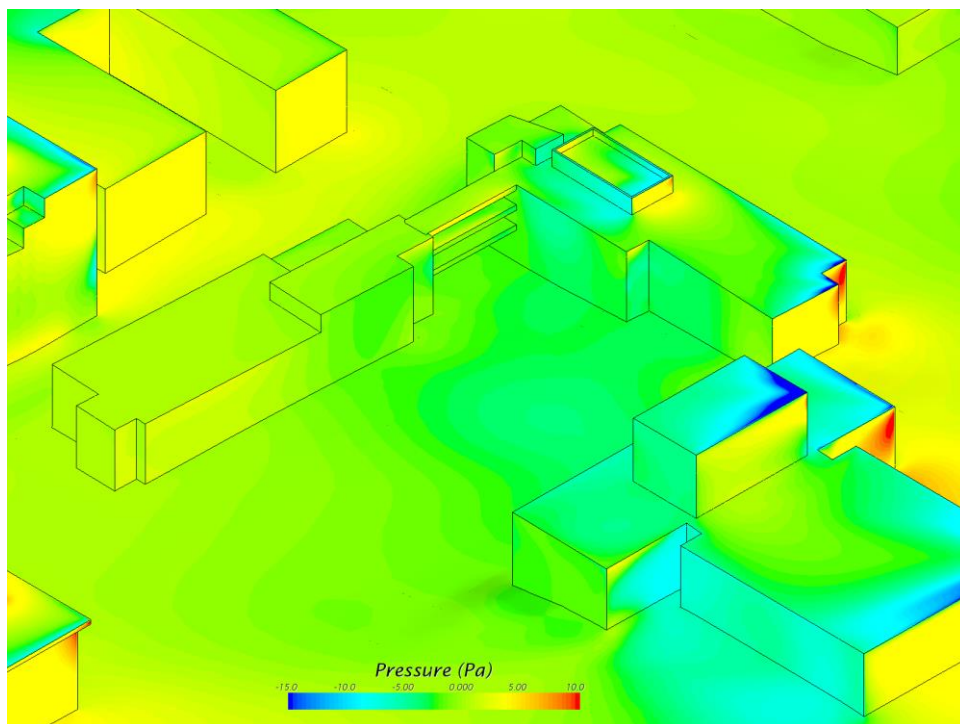


Figure 12: Detailed Isometric View (from SE) of Wind-Induced Pressure Distribution* on Keller Hall's Facades

* The minimum and maximum value of the above legend ranges do not indicate the minimum and maximum values of those maps.

NE-F	Approaching Wind Direction	Grid Resolution
	Northeast	Fine

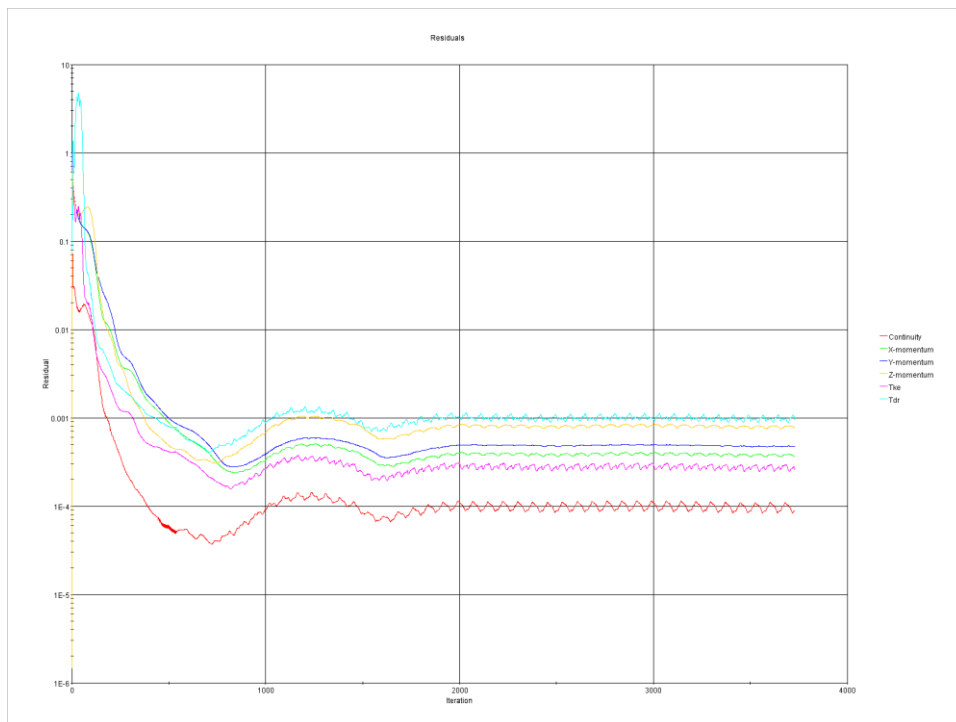


Figure 1: Convergence Residual Plot

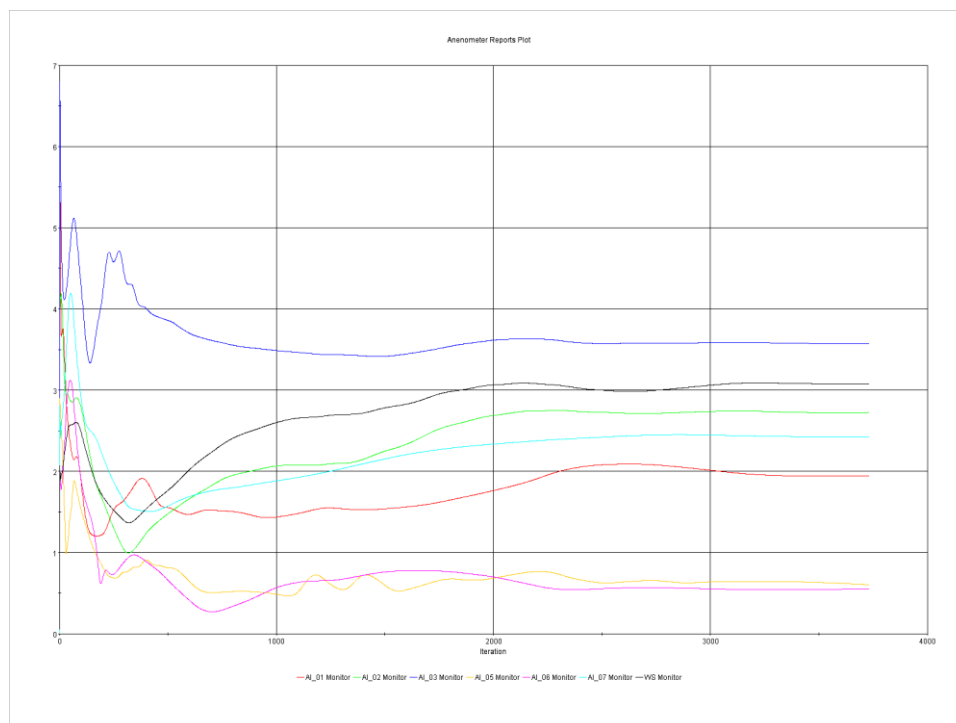


Figure 2: Convergence Anemometers' Simulated Wind Velocity Plot

NE-F	Approaching Wind Direction	Grid Resolution
	Northeast	Fine

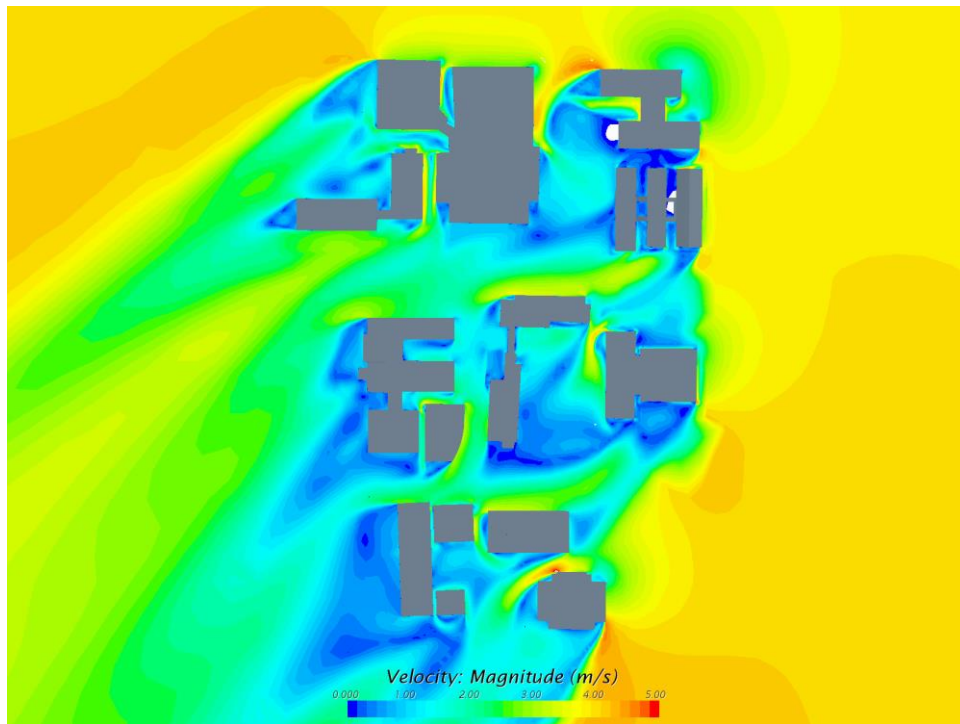


Figure 3: Overall Isometric View (from NE) of Wind Velocity Contour Map*,**

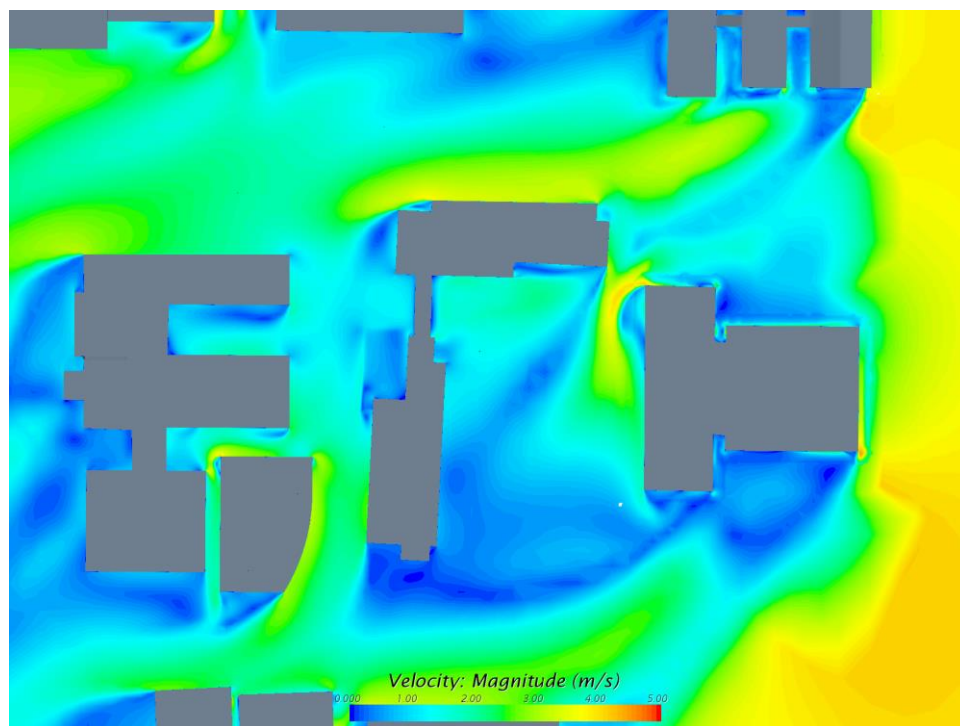


Figure 4: Plan View of Detailed Wind Velocity Contour Map*,** around Keller Hall

*On the horizontal plane at 1m height above finishing level of the 1st floor.

** The minimum and maximum value of the above legend ranges do not indicate the minimum and maximum values of those maps.

NE-F	Approaching Wind Direction	Grid Resolution
	Northeast	Fine

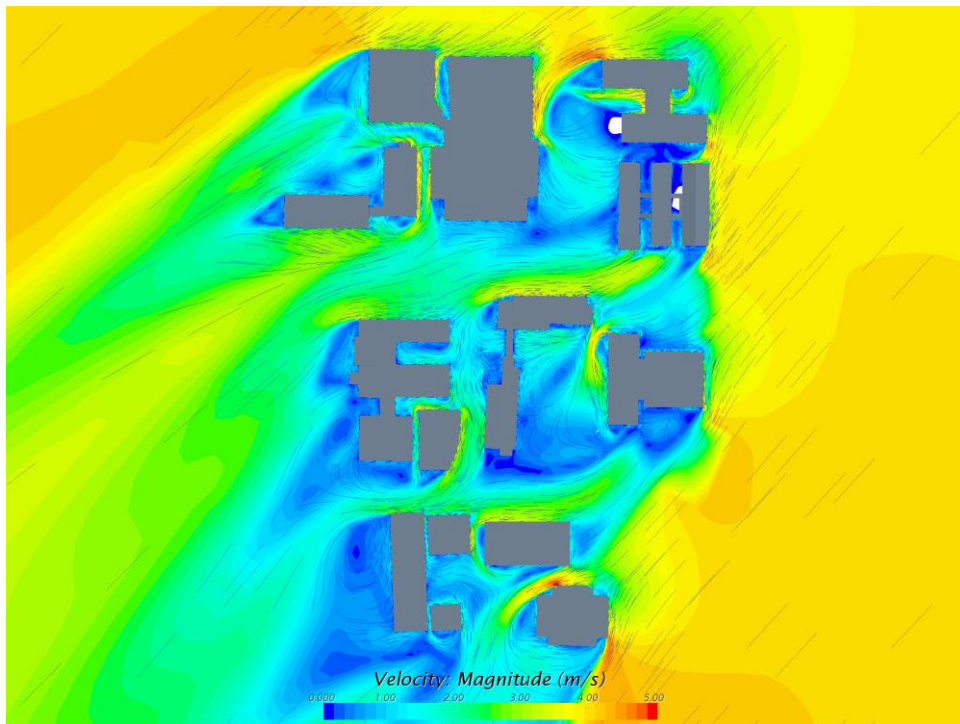


Figure 5: Plan View of Overall Wind Velocity Streamline Map*,**

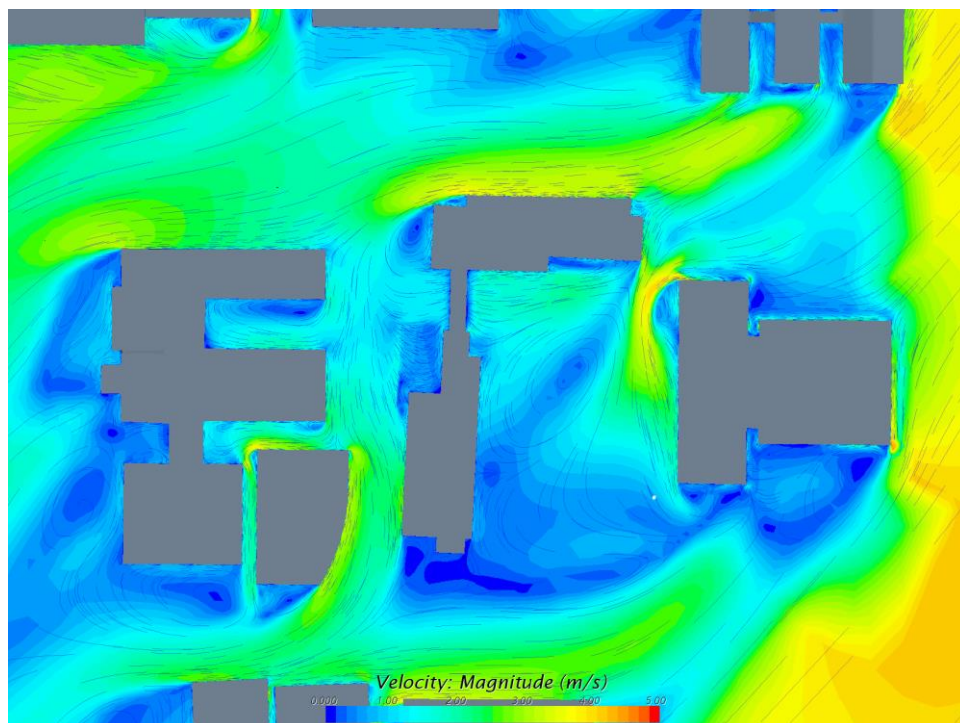


Figure 6: Plan View of Detailed Wind Velocity Stream Map*,** around Keller Hall

*On the horizontal plane at 1m height above finishing level of the 1st floor.

** The minimum and maximum value of the above legend ranges do not indicate the minimum and maximum values of those maps.

NE-F	Approaching Wind Direction	Grid Resolution
	Northeast	Fine

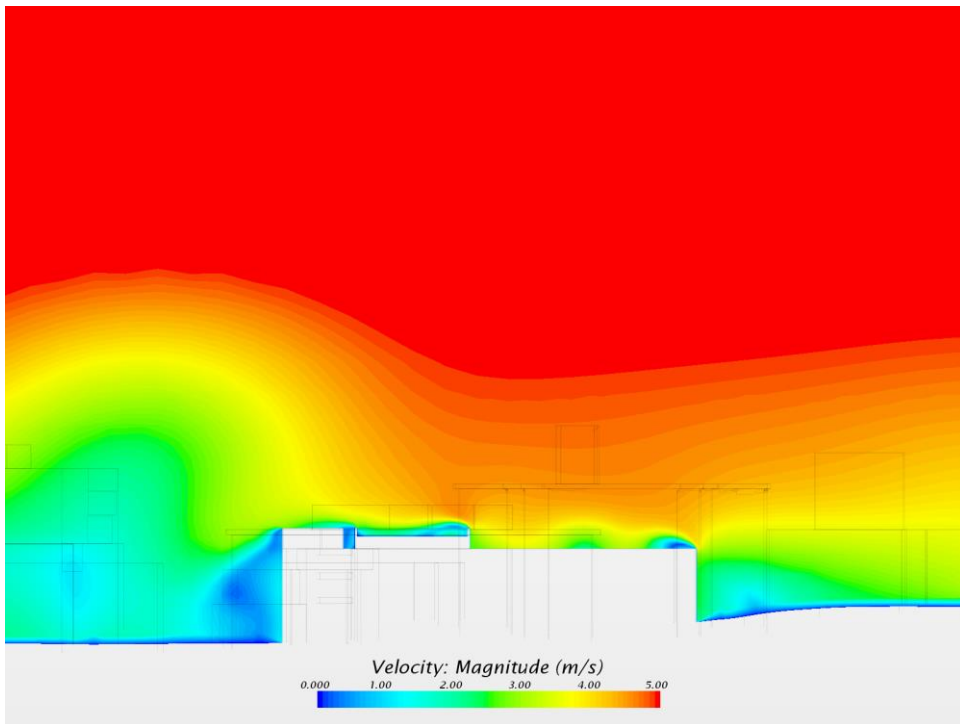


Figure 7: Detailed Wind Velocity Contour Map* on Cross Section Along Long Axis of Keller Hall

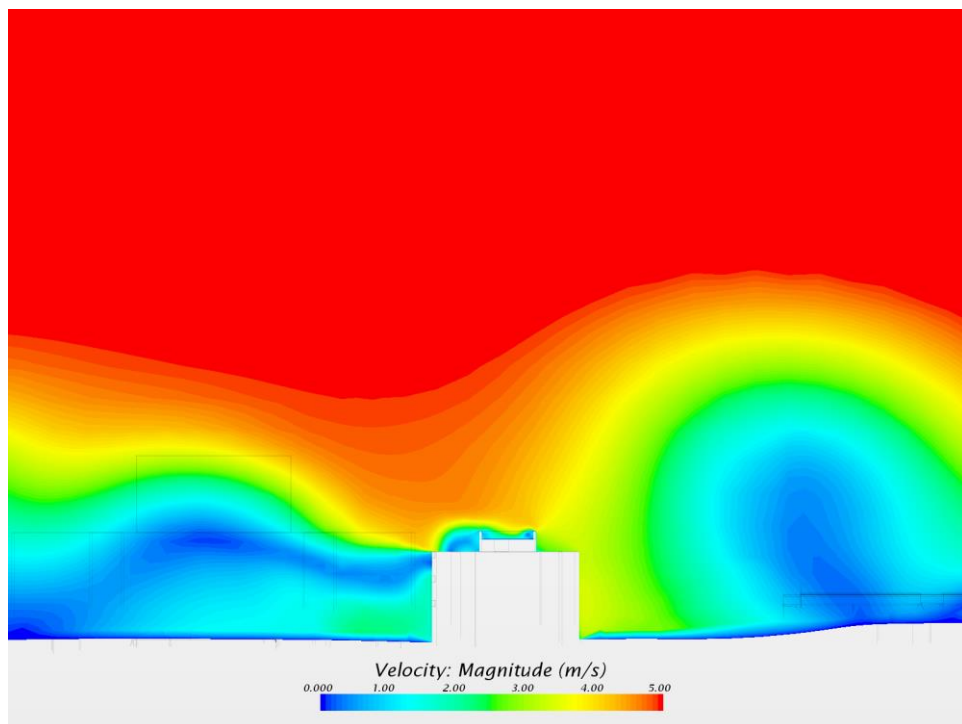


Figure 8: Detailed Wind Velocity Contour Map* on Cross Section Along Short Axis of Keller Hall

* The minimum and maximum value of the above legend ranges do not indicate the minimum and maximum values of those maps.

NE-F	Approaching Wind Direction	Grid Resolution
	Northeast	Fine

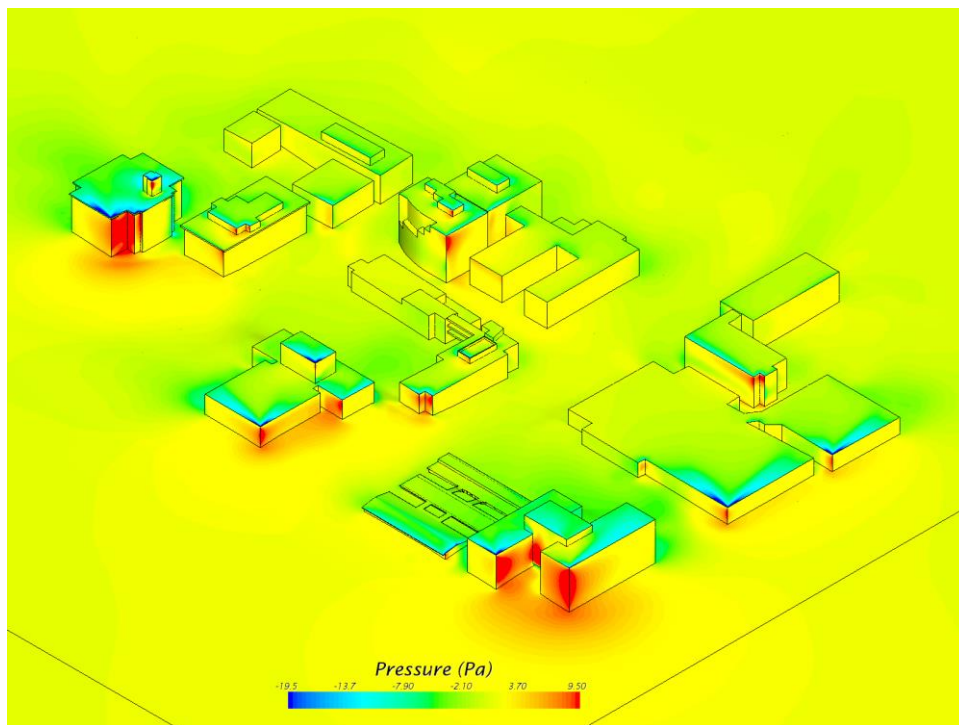


Figure 9: Overall Isometric View (from NE) of Wind-Induced Pressure Distribution* on Building Facades

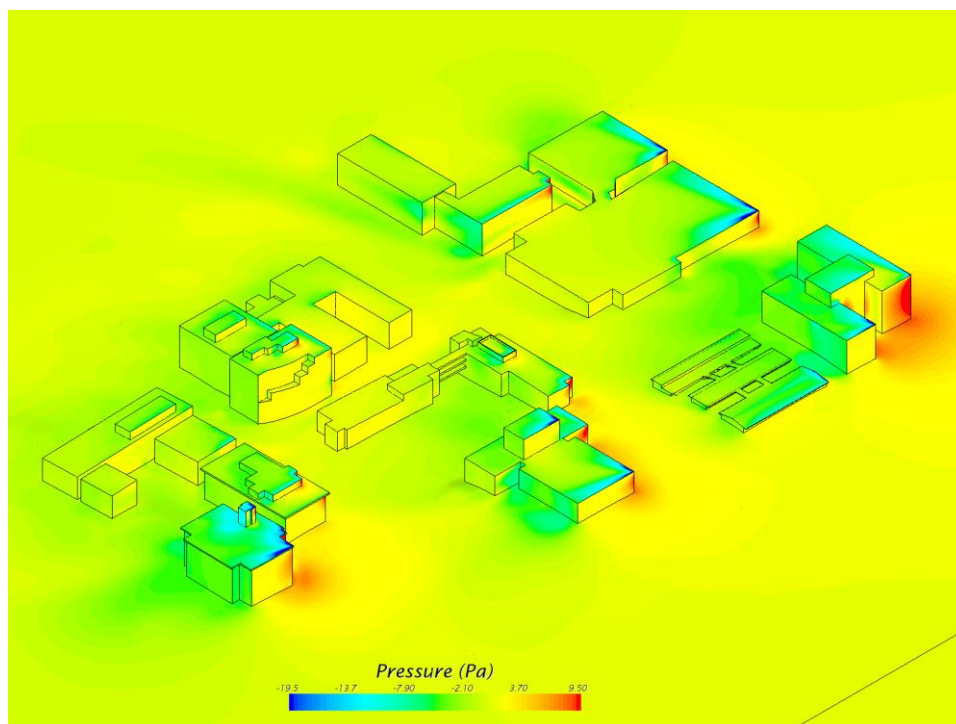


Figure 10: Overall Isometric View (from SE) of Wind-Induced Pressure Distribution* on Building Facades

* The minimum and maximum value of the above legend ranges do not indicate the minimum and maximum values of those maps.

NE-F	Approaching Wind Direction	Grid Resolution
	Northeast	Fine

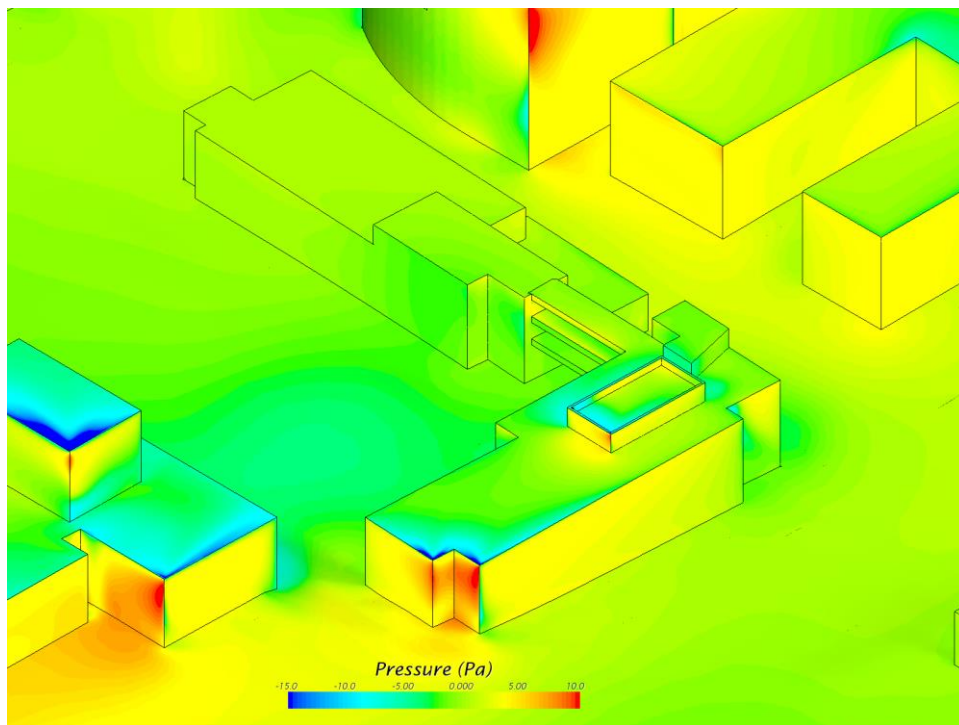


Figure 11: Detailed Isometric View (from NE) of Wind-Induced Pressure Distribution* on Keller Hall's Facades

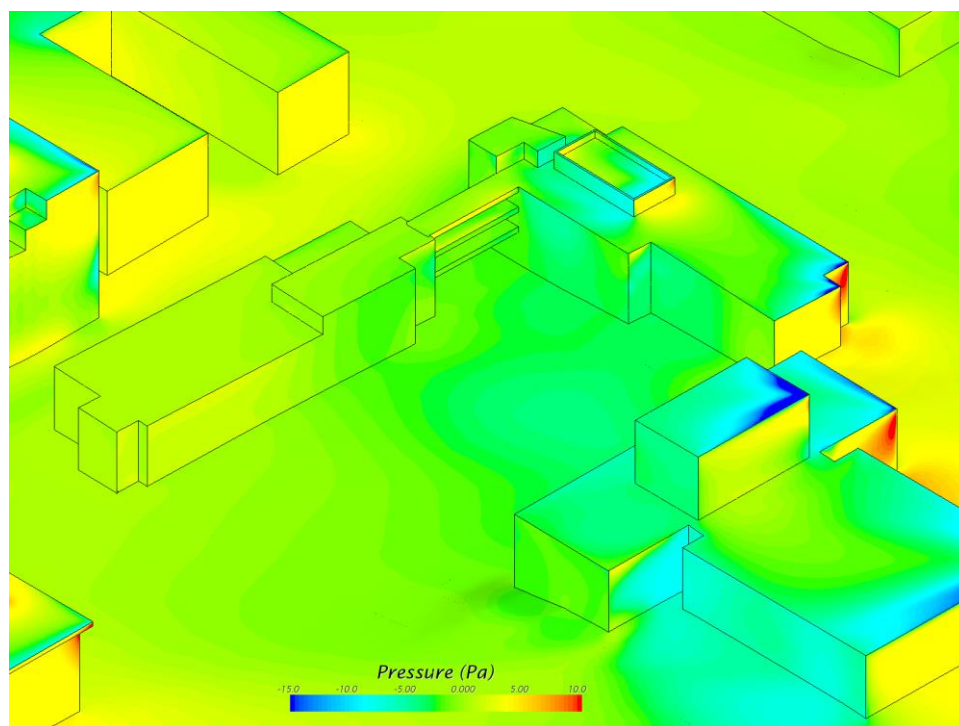


Figure 12: Detailed Isometric View (from SE) of Wind-Induced Pressure Distribution* on Keller Hall's Facades

* The minimum and maximum value of the above legend ranges do not indicate the minimum and maximum values of those maps.

APPENDIX B: INSTRUMENTATION USED IN THE FIELD TEST

Appendix B. Instrumentation

Equipment Specification Sheets are included in this appendix. Further information can be found at websites:

- National Instruments USB-6341
 - <http://sine.ni.com/nips/cds/view/p/lang/en/nid/209069>
- Onset HOBO U12 portable data loggers
 - <http://www.onsetcomp.com/products/data-loggers/U12-data-loggers>
- Setra Air Pressure Transducer Model 264
 - <http://www.setra.com/products/pressure/low-differential-pressure-transducer-model-264/>
- Halstrup Walcher P26 pressure transducer
 - http://www.iag.co.at/uploads/tx_iagproducts/pdf_handbuch/P26.en.pdf
- Degree Controls Accusense F900-0-5-1-9-2 anemometer with the XS blade
 - <http://www.degreec.com/en/airflow-sensing-products/embedded-sensing-products/f900-airflow-sensors.html>
- Onset HOBO U30 weather station
 - <http://www.onsetcomp.com/products/data-loggers/u30-nrc>

NI 6341/6343 Specifications

Français Deutsch 日本語 한국어 简体中文
ni.com/manuals

Specifications listed below are typical at 25 °C unless otherwise noted. Refer to the *X Series User Manual* for more information about NI PCIe-6341/6343, NI PXIe-6341, and NI USB-6341/6343 devices.

Analog Input

Number of channels

NI 6341	8 differential or 16 single ended
NI 6343	16 differential or 32 single ended

ADC resolution..... 16 bits

DNL..... No missing codes guaranteed

INL..... Refer to the [AI Absolute Accuracy Table](#)

Sample rate

Maximum..... 500 kS/s single channel,
500 kS/s multichannel (aggregate)

Minimum..... No minimum

Timing accuracy..... 50 ppm of sample rate

Timing resolution..... 10 ns

Input coupling..... DC

Input range..... ± 10 V, ± 5 V, ± 1 V, ± 0.2 V

Maximum working voltage for analog inputs
(signal + common mode)..... ± 11 V of AI GND

CMRR (DC to 60 Hz)..... 100 dB

Input impedance

Device powered on

AI+ to AI GND..... >10 G Ω in parallel with 100 pF

AI- to AI GND..... >10 G Ω in parallel with 100 pF

Device powered off

AI+ to AI GND..... 1200 Ω

AI- to AI GND..... 1200 Ω

Input bias current..... ± 100 pA

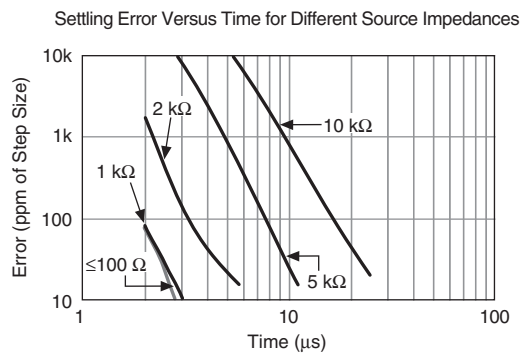


Crosstalk (at 100 kHz)	
Adjacent channels	-75 dB
Nonadjacent channels	-90 dB
Small signal bandwidth (-3 dB)	1.2 MHz
Input FIFO size	4,095 samples
Scan list memory	4,095 entries
Data transfers	
NI PCIe/PXIe-6341/6343	DMA (scatter-gather), programmed I/O
NI USB-6341/6343	USB Signal Stream, programmed I/O
Overvoltage protection (AI <0..31>, AI SENSE, AI SENSE 2)	
Device powered on	±25 V for up to two AI pins
Device powered off	±15 V for up to two AI pins
Input current during	
overvoltage condition	±20 mA max/AI pin

Settling Time for Multichannel Measurements

Accuracy, full scale step, all ranges	
±90 ppm of step (±6 LSB)	2 μ s convert interval
±30 ppm of step (±2 LSB)	3 μ s convert interval
±15 ppm of step (±1 LSB)	5 μ s convert interval
Analog triggers	None

Typical Performance Graph



Analog Output

Number of channels	
NI 6341	2
NI 6343	4
DAC resolution	16 bits
DNL	±1 LSB
Monotonicity	16 bit guaranteed
Maximum update rate (simultaneous)	
1 channel	900 kS/s
2 channels	840 kS/s per channel
3 channels	775 kS/s per channel
4 channels	719 kS/s per channel
Timing accuracy	50 ppm of sample rate
Timing resolution	10 ns
Output range	±10 V
Output coupling	DC
Output impedance	0.2 Ω
Output current drive	±5 mA
Overdrive protection	±15 V
Overdrive current	15 mA
Power-on state	±20 mV
Power-on/off glitch	
NI PCIe/PXIE-6341/6343	2 V for 500 ms
NI USB-6341/6343	1.5 V for 1.2 s ¹
Output FIFO size	8,191 samples shared among channels used
Data transfers	
NI PCIe/PXIE-6341/6343	DMA (scatter-gather), programmed I/O
NI USB-6341/6343	USB Signal Stream, programmed I/O
AO waveform modes:	
• Non-periodic waveform	
• Periodic waveform regeneration mode from onboard FIFO	
• Periodic waveform regeneration from host buffer including dynamic update	

¹ Typical behavior. Time period may be longer due to host system USB performance. Time period will be longer during firmware updates.

Settling time, full scale step	
15 ppm (1 LSB)	6 μ s
Slew rate	15 V/ μ s
Glitch energy	
Magnitude	100 mV
Duration	2.6 μ s

Calibration (AI and AO)

Recommended warm-up time	15 minutes
Calibration interval	2 years

AI Absolute Accuracy Table

Nominal Range		Residual Gain Error (ppm of Reading)	Gain Tempco (ppm/°C)	Reference Tempco (ppm/°C)	Residual Offset Error (ppm of Range)	Offset Tempco (ppm of Range/°C)	INLError (ppm of Range)	Random Noise, σ (μVrms)	Absolute Accuracy at Full Scale ¹ (μV)
Positive Full Scale	Negative Full Scale								
10	-10	65	7.3	5	13	23	60	270	2190
5	-5	72	7.3	5	13	23	60	135	1130
1	-1	78	7.3	5	17	26	60	28	240
0.2	-0.2	105	7.3	5	27	39	60	9	60

AbsoluteAccuracy = Reading · (GainError) + Range · (OffsetError) + NoiseUncertainty

GainError = ResidualGainError + GainTempco · (TempChangeFromLastInternalCal) + ReferenceTempco · (TempChangeFromLastExternalCal)

OffsetError = ResidualOffsetError + OffsetTempco · (TempChangeFromLastInternalCal) + INL_Error

NoiseUncertainty = $\frac{\text{RandomNoise} \cdot 3}{\sqrt{10,000}}$ For a coverage factor of 3 σ and averaging 10,000 points.

¹ Absolute accuracy at full scale on the analog input channels is determined using the following assumptions:

TempChangeFromLastExternalCal = 10 °C

TempChangeFromLastInternalCal = 1 °C

number_of_readings = 10,000

CoverageFactor = 3 σ

For example, on the 10 V range, the absolute accuracy at full scale is as follows:

GainError = 65 ppm + 7.3 ppm · 1 + 5 ppm · 10 GainError = 122 ppm

OffsetError = 13 ppm + 23 ppm · 1 + 60 ppm OffsetError = 96 ppm

NoiseUncertainty = $\frac{270 \mu\text{V} \cdot 3}{\sqrt{10,000}}$ Noise Uncertainty = 8.1 μV

AbsoluteAccuracy = 10 V · (GainError) + 10 V · (OffsetError) + NoiseUncertainty

AbsoluteAccuracy = 2,190 μV

Accuracies listed are valid for up to two years from the device external calibration.

AO Absolute Accuracy Table

Nominal Range		Residual Gain Error (ppm of Reading)	Gain Tempco (ppm/°C)	Reference Tempco (ppm/°C)	Residual Offset Error (ppm of Range)	Offset Tempco (ppm of Range/°C)	INL Error (ppm of Range)	Absolute Accuracy at Full Scale ¹ (μV)
Positive Full Scale	Negative Full Scale							
10	-10	80	11.3	5	53	4.8	128	3,271

¹ Absolute Accuracy at full scale numbers is valid immediately following internal calibration and assumes the device is operating within 10 °C of the last external calibration.

Accuracies listed are valid for up to two years from the device external calibration.

AbsoluteAccuracy = OutputValue · (GainError) + Range · (OffsetError)

GainError = ResidualGainError + GainTempco · (TempChangeFromLastInternalCal) + ReferenceTempco · (TempChangeFromLastExternalCal)

OffsetError = ResidualOffsetError + OffsetTempco · (TempChangeFromLastInternalCal) + INL_Error

Digital I/O/PFI

Static Characteristics

Number of channels	
NI 6341	24 total, 8 (P0.<0..7> 16 (PFI <0..7>/P1, PFI <8..15>/P2)
NI 6343	48 total, 32 (P0.<0..31> 16 (PFI <0..7>/P1, PFI <8..15>/P2)
Ground reference	D GND
Direction control	Each terminal individually programmable as input or output
Pull-down resistor	50 k Ω typical, 20 k Ω minimum
Input voltage protection ¹	± 20 V on up to two pins

Waveform Characteristics (Port 0 Only)

Terminals used	
NI 6341	Port 0 (P0.<0..7>)
NI 6343	Port 0 (P0.<0..31>)
Port/sample size	
NI 6341	Up to 8 bits
NI 6343	Up to 32 bits
Waveform generation (DO) FIFO	2,047 samples
Waveform acquisition (DI) FIFO	255 samples
DO or DI Sample Clock frequency	
NI PCIe/PXIe-6341/6343	0 to 1 MHz, system and bus activity dependent
NI USB-6341/6343	0 to 1 MHz, system and bus activity dependent
Data transfers	
NI PCIe/PXIe-6341/6343	DMA (scatter-gather), programmed I/O
NI USB-6341/6343	USB Signal Stream, programmed I/O
Digital line filter settings	160 ns, 10.24 μ s, 5.12 ms, disable

¹ Stresses beyond those listed under *Input voltage protection* may cause permanent damage to the device.

PFI/Port 1/Port 2 Functionality

Functionality	Static digital input, static digital output, timing input, timing output
Timing output sources.....	Many AI, AO, counter, DI, DO timing signals
Debounce filter settings	90 ns, 5.12 μ s, 2.56 ms, custom interval, disable; programmable high and low transitions; selectable per input

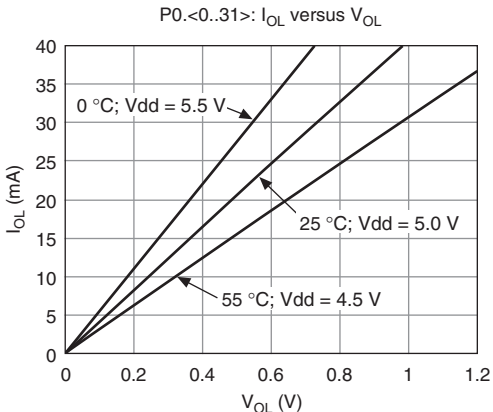
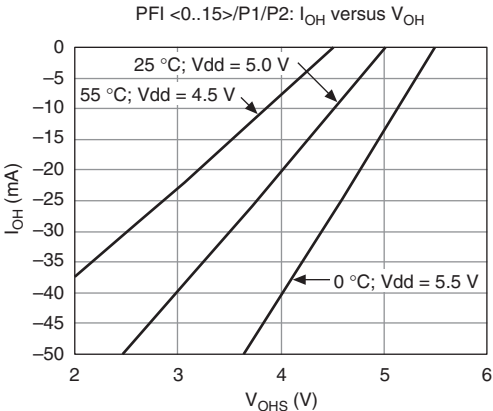
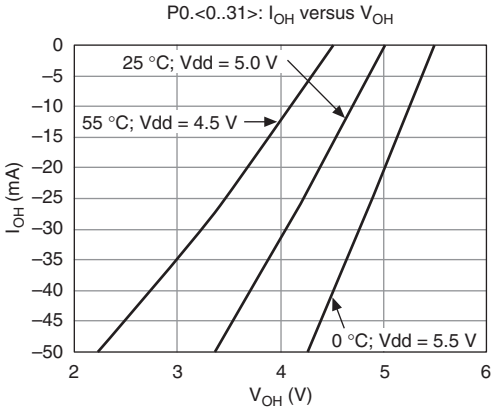
Recommended Operation Conditions

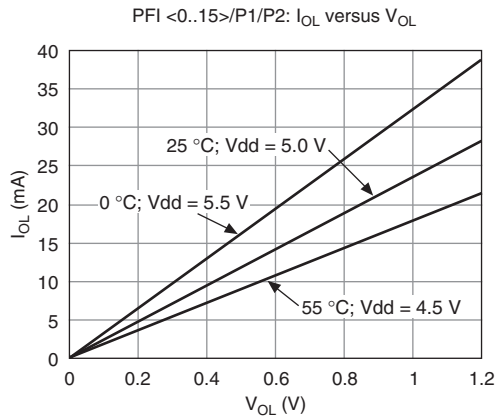
Level	Min	Max
Input high voltage (V_{IH})	2.2 V	5.25 V
Input low voltage (V_{IL})	0 V	0.8 V
Output high current (I_{OH}) P0.<0..31> PFI <0..15>/P1/P2	—	-24 mA -16 mA
Output low current (I_{OL}) P0.<0..31> PFI <0..15>/P1/P2	—	24 mA 16 mA

Electrical Characteristics

Level	Min	Max
Positive-going threshold (V_{T+})	—	2.2 V
Negative-going threshold (V_{T-})	0.8 V	—
Delta VT hysteresis ($V_{T+} - V_{T-}$)	0.2 V	—
I_{IL} input low current ($V_{in} = 0$ V)	—	-10 μ A
I_{IH} input high current ($V_{in} = 5$ V)	—	250 μ A

Digital I/O Characteristics





General-Purpose Counter/Timers

Number of counter/timers	4
Resolution	32 bits
Counter measurements	Edge counting, pulse, pulse width, semi-period, period, two-edge separation
Position measurements	X1, X2, X4 quadrature encoding with Channel Z reloading; two-pulse encoding
Output applications	Pulse, pulse train with dynamic updates, frequency division, equivalent time sampling
Internal base clocks	100 MHz, 20 MHz, 100 kHz
External base clock frequency	
NI PCIe/USB-6341/6343	0 MHz to 25 MHz
NI PXIe-6341	0 MHz to 25 MHz; 0 MHz to 100 MHz on PXIe-DSTAR<A,B>
Base clock accuracy	50 ppm
Inputs	Gate, Source, HW_Arm, Aux, A, B, Z, Up_Down, Sample Clock
Routing options for inputs	
NI PCIe-6341/6343	Any PFI, RTSI, many internal signals
NI PXIe-6341	Any PFI, PXIe-DSTAR<A,B>, PXI_TRIG, PXI_STAR, many internal signals
NI USB-6341/6343	Any PFI, many internal signals

FIFO..... 127 samples per counter

Data transfers

NI PCIe/PXIe-6341/6343 Dedicated scatter-gather DMA controller for each counter/timer, programmed I/O

NI USB-6341/6343..... USB Signal Stream, programmed I/O

Frequency Generator

Number of channels..... 1

Base clocks 20 MHz, 10 MHz, 100 kHz

Divisors..... 1 to 16

Base clock accuracy..... 50 ppm

Output can be available on any PFI or RTSI terminal.

Phase-Locked Loop (PLL)

Number of PLLs 1

Reference clock locking frequencies

Reference Signal	Locking Input Frequency (MHz)		
	PCIe	PXIe	USB
PXIe-DSTAR<A,B>	—	10, 20, 100	—
PXI_STAR	—	10, 20	—
PXIe_CLK100	—	100	—
PXI_TRIG <0..7>	—	10, 20	—
RTSI <0..7>	10, 20	—	—
PFI <0..15>	10, 20	10, 20	10

Output of PLL..... 100 MHz Timebase; other signals derived from 100 MHz Timebase including 20 MHz and 100 kHz Timebases

External Digital Triggers

Source

NI PCIe-6341/6343..... Any PFI, RTSI

NI PXIe-6341 Any PFI, PXIe-DSTAR<A,B>, PXI_TRIG, PXI_STAR

NI USB-6341/6343..... Any PFI

Polarity	Software-selectable for most signals
Analog input function	Start Trigger, Reference Trigger, Pause Trigger, Sample Clock, Convert Clock, Sample Clock Timebase
Analog output function	Start Trigger, Pause Trigger, Sample Clock, Sample Clock Timebase
Counter/timer functions	Gate, Source, HW_Arm, Aux, A, B, Z, Up_Down, Sample Clock
Digital waveform generation (DO) function	Start Trigger, Pause Trigger, Sample Clock, Sample Clock Timebase
Digital waveform acquisition (DI) function	Start Trigger, Reference Trigger, Pause Trigger, Sample Clock, Sample Clock Timebase

Device-To-Device Trigger Bus

Input source

NI PCIe-6341/6343	RTSI <0..7> ¹
NI PXIe-6341	PXI_TRIG <0..7>, PXI_STAR, PXIe-DSTAR<A,B>
NI USB-6341/6343	None

Output destination

NI PCIe-6341/6343	RTSI <0..7> ²
NI PXIe-6341	PXI_TRIG <0..7>, PXIe-DSTARC
NI USB-6341/6343	None

Output selections..... 10 MHz Clock, frequency generator output, many internal signals

Debounce filter settings 90 ns, 5.12 μ s, 2.56 ms, custom interval, disable; programmable high and low transitions; selectable per input

¹ In other sections of this document, *RTSI* refers to RTSI <0..7> for NI PCIe-6341/6343 or PXI_TRIG <0..7> for NI PXIe-6341.

² In other sections of this document, *RTSI* refers to RTSI <0..7> for NI PCIe-6341/6343 or PXI_TRIG <0..7> for NI PXIe-6341.

Bus Interface

NI PCIe-6341/6343

Form factor	x1 PCI Express, specification v1.1 compliant
Slot compatibility	x1, x4, x8, and x16 PCI Express slots ¹
DMA channels	8, analog input, analog output, digital input, digital output, counter/timer 0, counter/timer 1, counter/timer 2, counter/timer 3

NI PXIe-6341

Form factor	x1 PXI Express peripheral module, specification rev 1.0 compliant
Slot compatibility	x1 and x4 PXI Express or PXI Express hybrid slots
DMA channels	8, analog input, analog output, digital input, digital output, counter/timer 0, counter/timer 1, counter/timer 2, counter/timer 3

All NI PXIe-6341 devices may be installed in PXI Express slots or PXI Express hybrid slots.

NI USB-6341/6343

USB compatibility	USB 2.0 Hi-Speed or full-speed ²
USB Signal Stream	8, can be used for analog input, analog output, digital input, digital output, counter/timer 0, counter/timer 1, counter/timer 2, counter/timer 3

Power Requirements



Caution The protection provided by the NI 6341/6343 can be impaired if it is used in a manner not described in the *X Series User Manual*.

NI PCIe-6341/6343

Without disk drive power connector installed	
+3.3 V	1.4 W
+12 V	8.6 W
With disk drive power connector installed	
+3.3 V	1.4 W
+12 V	3 W
+5 V	15 W

¹ Some motherboards reserve the x16 slot for graphics use. For PCI Express guidelines, refer to ni.com/pciexpress.

² Operating on a full-speed bus will result in lower performance and you might not be able to achieve maximum sampling/update rates.

NI PXIe-6341	
+3.3 V	1.6 W
+12 V	19.8 W



Caution NI USB-6341/6343 devices *must* be powered with NI offered AC adapter or a National Electric Code (NEC) Class 2 DC source that meets the power requirements for the device and has appropriate safety certification marks for country of use.

NI USB-6341/6343	
Power supply requirements.....	11 to 30 VDC, 30 W, 2 positions 3.5 mm pitch pluggable screw terminal with screw locks similar to Phoenix Contact MC 1,5/2-STF-3,5 BK
Power input mating connector	Phoenix Contact MC 1,5/2-GF-3,5 BK or equivalent

Current Limits



Caution Exceeding the current limits may cause unpredictable behavior by the device and/or PC/chassis.

NI PCIe-6341/6343	
Without disk drive power connector installed	
P0/PFI/P1/P2 and +5 V terminals combined.....	1 A max
With disk drive power connector installed	
+5 V terminal (connector 0).....	1 A max ¹
+5 V terminal (connector 1).....	1 A max ¹
P0/PFI/P1/P2 combined.....	1 A max

NI PXIe-6341	
+5 V terminal (connector 0).....	1 A max ¹
P0/PFI/P1/P2 and +5 V terminals combined.....	2 A max

NI USB-6341/6343	
+5 V terminal.....	1 A max ¹
P0/PFI/P1/P2 and +5 V terminals combined.....	2 A max

¹ Has a self-resetting fuse that opens when current exceeds this specification.

Physical Requirements

Printed circuit board dimensions

NI PCIe-6341/6343.....	9.9 × 16.8 cm (3.9 × 6.6 in.) (half-length)
NI PXIe-6341	Standard 3U PXI

Enclosure dimensions (includes connectors)

NI USB-6341/6343	
Screw Terminal.....	26.4 × 17.3 × 3.6 cm (10.4 × 6.8 × 1.4 in.)
BNC.....	20.3 × 18.5 × 6.8 cm (8.0 × 7.3 × 2.7 in)

Weight

NI PCIe-6341	104 g (3.6 oz)
NI PCIe-6343.....	114 g (4.0 oz)
NI PXIe-6341	157 g (5.5 oz)
NI USB-6341	
Screw Terminal.....	1.406 kg (3 lb 1.6 oz)
BNC.....	1.520 kg (3 lb 5.6 oz)
NI USB-6343	
Screw Terminal.....	1.445 kg (3 lb 3 oz)
BNC.....	1.803 kg (3 lb 15.6 oz)

I/O connector

NI PCIe/PXIe-6341	1 68-pin VHDCI
NI PCIe/PXIe-6343	2 68-pin VHDCI
NI USB-6341	
Screw Terminal.....	64 screw terminals
BNC.....	20 BNCs and 30 screw terminals
NI USB-6343	
Screw Terminal.....	128 screw terminals
BNC.....	30 BNCs and 60 screw terminals

NI PCIe/PXIe-6341/6343 mating connectors:

- 68-Pos Right Angle Single Stack PCB-Mount VHDCI (Receptacle), MOLEX 71430-0011
- 68-Pos Right Angle Dual Stack PCB-Mount VHDCI (Receptacle), MOLEX 74337-0016
- 68-Pos Offset IDC Cable Connector (Plug) (SHC68-*), MOLEX 71425-3001

NI PCIe-6341/6343

disk drive power connector..... Standard ATX peripheral connector
(not serial ATA)

NI USB-6341/6343 screw terminal wiring..... 16-24 AWG

If you need to clean the chassis, wipe it with a dry towel.

Maximum Working Voltage¹

Channel to earth 11 V, Measurement Category I



Caution Do *not* use for measurements within Categories II, III, or IV.

Environmental

Operating temperature

NI PCIe-6341/6343 0 to 50 °C

NI PXIe-6341 0 to 55 °C

NI USB-6341/6343 0 to 45 °C

Storage temperature -40 to 70 °C

Operating humidity 10 to 90% RH, noncondensing

Storage humidity 5 to 90% RH, noncondensing

Pollution Degree 2

Maximum altitude 2,000 m

Indoor use only

Shock and Vibration (NI PXIe-6341 Only)

Operational shock 30 g peak, half-sine, 11 ms pulse
(Tested in accordance with IEC-60068-2-27.
Test profile developed in accordance with
MIL-PRF-28800F.)

Random vibration

Operating 5 to 500 Hz, 0.3 g_{rms}

Nonoperating 5 to 500 Hz, 2.4 g_{rms}

(Tested in accordance with IEC-60068-2-64.
Nonoperating test profile exceeds the
requirements of MIL-PRF-28800F, Class 3.)

¹ *Maximum working voltage* refers to the signal voltage plus the common-mode voltage.

Safety

This product meets the requirements of the following standards of safety for electrical equipment for measurement, control, and laboratory use:

- IEC 61010-1, EN 61010-1
- UL 61010-1, CSA 61010-1



Note For UL and other safety certifications, refer to the product label or the *Online Product Certification* section.

Electromagnetic Compatibility

This product meets the requirements of the following EMC standards for electrical equipment for measurement, control, and laboratory use:

- EN 61326-1 (IEC 61326-1): Class A emissions; Basic immunity
- EN 55011 (CISPR 11): Group 1, Class A emissions
- AS/NZS CISPR 11: Group 1, Class A emissions
- FCC 47 CFR Part 15B: Class A emissions
- ICES-001: Class A emissions



Caution When operating this product, use shielded cables and accessories



Note For EMC declarations and certifications and additional information, refer to the *Online Product Certification* section.

CE Compliance

This product meets the essential requirements of applicable European Directives as follows:

- 2006/95/EC; Low-Voltage Directive (safety)
- 2004/108/EC; Electromagnetic Compatibility Directive (EMC)

Online Product Certification

To obtain product certifications and the Declaration of Conformity (DoC) for this product, visit ni.com/certification, search by model number or product line, and click the appropriate link in the Certification column.

Environmental Management

NI is committed to designing and manufacturing products in an environmentally responsible manner. NI recognizes that eliminating certain hazardous substances from our products is beneficial to the environment and to NI customers.

For additional environmental information, refer to the *Minimize Our Environmental Impact* Web page at ni.com/environment. This page contains the environmental regulations and directives with which NI complies, as well as other environmental information not included in this document.

Waste Electrical and Electronic Equipment (WEEE)



EU Customers At the end of the product life cycle, all products *must* be sent to a WEEE recycling center. For more information about WEEE recycling centers, National Instruments WEEE initiatives, and compliance with WEEE Directive 2002/96/EC on Waste Electrical and Electronic Equipment, visit ni.com/environment/weee.htm.

电子信息产品污染控制管理办法（中国 RoHS）



中国客户 National Instruments 符合中国电子信息产品中限制使用某些有害物质指令 (RoHS)。关于 National Instruments 中国 RoHS 合规性信息，请登录 ni.com/environment/rohs_china。(For information about China RoHS compliance, go to ni.com/environment/rohs_china.)

Contact Information

National Instruments corporate headquarters
11500 North Mopac Expressway, Austin, Texas, 78759-3504
512 795 8248
ni.com/niglobal

Figure 1. NI PCIe/PXIe-6341 Pinout

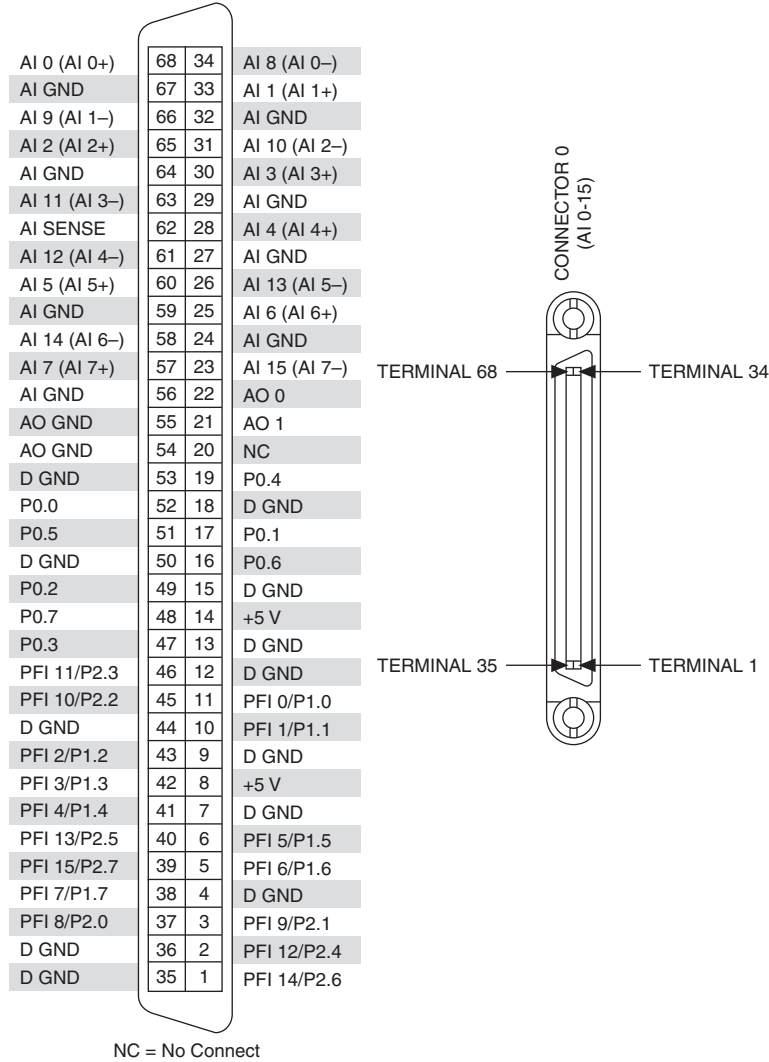
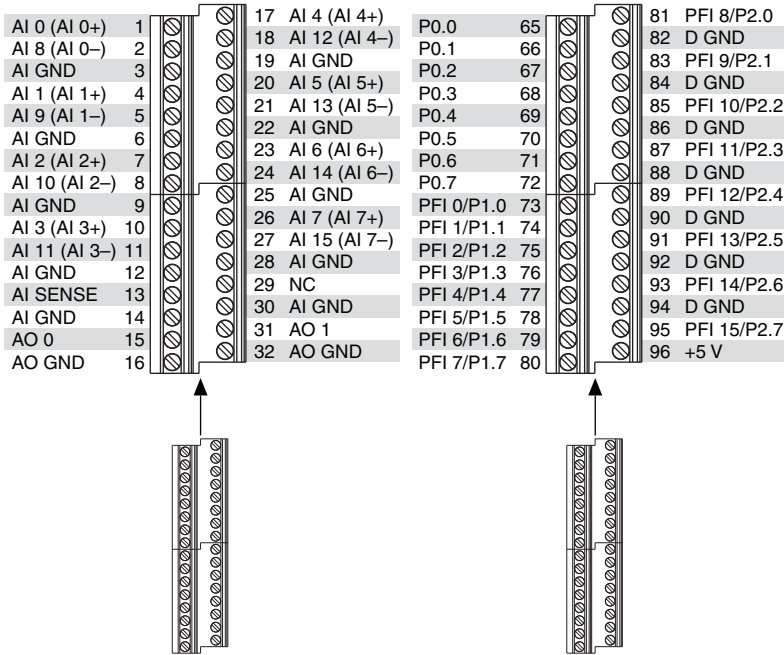


Figure 2. NI USB-6341 Screw Terminal Pinout



NC = No Connect

Figure 3. NI USB-6341 BNC Front Panel and Pinout

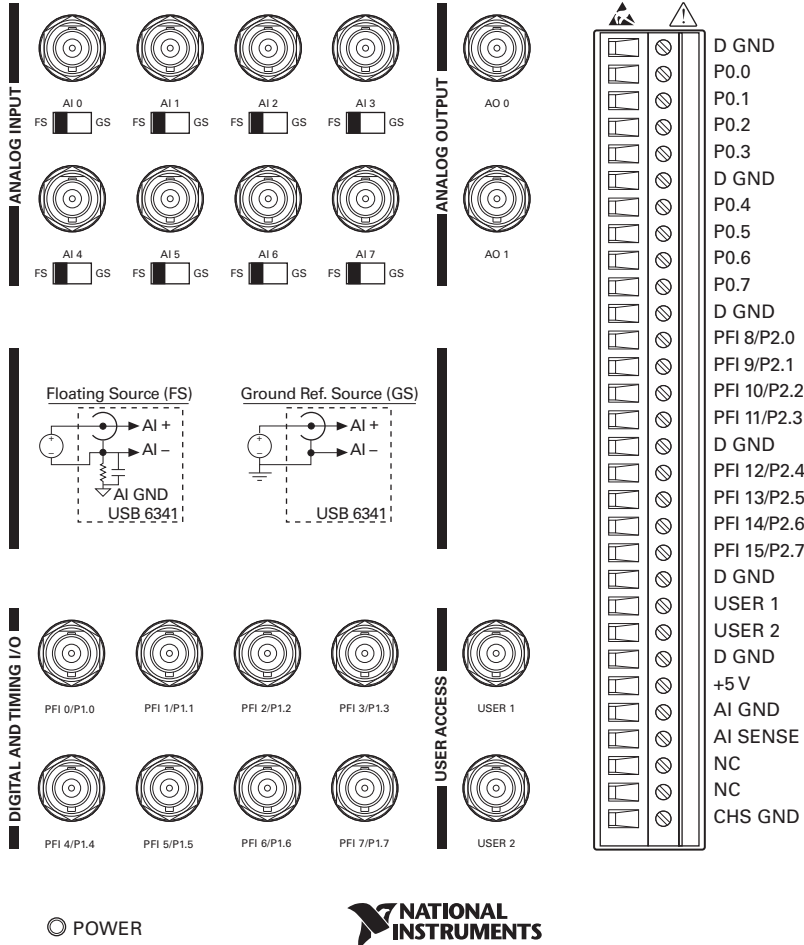


Figure 4. NI PCIe-6343 Pinout

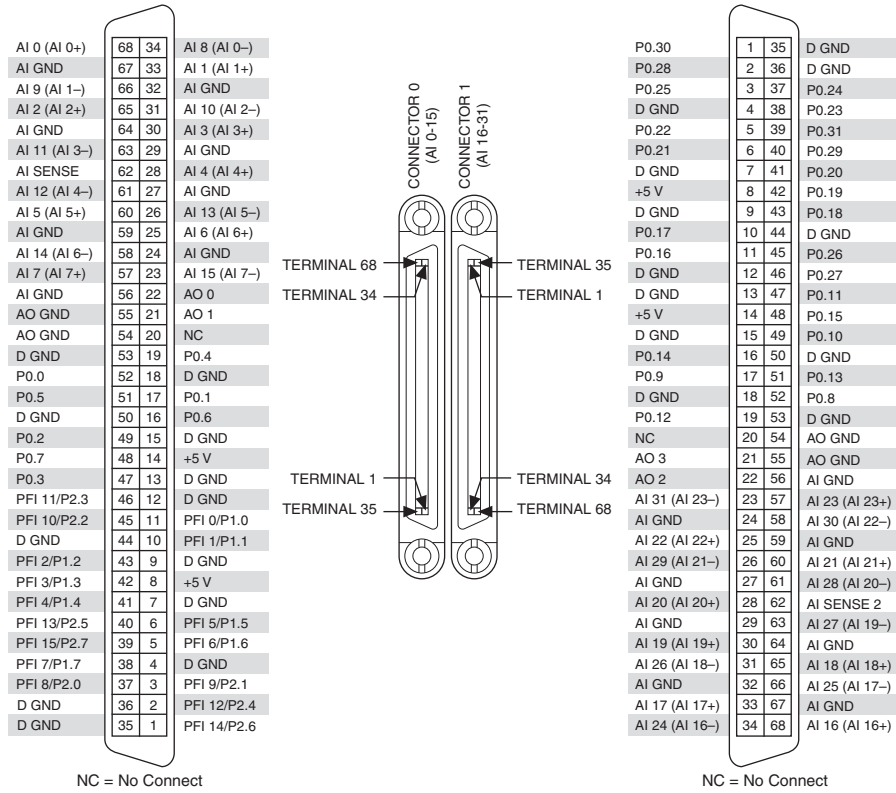
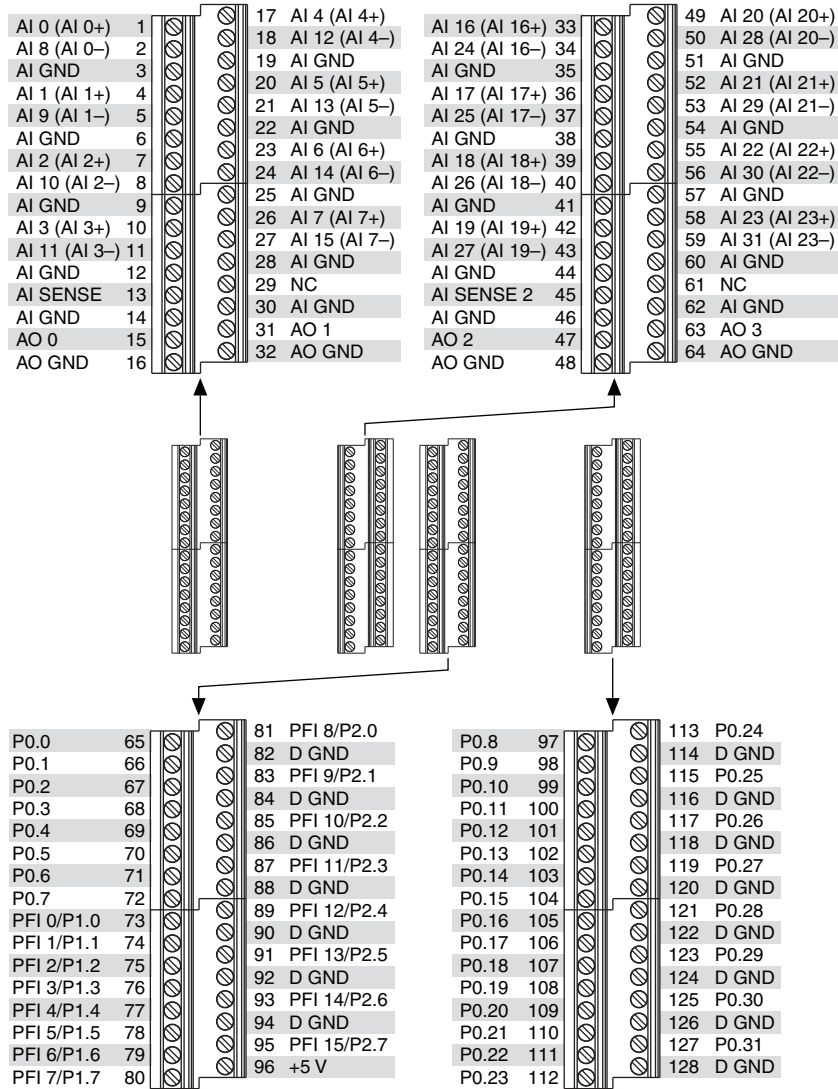
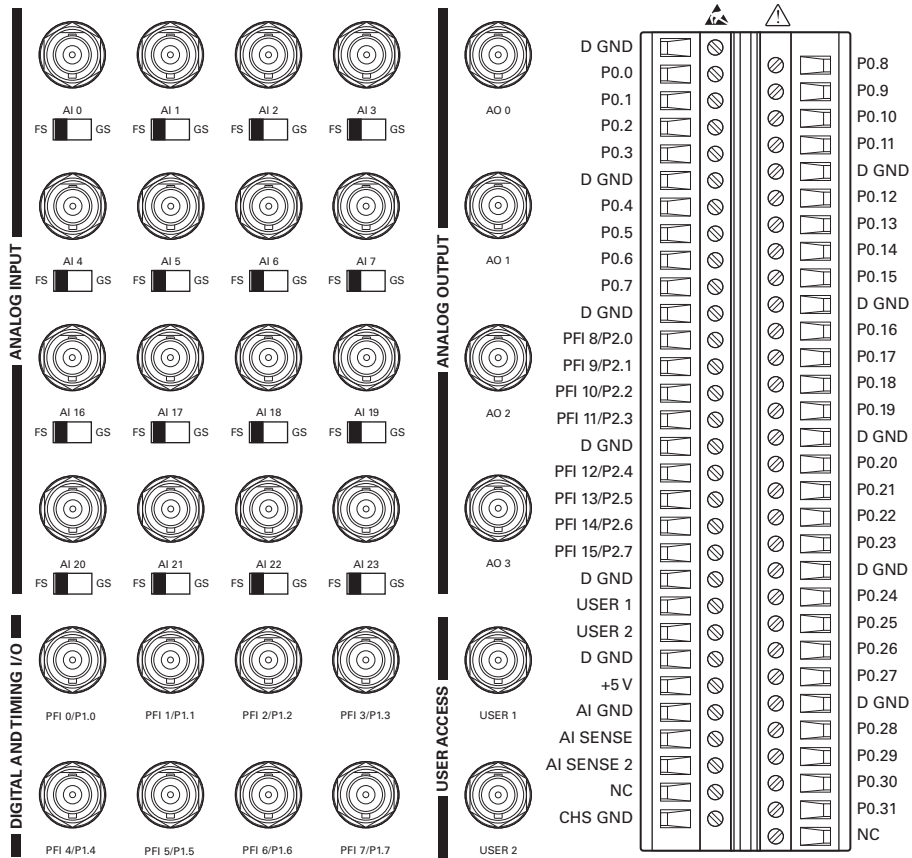


Figure 5. NI USB-6343 Screw Terminal Pinout



NC = No Connect

Figure 6. NI USB-6343 BNC Front Panel and Pinout



⊙ POWER



Refer to the *NI Trademarks and Logo Guidelines* at ni.com/trademarks for more information on National Instruments trademarks. Other product and company names mentioned herein are trademarks or trade names of their respective companies. For patents covering National Instruments products/technology, refer to the appropriate location: **Help»Patents** in your software, the `patents.txt` file on your media, or the *National Instruments Patents Notice* at ni.com/patents. You can find information about end-user license agreements (EULAs) and third-party legal notices in the readme file for your NI product. Refer to the *Export Compliance Information* at ni.com/legal/export-compliance for the National Instruments global trade compliance policy and how to obtain relevant HTS codes, ECCNs, and other import/export data.

© 2009–2013 National Instruments. All rights reserved.

370786D-01

Jan13



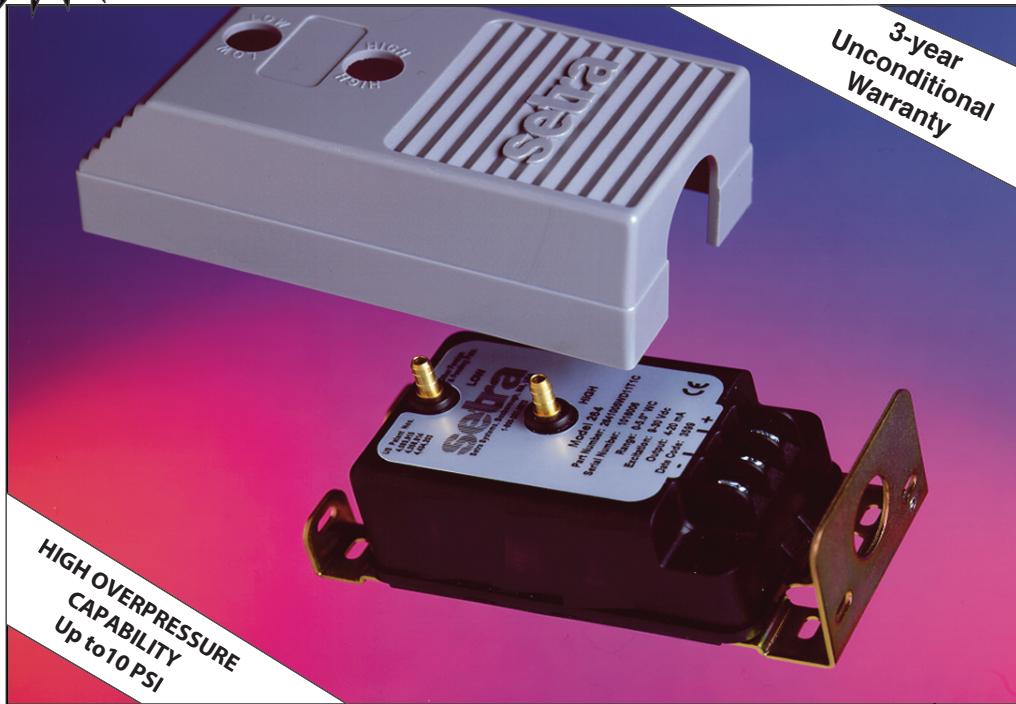
Model 264

Very Low Differential Pressure Transducer

Unidirectional Ranges: 0 - 0.1 to 0 - 100 in. W.C.

Bidirectional Ranges: 0 - ±0.5 to 0 - ±50 in. W.C.

Air or Non-Conducting Gas



3-year Unconditional Warranty

HIGH OVERPRESSURE CAPABILITY Up to 10 PSI

Applications

- Heating, Ventilating and Air Conditioning (HVAC)
- Energy Management Systems
- Variable Air Volume and Fan Control (VAV)
- Environmental Pollution Control
- Lab and Fume Hood Control
- Oven Pressurization and Furnace Draft Controls

Features

- Up to 10 PSI Overpressure (Range Dependent)
- Installation Time Minimized with Snap Track Mounting and Easy-To-Access Pressure Ports and Electrical Connections
- 0 to 5 VDC or 2-wire 4 to 20 mA Analog Outputs Are Compatible with Energy Management Systems
- Reverse Wiring Protection
- Internal Regulation Permits Use with Unregulated DC Power Supplies
- Fire Retardant Case (UL 94 V-0 Approved)
- Meets CE Conformance Standards

Setra Systems 264 pressure transducers sense differential or gauge (static) pressure and convert this pressure difference to a proportional electrical output for either unidirectional or bidirectional pressure ranges. The 264 Series is offered with a high level analog 0 to 5 VDC or 4 to 20 mA output.

Used in Building Energy Management Systems, these transducers are capable of measuring pressures and flows with the accuracy necessary for proper building pressurization and air flow control.

The 264 Series transducers are available for air pressure ranges as low as 0.1 in. W.C. full scale to 100 in. W.C. full scale. Static standard accuracy is ±1.0% full scale in normal ambient temperature environments, but higher accuracies are available. The units are temperature compensated to 0.033% FS/°F thermal error over the temperature range of 0°F to +150°F.

The Model 264 utilizes an improved all stainless steel micro-tig welded sensor. The tensioned stainless steel diaphragm and insulated stainless steel electrode, positioned close to the diaphragm, form a variable capacitor. Positive pressure moves the diaphragm toward the electrode, increasing the capacitance. A decrease in pressure moves the diaphragm away from the electrode, decreasing the capacitance. The change in capacitance is detected and converted to a linear DC electrical signal by Setra's unique electronic circuit.

The tensioned sensor allows up to 10 PSI overpressure (range dependent) with no damage to the unit. In addition, the parts that make up the sensor have thermally matched coefficients, which promote improved temperature performance and excellent long term stability.

When it comes to a product to rely on - choose the Model 264. When it comes to a company to trust - choose Setra.



Visit Setra Online:
<http://www.setra.com>

setra
800-257-3872

NOTE: Setra quality standards are based on ANSI-Z540-1. The calibration of this product is NIST traceable.

U.S. Patent nos. 4093915; 4358814; 4434203; 6019002; 6014800. Other Patents Pending.

Model 264 Specifications

Performance Data

	Standard	Optional
Accuracy* RSS(at constant temp)	±1.0% FS	±0.4% FS ±0.25% FS
Non-Linearity, BFSL	±0.96% FS	±0.38% FS ±0.22% FS
Hysteresis	0.10% FS	0.10% FS 0.10% FS
Non-Repeatability	0.05% FS	0.05% FS 0.05% FS

Thermal Effects**

Compensated Range °F(°C)	0 to +150 (-18 to +65)
Zero/Span Shift %FS/°F(°C)	0.033 (0.06)
Maximum Line Pressure	10 psi
Overpressure	Up to 10 psi (Range Dependent)
Long Term Stability	0.5% FS/1 YR

Position Effect	Range	Zero Offset (%FS/G)
(Unit is factory calibrated at 0g effect in the vertical position.)	To 0.5 in. WC	0.60
	To 1.0 in. WC	0.50
	To 2.5 in. WC	0.22
	To 5 in. WC	0.14

* RSS of Non-Linearity, Hysteresis, and Non-Repeatability.

**Units calibrated at nominal 70 °F. Maximum thermal error computed from this datum.

Environmental Data

Temperature	
Operating* °F (°C)	0 to +175 (-18 to +79)
Storage °F (°C)	-65 to +250 (-54 to +121)

*Operating temperature limits of the electronics only. Pressure media temperatures may be considerably higher.

Physical Description

Case	Fire-Retardant Glass Filled Polyester (UL 94 V-0 Approved)
Mounting	Four screw holes on removable zinc plated steel base (designed for 2.75" snap track)
Electrical Connection	Screw Terminal Strip
Pressure Fittings	3/16" O.D. barbed brass pressure fitting for 1/4" push-on tubing
Zero and Span Adjustments	Accessible on top of case
Weight (approx.)	10 ounces

Pressure Media

Typically air or similar non-conducting gases.

Specifications subject to change without notice.

Electrical Data (Voltage)

Circuit	3-Wire (Com, Exc, Out)
Excitation	9 to 30 VDC
Output*	0 to 5 VDC**
Bidirectional output at zero pressure:	2.5 VDC**
Output Impedance	100 ohms

*Calibrated into a 50K ohm load, operable into a 5000 ohm load or greater.
 **Zero output factory set to within ±50mV (±25 mV for optional accuracies).
 **Span (Full Scale) output factory set to within ±50mV. (±25 mV for optional accuracies).

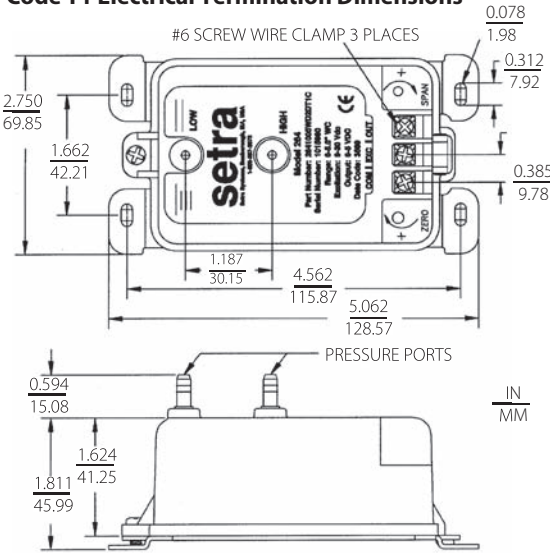
Electrical Data (Current)

Circuit	2-Wire
Output*	4 to 20mA**
Bidirectional output at zero pressure:	12mA**
External Load	0 to 800 ohms
Minimum supply voltage (VDC) = 9+ 0.02 x (Resistance of receiver plus line).	
Maximum supply voltage (VDC) = 30+ 0.004 x (Resistance of receiver plus line).	

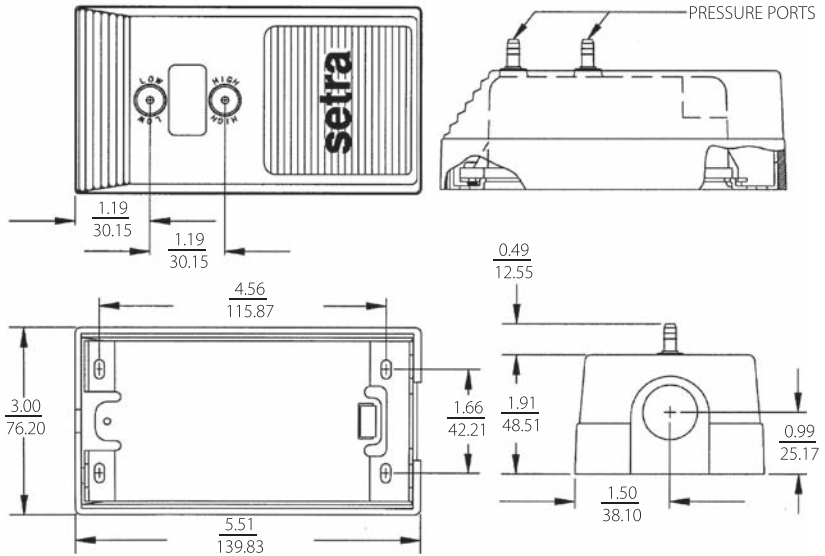
*Calibrated at factory with a 24 VDC loop supply voltage and a 250 ohm load.
 **Zero output factory set to within ±0.16mA (±0.08 mA for optional accuracies).
 **Span (Full Scale) output factory set to within ±0.16mA (±0.08 mA for optional accuracies).

Outline Drawings

Code T1 Electrical Termination Dimensions



Optional 1/2" Conduit Electrical Enclosure Dimensions



ORDERING INFORMATION

Code all blocks in table.

Example: Part No. 26412R5WD11T1C for a 264 Transducer 0 to 2.5 in. WC Range, 4 to 20 mA Output, Terminal Strip Electrical Connection, and ±1% Accuracy.

Model	Differential	Bidirectional	Output	Elec. Termination	Accuracy
2641 = 264	OR1WD = 0 to 0.1 in. WC R25WD = 0 to 0.25 in. WC OR5WD = 0 to 0.5 in. WC 001WD = 0 to 1 in. WC 2R5WD = 0 to 2.5 in. WC 003WD = 0 to 3 in. WC 005WD = 0 to 5 in. WC 010WD = 0 to 10 in. WC 015WD = 0 to 15 in. WC 025WD = 0 to 25 in. WC 050WD = 0 to 50 in. WC 100WD = 0 to 100 in. WC	R05WB = ±0.05 in. WC OR1WB = ±0.1 in. WC R25WB = ±0.25 in. WC OR5WB = ±0.5 in. WC 001WB = ±1 in. WC 1R5WB = ±1.5 in. WC 2R5WB = ±2.5 in. WC 005WB = ±5 in. WC 7R5WB = ±7.5 in. WC 010WB = ±10 in. WC 025WB = ±25 in. WC 050WB = ±50 in. WC	11 = 4-20 mA 2D = 0 to 5 VDC	Standard T1 = Terminal Strip Optional A1 = 1/2" Conduit Enclosure	Standard C = ±1% FS Optional (w/Cal. Cert.) E = ±0.4% FS F = ±0.25% FS G = ±1% FS

Please contact factory for versions not shown.

While we provide application assistance on all Setra products, both personally and through our literature, it is the customer's responsibility to determine the suitability of the product in the application.

150 Appendix on Broadborough, MA 01719/Tel: 978-263-1400
 Toll Free: 800-257-3872; Fax: 978-264-0292; email: sales@setra.com



SSP264 Rev.G 01/24/08

P 26

Intelligent differential pressure transmitter with scalable range



Special features

- range and display scalable
- switching contacts with adjustable switching thresholds
- NEW: Now optionally with air consumption counter
- output characteristics can be configured (root-extraction / linear)
- automatic zero-point calibration prevents zero-point drift
- unit conversion (e. g. mmH₂O, mmHg, etc.)
- integrated valve provides a high level of overpressure protection
- Manual or external activation of zero adjustment
- available with interface USB (optional)
- also for top-hat rail mounting
- multilingual menu (English, German, Italian, French)
- ± measuring ranges

Technical data

measurement ranges (others available upon request)	10/50/100/250/500 Pa 1/2.5/5/10/20/50/100 kPa free scalable from 10..100% within a range
margin of error (0.3 Pa margin of error for reference)	0.5% + 0.3 Pa of scaled range (40...100% of end value)
deflection drift / temperature	0.03 %/K (+10 °C...+50 °C)
zero point drift / temperature	± 0 % (cyclical zero-point correction)
overload capacity	600 kPa for measurement ranges ≥ 2.5 kPa 200x for measurement ranges < 2.5 kPa
medium	air, all non-aggressive gases
max. line pressure	600 kPa for measurement ranges ≥ 2.5 kPa 200x for measurement ranges < 2.5 kPa
sensor response time	25 ms
time constants	25 ms ... 60 s (adjustable)
operating temperature	+10 °C... +50 °C
storage temperature	-10 °C... +70 °C
power consumption	approx. 6 VA
weight	approx. 0.75 kg
cable glands	3 x M 16
pressure ports	for hose NW 6 mm, others available upon request
protection class	IP 65, USB IP 40
testing	CE, CSA, GOST

output*	A	power supply	B
0 ... 10 V ($R_L \geq 2 \text{ k}\Omega$)	1	24 V AC/DC	24ACDC
0...20 mA ($R_L \leq 500 \Omega$)	0	24 VAC <small>with galvanic separation</small>	24AC
4...20 mA ($R_L \leq 500 \Omega$)	4	230/115 VAC	230/115
± 5 V ($R_L \geq 2 \text{ k}\Omega$)	5		

* output signal selectable

measurement range	C	margin of error	D
measurement range e. g., 0 – 10 Pa, mbar, mmHg, etc.		standard	S
		±0.2% of end value, but min. 0.3 Pa (from ≥ 150 Pa)	2

LCD	E	contact points	F
none	0	none	0
LCD and buttons for configuration	LC	2 switching relays max. 230 VAC, 6 A	2
		2 relays, with air counter functionality	Z

interface / external zero-point calibration	G
none	0
USB, datacable included in delivery	US
external zero-point calibration	EX

Order key

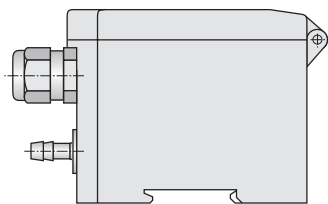
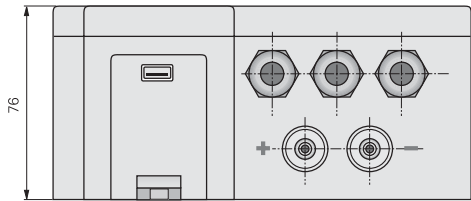
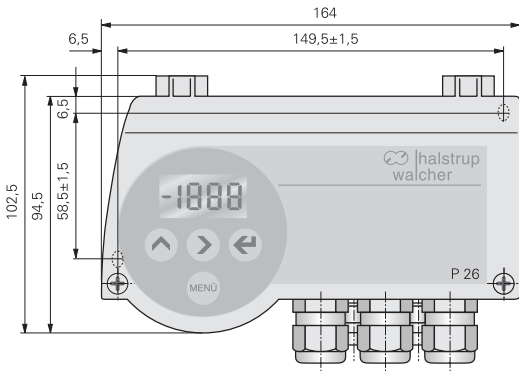
	A	B	C	D	E	F	G
P 26	-	-	-	-	-	-	-

accessories	
<input type="checkbox"/> DAkKS-DKD calibration certificate, German	9601-0003
<input type="checkbox"/> DAkKS-DKD calibration certificate, English	9601-0004
<input type="checkbox"/> factory calibration certificate	9601-0002

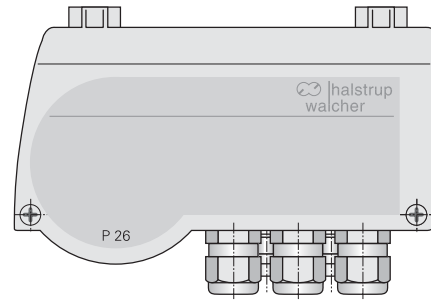
P 26

Dimension drawing

P 26 with LCD



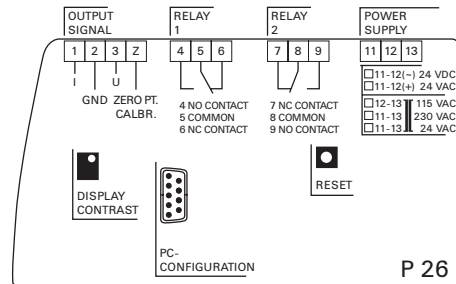
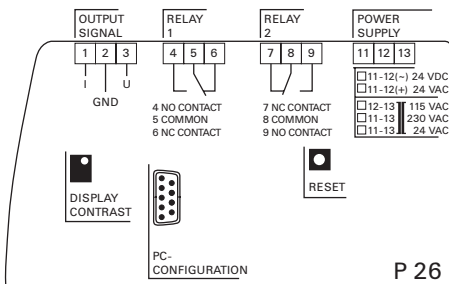
no LCD



P 26 Configuration software



Connection diagram



F900 Series Air Velocity and Air Temperature Sensors



applications

- HVAC
- Industrial Processes
- Automotive
- Air filtration Systems
- Electronics Enclosures, and
- Critical Containment Areas
- Biological Safety Cabinets
- Fume Hoods
- Clean Rooms

features

- Measures air & inert gas velocity and temperature
- Standard flow ranges between 0.15-10 m/s (approximately 30-2000 fpm)
- Temperature measurements from 0-70°C
- Digital UART Interface
- Linear 0-4 VDC airflow output from 0 to full-scale
- Wide voltage supply: 7-13VDC
- Temperature-compensated from 15-35°C
- Ideal for ducted or open airflow applications
- Available in multiple sensor heads
- Wide acceptance angle ($\pm 30^\circ$)

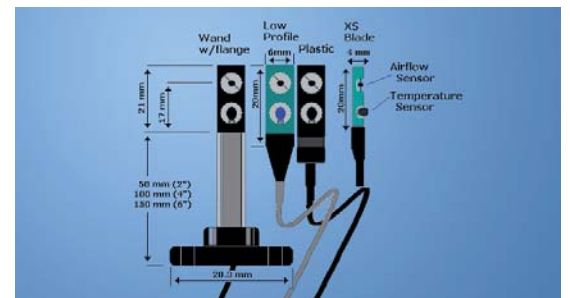
about

The F900 Airflow Sensor is designed to measure the velocity and temperature of airflows in applications such as HVAC, industrial processes, automotive, air filtration systems, electronics enclosures, and critical containment areas such as biological safety cabinets, fume hoods, and clean rooms.

With standard airflow sensing ranges from 0.15-2 m/s (30-400 fpm) to 0.15-10 m/s (30-2000 fpm), the Series F900 offers unparalleled price to performance, compact size, reliability with resistance to mechanical shock and vibration.



The F900 series has a linear 0-4V output and a digital 5v UART output depending on the model. The F900 is easy to install and operate. An adjustable mounting bracket is included with the sensor. In addition, the F900 can be ordered with any of the AccuSense remote sensing head options.



F900 Series Air Velocity and Air Temperature Sensors

airflow measurement

Air Velocity _____ Airflow Temperature _____
 Temperature compensation range: 15-35°C (60-95°F):
 Accuracy: ±5% of reading or ±0.05m/s (10fpm)
 ±10% of reading or ±0.05m/s (10fpm)
 Repeatability: ±1% of reading
 Airflow Temperature Measurement range: 0-70°C (32-158°F)
 Measurement Accuracy¹: ±1°C (1.8°F)
 Resolution: ±0.1°C

Temperature Compensation Range: The F900 is a thermal airflow sensor; it is sensitive to changes in air density and indicates velocity with reference to a set of standard conditions (25°C (77°F), 760mmHg (101.325kPa), and 0%RH). The F900 has been designed so that when used over the stated temperature compensation range, the sensor indicates very close to actual air velocity and minimal compensation is only required to account for changes in barometric pressure or altitude. Changes in relative humidity have a minimal impact and can usually be ignored.

¹ Above 0.5m/s (100fpm), ±1.5°C (2.7°F) below 0.5m/s (100fpm).

temperature measurement

Range 0-70°C (50-140°F)	Available on 5v UART output only
Accuracy ±1°C above 1 m/s (196 fpm) ±1.5°C below 1 m/s (196 fpm)	Resolution is ±0.1°C

electrical specifications

Supply Voltage 7-13 VDC	Warm-up Time <5 seconds
Supply Current 40-75 mA	Operating Temperature 0 – 70°C (32-158°F)
Response Time 1.5 seconds	Storage Temperature –10 to 100°C
Output is linearized 0-4.0 vdc, which equals 0 to full scale of calibrated range (airflow only).	

mechanical specifications

Dimensions	100 mm long X 12 mm diameter for standard unit, 91 mm X 12 mm for long tube with remote sensor heads
Vibration	Up to 25 G's
Acceptance Angles	Standard, rod w/flange, plastic heads are ±30°, low-profile is ±45°, XS blade is ±60° from perpendicular

connection specifications

Pin 1 Black	Supply Return
Pin 2 Red	Supply 7-13 VDC
Pin 3 White	Analog Airflow Output (0-4Vout) for calibrated range, up to 4.095V beyond calibrated range.
Pin 4 Orange	Digital serial output - 19200 BPS, 5v UART level, 8 bit, 1 stop bit
Pin 5 Yellow	Digital serial input – 19200 BPS, 5v UART levels, 8 bit, 1 stop bit -
Connector	Molex#22-01-2057 or equivalent

F900 - V - A - B - S - L

part number scheme

V = Velocity Range
 N = 0.15 - 2 m/s
 O = 0.15 – 5 m/s
 P = 0.15 - 10 m/s

A = Accuracy Specification
 5 = Greater of 5% of reading or ±0.05 m/s or 1% full-scale
 10 = Greater of 10% of reading or ±0.05 m/s or 1% full-scale

B = Body Type
 0 = Standard (Default) – short tube
 1 = Long tube (for remote sensor heads)

S = Sensor Head Type (for B = 1 ONLY)
 0 = Plastic
 1 = Low Profile
 2 = 50 mm (2") SS wand /w flange
 4 = 100 mm (4") SS wand /w flange
 6 = 150mm (6") SS wand /w flange
 9 = XS Blade

L = Sensor Cable Length (for B = 1 ONLY)
 2 = 2 m

User Manual available at www.degrec.com

© 2011 DEGREE CONTROLS, INC. rev A-1F

Onset Hobo U30 Specifications

Taken from Onset Website

- Normal operating range: -20°C to 40°C (-4°F to 104°F)
- Extended operating range: -40 to 60°C (-40 to 140°F) - see "Rechargeable Battery service Life" for impact of operations in Extended Operating Range.
- Sensor Inputs: 5 standard; option to expand to 10
- Smart Sensor Compatibility: Compatible with most Onset smart sensors, except for the S-BPA, S-TMA and S-THA
- Data Channels: Maximum of 15 (some sensors use more than one data channel)
- Alarm Output Relay: Can be configured to be activated, deactivated or pulsed on user-defined sensor alarms. The relay can be configured as normally open or normally closed, and is rated for 30 V and 1 amp max.
- Expansion Slot: One expansion slot is available for factory-installed expansion port.
- Local Communication: Full Speed USB via USB mini-B connector
- Size: 17.8 H x 11.7 D x 19.3 W cm (7.0 H x 4.6 D x 7.6 W inches)
- Weight: 2 kg (4 lbs 10 oz)
- Materials: Outer Enclosure: ABS blend with stainless steel hinge pins and bronze inserts
- Inner Enclosure: Polycarbonate with bronze inserts
- U-Bolts: Steel with zinc dichromate finish
- Gaskets: Silicone rubber
- Cable entry channel: EPDM rubber
- Cable entry bars: Aluminum with ABS plastic thumb screws
- Data Storage Memory: Nonvolatile flash data storage, 512K bytes local storage
- Memory Modes: Stop when full, wrap around when full
- Operational Indicators: Up to six (depending upon options) status lights provide basic diagnostics
- Logging Interval: 1 second to 18 hours, user-specified interval
- Battery Type: 4 Volt, 4.5 AHr or 10 AHr, Rechargeable sealed lead-acid
- Rechargeable Battery Service Life: Typical 3–5 years depending upon conditions of use. Operation within the extended operating range (but outside the normal range) will reduce battery service life.
- Time Accuracy: 0 to 2 seconds for the first data point and ± 5 seconds per week at 25°C (77°F)
- Environmental Rating: Weatherproof enclosure, tested to NEMA 6. (Requires proper installation of cable channel system)
- Mounting: 3.8 cm (1.5 inch) mast or wall mount
- Enclosure Access: Hinged door secured by two latches with eyelets for securing with user-supplied padlocks
- Sensor Network Cable Length: 100 m (328 ft) maximum
- External Power: External power is required. The system optionally accepts the following Onset solar panels:
 - SOLAR-1.2W
 - SOLAR-3W
 - SOLAR-6W
- Alternatively it accepts an AC power adapter:
 - AC-U30

- Optional Analog Sensor Port Specifications
- Input Channels: Two, single-ended
- Field Wiring: Two- or three-wire via screw terminals on detachable connector, 16–24 AWG.
- Replacement detachable connectors: Part of spares kit, Part No. A-FS-CVIA-7P-1
- Input Range: User-configurable: 0–20 mA DC, 0-2.5 VDC, 0-5 VDC, 0-10 VDC, or 0–20 VDC
- Minimum / Maximum Input Voltage: 0 / 24 VDC
- Minimum / Maximum Input Current: 0 / 24 mA DC
- Minimum Current Source Impedance: > 20 K Ω
- Accuracy: $\pm 0.25\%$ of FSR from 50mV to FSV
- ADC Resolution 12 bits
- Excitation Power: Switched 12 VDC, up to 50 mA; user-selectable warm-up from 5msec to 2 minutes

Wind Speed Smart Sensor (S-WSA-M003)

The Wind Speed smart sensor is designed to work with HOBO® Station loggers. The smart sensor has a plug-in modular connector that allows it to be added easily to a HOBO Station. All sensor parameters are stored inside the smart sensor, which automatically communicates configuration information to the logger without the need for any programming or extensive user setup.



Inside this Package

- Wind Speed smart sensor with mounting rod

Specifications

Measurement Range	0 to 45 m/sec (0 to 100 mph)
Accuracy	±1.1 m/sec (2.4 mph) or ±4% of reading, whichever is greater
Resolution	0.38 m/sec (0.8 mph)
Service Life	> 5 year life typical, factory replaceable mechanism
Distance Constant	3 m (9.8 ft)
Starting Threshold	≤ 1 m/sec (2.2 mph)
Maximum Wind Speed Survival	54 m/sec (120 mph)
Measurements	Wind speed: Average wind speed over logging interval Gust: Highest 3-second gust during the logging interval See <i>Measurement Operation</i> for more information.
Operating Temperature Range	-40° to 75°C (-40° to 167°F)
Environmental Rating	Sensor and Cable Jacket: Weatherproof
Housing	Three cup polycarbonate anemometer: Modified Teflon® bearings and hardened beryllium shaft with ice shedding design
Dimensions	41 x 16 cm (16 x 6.5 in.) including 1.27 cm (0.5 in) diameter mounting rod; 5.5 cm (2.1 in.) drip overhang
Weight	300 g (10 oz)
Bits per Sample	8 for each channel, 16 total
Number of Data Channels*	2
Measurement Averaging Option	No
Cable Length Available	3.5 m (11.5 ft)
Length of Smart Sensor Network Cable*	0.5 m (1.6 ft)
Part Number	S-WSA-M003
	The CE Marking identifies this product as complying with all relevant directives in the European Union (EU).

* A single HOBO Weather Station can accommodate 15 data channels and up to 100 m (328 ft) of smart sensor cable (the digital communications portion of the sensor cables).

Wind Direction Smart Sensor (S-WDA-M003)

The Wind Direction smart sensor is designed to work with HOBO® Stations. The smart sensor has a plug-in modular connector that allows it to be added easily to a HOBO Station. All sensor parameters are stored inside the smart sensor, which automatically communicates configuration information to the logger without the need for any programming or extensive setup.



Inside this Package

- Wind Direction smart sensor with mounting rod

Specifications

Measurement Range	0 to 355 degrees, 5 degree dead band
Accuracy	± 5 degrees
Resolution	1.4 degrees
Starting Threshold	1 m/s (2.2 mph)
Maximum Wind Speed Survival	60 m/s (134 mph)
Measurement Definition	Unit vector averaging used; vector components for each wind measurement are calculated every three seconds for duration of logging interval (see <i>Measurement Operation</i>)
Operating Temperature Range	-40°C to 70°C (-40°F to 158°F)
Environmental Rating	Weatherproof
Service Life	4 to 6 years typical depending upon environmental conditions
Housing	Injection-molded plastic housing and vane, static dissipating base, lead-free silicon bronze nose and aluminum mounting rod
Bearing Type	Two shielded stainless steel ball bearing
Turning Radius	Approximately 13.5 cm (5.25 in.)
Dimensions	46 x 20 cm (18 x 8.5 in.) including 1.27 cm (0.5 in) diameter mounting rod; 2.5 mm (0.1 in.) drip overhang
Weight	370 g (13 oz)
Bits per Sample	8
Number of Data Channels*	1
Measurement Averaging Option	Automatic averaging (see <i>Measurement Operation</i>)
Cable Length Available	3.5 m (11.5 ft)
Length of Smart Sensor Network Cable*	0.5 m (1.6 ft)
Part Number	S-WDA-M003
	The CE Marking identifies this product as complying with all relevant directives in the European Union (EU).

* A single HOBO Station logger can accommodate 15 data channels and up to 100 m (325 ft) of smart sensor cable (the digital communications portion of the sensor cables).